Title

Microlensing results toward the Galactic Bulge, theory of fitting blended light curves, and discussion of weak Lensing corrections

Author

Thomas, Christian L.

Publication Date

2006

Peer reviewed|Thesis/dissertation

UNIVERSITY OF CALIFORNIA, SAN DIEGO

Microlensing Results Toward the Galactic Bulge, Theory of Fitting Blended Light Curves, and Discussion of Weak Lensing Corrections

A dissertation submitted in partial satisfaction of the
requirements for the degree Doctor of Philosophy
in
Physics

by

Christian L. Thomas

Committee in charge:

Professor Kim Griest, Chair
Professor Tom Murphy
Professor Mike Norman
Professor Jeff Rabin
Professor Barney Rickett

2006

The dissertation of Christian L. Thomas is approved, and it is acceptable in quality and form for publication on microfilm:

Chair

University of California, San Diego

2006

TABLE OF CONTENTS

LIST OF FIGURES

LIST OF TABLES

ACKNOWLEDGEMENTS

I would like to thank my parents and brother and sister who have supported me for the past 26 years. Without their faith in me, support, and encouragement I would not be who I am today.

I thank my advisor, Kim Griest, who always had an open door and open ear. I appreciate your guidance, patience, and help. There are also many fellow graduate students that deserve thanks. I thank my officemates, Phil Amanik, Chad Kishimoto, Greg Bravo, and Cristel Smith with whom I have shared many stimulating, useful, and/or entertaining conversations. The same appreciation goes to Adam Orin and Nathan Miller. I want to especially thank Nao Suzuki (and all the graduate students back through the ages from which he gleaned his knowledge) for giving me several LaTeX files from his thesis. With out his help I might still be trying to format tables.

I must also thank everyone in the MACHO Collaboration, particularly Kim Griest and Piotr Popowski, but also Ken Freeman, Kem Cook, Charles Alcock, Tim Axelrod, Andrew Drake, Peter Quinn, Austin Tomaney, Robyn Allsman, Chris Stubbs, Dave Alves, Dave Bennett, Doug Welch, Bruce Peterson, Simon Chan, Stuart Marshall, Will Sutherland, Susannah Sabine, Elizabeth Turner. Andy Becker, Matt Lehner, Dante Minniti, Mark Pratt, Alex Rodgers, Andy Rorabeck, Jon Smillie, and Thor Vandehei. Chapters 2-5 are based on work they laid the groundwork for. While I have only met a few of you, I appreciate all the work you put in to the MACHO Project.

The text of Chapter 6, in full, is a reprint of material previously published in the Astrophysical Journal as Thomas, C. & Griest, K., "Fitting Photometry of Blended Microlensing Events", ApJ, Vol. 640, Issue 1, 299-307. I was the primary researcher and author and the research was conducted under the supervision of my advisor and coauthor, Kim Griest.

I am grateful for the support of the DoE under grant DEFG0390ER40546.

Lastly, I couldn't have made it through my time here in San Diego without all my friends from 29:11 who have become like family to me here.

Thank you all.

VITA

2001	B.S. California Institute of Technology
2001-2002	Teaching Assistant, Summer Science Program, Ojai, California
2001-2006	Teaching Assistant, Department of Physics, University of California, San Diego
2002-2006	Research Assitant, Department of Physics, University of California, San Diego
2003	M.S., Physics, University of California, San Diego
2006	Ph.D., Physics, University of California, San Diego

PUBLICATIONS

Thomas, C.L. & Griest, K., 2006, "Fitting Photometry of Blended Microlensing Events", ApJ, in press, astro-ph/0507218

Thomas, C.L., et al. 2005, "Galactic Bulge Microlensing Events from the MACHO Collaboration", ApJ, 631, 906

Popowski, P., et al. 2005, "Microlensing Optical Depth towards the Galactic Bulge Using Clump Giants from the MACHO Survey", ApJ, 631, 879

Griest, K. & Thomas, C.L. 2005, "Contamination in the MACHO dataset and the puzzle of LMC Microlensing", MNRAS, 359, 464

Thomas, C.L., et al. 2004, "New Measurement of Microlensing Optical Depth and Examination of Blending in Microlensing Events", AAS, 205, 2803

ABSTRACT OF THE DISSERTATION

Microlensing Results Toward the Galactic Bulge, Theory of Fitting Blended Light Curves, and Discussion of Weak Lensing Corrections

by

Christian L. Thomas
Doctor of Philosophy in Physics
University of California, San Diego, 2006
Professor Kim Griest, Chair

Analysis and results (Chapters 2-5) of the full 7 year Macho Project dataset toward the Galactic bulge are presented. A total of 450 high quality, relatively large signal-to-noise ratio, events are found, including several events exhibiting exotic effects, and lensing events on possible Sagittarius dwarf galaxy stars. We examine the problem of blending in our sample and conclude that the subset of red clump giants are minimally blended. Using 42 red clump giant events near the Galactic center we calculate the optical depth toward the Galactic bulge to be $\tau = 2.17^{+0.47}_{-0.38} \times 10^{-6}$ at $(l, b) = (1\overset{\circ}{.}50, -2\overset{\circ}{.}68)$ with a gradient of $(1.06 \pm 0.71) \times 10^{-6}\,\mathrm{deg}^{-1}$ in latitude, and $(0.29 \pm 0.43) \times 10^{-6}\,\mathrm{deg}^{-1}$ in longitude, bringing measurements into consistency with the models for the first time.

In Chapter 6 we reexamine the usefulness of fitting blended light-curve models to microlensing photometric data. We find agreement with previous workers (e.g. Woźniak & Paczyński) that this is a difficult proposition because of the degeneracy of blend fraction with other fit parameters. We show that follow-up observations at specific points along the light curve (peak region and wings) of high magnification events are the most helpful in removing degeneracies. We also show that very small errors in the baseline magnitude can result in problems in measuring the blend fraction, and study the importance of non-Gaussian errors in the fit results. The biases and skewness in the distribution of the recovered blend fraction is discussed. We also find a new approximation formula relating the blend

fraction and the unblended fit parameters to the underlying event duration needed to estimate microlensing optical depth.

In Chapter 7 we present work-in-progress on the possibility of correcting standard candle luminosities for the magnification due to weak lensing. We consider the importance of lenses in different mass ranges and look at the contribution from lenses that could not be observed. We conclude that it may be possible to perform this correction with relatively high precision (1-2%) and discuss possible sources of error and methods of improving our model.

1

Introduction

The Galaxy's structure and composition is one of the remaining problems of modern astrophysics. While the straightforward task of cataloguing bright stars has been done, the much harder task of taking inventory of the dimmer objects, brown dwarfs, faint stars, extra-solar planets, and stellar remnants such as white dwarfs and black holes is impossible to do directly. Gravitational microlensing was suggested as a method of observing and cataloguing these faint objects (Paczyński 1986; Griest 1991; Nemiroff 1991) and observed for the first time in 1993 (Alcock et al. 1993; Aubourg et al. 1993; Udalski et al. 1993). While the line of sight toward the Large Magellanic Cloud (LMC) is better for detection of dark matter, due to the large number density of stars in the disk, the line of sight toward the Galactic bulge is superior for detection of faint objects (Griest et al. 1991; Paczyński 1991). Observational results can be compared to models allowing a check on our understanding of Galactic structure.

To measure the mass along a line-of-sight, observing programs monitor many stars over a long period watching for microlensing events, specific transient brightenings of a star. This microlensing effect depends only on the mass of the lensing object and the geometry of the lens and source star, thus microlensing is a good way to "see" dim objects that would otherwise be invisible, even to the largest telescopes. Because it is sensitive to all objects microlensing results are a good check on galactic models. The results presented in §5 mark the first time observational results for the Galactic bulge have agreed with the predictions from models. This is due both to a decrease in the observational values and an increase in the theoretical predictions as described in §1.2.

1.1 Microlensing

1.1.1 History

> *Query 1.* Do not Bodies act upon Light at a distance, and by their action bend its rays, and is not this action *(cateris paribus)* strongest at the least distance?
>
> –Sir Isaac Newton,
> *Opticks*, 1704

The gravity of massive objects has been thought to bend light for over three centuries. First speculated upon by Newton in the late 17th century, the bending, or lensing, of light by massive objects was further examined by several others throughout two centuries before Einstein's General Theory of Relativity solidified our modern understanding of gravity and its interaction with light. Seventy-nine years after Newton first published *Opticks*, John Mitchell, in a letter to Cavendish, suggested the existence of objects that would now be called black holes, objects whose surface gravity was so strong it would prevent light from escaping. Cavendish later calculated the deflection of light due to a massive body but did not publish his work. Soldner (1804) did calculate and publish the deflection of light due to a massive body in Newtonian mechanics. He found

$$\tan\frac{\alpha}{2} = \frac{GM}{v^2 r}, \tag{1.1}$$

which, for the speed of light in the small angle limit, becomes

$$\alpha \approx \frac{2GM}{c^2 r}. \tag{1.2}$$

In 1911 Einstein arrived at the same result, albeit by different means. In 1915 Einstein repeated the calculation using the full equations of General Relativity and found a value for the deflection that was twice his previous result,

$$\alpha = \frac{4GM}{c^2 r}. \tag{1.3}$$

Shortly after the end of the first World War a test was made using the Sun as a "gravitational lens"[1] during a solar eclipse. These observations ruled out the Newtonian theory of gravity and, though errors were large, supported the new theory of General Relativity.

From this initial work and experimental test it took relatively little time to lay the groundwork for microlensing. In 1920 Eddington realized that if the angle of deflection is larger than the separation of the lens and source a second apparent image is formed. A few years later Chwolson (1924) pointed out that all stars within the maximum angle of deflection, α_{max} due to a given lens star should have secondary images on the opposite side of the lens and that if the background, or source, star and the lens were perfectly aligned a ring would be formed. Despite Chwolson's work such rings are now called "Einstein rings". Einstein later concluded that it was unlikely this lensing effect would be seen, due largely to the very high resolution required. While the deflection is too small for the two images near a compact lens to be resolved, it is possible to observe the magnification of the source. This magnification effect was first examined by Tikhov in 1938.

1.1.2 Calculations

Since surface brightness is not changed by gravitational lensing it is straightforward to calculate the magnification of a given star from the ratio of the area of the images to the area of the star. In order to calculate the ratio of areas we need the relationship between the image positions, $\theta_\pm$, and the real position, β as shown in Figure 1.1. Using the deflection angle $\frac{4GM}{c^2 r}$ and the geometry of the lens system the position of the source can be written as,

$$\beta = \theta_\pm - \frac{4GM}{c^2}\frac{D_{ls}}{D_l D_s}\frac{1}{\theta_\pm}\,, \tag{1.4}$$

where the "+" and "−" distinguish between the two solutions or the two images. The angle between the lens and the source star is β and the angles between the

[1]While perhaps a misnomer, in this context a massive object that is bending light from a more distant object is called a lens. Technically such an object does not focus light and no image is created, so "lens" and "image" are used here in a different sense than they are usually used in optics.

lens and the images are θ_+ and θ_-, choosing "+" gives the image on the same side of the lens as the real source and choosing "−" gives the image closer to the lens on the opposite side of the lens as the source. The distances[2], D_l, D_s, and D_{ls}, refer to the observer-lens distance, observer-source distance, and lens-source distance respectively. Solving equation (1.4) for θ with source position equal to zero (a perfectly aligned source and lens) gives us the Einstein ring angular radius:

$$\alpha_{\rm E} = \sqrt{\frac{4GM}{c^2}\frac{D_{ls}}{D_l D_s}}\,. \tag{1.5}$$

By symmetry the two images are confined to the line connecting the source and lens on the sky except in the special case of perfect alignment, when no such line can be defined. For an extended source each point in the source is mapped to a point along the line connecting it and the center of the lens.

Typically the Einstein ring radius is used to normalize the angles and make the problem dimensionless. When the lensing equation (1.4) is rewritten with angles normalized by this characteristic angle it becomes

$$u = x - 1/x, \tag{1.6}$$

where x is the observed position and u the real position or impact parameter. By solving equation (1.6) for x we can find the positions of the two images,

$$x_\pm = \frac{1}{2}(u \pm \sqrt{4 + u^2}). \tag{1.7}$$

We can use this equation to map an image in the source plane into an image in the lens plane as is illustrated in Figure 1.2 for different values of u.

The lensing equation (1.4) and the Einstein radius (1.5) can also be written in terms of distances instead of angles; presented in this manner they are

$$r = \frac{D_s}{D_l} r_\pm - \frac{4GM}{c^2}\frac{D_{ls}}{r_\pm} \tag{1.8}$$

and

$$R_{\rm E} = \sqrt{\frac{4GM}{c^2}\frac{D_l D_{ls}}{D_s}} = D_l \alpha_{\rm E}\,. \tag{1.9}$$

[2]For lensing on cosmological scales angular diameter distances should be used. In the first 6 Chapters of this dissertation the lensing considered will be exclusively galactic and distance measures will all be equal. In Chapter 7 we will introduce weak lensing and angular diameter distances.

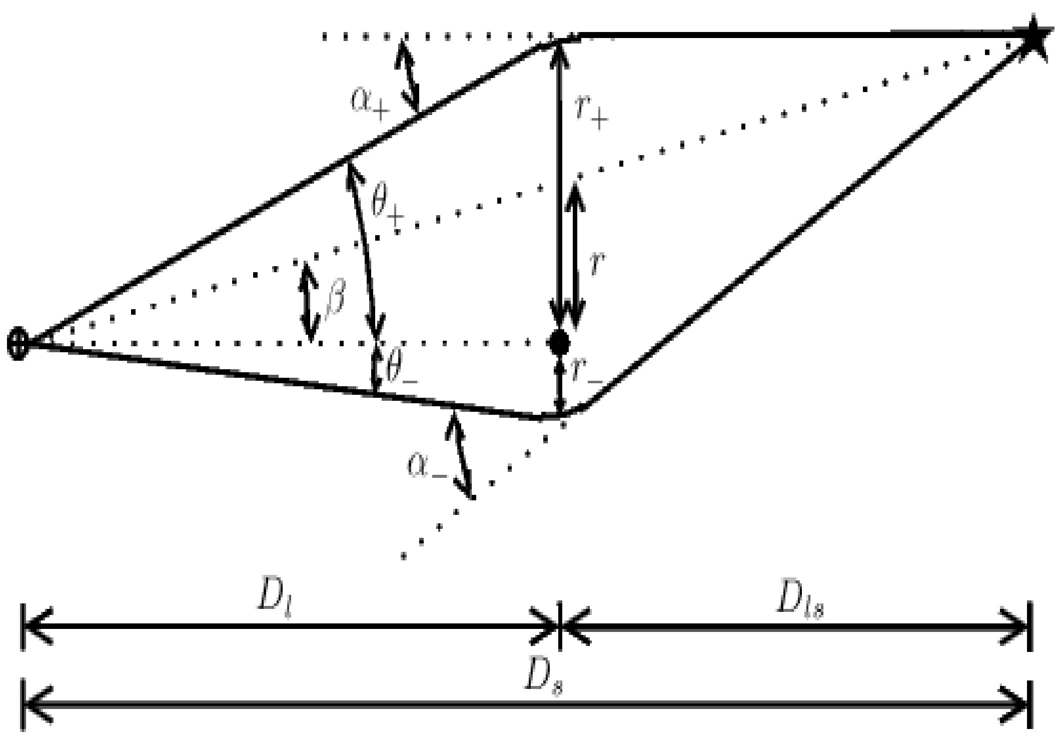

Figure 1.1 Geometry of lensing by a single compact lens. The observer is on the left, lens in the middle, and source star on the right.

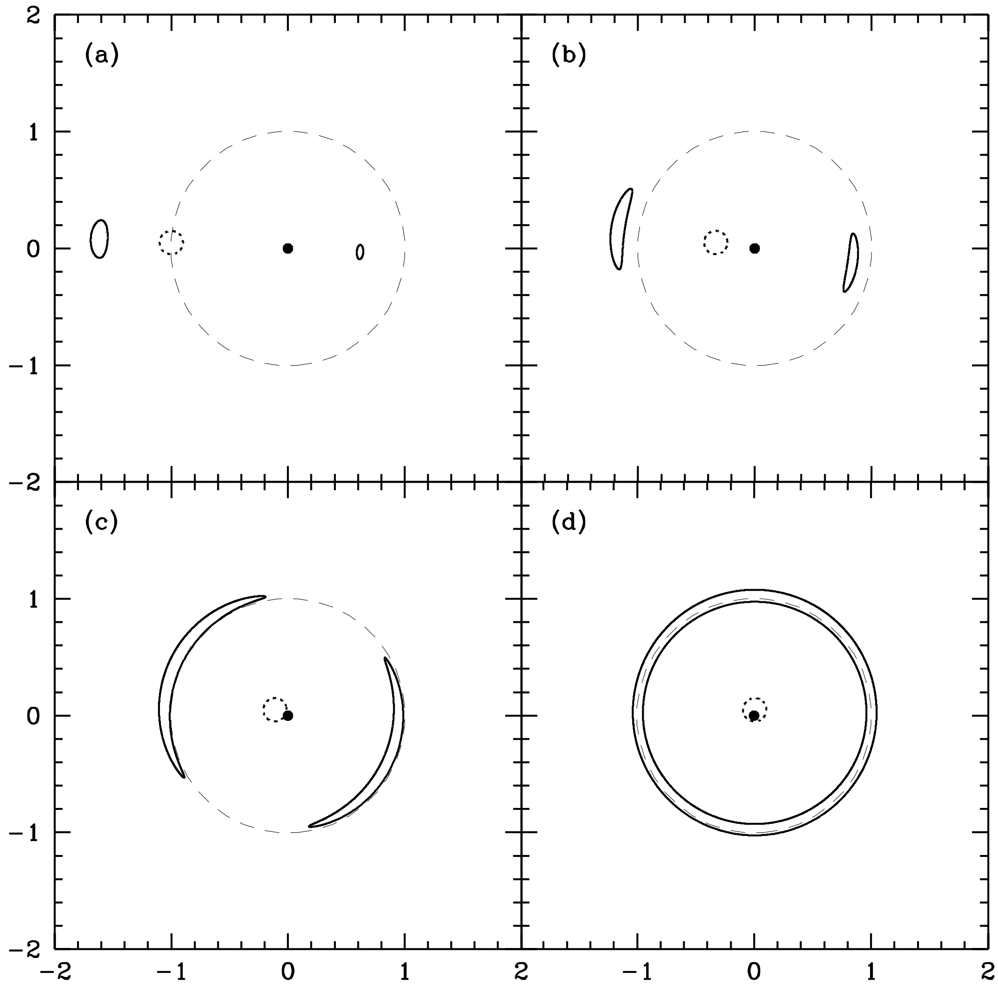

Figure 1.2 Examples of the multiple images in microlensing for various positions of the source star as it passes behind a lens (i.e. varying u). The source star's position is shown by the dotted line and the Einstein ring is shown by a dashed line. The two images are shown by a solid line. In pane (d) part of the source star is directly behind the lens and the two images join to form an Einstein ring.

We are now ready to calculate the magnification, or amplification, A, for each image as the ratio of the areas of the source and the image. Because each point is mapped to a point along the line joining it to the lens, the transverse length scales with x/u. In the radial dimension the width is proportional to $\frac{dx}{du}$ so the magnification for each image is

$$\begin{aligned} A_{\pm} &= \frac{x_{\pm}}{u}\frac{dx_{\pm}}{du} \\ &= \frac{1}{4u}\left(1 \pm \frac{u}{\sqrt{u^2+4}}\right)\left(u \pm \sqrt{u^2+4}\right) \\ &= \frac{1}{2}\left(1 \pm \frac{u^2+2}{u\sqrt{u^2+4}}\right) . \end{aligned} \tag{1.10}$$

Here it is possible for A to be negative, in fact, for our case $A_{-} \leq 0$. This denotes an image of negative parity or, in other words, an inverted image; in the negative parity case the total flux is proportional to the absolute value of A. The total magnification is then

$$\begin{aligned} A &= |A_{+}| + |A_{-}| = A_{+} - A_{-} \\ &= \frac{1}{2}\left[\left(1 + \frac{u^2+2}{u\sqrt{u^2+4}}\right) - \left(1 - \frac{u^2+2}{u\sqrt{u^2+4}}\right)\right] \\ &= \frac{u^2+2}{u\sqrt{u^2+4}} . \end{aligned} \tag{1.11}$$

The magnification will change with time because there will be relative motion between the observer, lens, and source. Assuming linear motion the impact parameter will vary as

$$u(t) = \sqrt{u_{min}^2 + \left(\frac{t-t_0}{\hat{t}/2}\right)^2} . \tag{1.12}$$

Here u_{min} is the minimum impact parameter, t_0 is the time of maximum magnification, and $\hat{t}$ is the Einstein ring diameter crossing time,

$$\hat{t} \equiv \frac{2R_{\mathrm{E}}}{v_{\perp}} . \tag{1.13}$$

The flux as a function of time is given by

$$F(t) = A[u(t)], \tag{1.14}$$

and shown in Figure 1.3. Since the magnification is strictly greater than zero a threshold must be chosen when looking for events. Usually this is chosen as $u_{min} = 1$ which corresponds to a maximum magnification $A_{max} = 1.34$. While technically a given lens is lensing all stars, a star is usually said to be lensed only if $A_{max} \geq 1.34$ ($u_{min} \leq 1$).

To get to this point we have assumed a point source, point lens, small angles and linear motion. When these assumptions hold, a given light curve, or the flux as a function of time, is described by three parameters: minimum impact parameter, u_{min}; Einstein diameter crossing time, $\hat{t}$; and time of maximum magnification, t_0. Since there is a one-to-one relation given by equation (1.11) it possible to use A_{max} rather than u_{min}. The event duration is perhaps the most confusing parameter as it can be given in three ways: Einstein diameter crossing time, $\hat{t}$, as above; Einstein *radius* crossing time, $t_{\mathrm{E}} = \hat{t}/2$; or the time spent with $u < 1$ which is given by

$$t = \hat{t}\sqrt{1 - u_{min}^2}\,. \tag{1.15}$$

Of the three measurable quantities ($\hat{t}$, u_{min}, and t_0), the only one that contains information about the lens is $\hat{t}$, which depends on lens mass, position, and velocity. The other two parameters, u_{min} and t_0, are uniformly distributed and yield no information concerning the lens. With a set of potential microlensing events, or candidates, the distribution of u_{min} can be used to check whether the set is consistent with microlensing. The u_{min} distribution will also be used as a check for the presence of blending, an effect described in the next section. This degeneracy between three physical parameters and one measured quantity makes it impossible to measure information on a single lens from a single event, thus results will be of a statistical nature.

The average number of lenses within a projected distance $u_T R_{\mathrm{E}}$ of a source is known as the microlensing optical depth, where u_T denotes the threshold impact parameter or maximum detectable u_{min}. If the distribution of lenses is known the optical depth can be calculated as the integral of the number density

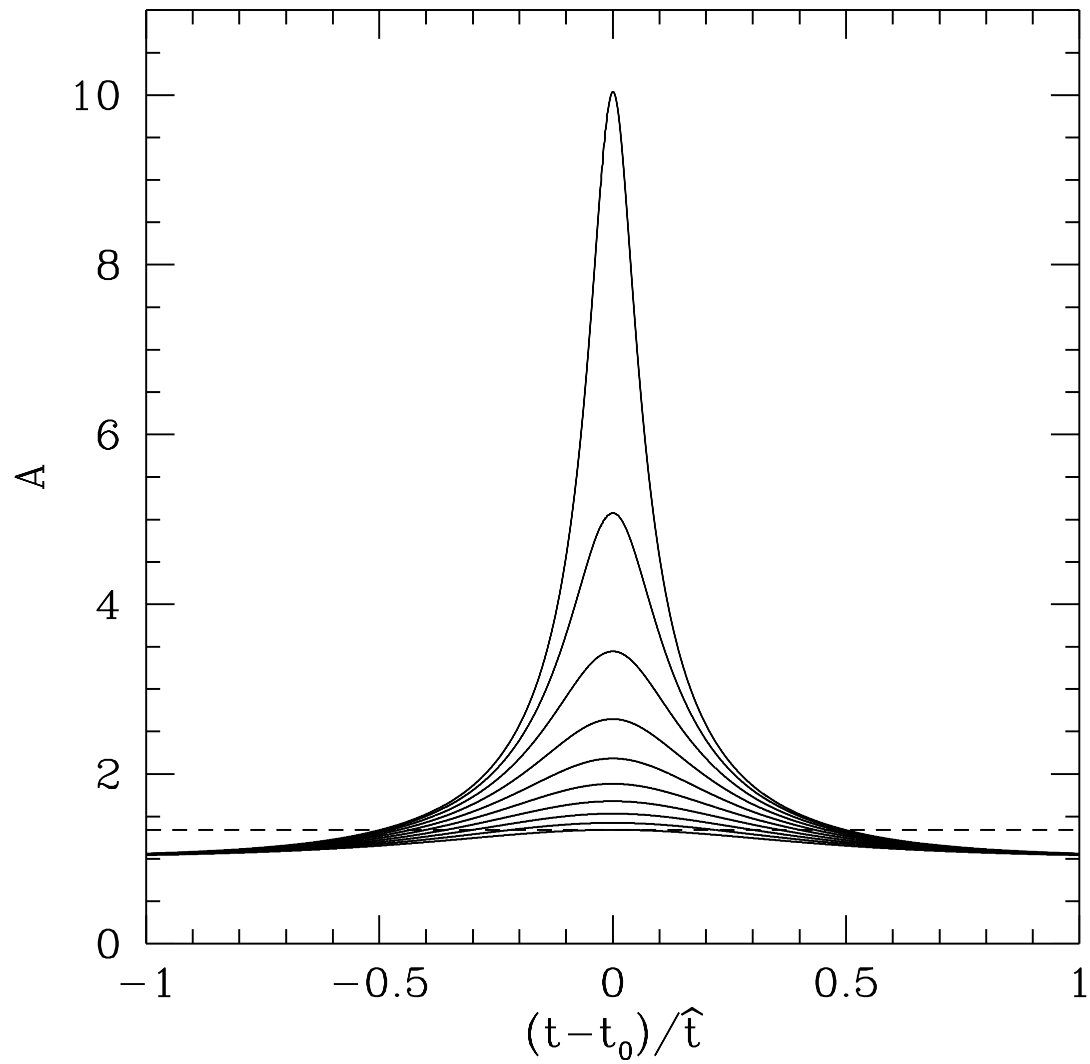

Figure 1.3 Plot of magnification versus time (light curves) for u_{min} = $(0.1, 0.2, ..., 1.0)$. The dashed line indicates the magnification threshold for an event, 1.34, or equivalently an impact parameter of 1.

of lenses over the volume of the "microlensing tube",

$$\tau = \int_0^{D_s} \frac{\rho(D_l)}{m} \pi u_T^2 R_{\mathrm{E}}^2 \, dD_l \, . \tag{1.16}$$

Because the area of the Einstein disk is proportional to m ($\pi R_{\mathrm{E}}^2 \propto m$) the integral depends only on the total density of matter, not the mass distribution of lenses, making the optical depth a good measure of the line of sight mass density toward any set of source stars.

1.1.3 Blending

So far we have assumed a single point source. Because observing programs want to see many events they usually monitor dense fields where the number of stars observed with each exposure is high. Often several stars are blended together to appear as one object, but the Einstein ring is so small that only one of them is lensed. This changes the shape of the light curve and distorts the recovered parameters of an event. If a star is blended we measure a baseline flux that is higher than the real flux from the star. The fraction of light that is lensed is usually referred to as the blend fraction, f_b. There is some confusion because the term blend fraction has been used both as the fraction of light coming from the lensed star at the baseline and as the fraction of unlensed light at the baseline. In our analysis of blending in Chapter 6 we use "fraction of lensed light", f_{ll}, as we believe it is a more accurate name, but for consistency with previous MACHO collaboration papers we use f_b in the analysis of the MACHO data. The magnification of the event becomes

$$A'(u) = f_b A(u) - f_b + 1 \, . \tag{1.17}$$

The parameters of an event, as measured from a fit to the light curve, will be changed by blending as well. Because the amplification is suppressed the value of A_{max} will be decreased and the event will seem shorter, $\hat{t}$ is reduced. If a sample of events is blended these effects have to be carefully considered before an accurate optical depth can be calculated. The effects of blending are analyzed in §5.2 and examined in detail in Chapter 6.

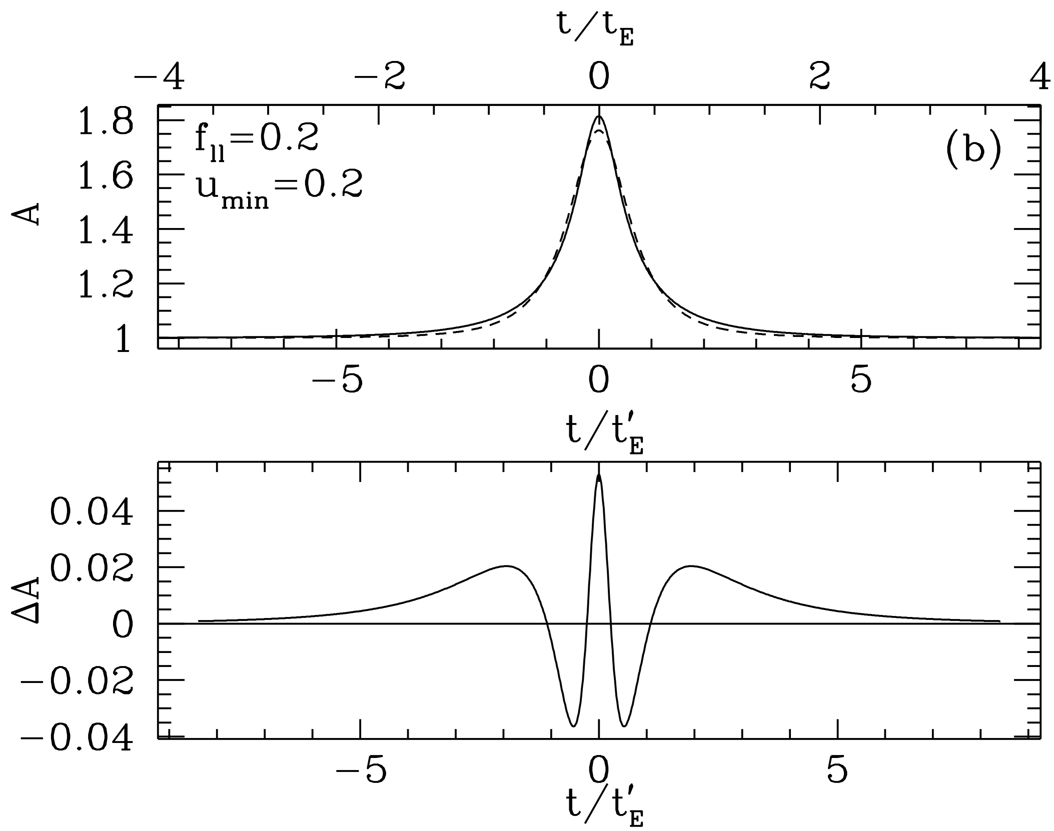

Figure 1.4 Comparison of blended light curve to unblended. The top shows a blended light curve (solid line) and a light curve with no blending (dashed line); the bottom shows the difference between the two light curves. For the blended light curve 20% of the baseline flux is lensed. The two are very similar and hard to distinguish.

1.1.4 Observational Microlensing

Observationally the optical depth can be estimated as the fraction of sky covered by Einstein disks. For the small values of optical depth that have been predicted and measured ($\sim 10^{-6}$) this is equivalent to the probability that a given star is lensed at any given time. Because the probability of a star being lensed is so low, microlensing experiments monitor millions of stars for long periods of time looking for microlensing events. It is also important that the observed events be weighted by efficiency, or probability of detection. The optical depth calculation will be discussed extensively in Chapter 5.

1.2 Measurements and Calculations of the Optical Depth

Because of its direct relationship to the matter density the optical depth, τ, is the primary result of microlensing experiments. Microlensing optical depths are used as one of the few checks on models of the Milky Way. Early theoretical estimates of the optical depth toward the Galactic bulge found optical depths near $\tau = 0.5 \times 10^{-6}$ (Griest et al. 1991, Paczyński 1991), but included only disk objects. Early measurements indicated a higher rate than this (Udalski et al. 1993, 1994b) and estimates were made including the contributions of bulge stars bringing τ up to 0.85×10^{-6} (Kiraga & Paczyński, 1994). Early measurements were much higher than this, $\tau \geq (3.3 \pm 1.2) \times 10^{-6}$ (Udalski et al., 1994a) from 9 events and $\tau = 3.9^{+1.8}_{-1.2}$ (Alcock et al., 1997b) from 13 of their events and an efficiency calculation. The early results spawned a series of calculations including additional components including an elongated bulge and a bar with various orientations (e.g., Zhao et al. 1995; Metcalf 1995; Zhao & Mao 1996; Bissantz et al. 1997; Gyuk 1999; Nair & Miralda-Escudé 1999; Binney et al. 2000; Sevenster & Kalnajs 2001; Evans & Belokurov 2002; Han & Gould 2003) yielding values of $(0.8 - 2) \times 10^{-6}$. Values as large as $\tau = 4 \times 10^{-6}$ were found to be incompatible with any reasonable model.

More recent results, all using efficiency calculations, have been lower: $\tau =$

$2.43^{+0.39}_{-0.38} \times 10^{-6}$ at $(l, b) = (2^\circ\!.68, -3^\circ\!.35)$ using 99 events in 8 fields and difference imaging analysis (Alcock et al., 2000c), $\tau = 2.59^{+0.84}_{-0.64}$ at $(l, b) = (1^\circ\!.0, -3^\circ\!.9)$ from 28 events using difference imaging analysis (Sumi et al., 2003), $\tau = (0.94 \pm 0.29) \times 10^{-6}$ at $(l, b) = (2^\circ\!.5, -4^\circ\!.0)$ for 16 clump giant microlensing events (Afonso et al., 2003), and a preliminary result of $\tau = (2.0 \pm 0.4) \times 10^{-6}$ at $(l, b) = (3^\circ\!.9, -3^\circ\!.8)$ from about 50 events from the partial (5 year) MACHO data (Popowski et al., 2001a). The difference imaging results do not have any form of source selection so the reported optical depth is characteristic of the direction and not the line-of-sight to a particular location. To calculate an optical depth to the Galactic bulge with difference imaging analysis a correction factor is used. The correction factor is calculated assuming the only significant contributions to the star count are the disk and the bulge and that disk stars are unlikely to be lensed. This correction factor is very uncertain so comparisons are hard to make.

Herein, seven seasons of Galactic bulge data are analyzed. More than 500 likely microlensing events are found, including several events exhibiting exotic effects. Although supplemented by additional events selected by eye, the bulk of the events are from a computerized selection, which finds 337 events. All events are presented with lensing parameters and data on the source star.

To measure the optical depth to the Galactic bulge one must observe source stars located in the bulge. It is also important to select objects that are not affected by blending, the distortion of the light curve due to inclusion of flux from multiple objects. In order to calculate the optical depth blending must be avoided or accounted for. To allow a correction for sampling efficiency only computer selected events can be used for the optical depth calculation. Of the large sample of computer selected events, color cuts are use to select 62 events on red clump giants[3]. These 62 events are on very bright stars that are most numerous in the bulge and thus suitable for an optical depth calculation. Using these events the optical depth is found to be $\tau = 2.17^{+0.47}_{-0.38} \times 10^{-6}$ at $(l, b) = (1^\circ\!.50, -2^\circ\!.68)$ with a gradient of $(1.06 \pm 0.71) \times 10^{-6}\,\mathrm{deg}^{-1}$ in l and $(0.29 \pm 0.43) \times 10^{-6}\,\mathrm{deg}^{-1}$ in b,

[3]This number includes two duplicates that are found in overlapping regions of fields. 60 unique events are found.

consistent with the recent theoretical estimate of 1.63×10^{-6} by Han & Gould (2003).

Evaluating the effect of blending on our sample was a large fraction of the work that went into the optical depth calculation. This work brought about a detailed understanding of the properties of photometric fits on blended light curves. We present this work on blending and extend it to include methods for reducing the effect of blending in Chapter 6. Unfortunately blended fits for microlensing are degenerate and small changes in the data can lead to widely varying fit parameters. This has been known for some time (Woźniak & Paczyński, 1997), but previous work has only looked at very narrow cases. We make fewer assumptions and examine the error sources. Unlike previous work, the baseline is allowed to vary and found to have a very strong effect on the recovered blend fraction. We examine what data is most important in constraining the blend fraction and suggest observational methods for reducing it. Specifically we examine non-uniform time spacing of observations and the benefits of such an observing strategy for reducing errors with minimal additional observing time.

2

The MACHO Project [1]

In order to find many events the MACHO Project observed the Galactic bulge for seven years with the 50 inch Great Melbourne telescope at Mount Stromlo observatory from July of 1992 through December 1999. The LMC was the priority (for results of the LMC observing program see Vandehei (2000) and Alcock et al. (2000b)), so the bulge was not observed during prime LMC observing seasons: November through February.

2.1 Telescope and CCD

The 50 inch Great Melbourne telescope (Figure 2.1) at Mount Stromlo Observatory[2] was re-commissioned especially for the MACHO Project. In addition to being available for dedicated use, it was adaptable to wide-field imaging and automation. For the MACHO Project a wide-field prime-focus corrector incorporating a dichroic element and detectors was used to allow wide-field imaging in two color bands simultaneously. With its 5671.8mm focal length the Great Melbourne telescope had a focal ratio of $f/4.5$ before being adapted for wide-field use; the addition of the wide-field corrector reduced the focal ratio to $f/3.8$. With the wide-field corrector the telescope had a flat, coma-free focal plane $60'$ wide allowing

[1] Chapters 2-5 are based on work that has already been published as Thomas et al. (2005) and Popowski et al. (2005).

[2] In January of 2003 a fire tragically razed the Mount Stromlo observatory.

a large numbers of stars to be observed simultaneously.

The dichroic filter had a transition around 610 nm allowing imaging in two bands centered at 560 nm and 710 nm simultaneously, thus allowing important color information to be gathered even in non-photometric weather. Each focal plane is imaged with a mosaic of four 2k × 2k Loral CCDs with a pixel scale of 0.62 arcsec/pixel. Additional filters were used between the corrector and the focal planes to filter out the light pollution from nearby Canberra. The dichroic filter produces bands that are different from standard filters. To relate MACHO magnitudes, b_M and r_M, to Johnson's V and Kron-Cousins' R the relations,

$$V = b_M - 0.18(b_M - r_M) + 23.70 \tag{2.1}$$

$$R = r_M + 0.18(b_M - r_M) + 23.41, \tag{2.2}$$

are used. A schematic of the dichroic and camera system is shown in Figure 2.2. For full details of the camera system see Stubbs et al. (1993) and Marshall (1994).

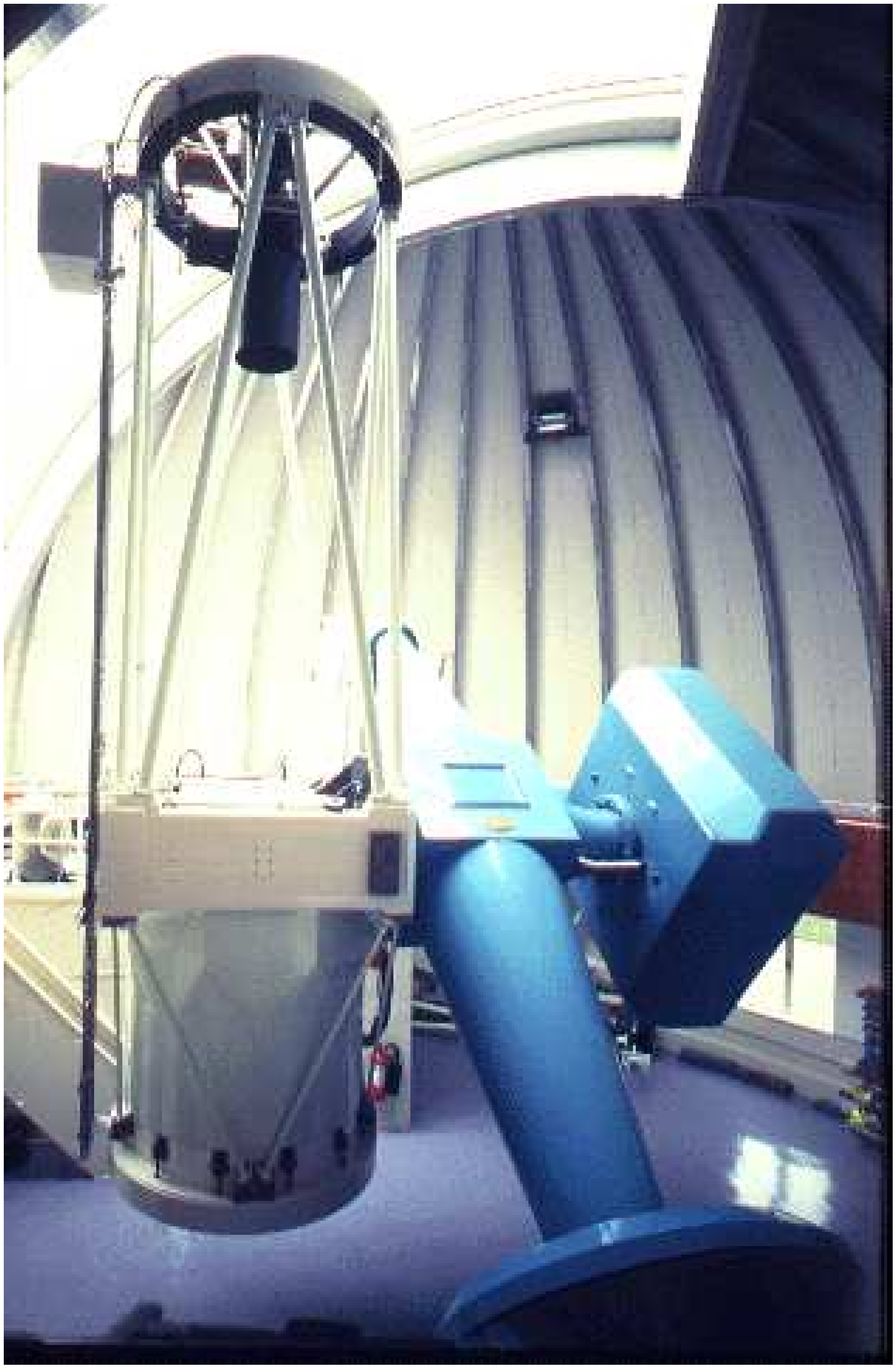

Figure 2.1: The Great Melbourne telescope at Mount Stromlo Observatory.

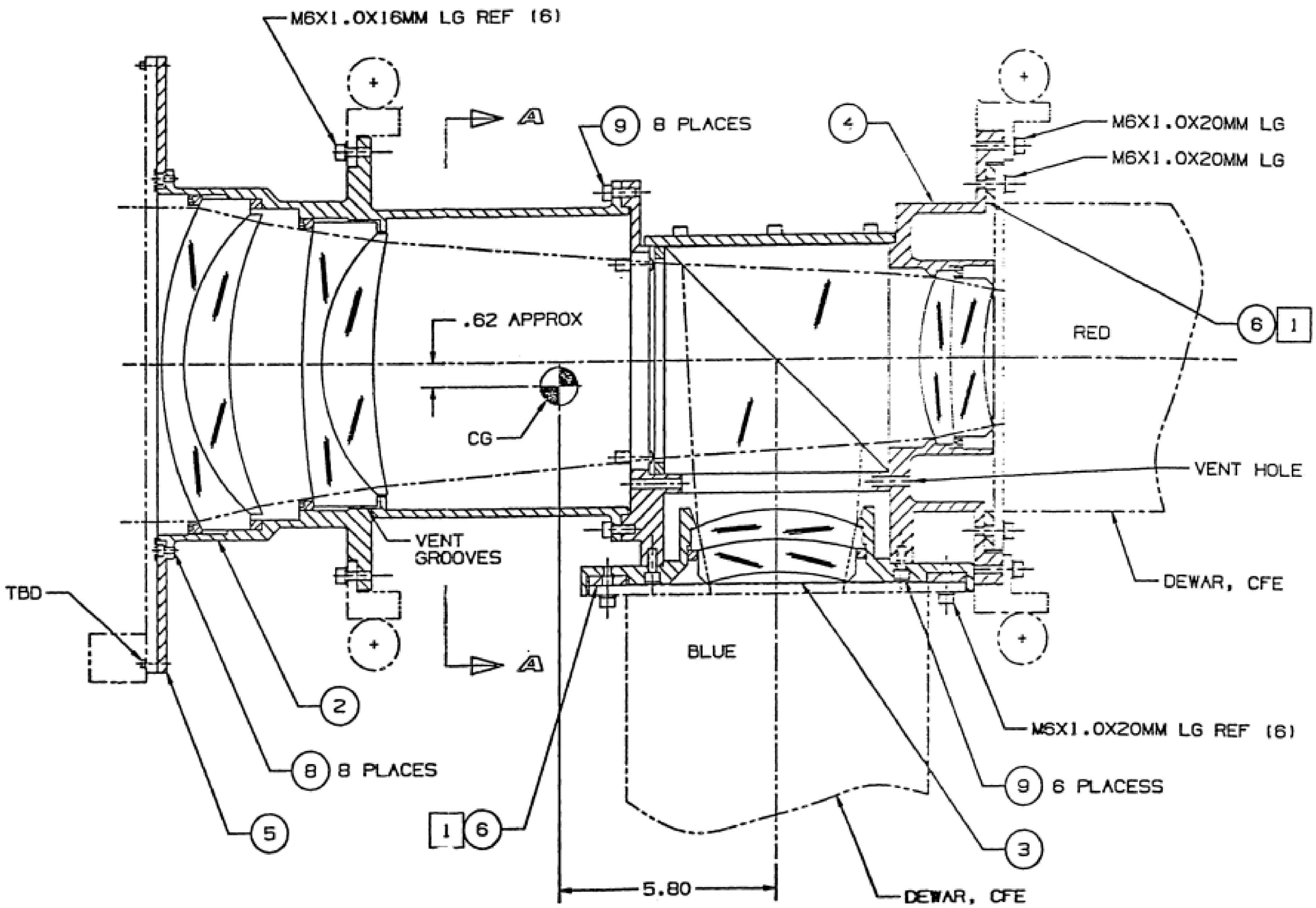

Figure 2.2: Schematic of the MACHO camera system. The dichroic filter transmits red light and reflects blue light.

2.2 Data

The Galactic bulge was observed 32,700 times, creating light curves for 50.2 million objects and approximately 3 terabytes of image data. Observations covered the 94 fields near the bulge shown in Figure 2.3, with the number of observations varying from field 106 with 12 observations to field 119 with 1815 observations; year to year coverage of a given field also varied substantially. Data on the 94 fields including position in galactic coordinates, number of stars, number of clump giants, number of events, and number of exposures are listed in Table 2.1.

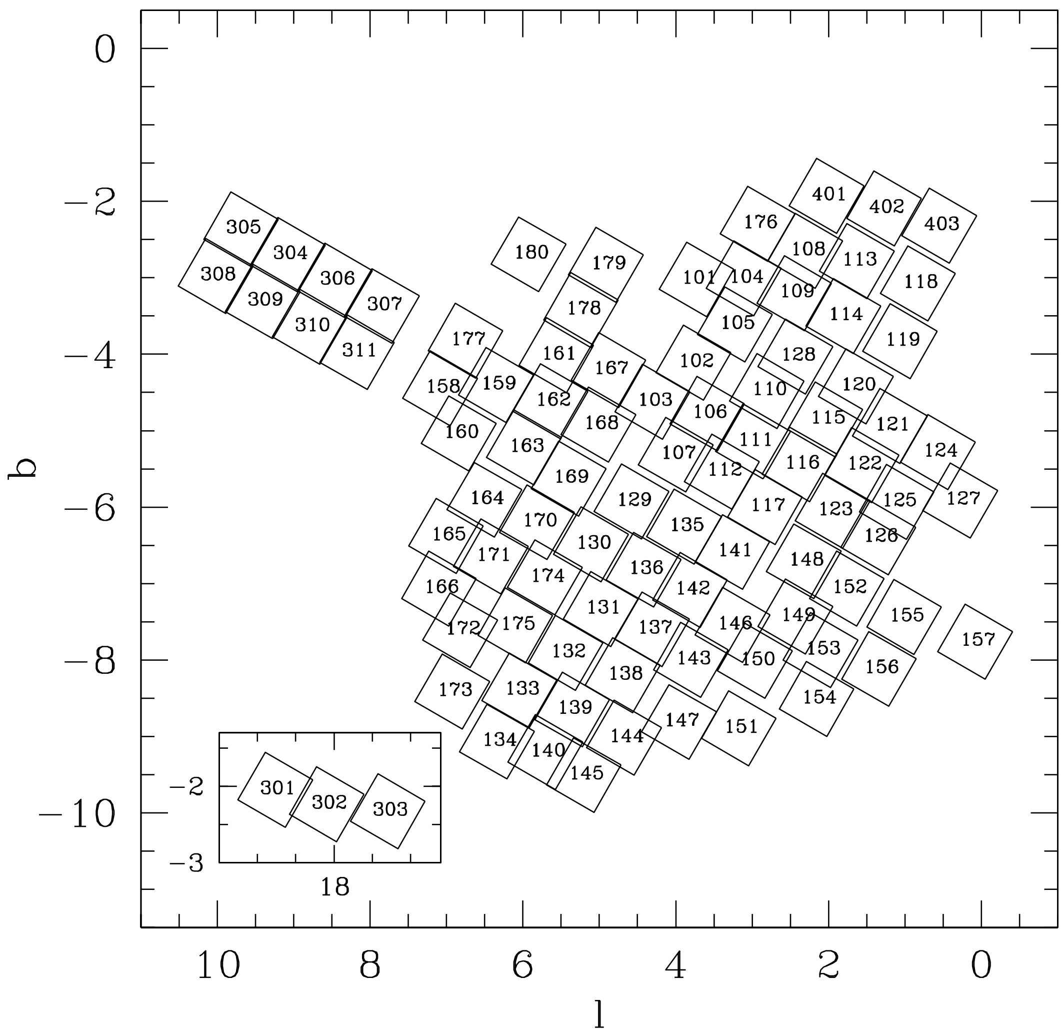

Figure 2.3: Location of the bulge fields in galactic coordinates.

Table 2.1: Data On The 94 Bulge Fields

field	l	b	$\frac{n_{stars}}{100}$	$\frac{n_{clumps}}{100}$	n_{events}	$n_{exposures}$
101	3.73	−3.02	6284	629.5	30	804
102	3.77	−4.11	6545	444	15	421
103	4.31	−4.62	6349	368	5	331
104	3.11	−3.01	5813	652	28	1639
105	3.23	−3.61	6375	539	21	640
106	3.59	−4.78	6648	346	0	12
107	4.00	−5.31	6159	269	0	51
108	2.30	−2.65	6498	790	32	1031
109	2.45	−3.20	6926	661	19	761
110	2.81	−4.48	6649	408	11	650
111	2.99	−5.14	6036	298	5	305
112	3.40	−5.53	5147	246.5	0	43
113	1.63	−2.78	6252	834	31	1127
114	1.81	−3.50	6665	617	20	776
115	2.04	−4.85	5756	325.5	9	357
116	2.38	−5.44	5812	268.5	4	314
117	2.83	−6.00	5185	198	0	39
118	0.83	−3.07	6347	741.5	29	1053
119	1.07	−3.83	7454	542.5	27	1815
120	1.64	−4.42	5599	394	9	676
121	1.20	−4.94	5855	344	10	352
122	1.57	−5.45	4890	266	3	186
123	1.95	−6.05	5119	210.5	1	40
124	0.57	−5.28	5716	265.5	3	337
125	1.11	−5.93	5839	189	1	287
126	1.35	−6.40	4789	182	0	36
127	0.28	−5.91	4975	192	0	178
128	2.43	−4.03	6160	516.5	9	711
129	4.58	−5.93	5123	234.5	0	31
130	5.11	−6.49	4864	169.5	2	20
131	4.98	−7.33	4256	130	1	106
132	5.44	−7.91	4533	102	2	180
133	6.05	−8.40	4174	70.5	0	176
134	6.34	−9.07	3370	46.5	1	197
135	3.89	−6.26	5476	179	0	30
136	4.42	−6.82	5623	137.5	1	207
137	4.31	−7.60	4488	101	4	193
138	4.69	−8.20	4380	95.5	0	201
139	5.35	−8.65	4112	81	1	191
140	5.71	−9.20	3723	64	0	209
141	3.26	−6.59	5001	159	0	28
142	3.81	−7.08	4985	126.5	2	218
143	3.80	−8.00	4767	97	0	210
144	4.68	−9.02	3798	50.5	1	210
145	5.20	−9.50	3385	49.5	1	210
146	3.26	−7.54	3798	106	0	207

Continued on Next Page...

Table 2.1

... Continued from Previous Page

field	l	b	$\frac{n_{stars}}{100}$	$\frac{n_{clumps}}{100}$	n_{events}	$n_{exposures}$
147	3.96	−8.81	4135	66	0	208
148	2.33	−6.71	5824	161.5	2	229
149	2.43	−7.43	4042	112.5	2	236
150	2.96	−8.01	4474	98.5	1	229
151	3.17	−8.89	3432	85	1	194
152	1.76	−7.07	4995	124	2	235
153	2.11	−7.87	4763	85.5	3	231
154	2.16	−8.51	3936	82	3	247
155	1.01	−7.44	4481	95.5	1	247
156	1.34	−8.12	4660	88.5	1	249
157	0.08	−7.76	3822	105.5	0	258
158	7.08	−4.44	4703	246.5	4	260
159	6.35	−4.40	5890	258.5	6	464
160	6.84	−5.04	4940	248	1	208
161	5.56	−4.01	5878	366	6	467
162	5.64	−4.62	5914	301	5	382
163	5.98	−5.22	5311	259	2	251
164	6.51	−5.90	4901	167.5	0	20
165	7.01	−6.38	4349	135	0	14
166	7.10	−7.07	4175	131.5	1	110
167	4.88	−4.21	6268	388.5	5	364
168	5.01	−4.92	4724	298	3	210
169	5.40	−5.63	4896	208	0	24
170	5.81	−6.20	4886	170	0	17
171	6.42	−6.65	4834	120.5	0	125
172	6.82	−7.61	4036	89	2	132
173	6.92	−8.41	3532	87	1	146
174	5.71	−6.92	4979	143.5	1	144
175	6.10	−7.55	4173	111.5	1	97
176	2.93	−2.30	7741	814.5	10	423
177	6.75	−3.82	5950	319	3	416
178	5.24	−3.42	8186	477	7	376
179	4.92	−2.83	7159	510	10	349
180	5.93	−2.69	6388	478	6	343
301	18.77	−2.05	5608	–	6	925
302	18.09	−2.24	5175	–	3	365
303	17.30	−2.33	4029	–	0	369
304	9.07	−2.70	5080	–	6	458
305	9.69	−2.36	4628	–	3	411
306	8.46	−3.03	5886	–	3	423
307	7.84	−3.37	6565	–	4	435
308	10.02	−2.98	5038	–	2	360
309	9.40	−3.31	5494	–	1	347
310	8.79	−3.64	6488	–	10	387
311	8.17	−3.97	7514	–	10	396
401	2.02	−1.93	6630	964.5	17	429

Continued on Next Page...

Table 2.1
... Continued from Previous Page

field	l	b	$\frac{n_{stars}}{100}$	$\frac{n_{clumps}}{100}$	n_{events}	$n_{exposures}$
402	1.27	−2.09	7098	1153	29	1256
403	0.55	−2.32	6798	1085	24	473

The classification of stars as clump giants is expected to be very difficult in 300 series fields, so we refrain from quoting specific numbers for these fields.

A variation of the DOPHOT (Schechter et al., 1993) point-spread function (PSF) fitting is used for the photometric reduction. A high quality image of each field is chosen to be the template, from which stellar positions and magnitudes are found. The template data are used to "warm-start" subsequent analysis for each field. To make the templates the analysis code, SoDoPhot, is run on a pair of red and blue chunks, or images, that are a roughly $5' \times 5'$ overlapping sections of the entire image. The red chunk is analyzed first and the results are used to warm-start the analysis of the corresponding blue chunk, and initial templates are made. After all the chunks from a single exposure have been analyzed some data from the adjacent chunks (about 90 pixels) are added so errors in pointing will not interfere with analysis. Once complete each template contains a list of detected stars with their positions and magnitudes.

Subsequent analysis uses the template to warm-start the procedure. First, 50 bright non-saturated stars are found and used to fit the PSF, create a coordinate transformation, and find the photometric zero relative to the template image. The stars are then subtracted from the image using the template and the model PSF and errors are adjusted for imperfect subtraction. Photometric fitting is done on each star starting with the brightest by first adding the model fit back to the image and then fitting the star's flux and background. If an object is found to vary it is refit along with the surrounding stars. For each star the following are kept:

1. magnitude and error estimate

2. object type – single, blended, &c
3. χ^2 of the PSF fit
4. "Crowding" – flux contributed by nearby stars
5. flux rejected due to cosmic rays
6. flux rejected due to bad pixels
7. fit sky value.

The resulting data are organized into light curves for the microlensing and variable searches. Each object is identified by the field it is in, the tile (section of the field) it is in, and a sequence number. A more detailed description of the MACHO data reduction can be found in Alcock et al. (1999). For MACHO data the limiting magnitude is about 21.5 in V, and the average seeing is $2\farcs2$ in both bands.

3

Event Selection

It is very difficult to find the few real events amongst 50.2 million light curves. Ideally we would develop a selection method that would identify all of the real microlensing events and exclude all of the other light curves, but in practice many of the events will be missed, either due to the noise in the data or the large gaps in the data. Even in the most frequently sampled fields an event that lasted one or two days would be impossible to detect simply because there would be at most a single datum above the baseline. In practice we are left with two choices: a selection criterion that gets as many events as possible, or one that gets as few false positives as possible. We choose the latter because we can correct our optical depth for missing events with an efficiency calculation but not for non-events included in our sample.

The selection process is done in three levels: level 1, level 1.5, and level 2. A small set of statistics is calculated for each of the 50.2 million light curves and used to find the few percent of light curves showing some variability. These light curves are advanced to level 1. A full set of over 150 statistics is then calculated for all of the level 1 light curves. Using these statistics a broad set of about 90,000 light curves is advanced to level 1.5. Here the selection criteria are fine tuned to produce a set of events with minimal false positives, advancing 337 (318 unique and

19 duplicated in overlapping fields) events to level 2, also called selection criteria "c". The selection criteria used are given with explanations in Table 3.1. Seven of these criteria "c" events are most likely not microlensing. While it is important that there are no false-positives in the sample we use for the optical depth, contaminants in this set do not pose a problem as the optical depth calculation will only use a small subset of events based on their position on the color-magnitude diagram (CMD). Because there are dimmer stars with larger errors in this complete set it is not surprising that there is some contamination. The lower signal to noise ratio for some of these stars means it is harder to distinguish events from non-events.

Table 3.1: Selection Criteria

Selection	Description
microlensing fit parameter cuts:	
$N_{(V-R)} > 0$	require color information
$\chi^2_{out} < 3.0,\ \chi^2_{out} > 0.0$	require high quality baselines
$N_{amp} \geq 8$	require 8 points in the amplified region
$N_{rising} \geq 1,\ N_{falling} \geq 1$	require at least one point in the rising and falling part of the peak
$A_{max} > 1.5$	magnification threshold
$(A_{max} - 1) > 2.0(\sigma_R + \sigma_B)$	signal-to-noise cut on amplification
$(\sigma_R + \sigma_B) < (0.05\,\delta\chi^2)/(N_{amp}\,\chi^2_{in}\,\chi^2_{out})$	
$(N_{amp}\,\chi^2_{out}\,f_{chrom})/(befaft\,\delta\chi^2) < 0.0003$	remove spurious photometric signals caused by nearby saturated stars
$(N_{amp}\,\chi^2_{in})/(befaft\,\delta\chi^2) < 0.00004$	
$\delta\chi^2/fc2 > 320.0$	good overall fit to microlensing light curve shape
$\delta\chi^2/\chi^2_{peak} \geq 400.0$	same quality fit in peak as whole light curve
$0.5(rcrda + bcrda) \leq 143.0$	source star not too crowded
$\xi^{auto}_B/\xi^{auto}_R < 2.0$	remove long period variables
$t_0 > 419.0$, $t_0 < 2850.0$	constrain the peak to period of observations
$\hat{t} < 1700$	limit event duration to ∼half the span of observations
clump giant cuts:	
$V \geq 15$, $V \leq 20.5$	select bright stars with reliabale photometry
$V \geq 4.2(V-R) + 12.4$	define bright boundary of extinction strip
$V \leq 4.2(V-R) + 14.2$	define faint boundry of extinction strip
$(V-R) \geq (V-R)_{boundary}$	avoid main sequence contamination
exclude fields $301 - 311$	avoid disk contamination

Designations V and $(V-R)$ indicate baseline quantities, i.e. the ones in the limit of no microlensing-induced amplification.

For the catalogue, which includes events not used in the optical depth calculation, other events are included for completeness. Events from the alert system (Alcock et al., 1996), events from an earlier binary search (Alcock et al., 2000a), and events selected by eye from a broader, modified version of criteria "c" are included in the catalogue in addition to the criteria "c" events. Some of these events may be of interest as they exhibit exotic effects: binary lenses, lensing of periodic variable stars, or extended source effects. These are missed by the computer selection at least partly because they deviate from the standard point-lens point-source light curve, but because of this they may allow more information about the lens to be gathered. Some of these events are listed in § 4.1.

4

Microlensing Events

We present a total of 526 likely events. The positions of events are plotted in Figure 4.1 and microlensing fit parameters along with data on the source star and a subjective grade of each event are listed in Table A.1 by field.tile.seq identification number in Appendix A. All events are subjectively graded A to F. Table A.1 also presents the method or methods of selection: "c" for selection criterion "c", "a" for alert system, "b" for binary search, and "e" for by eye. The final column contains comments on each event where warranted: "CV" for suspected cataclysmic variables or supernovae, "var" for suspected variable stars, "bin" for suspected binary lensing events, and "$R \neq B$" for events whose red and blue curves differ in shape and/or amplitude. The difference in light curves between colors may indicate systematic error or blending. We also mark events that pass the color cuts used to find clump giants for the optical depth determination with a † flag. The light curves are too numerous to present here so we present only a sample of the light curves in Appendix B.1 and contaminant event light curves in Appendix B.2. We present the entire sample of lensed clump-giant stars, which are used for the optical depth calculation, in Appendix B.3.

Some events that pass selection criteria "c" but are most likely not microlensing are listed in Table A.2 along with a sample of common background events, primarily cataclysmic variables, and "photometric doubles". These photometric doubles are the result of flux from a real event being shared with nearby events. Generally the worse of the two events is moved to Table A.2 and in the occasional case where the quality of the two events was roughly the same one was moved to this Table to prevent any double counting. As mentioned in Chapter 3 these do not present a problem for the optical depth determination because none of them pass the color cuts used to select clump giant events and will not be included in the optical depth calculation.

In total we present 252 grade A, very good signal-to-noise events; 198 grade B, good signal-to-noise events; and 76 grade C, poor signal-to-noise events. Criteria "c" selected 220 grade A events, 97 grade B events, and 11 grade C events, plus 5 events believed to be cataclysmic variables and 4 photometric doubles. Events from the alert system added 6 A's, 15 B's, and 12 C's. The binary search produced an additional 4 A's, 2 B's, and 1 C. The events selected by eye added 22 A's, 84 B's, and 52 C's. 32 pairs of events at the same location are identified along with 1 triplet. These are either events in the overlapping region of two fields (14 cases) or photometric doubles (19 cases). In the latter case the lesser quality event is listed in Table A.2 and should be ignored.

4.1 Rare Events

Several rare events are identified including events with binary lenses, lensing of periodic variable stars, and an event exhibiting extended source effects.

4.1.1 Binaries

Previously the MACHO Collaboration presented 17 binaries with binary fits (Alcock et al., 2000a), these are catalogued with an additional 24 potential binary events. These events deviate from the standard light-curve shape and may

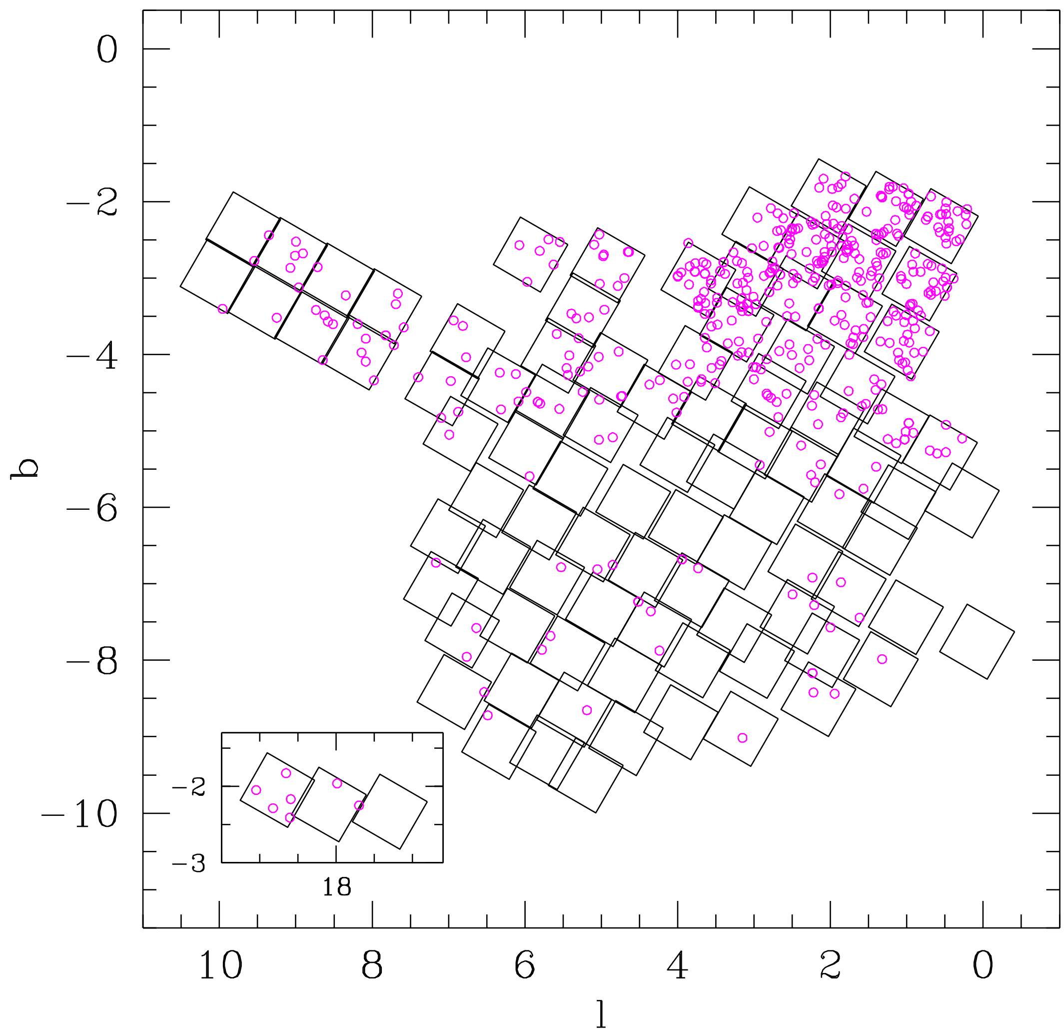

Figure 4.1: Spatial distribution of microlensing events.

be better fit with a binary lens or source. This fitting is not done and it is possible that the deviation is due to large errors or that the event is not microlensing.

4.1.2 Lensed Variable Stars

Several good-quality events were lensed periodic, or nearly periodic, variable stars including events 108.18689.1979, 108.19602.415, 118.18009.35, and 403. 47848.35. These are of interest because the variability allows a more accurate measure of blending. In some cases, where additional information about the star's distance or radius can be found, the lens mass, distance, and velocity degeneracy may be partially broken.

4.1.3 Extended Source

Event 121.22423.1032 seems to exhibit extended source effects. The magnification in the peak is suppressed as the point source approximation breaks down.

4.2 Contamination

When the signal-to-noise ratio is low and the sampling irregular, several astronomical events can mimic microlensing. Most of the contaminants are probably cataclysmic variables (CVs), e.g., novae or dwarf novae (DNe), and are marked "CV". Sixteen such events are listed, seven of which show more than one outburst. Typically there is an approximately 4 day rise followed by a slower decline over roughly 20 days. The outburst is typically peaked about 4 magnitudes brighter than the baseline in V and 2.7 brighter in R, consistent with CVs (Sterken & Jaschek, 1996). For microlensing studies of the Large and Small Magellanic Clouds supernovae (SNe) are a source of contamination. Here, with the high extinction through the Galactic disk and bulge, SNe are not expected to be visible, and the observed light curves decay too rapidly to be consistent with SNe. We present a sample of these light curves in Appendix B.2.

Since one expects flickering on timescales of minutes to hours in DNe, it would be straightforward to confirm the nature of these objects with more observations. Unfortunately, nearly all MACHO observations are separated by at least one day making it impossible to positively identify these objects as DNe without more observations. The non-repeating events could be long-period DNe or heavily blended classical novae.

4.3 Sagittarius Dwarf Galaxy Signatures

The Sagittarius dwarf galaxy (Sgr) (Ibata et al., 1995) is the Milky Way's closest neighbor at about 25 kpc from the Sun. It is centered on the globular cluster M54 at $(l, b) = (5^\circ\!.6, -14^\circ\!.0)$ and extends several degrees in Galactic latitude. While mostly obscured by the large extinction toward the Galactic bulge, traces of the Sgr can be seen in some of the fields furthest from the plane of the Galaxy. It is likely that some events may be lensed Sgr stars. Identifying these events serves at least three goals: removing contaminates from the sample of lensed bulge stars, allowing a measure of mass along the entire 25 kpc line-of-sight, and helping better constrain the mass distribution of lenses.

The primary goal of Galactic microlensing experiments is to better understand the structure of the Galaxy. To do this we need to know what is being lensed and where the lenses are. If we can find sources that are past the bulge it is most likely that the lenses are in the bulge. This can be a great probe of the inner structure of the galaxy, probing regions that cannot be probed with sources in the bulge.

Another goal of microlensing experiments is to find the mass function of the lenses. Because the duration of an event is a degenerate combination of lens mass, velocities, and position, any additional information can be useful in constraining the mass of the lens. In the case of source stars in the Sgr their distinct bulk velocity and low velocity dispersion could be very useful in constraining the lens mass.

We considered multiple methods for identifying Sgr source stars, but none were satisfactory. First we select all stars far enough below the galactic plane to be lensed Sgr stars shown in Figure 4.2. We look at the distribution of baseline magnitudes in Figure 4.3 and note that they do have a significantly different distribution. After examining their position on a color-magnitude diagram and finding their distribution to overlap significantly with the rest of the events we conclude that it is impossible to distinguish Sgr source stars without spectra.

Due to the distinct bulk velocity and low velocity dispersion we conclude that radial velocities determined from spectra of these stars could help identify them very easily and we recommend this be done for the stars listed in Table 4.1. While radial velocities may not be able to conclusively confirm membership in the Sgr, they could exclude events and strongly support other evidence. In a study by Cavallo et al. (2003) the spectra of 136.27650.2370 (also found in field 142 as 142.27650.6057) was measured and the radial velocity found to be $60 \pm 2\mathrm{kms}^{-1}$, inconsistent with the bulk velocity of the Sgr, $140 \pm 10\mathrm{kms}^{-}1$. Other studies (Cook, 2005) have found microlensing events that are consistent with having sources in the Sgr. A much more detailed analysis would be required to conclusively determine the nature of the lensed star. Several methods for identifying Sgr sources are discussed by Popowski (2004).

4.4 Statistical Properties of the Events

4.4.1 Spatial Clustering of Microlensing Events

The positions of all the events on the sky are shown in Figure 4.1, showing a noticeable concentration of events toward the Galactic plane and toward the

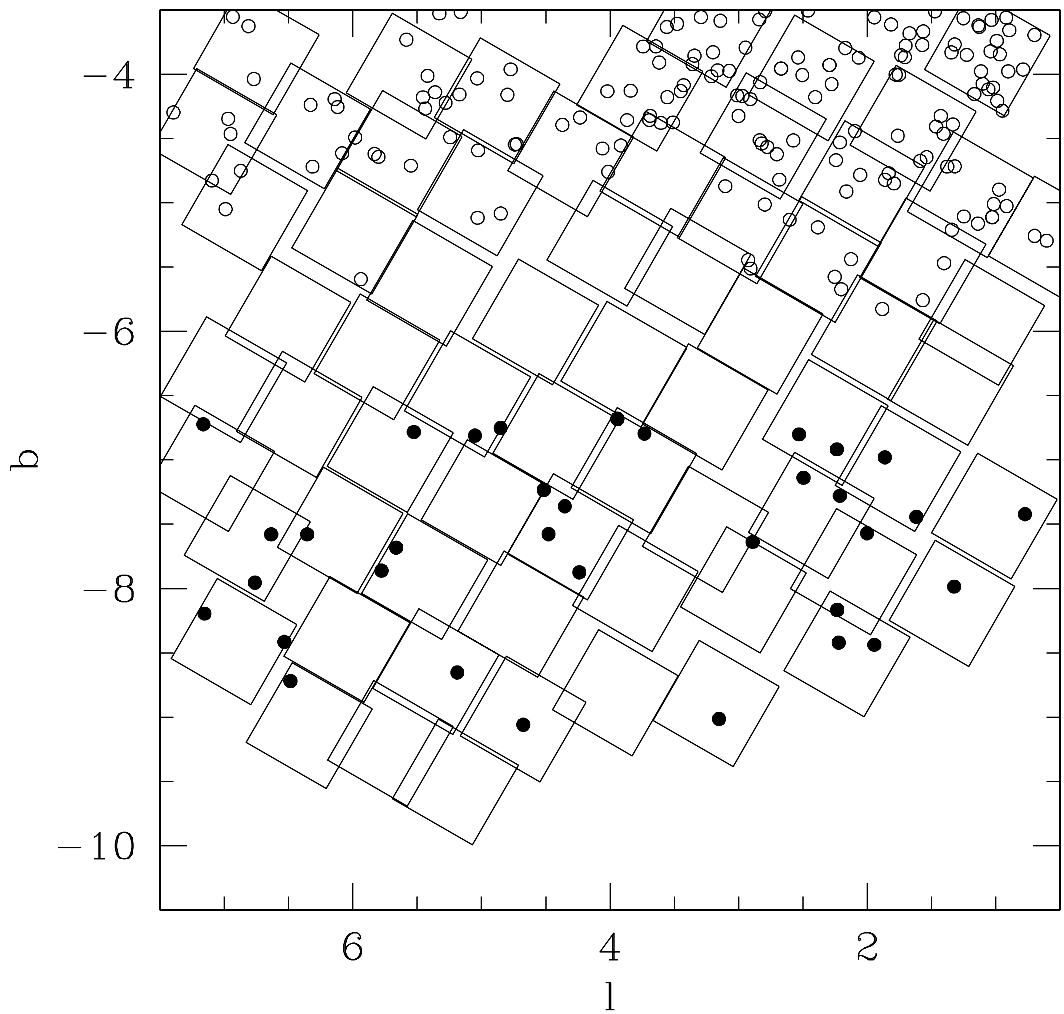

Figure 4.2 We show potential lensed Sagittarius dwarf galaxy stars by filled circles.

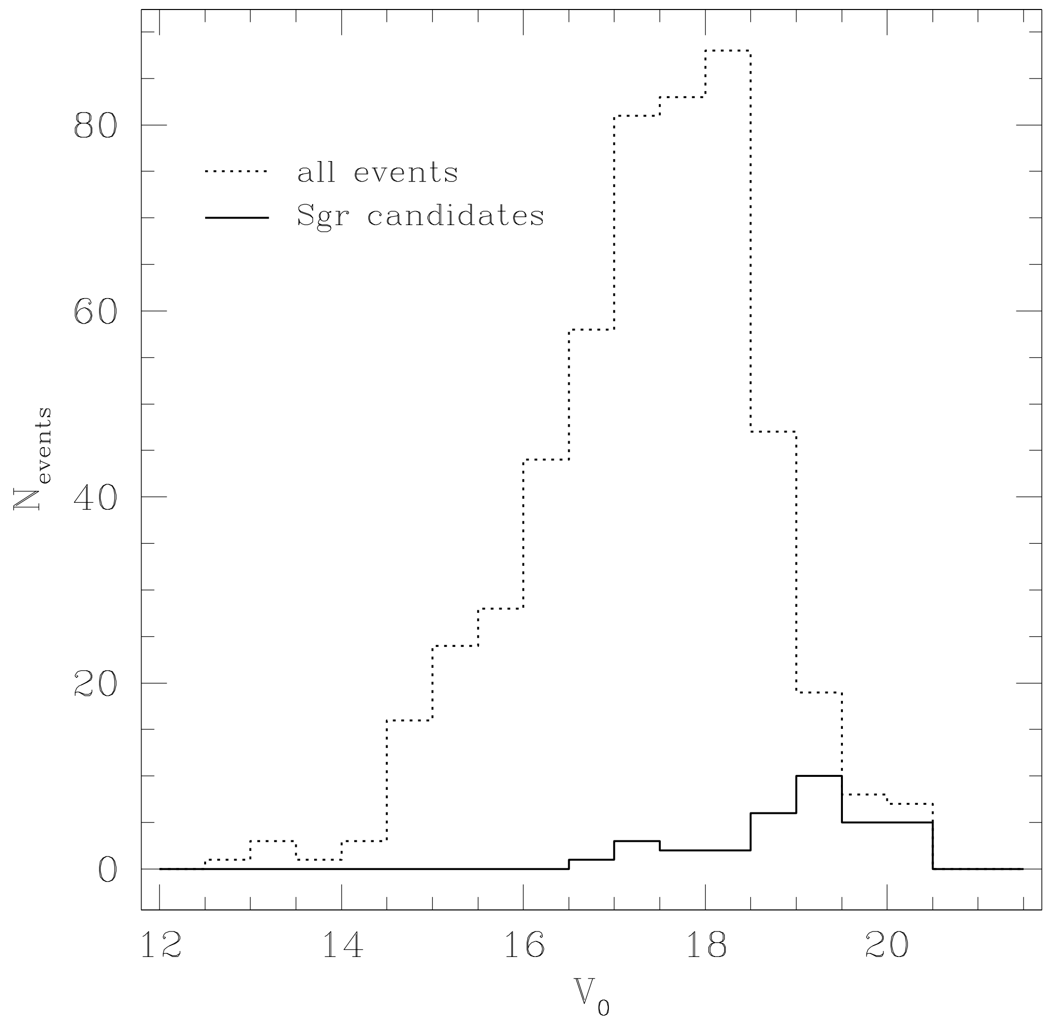

Figure 4.3 We show the distribution of V magnitude for potential lensed Sagittarius dwarf galaxy stars (34) and the entire sample (511).

Table 4.1. Candidate Sagittarius Events

Event ID	l	b	V	$(V-R)$
130.28701.2042	4.8512	−6.7517	20.70	0.53
130.28964.2444	5.0507	−6.8103	20.26	0.56
131.29214.519/137.29214.59	4.5149	−7.2331	18.21	0.57
132.30916.803	5.6640	−7.6825	19.14	0.60
132.31306.841	5.7772	−7.8612	19.16	0.63
134.33390.299	6.4858	−8.7196	18.25	0.56
136.27650.2370/142.27650.6057	3.9432	−6.6806	19.90	0.71
137.29210.2447	4.3518	−7.3602	20.16	0.66
137.29731.2320	4.4779	−7.5769	20.19	0.67
137.29986.2769	4.2386	−7.8740	20.56	0.58
139.32203.2073	5.1877	−8.6533	20.27	0.57
142.27776.3952	3.7321	−6.7952	20.91	0.73
144.32453.1528	4.6748	−9.0594	20.43	0.73
148.26586.2310	2.2356	−6.9174	19.72	0.59
148.26590.3689	2.5305	−6.8008	21.24	1.18
149.27233.2244	2.2123	−7.2793	20.71	0.62
149.27237.3033	2.4953	−7.1386	20.87	0.72
150.28409.2370	2.8904	−7.6381	20.48	0.38
151.31133.1607	3.1521	−9.0148	19.88	0.46
152.26320.2643	1.8618	−6.9798	20.17	0.46
152.26964.3183	1.6179	−7.4432	20.41	0.64
153.27488.3450	2.0007	−7.5704	20.55	0.38
153.28787.720/154.28787.2812	2.2335	−8.1667	18.03	0.63
154.29041.2113	1.9448	−8.4379	20.31	0.53
154.29175.2554	2.2214	−8.4213	20.85	0.61
155.26043.1938	0.7719	−7.4219	19.67	0.44
156.27606.899	1.3232	−7.9849	19.12	0.50
166.30682.3768	7.1637	−6.7227	21.19	0.82
172.31579.2624	6.6359	−7.5785	20.37	0.69
172.32358.313	6.7620	−7.9545	18.15	0.58
173.33002.479	6.5333	−8.4153	19.54	0.50
173.33142.1986	7.1540	−8.1955	20.40	0.62
174.29360.352	5.5261	−6.7824	17.59	0.66
175.31446.1290	6.3557	−7.5785	20.96	0.82

Galactic Center. The figure seems to indicate spatial clustering of events, especially in fields 104, 108, and 113. If statistically significant, this clustering could indicate a local over-density of lenses in a relatively small region, possibly due to some bound substructure in the Galaxy. To test the significance of this apparent clustering 10,000 sets of 318 unique artificial events were generated to simulate the current set of events. The sizes of the smallest three and four-event clusters are used to measure the clustering. From these simulations the probability of finding three events as close as observed is between 7% and 36%, depending on the assumed optical depth gradient. The chance of finding a four-cluster as small as the smallest observed four-cluster varies with optical depth gradient between 4% and 32%. With such high probabilities of finding the observed clumping it unlikely that the observed clumping is significant.

4.4.2 Impact Parameters

One way to test if a set of events is consistent with microlensing is to test the distribution of impact parameter, u_{min}, which should be uniform between 0 and the maximum allowed by the selection criteria (In this case the requirement that $A_{max} \geq 1.5$ is equivalent to a maximum $u_{min} = 0.826$). The cumulative distribution is used here and should be a straight line from zero to the maximum impact parameter, 0.826.

The cumulative distribution of impact parameters for 247 unique, non-binary events selected by criteria "c" is plotted in Figure 4.4, and the same is plotted in Figure 4.5 for the 55 clump giants in the sample. Figure 4.4 shows a lack of events at very small u_{min} and an excess of events with values in the range $0.1 \lesssim u_{min} \lesssim 0.5$. For the clump giant sample the deviation is similar but the distribution is statistically consistent with a uniform distribution, the Kolmogorov-Smirnov (KS) test confirms this. For all 247 events the KS statistic, D, is 0.095 and the KS test indicates a probability of 2.1% of finding a deviation this large, while for the 55 clump events, $D = 0.103$, and the probability to find this large a deviation is 58.0%. Two effects can explain the deviation for the set of events on all stars: blending and efficiency variation. For the set of non-clump events blending is a significant effect and tends to decrease the measured A_{max} or increase the measured u_{min}. Efficiency of event detection may vary over the range of impact parameters which may lead to a non-uniform distribution, but this appears not to be significant, at least for the clump sample for which this test is repeated with efficiency correction in §5.2.4.

4.4.3 Distributions

The complete set of events is affected by blending and distributions of all parameters are expected to be biased, nevertheless the statistics of the event parameters are given for all grade A and B events and for the clump giant sample. The average value of $\hat{t}$ is 49 days with a standard deviation of 62 days for the non-clump sample. The clump sample has a mean $\hat{t}$ of 56 days and standard deviation of 64 days. Since the distributions are non-Gaussian the median and quartiles of the $\hat{t}$ distribution are a more useful description and are 31.1, 17.4, and 57.0 for non-clumps and 30.8, 15.9, and 60.9 for clumps. The longer event timescale for clumps is consistent with blending in the rest of the sample, but does not add any substantial evidence to support that conclusion.

The distribution of the times of event peaks, t_0, is shown in Figure 4.6. The most prominent feature is the variation due to yearly gaps in observations, also equipment problems in the second year and observing strategy changes to look for short events in the second and final year lead to lower event rates in those years. Taking these things into account the event rate is roughly constant.

A color-magnitude diagram (CMD) of the events and the rest of the objects monitored is presented in Figure 4.7. As expected, the event distribution is similar to the distribution of all objects. In the next chapter event positions on

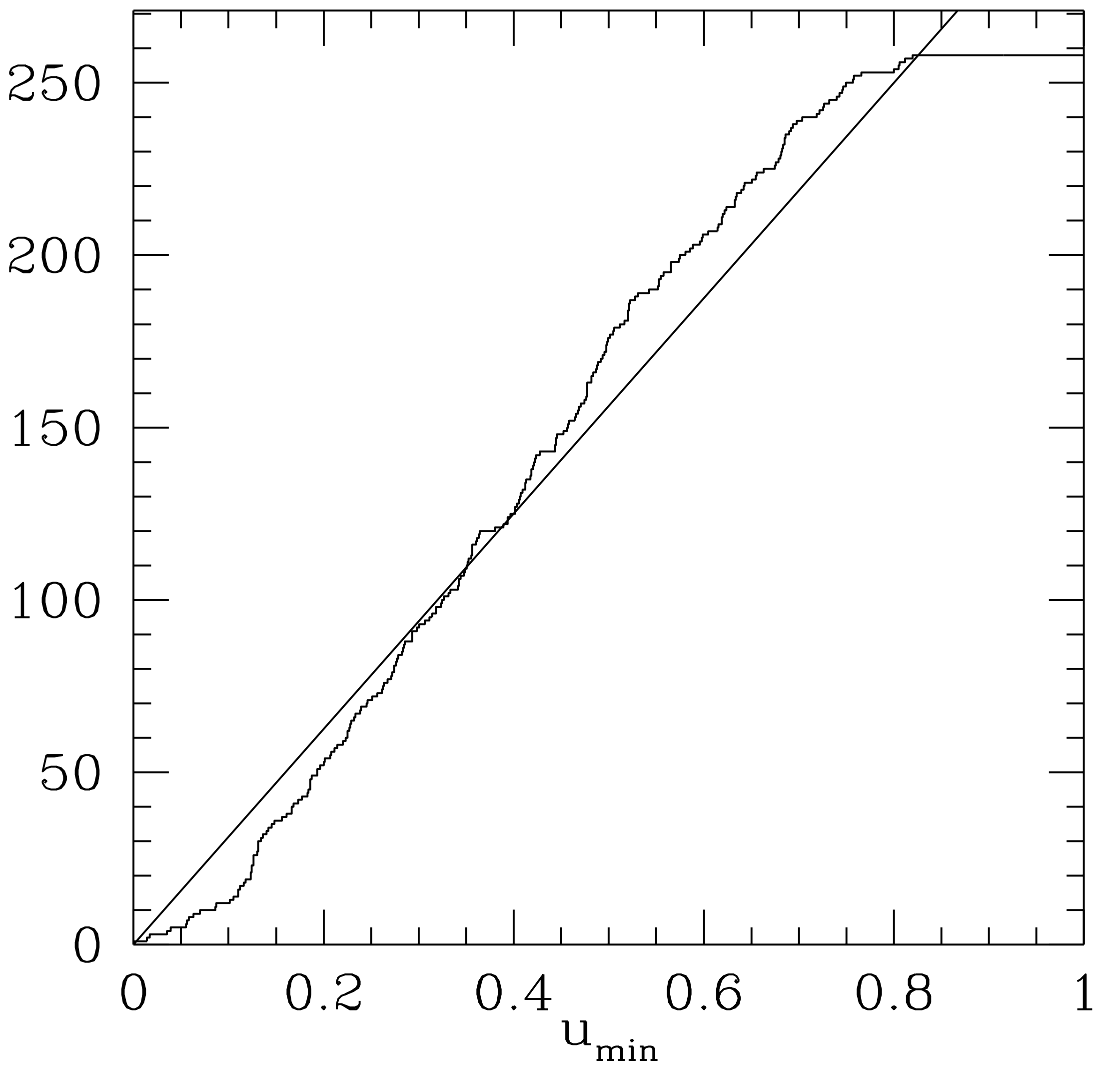

Figure 4.4 Cumulative distribution of impact parameter (u_{min}) for all unique, non-binary, computer selected events.

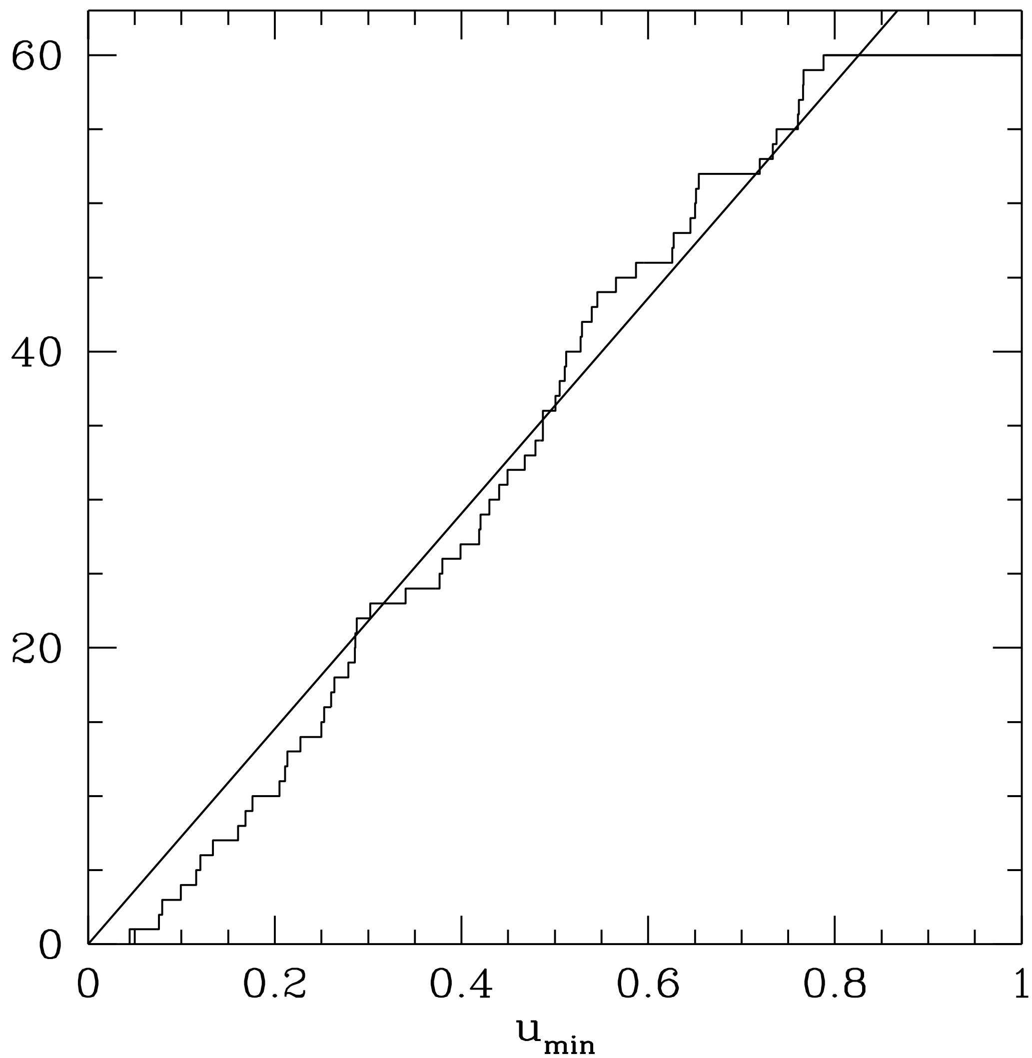

Figure 4.5 Cumulative distribution of impact parameter (u_{min}) for unique, non-binary, computer selected clump giant events.

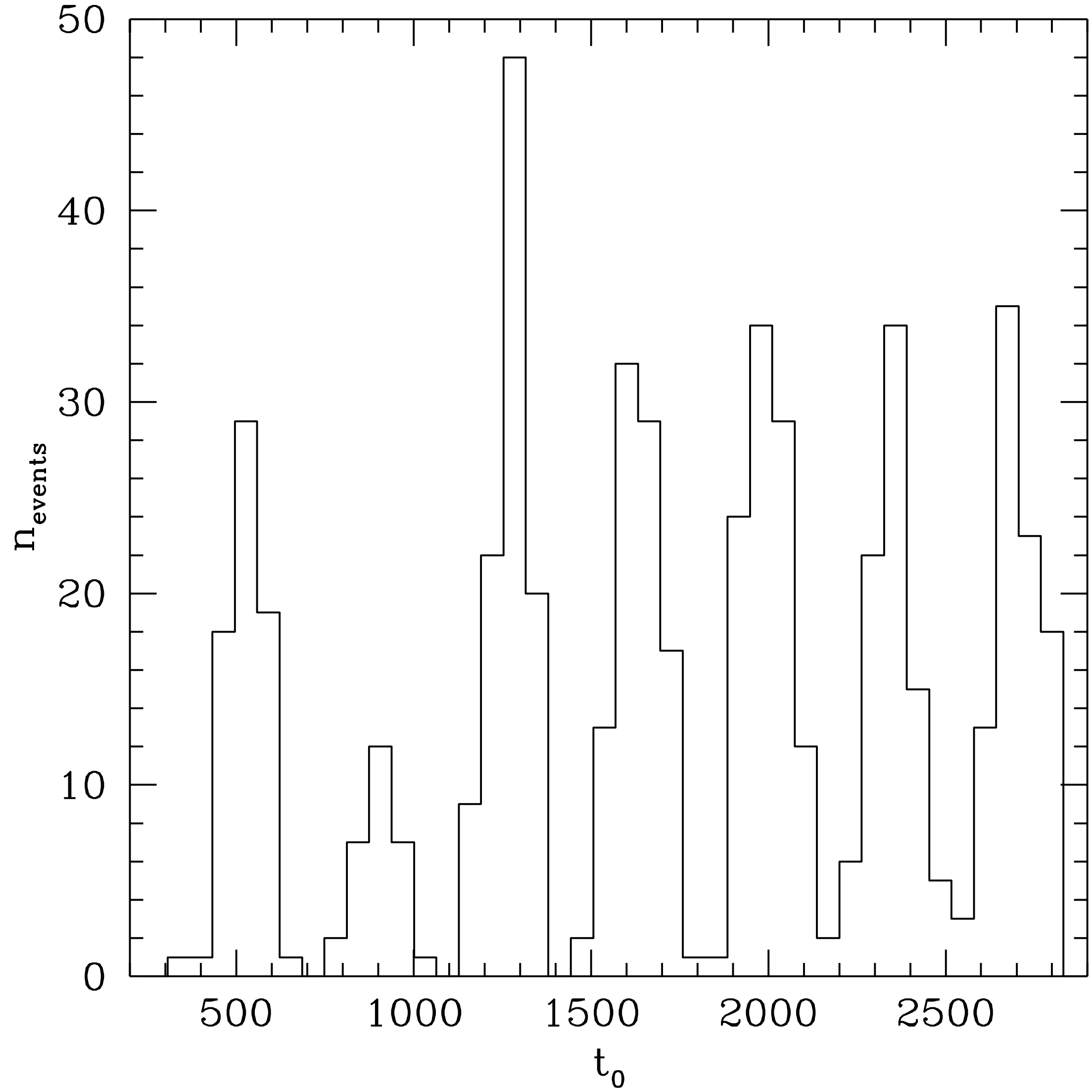

Figure 4.6 Histogram of t_0, the time of peak magnification. Most of the variation is due to large gaps in the data during prime LMC observing times; taking that into account the distribution is consistent with a uniform distribution as expected.

the CMD will be used to select events on clump giants to create the subsample for the optical depth calculation.

Another microlensing experiment, OGLE, also observed several of our events. We report the designations used by OGLE for events found by multiple experiments in Table 4.2.

Table 4.2. Alternative designations of our events

field.tile.seq	OGLE ID	field.tile.seq	OGLE ID
104.20515.498	BUL_SC35_144974	118.19182.891	BUL_SC38_95103
104.20640.8423	BUL_SC35_451130	118.19184.1814	sc38_3314
104.20779.9616	BUL_SC35_770398	118.19184.939	BUL_SC38_120518
104.20906.3973	sc36_6759	119.19442.370	BUL_SC38_627315
105.21287.3893	sc36_1245	119.19701.1513	sc1_1943
108.19073.2291	BUL_SC21_833776	119.19832.5483	BUL_SC1_460673
108.19204.267	BUL_SC30_165305	119.20092.3109	sc45_1286
108.19333.1878	BUL_SC30_352272	119.20219.2348	sc45_810
108.19464.254	BUL_SC30_559419	178.23136.5133	BUL_SC16_436041
108.19464.5201	BUL_SC30_553231	178.23398.4814	BUL_SC17_270411
108.19853.8058	BUL_SC31_513194	308.38595.1020	BUL_SC10_454300
109.19853.2074	BUL_SC31_513194	401.48406.2341	sc20_5229
109.19853.4889	sc31_2369	401.48408.649	BUL_SC20_395103
109.19987.2565	sc32_4302	401.48467.4621	BUL_SC20_391296
109.20370.5166	sc2_3095	402.48158.1296	BUL_SC34_144644
109.20640.360	BUL_SC35_451130	402.48219.2582	sc34_4536
109.20893.3423	BUL_SC33_164492	402.48279.1043	BUL_SC34_639703
113.18674.756	sc21_1395	403.47427.353	sc4_3503
113.18810.2999	BUL_SC21_388360	403.47491.770	BUL_SC4_522952
113.19196.3672	sc30_1782	403.47546.2003	BUL_SC4_463924
113.19325.2001	BUL_SC30_236837	403.47550.807	BUL_SC4_708424
114.19587.3861	BUL_SC31_24931	403.47554.630	BUL_SC4_568740
114.19589.4149	BUL_SC31_48308	403.47669.1859	BUL_SC39_323517
114.20370.6070	sc2_3095	403.47671.57	BUL_SC39_361372
114.20494.3907	BUL_SC2_27414	403.47728.5938	sc39_3550

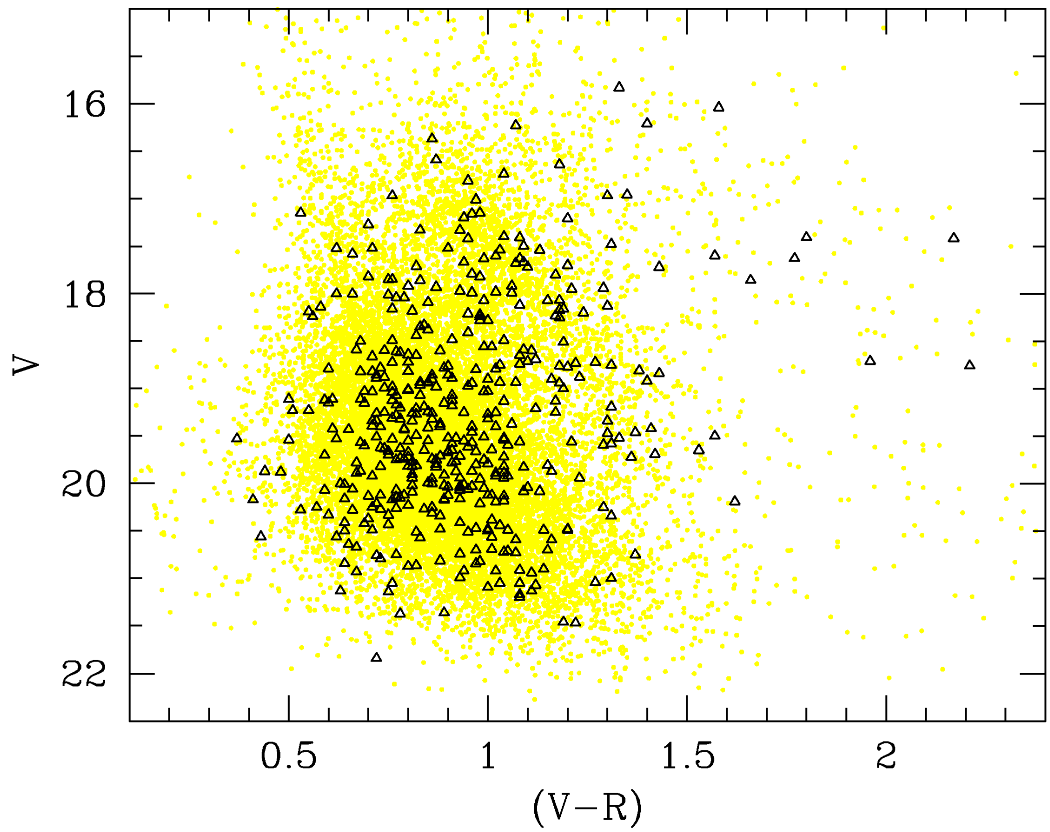

Figure 4.7 Color-magnitude diagram of the events and a representative sample of all objects monitored. As expected, events follow the same distribution as the entire sample.

5

Optical Depth

The optical depth, τ, is calculated and presented as the primary measure of the amount of lensing matter between the observer (us) and the source (the Galactic bulge). The procedure is as follows:

1. Events are selected from the larger set of computer selected events (criteria "c") based on their color and magnitude.

2. Blending is examined and determined to be a small, if not negligible, effect for our sample.

3. Efficiency for detecting each event is calculated.

4. Optical depth is calculated from event parameters, field parameters, and efficiencies.

5.1 Selection of Clump Giant Events for Optical Depth

For the optical depth calculation we would like to select a set of unblended bulge source stars. These two requirements lead us to choose red clump giant stars

(RCGs). RCGs are numerous in the bulge and very bright so they are an ideal set of sources. Including other sources either in front of or behind the bulge would distort our measurement as closer objects are less likely to be lensed and further objects are more likely to be lensed. Dimmer stars included in our sample would also distort our result because blending is more likely to affect them.

We use stars' positions on the color-magnitude diagram (CMD) to select red clump giants. A new, more sophisticated, method is used to correct for extinction, the reddening and dimming of stars due to interstellar dust. Despite this the possibility of contamination by non clump-giant stars still exists.

The problem of selection is first examined through the properties of the CMD in the Galactic bulge. RCGs can be found on the dereddened CMD using the accurately measured extinction toward Baade's window (Stanek (1996) with zero point correction from Gould et al. (1998) and Alcock et al. (1998)). From this dereddened CMD the positions of RCGs on the apparent CMD can be predicted for different extinctions. From Baade's window data we find that red clump giants are found in the range $(V-R) \in (0.40, 0.60)$ and are concentrated along the line $V_0 = 14.35 + 2.0(V-R)_0$, where the uncertainty in the zero point is at least 0.1 magnitudes. A range of $0.6-0.7$ magnitudes either way is allowed to account for intrinsic brightness variation in the population and variation in the distance. The parallelogram in the upper left corner of Figure 5.1 is given by this analysis. Specifically, the parallelogram is defined by the four points in $((V-R)_0, V_0)$ space: (0.40, 14.52), (0.40, 15.88), (0.60, 16.28), and (0.60, 14.92). Assuming the populations of red clump giants have the same properties as that in Baade's window, the parallelogram defined above can be shifted along the reddening vector of a field to find the expected location of red clump giants in that field. The long parallel lines are the boundaries of the region where one expects to find clump giants with various values of extinction.

This universal RCG selection described above allows contamination by main sequence stars in areas of the sky with high extinction. Previous MACHO Collaboration analysis (Popowski et al. 2001a, 2001b) tried to reduce this by introducing a color cut $(V-R) > 0.7$. For very high extinction fields, main sequence stars may be reddened enough that they enter the clump region, but to move the $(V-R) > 0.7$ cut would remove clumps from the low extinction fields. To remedy this a variable cut is used depending on the properties of the CMD for each tile, a $4' \times 4'$ patch containing a few thousand objects on average.

For the tile specific cuts, the procedure remains the same except for the introduction of a a variable $(V-R)$ cut to allow for the varying extinction across the observed fields. First we checked that the MACHO tiles are large enough to give a reasonable CMD for selection and that they are small enough that extinction does not vary much in a single tile. Because there are more than 10,000 tiles in the MACHO bulge fields we form a training set of 240 tiles. For this we use tiles at the location of suspected microlensing events from the analysis of the first 5 years of data. This set of tiles contains a range of both extinction and stellar densities and reasonably covers the entire range of both. We use a blue clump limit at $(V-R)$ halfway between the central clump and main-sequence over-density at the V magnitude of the clump. For each of the 240 training tiles a cut was chosen after a visual inspection.

To relate the training set cuts to the rest of the tiles we use the moments of the color distribution on each field. We calculated the first four moments of the $(V-R)$ distribution for each tile. After some fitting we decided that we need only use the mean and dispersion. We started with the form

$$(V-R)_{bound} = \alpha + \beta \, \langle V-R \rangle_{CMD} + \gamma f(\sigma(V-R)_{CMD}) \, . \qquad (5.1)$$

We tried $f(x) = x, x^2, \ln(x)$ and found $\ln(x)$ to give the best results, although the others gave similar results. Using this form we require clump giants to be redder than

$$\begin{aligned} (V-R)_{bound} = (&-0.001 \pm 0.33) \\ &+ (0.872 \pm 0.014)\,\langle V-R\rangle_{CMD} \\ &+ (-0.042 \pm 0.012)\ln(\sigma(V-R)_{CMD})\,, \end{aligned} \tag{5.2}$$

where the coefficient errors are found by requiring $\chi^2/n_{dof} = 1$ and assuming the errors on each point are the same. The correlation matrix for α, β, and γ is

$$\begin{pmatrix} 1.0000 & -0.9084 & 0.9720 \\ -0.9084 & 1.0000 & -0.7872 \\ 0.9720 & -0.7872 & 1.0000 \end{pmatrix} \tag{5.3}$$

Our training set is found to be consistent with a normal distribution, the furthest boundary from the fit being at 3.28σ, and for this and other boundaries with large deviations either the fit boundary or the initial (visually selected) boundary are reasonable choices. In fact, the scatter of the visually selected bounds around the values from the fit is 0.02 magnitudes, an order of magnitude smaller than the typical range of clump colors. We then use equation (5.2), without the coefficient errors to calculate the blue bound for each tile.

The final set of selection criteria for clump giants is then

$$15.0 \le V_{base} \le 20.5\,, \tag{5.4}$$

$$V_{base} \ge 4.2(V-R)_{base} + 12.4\,, \tag{5.5}$$

$$V_{base} \le 4.2(V-R)_{base} + 14.2\,, \tag{5.6}$$

$$(V-R)_{base} > (V-R)_{bound}\,, \tag{5.7}$$

$$\text{field} < 301 \quad \text{or} \quad \text{field} > 311\,, \tag{5.8}$$

where the subscript “base” refers to the magnitude or color at the baseline, away from the event, as measured from the fit to the light curve. The cuts on V magnitude, equation (5.4) are intended to eliminate source objects with saturated photometry or dim objects that may be heavily blended; in practice it is not needed as the color dependent cuts, equations (5.5) and (5.6), are more restrictive. The color dependent cuts, (5.5) and (5.6), define the reddening channel where clumps are expected to be. Condition (5.7) is the tile dependent cut eliminating bright foreground stars which will be bluer than the clump sample. The final condition, equation (5.8), removes the disk dominated fields, the 300 series, where disk stars are dominant. The clump giant region defined by equations (5.4)-(5.8) is shown on the CMD in Figure 5.1, events are marked with triangles, open for non-clumps and filled for events that pass our clump cuts.

The slope of the reddening cuts, equations (5.5) and (5.6), is given by the reddening relation. We use the relation found by Popowski et al. (2003) in Baade's window, $R_{V,VR} = 4.2$. We found that these results were similar to those obtained with a reddening slope of 4.5 as used in the previous MACHO analysis, but inconsistent with a slope of 5.0. Previous results (Popowski et al., 2001a) using $R_{V,VR} = 5.0$ did not have many high extinction events and used a redder intrinsic clump color and so their results were not much different. The properties of extinction in the bulge are not fully understood and may have caused the selection to fail, but this was not the case. From visual inspections of CMDs of smaller regions we find the selection method used to be adequate for the range of extinctions found in the bulge.

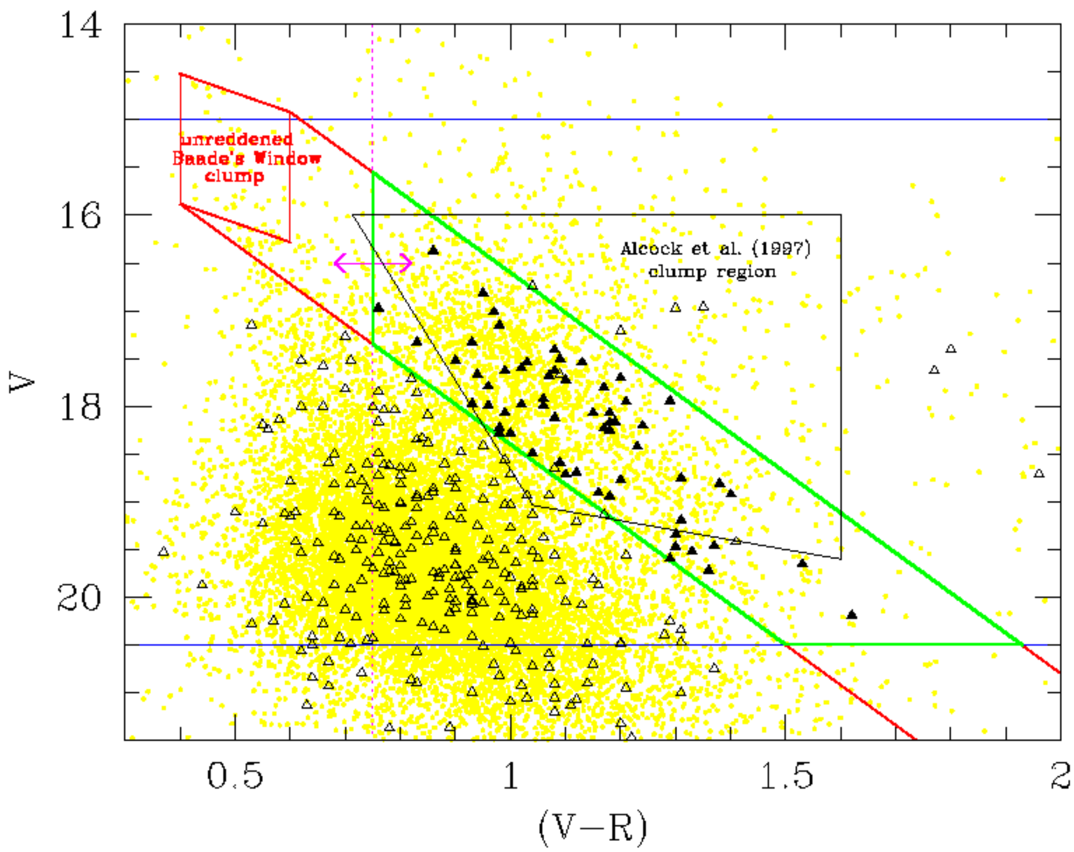

Figure 5.1 The color-magnitude diagram of MACHO objects. The positions of events are shown with open triangles for events on non-clumps and closed triangles for events on clump giants. The cuts (5.4)-(5.8) are shown as well along with the cuts from a previous MACHO analysis.

Table 5.1: Event parameters

field.tile.seq	RA (J2000)	DEC (J2000)	l	b	V	$(V-R)$	$(V-R)_{\mathrm{boundary}}$	t_0	$\hat{t}$	$A_{\max}$	$\frac{\chi^2}{n_{dof}}$
101.21689.315	18 06 58.32	−27 27 45.7	3.639	−3.327	17.50	1.09	0.81	593.5	165	4.80	1.19
102.22466.140	18 08 47.04	−27 40 47.3	3.643	−3.783	16.81	0.95	0.81	1275.6	153	3.88	0.95
104.19992.858	18 02 53.76	−27 57 50.0	2.761	−2.784	18.59	1.09	0.85	1169.7	106	2.23	2.15
104.20119.6312[a]	18 03 20.64	−28 08 14.6	2.658	−2.955	17.99	1.06	0.78	1975.3	38.7	1.62	1.62
104.20251.50	18 03 34.08	−28 00 19.1	2.797	−2.933	17.33	0.93	0.82	493.9	287	10.1	1.75
104.20251.1117	18 03 29.04	−28 00 31.0	2.785	−2.919	18.22	0.98	0.82	463.2	45.5	2.09	0.93
104.20259.572	18 03 33.36	−27 27 47.2	3.269	−2.665	18.16	1.19	0.91	538.5	14.2	1.58	1.56
104.20382.803	18 03 53.28	−27 57 35.6	2.872	−2.973	17.79	0.96	0.84	1765.8	254	5.72	4.40
104.20515.498	18 04 09.60	−27 44 35.2	3.090	−2.919	17.63	0.99	0.81	2061.7	53.6	1.76	1.42
104.20640.8423[b]	18 04 33.60	−28 07 31.8	2.800	−3.183	17.15	0.98	0.79	2374.9	30.8	1.65	2.23
104.20645.3129	18 04 26.16	−27 47 35.2	3.077	−2.997	17.68	1.07	0.83	1558.3	152	1.82	0.77
105.21813.2516	18 07 06.96	−27 52 34.3	3.292	−3.555	17.41	1.08	0.83	1928.5	17.5	13.2	1.14
108.18947.3618	18 00 29.04	−28 19 20.3	2.186	−2.498	17.72	1.10	0.89	1287.9	45.6	2.05	0.94
108.18951.593[‡]	18 00 33.84	−28 01 10.6	2.458	−2.363	18.07	1.18	0.95	1991.6	47.3	4.05	7.02
108.18951.1221	18 00 25.92	−28 02 35.2	2.423	−2.350	18.94	1.18	0.95	583.6	45.8	2.16	0.92
108.18952.941	18 00 36.00	−27 58 30.0	2.501	−2.348	18.90	1.16	1.02	1324.9	66.9	2.39	1.11
108.19074.550	18 00 52.32	−28 29 52.1	2.076	−2.659	17.54	1.03	0.88	2050.6	9.30	1.78	0.97
108.19334.1583	18 01 26.40	−28 31 14.2	2.117	−2.779	17.67	0.94	0.86	1231.4	18.5	4.09	0.38
109.20119.1051[a]	18 03 20.64	−28 08 14.6	2.658	−2.955	18.09	0.97	0.78	1977.6	28.7	1.62	1.01
109.20640.360[b]	18 04 33.60	−28 07 32.5	2.799	−3.183	17.33	1.05	0.79	2375.1	28.7	1.67	0.72
110.22455.842	18 08 51.36	−28 27 11.2	2.971	−4.169	18.28	0.98	0.76	1900.1	19.8	2.54	0.84
113.18552.581	17 59 36.00	−28 36 24.1	1.842	−2.470	17.60	1.02	0.86	603.7	27.9	1.77	1.11
113.18804.1061	18 00 03.36	−29 11 04.2	1.390	−2.843	18.28	1.00	0.84	1166.6	6.50	1.62	0.96
113.19192.365	18 01 06.96	−29 18 53.6	1.391	−3.109	17.80	1.17	0.96	2092.6	36.9	1.97	0.52
114.19712.813	18 02 11.52	−29 19 20.6	1.500	−3.317	18.12	1.08	0.87	1643.4	23.7	3.58	0.62
114.19846.777	18 02 36.72	−29 01 41.9	1.801	−3.252	17.98	1.02	0.80	545.4	65.0	1.55	1.86
114.19970.843	18 02 54.48	−29 26 29.4	1.472	−3.511	17.99	0.96	0.85	1281.9	14.7	4.47	0.65
118.18014.320	17 58 25.20	−29 47 59.6	0.678	−2.840	17.01	0.97	0.89	877.6	25.5	1.58	1.05
118.18141.731[‡]	17 58 36.72	−30 02 19.3	0.491	−2.995	17.92	1.06	0.94	884.1	9.80	12.6	0.65

Continued on Next Page...

Table 5.1

... Continued from Previous Page

field.tile.seq	RA (J2000)	DEC (J2000)	l	b	V	$(V-R)$	$(V-R)_{\rm boundary}$	t_0	$\hat{t}$	$A_{\max}$	$\frac{\chi^2}{n_{dof}}$
118.18271.738	17 58 52.56	−30 02 08.2	0.522	−3.043	18.25	1.18	0.96	456.4	53.7	2.23	0.69
118.18402.495	17 59 13.92	−29 55 53.4	0.651	−3.058	17.63	1.08	0.93	454.1	23.8	3.60	0.96
118.18797.1397	18 00 06.96	−29 38 06.0	1.004	−3.078	19.34	1.30	0.97	2013.1	126	8.35	1.07
118.19182.891	18 01 09.84	−29 56 19.0	0.852	−3.425	17.97	0.93	0.84	2367.0	13.6	6.28	1.20
118.19184.939	18 01 10.32	−29 48 55.4	0.960	−3.366	18.07	0.99	0.83	2692.8	74.4	2.14	1.13
121.22032.133	18 07 46.80	−30 39 41.4	0.915	−5.025	16.37	0.86	0.75	1287.3	19.5	1.58	2.51
158.27444.129	18 20 10.32	−25 08 25.8	7.097	−4.827	16.97	0.76	0.63	2376.4	41.7	2.31	1.80
162.25865.442	18 16 30.72	−26 26 58.2	5.549	−4.712	17.52	0.90	0.73	1225.3	60.9	1.58	1.32
162.25868.405	18 16 46.08	−26 11 43.1	5.801	−4.643	17.33	0.83	0.77	1222.8	30.8	2.77	1.39
176.18826.909	18 00 15.36	−27 42 47.9	2.691	−2.153	18.77	1.20	1.01	2364.7	24.3	1.77	1.17
178.23531.931	18 11 17.52	−25 59 51.4	5.391	−3.467	18.71	1.10	0.92	1590.3	13.7	2.18	1.08
180.22240.202	18 07 57.84	−25 24 48.2	5.542	−2.528	18.92	1.40	0.98	1286.9	311	3.42	1.15
401.47991.1840	17 57 07.44	−28 13 44.0	1.899	−1.810	19.46	1.37	1.12	1953.0	44.7	1.92	0.61
401.47994.1182	17 57 07.92	−28 00 27.7	2.091	−1.701	19.65	1.53	1.23	2362.7	60.6	3.68	1.05
401.48052.861	17 57 23.76	−28 10 24.6	1.977	−1.834	18.75	1.31	1.13	2291.5	72.0	2.65	0.69
401.48167.1934	17 57 57.36	−28 27 09.7	1.796	−2.080	18.42	1.23	1.09	2179.0	125	2.53	0.89
401.48229.760‡	17 58 13.44	−28 20 32.3	1.921	−2.076	18.07	1.15	1.00	2694.5	20.1	1.82	1.18
401.48408.649‡	17 59 08.88	−28 24 54.7	1.959	−2.289	17.70	1.20	0.92	2325.4	74.6	3.07	1.30
401.48469.789	17 59 22.32	−28 20 21.8	2.050	−2.294	18.23	1.17	0.92	1554.8	5.70	5.96	0.42
402.47678.1666	17 55 22.56	−29 04 12.7	0.978	−1.901	19.19	1.31	1.07	2393.1	13.6	2.48	0.88
402.47737.1590	17 55 41.52	−29 09 00.7	0.944	−2.001	18.49	1.04	0.99	1552.3	5.50	2.79	1.03
402.47742.3318	17 55 42.96	−28 49 17.4	1.230	−1.840	20.19	1.62	1.10	1377.1	50.1	8.64	1.21
402.47796.1893	17 56 10.80	−29 10 44.4	0.972	−2.107	19.52	1.33	1.03	1678.7	19.3	22.5	1.47
402.47798.1259	17 56 11.04	−29 06 14.0	1.038	−2.070	19.72	1.36	1.10	1583.7	47.6	4.94	1.38
402.47799.1736	17 56 07.20	−28 58 32.5	1.142	−1.994	19.59	1.29	1.16	2410.0	115	2.26	0.47
402.47856.561	17 56 24.96	−29 12 56.5	0.966	−2.170	18.81	1.38	1.15	1566.6	12.3	2.14	1.63
402.47862.1576‡	17 56 20.64	−28 47 42.0	1.323	−1.945	19.47	1.30	1.15	2028.5	54.3	7.52	6.13
402.48158.1296	17 57 47.52	−29 03 54.4	1.247	−2.346	18.69	1.12	1.01	2325.7	15.9	3.94	0.98
402.48280.502	17 58 24.96	−28 57 46.4	1.404	−2.422	18.17	1.18	0.90	1342.5	25.5	2.08	1.14

Continued on Next Page...

Table 5.1

. . . Continued from Previous Page

field.tile.seq	RA (J2000)	DEC (J2000)	l	b	V	$(V-R)$	$(V-R)_{\mathrm{boundary}}$	t_0	$\hat{t}$	$A_{\max}$	$\frac{\chi^2}{n_{dof}}$
403.47491.770	17 54 38.64	−29 33 13.0	0.480	−2.007	17.94	1.29	1.04	2633.9	48.5	2.43	0.99
403.47550.807	17 55 00.00	−29 35 03.8	0.492	−2.089	17.95	1.21	1.04	2774.3	11.6	3.60	0.87
403.47610.576	17 55 17.04	−29 37 40.8	0.486	−2.164	17.54	1.13	0.98	2657.9	9.60	4.75	2.56
403.47845.495	17 56 22.80	−29 55 16.3	0.351	−2.517	18.20	1.24	1.07	1945.8	15.0	2.03	0.88

Designations:

‡: binary event,

^{a} and ^{b}: each superscript marks two members of a pair that represents a single microlensing event in two overlapping fields.

The 62 lensed clump giant stars that pass the cuts above are listed with their positions, magnitudes, colors, and microlensing parameters in Table 5.1, their locations are shown in Figure 5.2, and the light curves are presented in Appendix B.3. In Table 5.1 and hereafter V and $(V - R)$ will refer to baseline magnitudes; the "base" subscript is dropped to reduce clutter. Two events are found in overlapping regions of fields and marked with letters ("a" or "b"). For the optical depth calculation we will count both of the duplicate events since field overlaps increase both the total number of stars monitored and the number of events detected proportionally. The overlap is small and should not strongly affect the results. Five of the clump giant microlensing events are potential binary events and are marked with a ‡ symbol.

Figure 5.3 graphically summarizes the basic properties of clump events. Included are plots of distributions of V, $(V - R)$, t_0, $\log(\hat{t})$, $\log(A_{max})$, and $\log(\chi^2/n_dof)$. The distributions are as expected. The distribution of t_0 is not uniform, but this is due to gaps when the LMC was being observed, equipment problems in year two, and observing strategy changes. In the second and last year some fields were observed more frequently to look for shorter duration events; necessarily other fields were observed less frequently and the efficiency of detecting events in them decreased. In Figure 5.4 we test systematic effects in microlensing parameters. The top four panels show impact parameters, u_{min}, and Einstein diameter crossing times, $\hat{t}$, as a function of Galactic coordinates, l and b. The parameters seem to have no dependence on position. Similarly, the lower two panels suggest that there is no correlation between the impact parameter and duration or impact parameter and event color. If many of our events were not microlensing we would expect to see some grouping or correlation here.

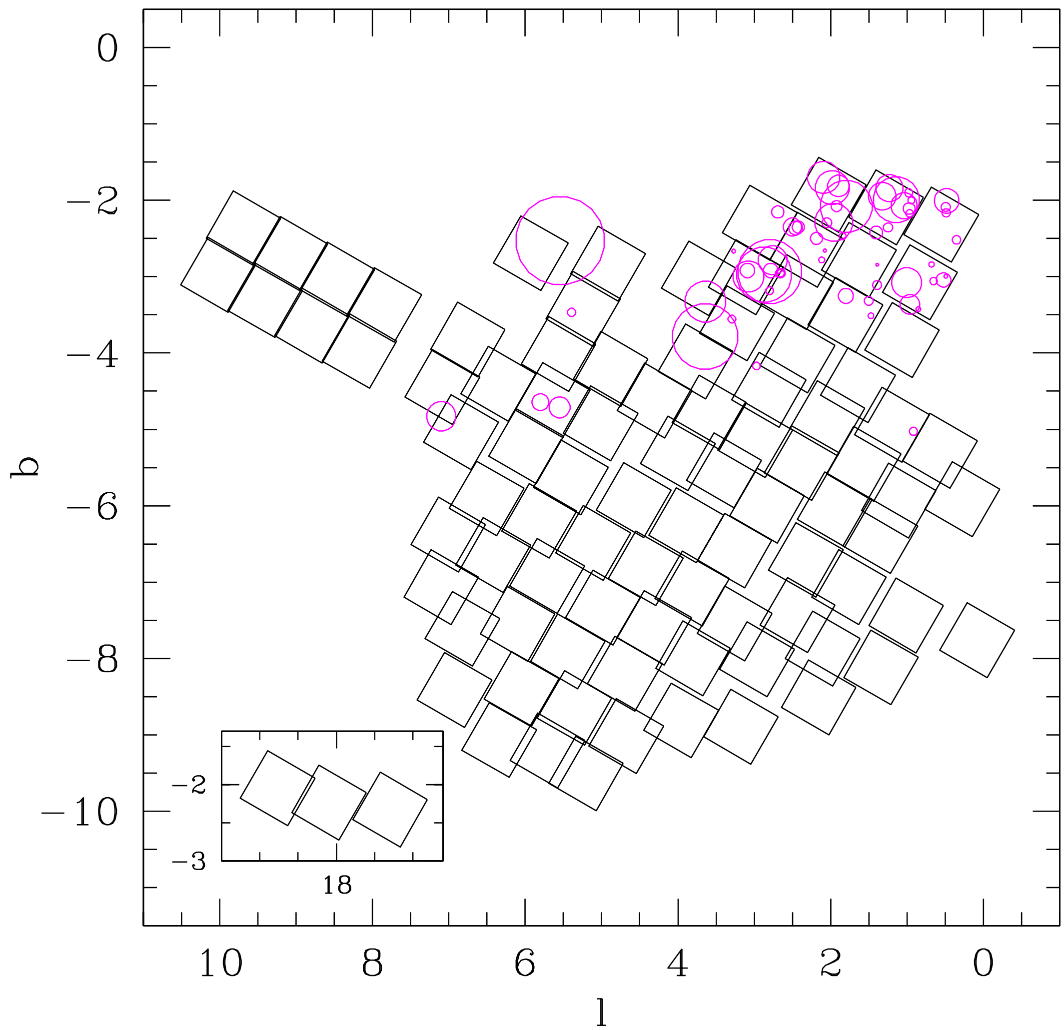

Figure 5.2 Distribution of events with clump giants as sources in galactic coordinates. Radii are proportional to events contribution to the optical depth, $t/\epsilon(t, A_{max})$, see §5.3 for details.

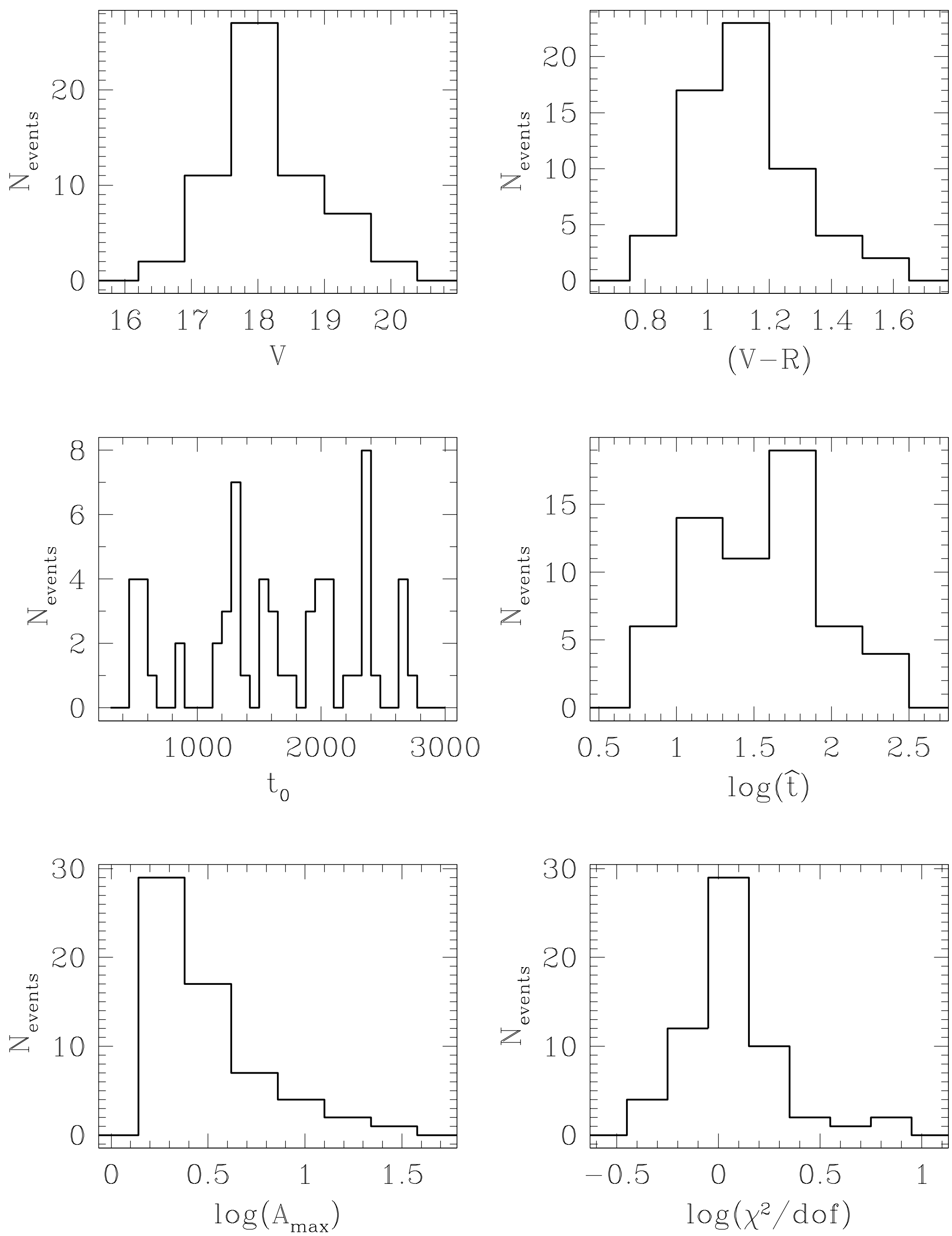

Figure 5.3: Basic properties of the clump sample.

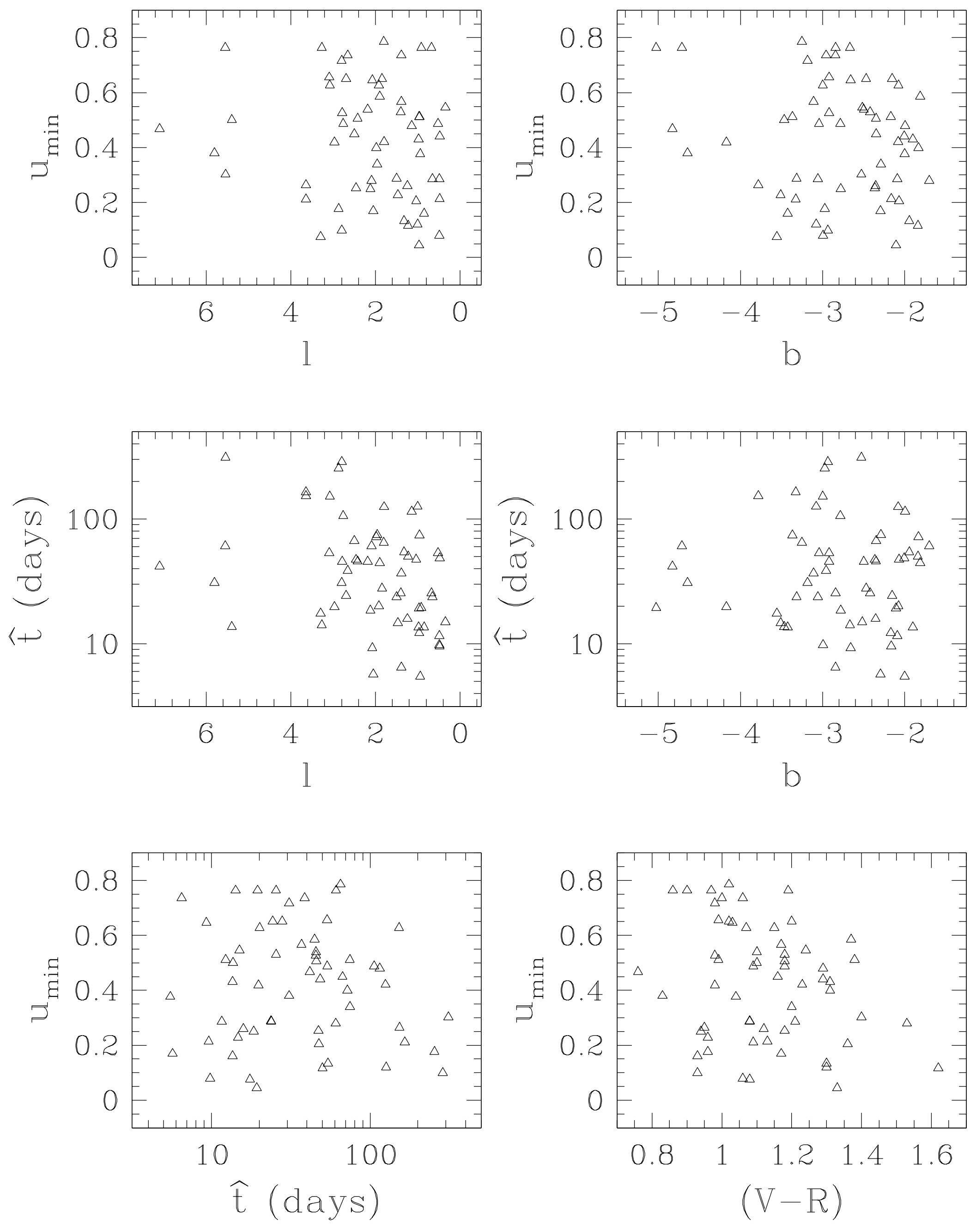

Figure 5.4 Distributions of microlensing parameters as a function of position, duration, or color.

5.2 Does Blending Affect Our Sample?

We make an analytical estimate of blending and several tests of the effect of blending on our sample: a visual inspection, a test of color shift in the peak, a test of the recovered distribution of impact parameter. We estimate the blend fraction from photometric shifts, and analyze blend fits of binary events where the blend fraction is better constrained.

5.2.1 An Analytical Estimate of Blending and its Effect on the Optical Depth

We can make a simple theoretical estimate of the effect of blending on our clump giant sample using the luminosity function in Baade's window as measured by Holtzman et al. (1998). The region we calculate the optical depth for is at a lower Galactic latitude than Baade's window. To account for this we multiply Holtzman's luminosity function by 1.5. Faint stars within one full-width half-maximum (FWHM) of the PSF of the clump source will not be resolved as separate objects and will be blended with it. Since the microlensing fits are dominated by observations with better than median seeing, both in the baseline and in the peak, we use the median seeing for MACHO observations of $2\farcs1$ and expect our result to be an upper limit for the amount of blending. From our modified Holtzman luminosity function we calculate an expectation of 16 stars with absolute magnitude $M_V > 1.3$ in the seeing disk of an average clump. These 16 stars should have a combined flux of $M_V = 3.13$, brighter than the average main-sequence star in the bulge, but 2.13 magnitudes fainter than the average clump giant.

We consider a similar case that would result in a slightly larger effect from blending: a single clump, $f_{cg} = 0.877$, blended with 3 main-sequence stars each with $f_{ms} = 0.041$. The fraction of light coming from the clump is the same as above, but the 16 faint stars are replaced with 3 stars with the same total brightness. Our threshold for detection is $A_{max} \geq 1.5$. In order for the object to pass this cut the clump would have to be lensed with $A_{max} \geq 1.57$; this corresponds to a impact parameter cut of $u_{\rm cut} = 0.771$ instead of $u_{\rm cut} = 0.826$. Since u_{min} is uniformly distributed a fraction $\kappa_{\rm cg} = 0.771/0.826 = 0.93$ of the clump events will pass our cut. For each of the three faint stars in the blended object the effective cuts would be $A_{max} \geq 13.2$ or $u_{\rm cut} = 0.076$. Each of these is just as likely to be lensed as the clump, so we should expect to have three lensed faint stars for each clump event, $\kappa_{\rm ms} = 3 \times 0.076/0.82 = 0.27$. The efficiency of detecting these events will also change because the observed duration of the event will also be reduced due to blending. Using a typical value of $A_{max} = 2.5$ we can find the shift in $\hat{t}$ with the methods described in Chapter 6. We find the duration of an event on the clump will appear to be 0.94 times the actual duration and an event on one of the faint main-sequence stars will appear to be 0.12 times the actual duration. For an actual clump event with $\hat{t} \sim 50$ days the detection efficiency, or probability of detection, is essentially unchanged for the clump event, $\xi_{\rm cg} = 1.0$; however, the detection efficiency for the event on the main-sequence star is reduced by at least a factor of $\xi_{\rm ms} = 1.5$. Since the impact parameter of events is uniformly distributed we can calculate the ratio of detected events on the clump giant to detected events on main-sequence stars:

$$\frac{N_{cg}}{N_{ms}} = \frac{u_{\rm cut,cg}/\xi_{\rm cg}}{3u_{\rm cut,ms}/\xi_{\rm ms}} = 5.08\,. \qquad (5.9)$$

We expect roughly 83% or more apparent clump giant events to be lensed clump giants and roughly 17% or less to be faint lensed stars blended with a clump. In addition, the 17% of apparent clump giant events that are actually lensed faint stars will have a significantly shortened duration.

There is the possibility that many faint stars could be blended to form one object that appears to be a clump. While this is possible, it is unlikely since the luminosity function in the bulge drops very quickly just below the clump region.

The stars that are only slightly fainter than the clump giants are mainly foreground stars and are much less likely to be lensed.

Using the same values as above and the ratio of real clump giant events to apparent clump giant events derived above we can estimate the effect on the optical depth. The usual formula for the optical depth is

$$\tau = \frac{\pi}{4E} \sum_{i=1}^{N_{events}} \frac{\hat{t}_i}{\epsilon(\hat{t}_i)}\,, \tag{5.10}$$

where $\epsilon(\hat{t}_i)$ is the efficiency of detecting event i and $E = NT_{obs}$ is the exposure – the product of the number of stars observed, N, and the period of time they are observed, T_{obs}. In what follows we assume that the exposure is not affected by blending and is accurately estimated.

Blending will change the number of events we measure in two ways: decrease the number of lensed clump giants we observe with $A_{max} \geq 1.5$, and add lensed non-clump stars. The decrease in the number of clump giant events will decrease the optical depth, but the non-clump events will increase it. If we only use clump giant events the optical depth will be changed by three things: the fraction of events that meet our cuts, the change in the efficiency, and the change in the observed $\hat{t}$. The total change of the optical depth will be a factor of

$$\frac{\kappa_{\rm cg}}{\xi_{\rm cg}} \frac{\hat{t}_{obs}}{\hat{t}_{actual}} = 0.87\,. \tag{5.11}$$

Similarly the contribution to the optical depth by events on the main-sequence stars will will be

$$\frac{\kappa_{\rm ms}}{\xi_{\rm ms}} \frac{\hat{t}_{obs}}{\hat{t}_{actual}} = 0.02\,. \tag{5.12}$$

The net effect on the measured optical depth will be to reduce it to roughly 90% its real value.

There is another case that should be considered. It is possible that the photometry code will include the flux from the three main sequence stars in the background "sky" brightness. In this case the the contribution to the optical depth from the clump giant will be unchanged from its contribution if it was not blended. The main-sequence stars would still contribute, with $\tau_{obs}/\tau_{actual} = 7.4$ and $\kappa_{ms} = 3 \times 0.086/0.826 = .31$. Adding this contribution we find the observed optical depth to be 1.03 times the true optical depth.

These two estimates should bracket the true value of τ. The real case is likely to fall somewhere between the two and the error induced in τ would be less than 10%.

5.2.2 Visual Inspection For Blending

We review the color light curves of all events with particular emphasis on the peak region to inspect for blending. Red clump giants are more likely to be blended with stars that are bluer rather than stars with identical color, thus a color shift should be present in the light curve if it is blended. The light curves of all clump events showing blue and red magnitudes and the difference between them for simultaneous observations are shown in Figure 5.5. Here we display two example events; the entire sample of clump giant event light curves without the difference plot is in Appendix B.3. The fit plotted with the data assumes no blending, in most cases they properly represent observational points.

We examine the light curves for deviations from the unblended fits. We note that events 109.20640.360, 113.19192.365, 176.18826.909, 401.47994.1182, 401.48052.861, 401.48167.1934, 402.47856.561, and 403.47491.770 have extremely sparse color coverage in the peak region or lack it completely; therefore, any blending-related information that can be extracted from their light curves is very limited. The events for which there is an apparent achromatic signal, however slight, are listed in Table 5.2. Some of these events have deviations from their fitted light curve due to their exotic character: either binarity or parallax effect. We are left with 11 events of 62 that are not immediately explained by known effects. In addition, 3 of the 11 have either asymmetric or caustic type deviations which is

Table 5.2. Events with light curve deviations

field.tile.seq	Comments
101.21689.315	possible parallax
104.20119.6312/109.20119.1051	parallax or xallarap
104.20251.50	parallax
104.20382.803	parallax
104.20640.8423	—
105.21813.2516	possible red blend
108.18951.593	binary
114.19970.843	weak signal
118.18141.731	binary
118.18797.1397	asymmetry in blue peak
158.27444.129	—
180.22240.202	post-peak blue points preferentially low
401.48229.760	binary
401.48408.649	binary
402.47742.3318	—
402.47799.1736	coherent steep variation in blue
402.47862.1576	binary
402.48280.502	possible blue blend
403.47610.576	possible red blend

more likely a weak signal of a binary lens rather than blending. We conclude that only 8 events (13%) can be suspected of significant blending based on the visual inspection of their light curves.

5.2.3 Test For Color Shift

Next we examine the color near the center of the peak ($|t - t_0| < \hat{t}/\sqrt{2}$) and compare it to the baseline of the light curve. We start with a small region of width $\hat{t}/8$ centered on t_0 and expand it until we have at least 2 points with simultaneous observations in each filter. Using these points in each light curve we calculate the difference in flux between the peak and the baseline in each filter (ΔV

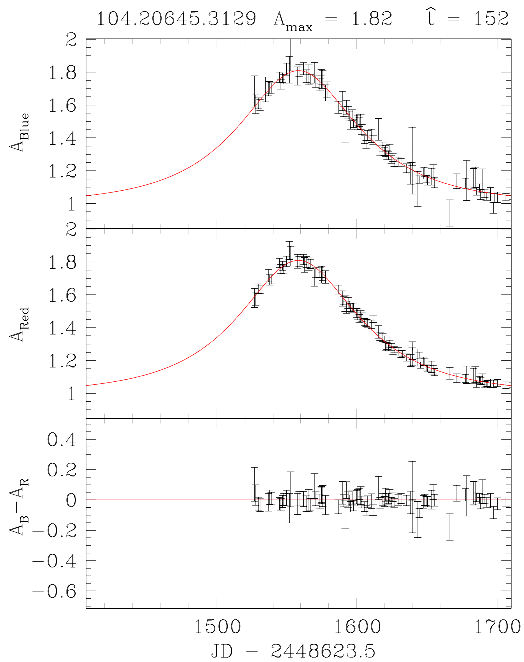

Figure 5.5 The left panel shows an event with no color signal, and the right panel the event with a weak signal. For each event the top box shows the amplification in the blue filter (normalized so baseline flux is 1), the middle box shows the amplification in the red filter, and the bottom box the difference between in flux between the two filters, or the color. Here only the peak region is shown, within $\hat{t}$ of the time of maximum amplification t_0.

or ΔR). In Figure 5.6 we plot the ratio $\Delta V/\Delta R$ versus A_{max} for the 53 clump giant events that have observations in both colors in the peak. For blending-free microlensing events $\Delta V/\Delta R$ should be unity since gravitational lensing is achromatic. Of the 53 events 20.7% were more than 1σ away from unity, consistent within errors with no blending in our sample. Two events differ by more than 6σ, 108.18951.593 and 403.47610.576, perhaps indicating blending. One event, 108.18951.593, is likely blended with a faint star of a very different color, and examination of the light curve of the second event (403.47610.576) shows that it has many points far off the microlensing fit (403.47610.576), probably indicating problems with the photometry or intrinsic variability. If we ignore these two events we have 17.6% more than 1σ from unity and the distribution is roughly Gaussian.

5.2.4 Impact Parameter Distribution

For a sample of microlensing events the distribution of the impact parameters, u_{min}, should be uniform. If the sample is significantly blended the apparent amplification of many events will be reduced and u_{min} will be shifted to higher values. The distribution will be non-uniform. We use this to test for the presence of blending.

We expect the cumulative distribution of u_{min} to rise uniformly from 0 to N_{events} over the interval (0, 0.826), where 0.826 is the upper limit on impact parameters due to our cuts. We show the actual distribution along with the expected distribution in Figure 5.7. Using the Kolmogorov-Smirnov (K-S) test we find good agreement with a uniform distribution. We find the K-S $D = 0.107$ for 55 events (60 unique events minus 5 binaries) corresponding to a probability of 53% of finding D this large or larger. In this analysis we have used the efficiency corrected distribution, but even with no correction for efficiency we find agreement: $D = 0.103$ and a probability of 58%.

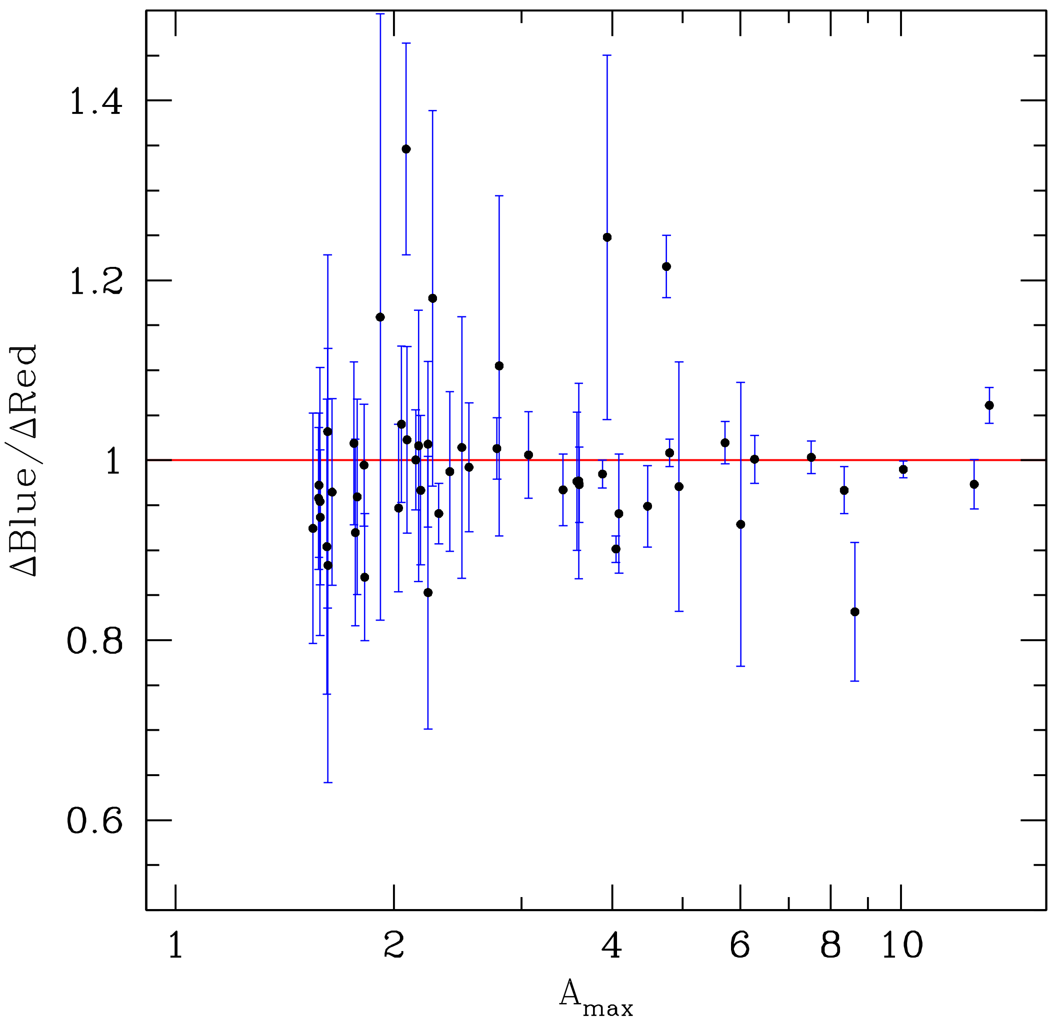

Figure 5.6 Ratio of $\Delta V/\Delta R$ for the 53 clump giant events with multiple observations in the peak of the light curve.

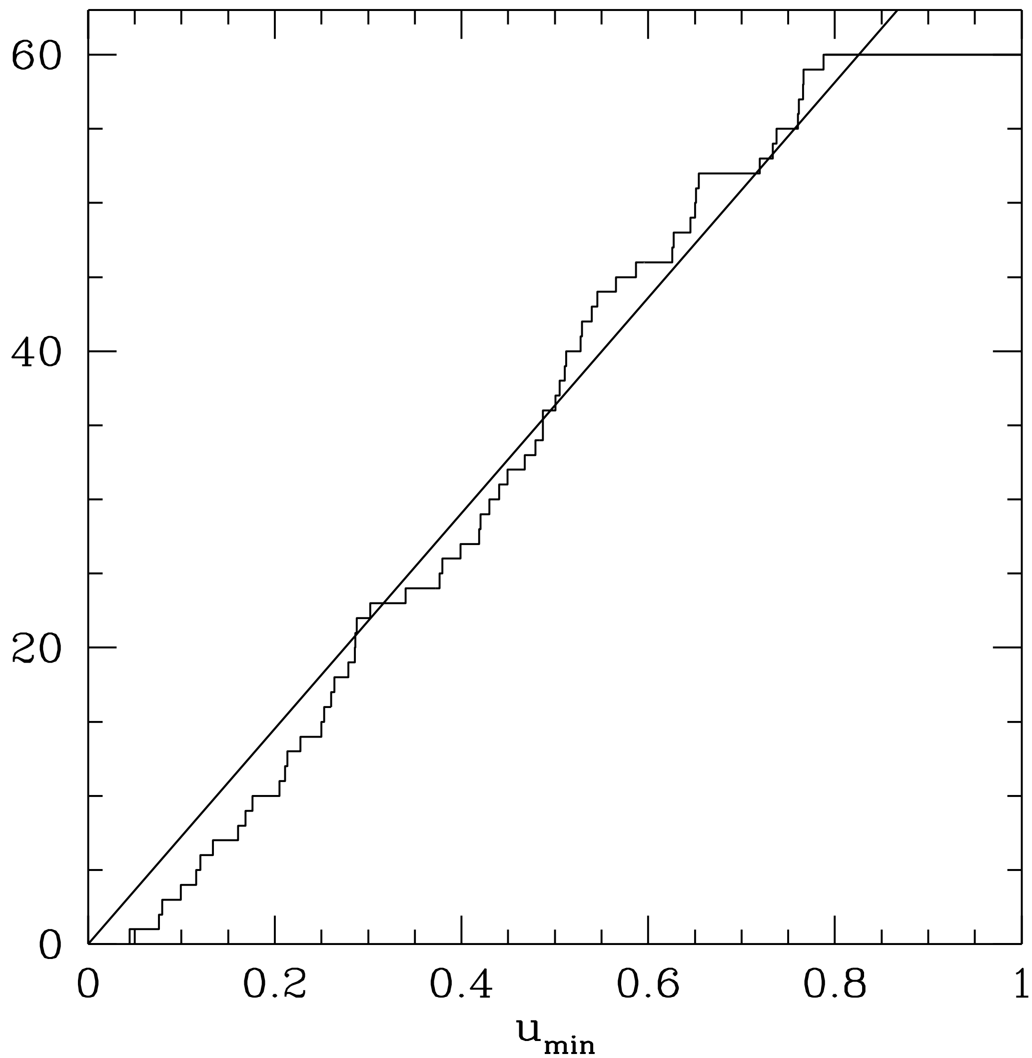

Figure 5.7 Cumulative distribution of u_{min} weighted by inverse efficiency and renormalized to 55, the number of unique non-binary events. Our cuts restrict the impact parameter, requiring $u_{min} \leq 0.826$.

5.2.5 Blend Fits

We now fit our light curves with a blended light curve as described in §1.1.3. We use MINUIT (James, 2003) to fit each light curve with the formula

$$\frac{F(t)}{F_{base}} = f_b A(t) - f_b + 1 \tag{5.13}$$

where $A(t)$ is the standard form of the microlensing light curve, f_b is the fraction of baseline flux that is lensed, and F_{base} is the baseline flux of the object. For an unblended source one would expect $f_b = 1$. The blend fraction is allowed to differ between filters, but the microlensing parameters are the same for both filters.

The results of the fits are shown in Table 5.3. We show the distribution of recovered blend fractions for the blue filter in Figure 5.8. Many of our events have a recovered blend fraction, f_b, near 1.0 as we would expect, but the distribution is very broad and there are a significant number with very small f_b and a few with f_b significantly greater than 1.0, the maximum physical limit. This calls into question the accuracy of blend fits and leads us to investigate further.

To test how accurately we can recover blend fractions we perform a Monte Carlo simulation. For each of our light curves we generate a few hundred light curves with the parameters from its fit assuming no blending. We use errors of observed light curves to distribute each point around the ideal value with a Gaussian distribution. We generate two sets of events, one with no blending ($f_b = 1$) and the other 50% blended ($f_b = 0.5$) and fit them using the same method as the real events. To generate the blended events we adjust the parameters so the apparent A_{max} and u_{min} remain the same. We show the distribution of recovered blend fraction for both sets of generated light curves in Figure 5.9. For each event we get a distribution of likely values for the recovered blend fraction if $f_b = 1$ for that event. The combined distribution of recovered blend fractions should be similar to the distribution we would get if our sample was entirely free of blending. We see that it is not. From the two sets of Monte Carlo events we see that the peak of the distribution follows the blend fraction; our distribution peaks at $f_b = 1$, but there are also many excess events at very small blend fraction. It could be that we have a wide distribution of blend fractions in the observed events, but we also find some events with $f_b \sim 3$ which is an unphysical value so we investigate further.

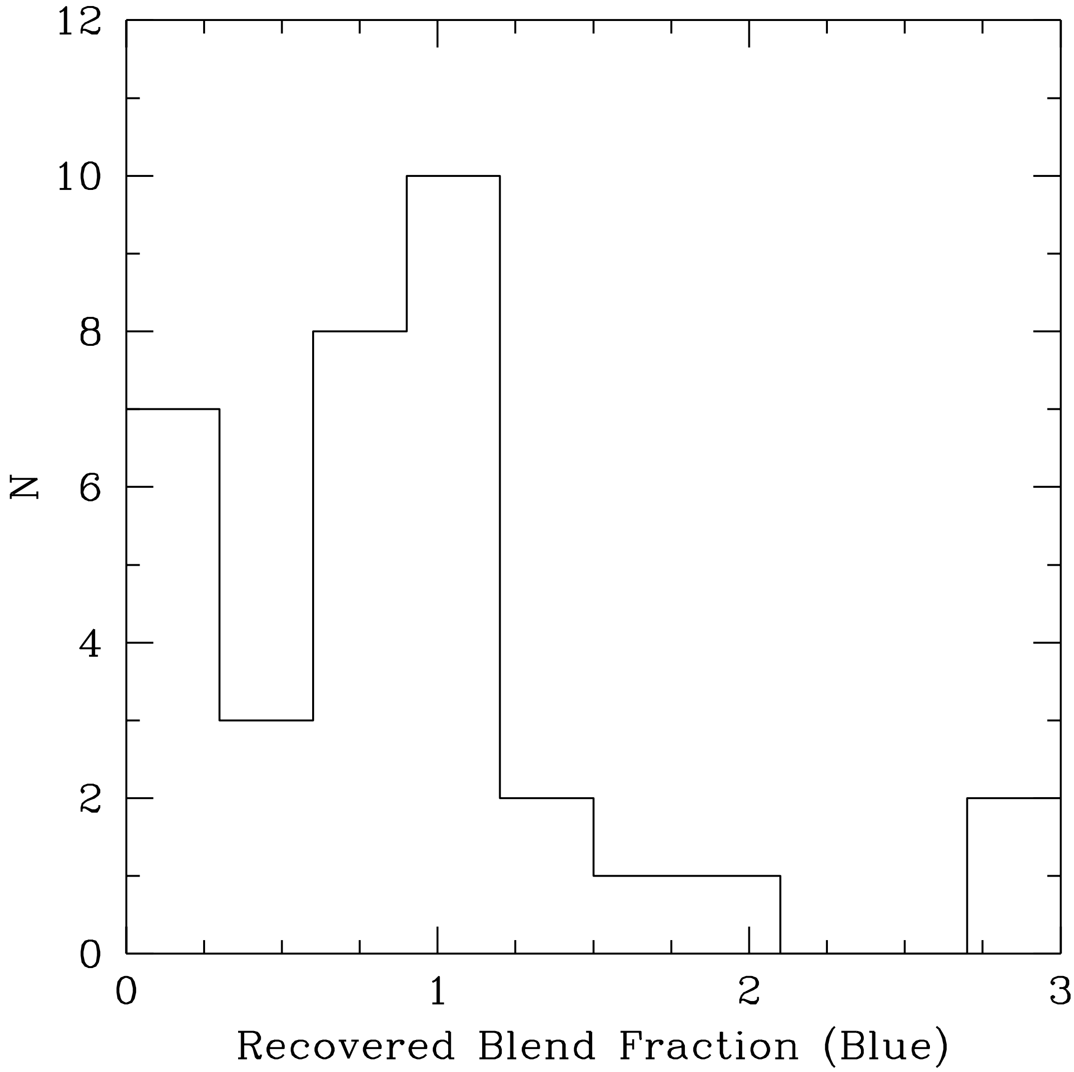

Figure 5.8 Recovered blend fraction in the blue filter for the sample of events used for the optical depth calculation towards the CGR.

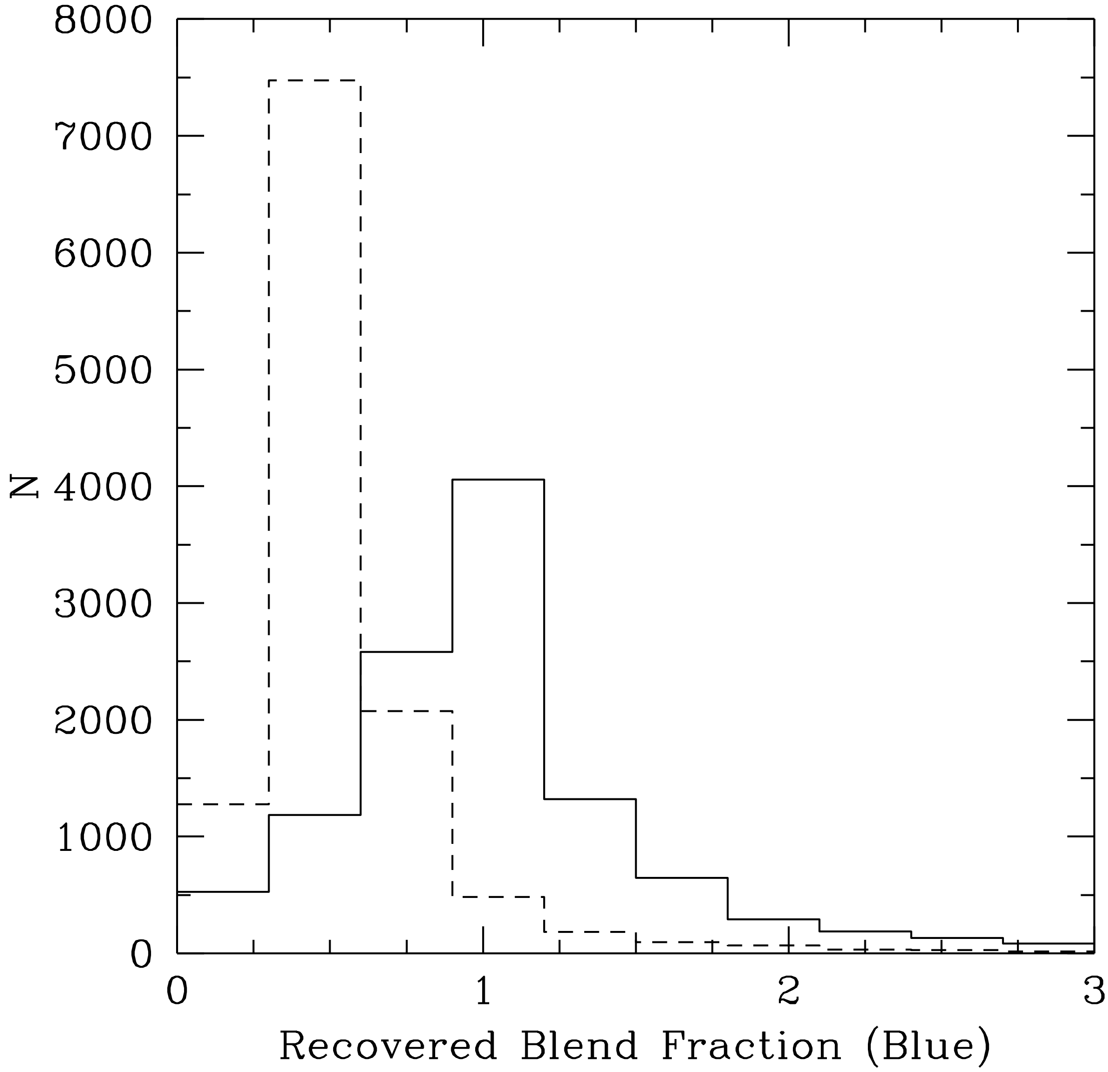

Figure 5.9 Recovered blend fraction in the blue filter for simulated events. A set of unblended events is shown (solid line) with a set of events with $f_b = 0.5$ (dashed line).

Table 5.3: Event parameters from blend fits

field.tile.seq	$\hat{t}$	$u_{\min}$	f_{r_M}	f_{b_M}
101.21689.315	196.6 ± 4.1	0.1609 ± 0.0051	0.726 ± 0.026	0.736 ± 0.026
102.22466.140	148.0 ± 6.9	0.276 ± 0.019	1.059 ± 0.089	1.049 ± 0.088
104.19992.858	103 ± 19	0.52 ± 0.17	1.09 ± 0.56	1.11 ± 0.57
104.20119.6312	46 ± 11	0.56 ± 0.22	0.65 ± 0.40	0.58 ± 0.37
104.20251.1117	68.7 ± 8.0	0.274 ± 0.048	0.413 ± 0.089	0.413 ± 0.089
104.20259.572	14.2 ± 1.5	0.77 ± 0.11	1.01 ± 0.28	1.010 ± 0.27
104.20515.498	43 ± 10	0.92 ± 0.33	1.8 ± 1.3	1.9 ± 1.4
104.20640.8423	78 ± 14	0.178 ± 0.045	0.150 ± 0.043	0.134 ± 0.038
104.20645.3129	133 ± 13	0.78 ± 0.13	1.47 ± 0.44	1.48 ± 0.44
105.21813.2516	17.84 ± 0.72	0.0741 ± 0.0049	0.952 ± 0.062	1.01 ± 0.066
108.18947.3618	46.2 ± 4.2	0.529 ± 0.080	0.95 ± 0.22	1.01 ± 0.23
108.18951.1221	31 ± 22	0.92 ± 0.98	2.7 ± 5.8	2.9 ± 6.2
108.18952.941	63.3 ± 4.3	0.491 ± 0.053	1.14 ± 0.18	1.14 ± 0.18
108.19074.550	12.7 ± 2.0	0.36 ± 0.10	0.44 ± 0.16	0.42 ± 0.15
108.19334.1583	16.7 ± 2.5	0.294 ± 0.067	1.22 ± 0.34	1.19 ± 0.33
109.20119.1051	3.92 ± 0.30	8.75 ± 0.64	1930 ± 550	1840 ± 520
109.20640.360	25.7 ± 9.6	0.84 ± 0.49	$--$	1.4 ± 1.5
110.22455.842	16.5 ± 3.4	0.55 ± 0.17	1.49 ± 0.71	1.50 ± 0.72
113.18552.581	614800 ± 102700	$(1.23 \pm 0.20) \times 10^{-5}$	$(1.03 \pm 0.17) \times 10^{-5}$	$(9.00 \pm 1.50) \times 10^{-6}$
113.18804.1061	19 ± 14	0.17 ± 0.16	0.13 ± 0.14	0.14 ± 0.15
113.19192.365	30 ± 18	0.86 ± 0.84	1.5 ± 2.9	2.0 ± 3.7
114.19712.813	24.0 ± 2.0	0.283 ± 0.036	0.98 ± 0.16	0.97 ± 0.16
114.19846.777	122 ± 14	0.284 ± 0.052	0.226 ± 0.051	0.211 ± 0.048
114.19970.843	16.8 ± 1.5	0.181 ± 0.025	0.79 ± 0.12	0.73 ± 0.11
118.18014.320	15.7 ± 8.6	1.6 ± 1.3	5 ± 11	5 ± 11
118.18271.738	93 ± 17	0.213 ± 0.057	0.35 ± 0.11	0.33 ± 0.10
118.18402.495	26 ± 1.8	0.246 ± 0.027	0.83 ± 0.11	0.85 ± 0.11
118.18797.1397	121.3 ± 2.5	0.1274 ± 0.0039	1.069 ± 0.034	1.043 ± 0.034
118.19182.891	12.48 ± 0.91	0.195 ± 0.030	1.21 ± 0.19	1.22 ± 0.20

Continued on Next Page...

Table 5.3

. . . Continued from Previous Page

field.tile.seq	$\hat{t}$	$u_{\min}$	f_{r_M}	f_{b_M}
118.19184.939	88.5 ± 5.4	0.388 ± 0.037	0.673 ± 0.087	0.675 ± 0.088
121.22032.133	15.0 ± 9.3	1.2 ± 1.2	2.3 ± 5.0	2.4 ± 5.2
158.27444.129	48.7 ± 3.0	0.362 ± 0.036	0.710 ± 0.093	0.689 ± 0.090
162.25865.442	61 ± 10	0.75 ± 0.21	1.01 ± 0.50	0.95 ± 0.47
162.25868.405	30.6 ± 2.5	0.386 ± 0.057	1.00 ± 0.19	1.04 ± 0.20
176.18826.909	3.68 ± 0.38	7.27 ± 0.70	$--$	1120 ± 410
178.23531.931	13.1 ± 2.9	0.54 ± 0.22	1.14 ± 0.71	1.11 ± 0.70
180.22240.202	454 ± 20	0.183 ± 0.010	0.547 ± 0.035	0.551 ± 0.035
401.47991.1840	38 ± 18	0.77 ± 0.62	1.6 ± 2.3	1.6 ± 2.4
401.47994.1182	61 ± 12	0.273 ± 0.085	$--$	0.97 ± 0.36
401.48052.861	83 ± 15	0.304 ± 0.091	0.74 ± 0.28	0.70 ± 0.27
401.48167.1934	48.5 ± 8.2	2.83 ± 0.62	37.1 ± 24.0	39.8 ± 26.0
401.48469.789	7.5 ± 4.2	< 0.26	0.58 ± 0.58	0.54 ± 0.55
402.47678.1666	13.4 ± 6.8	0.45 ± 0.43	1.0 ± 1.4	1.1 ± 1.5
402.47737.1590	11.0 ± 3.5	0.111 ± 0.055	0.26 ± 0.13	0.29 ± 0.15
402.47742.3318	64.7 ± 8.5	0.065 ± 0.020	0.72 ± 0.14	0.61 ± 0.12
402.47796.1893	21.8 ± 1.4	< 0.03	0.801 ± 0.081	0.832 ± 0.078
402.47798.1259	97800 ± 19500	$(6 \pm 20219) \times 10^{-7}$	$(2.59 \pm 0.52) \times 10^{-4}$	$(2.31 \pm 0.47) \times 10^{-4}$
402.47799.1736	80 ± 44	0.84 ± 0.70	2.5 ± 4.0	2.7 ± 4.4
402.47856.561	52000 ± 16000	$(2.0 \pm 1.1) \times 10^{-5}$	$(3.8 \pm 1.2) \times 10^{-5}$	$(5.0 \pm 1.6) \times 10^{-5}$
402.48158.1296	20.7 ± 4.9	0.148 ± 0.082	0.56 ± 0.26	0.61 ± 0.28
402.48280.502	119 ± 28	0.035 ± 0.011	0.064 ± 0.018	0.084 ± 0.024
403.47491.770	45.3 ± 5.3	0.494 ± 0.098	1.19 ± 0.35	1.18 ± 0.35
403.47550.807	10.9 ± 1.9	0.33 ± 0.12	1.17 ± 0.47	1.13 ± 0.45
403.47610.576	14.5 ± 1.2	0.123 ± 0.014	0.492 ± 0.059	0.608 ± 0.073
403.47845.495	13.9 ± 2.7	0.62 ± 0.19	1.23 ± 0.64	1.20 ± 0.62

Known binaries and two strong parallax events (104.20251.50 and 104.20382.803) are not included.

To decide if our sample is blended we cannot look only at the distribution of recovered blend fractions, we need to look at the uncertainty in the blend fractions as well. Some events may appear to be heavily blended but be consistent with $f_b = 1$ due to large errors. We look at the normalized deviation from unity,

$$\delta = \frac{f_B - 1.0}{\sigma_{f_b}}, \tag{5.14}$$

and we expect this distribution to be roughly Gaussian with a mean of 0 and variance of 1. We show the distribution of δ for our events in Figure 5.10 and for the Monte Carlo events in Figure 5.11. The distributions of δ are fairly similar; both show a number of events fit very low and the distribution is skewed heavily towards negative values of δ. The broad distribution and apparent bias in the results of blend fits indicates that the result for any one event has very little weight. Even with all our events we cannot draw any strong conclusions about blending.

5.2.6 Blend Fits With Binaries

Caustic-crossing binary events constrain the blend fraction better with their more complicated light curve shape. There are four binary events in our clump giant sample that have already been analyzed (Alcock et al., 2000a). The four events are listed in Table 5.4. The first three have blend fractions from Alcock et al. (2000a) and the fourth has two solutions: a binary with a planet suggested by Bennett et al. (1999), and a rotating binary suggested by Albrow et al. (2000). Of the 16 bulge binaries (clump and non-clump) only six are completely consistent with no blending. On the other hand, of the four clump binaries three are not blended and the fourth is only blended very weakly. Furthermore, the one clump event that appears to be blended can be well fit with at least two models, each giving a different blend fraction, adding uncertainty to its blend fraction.

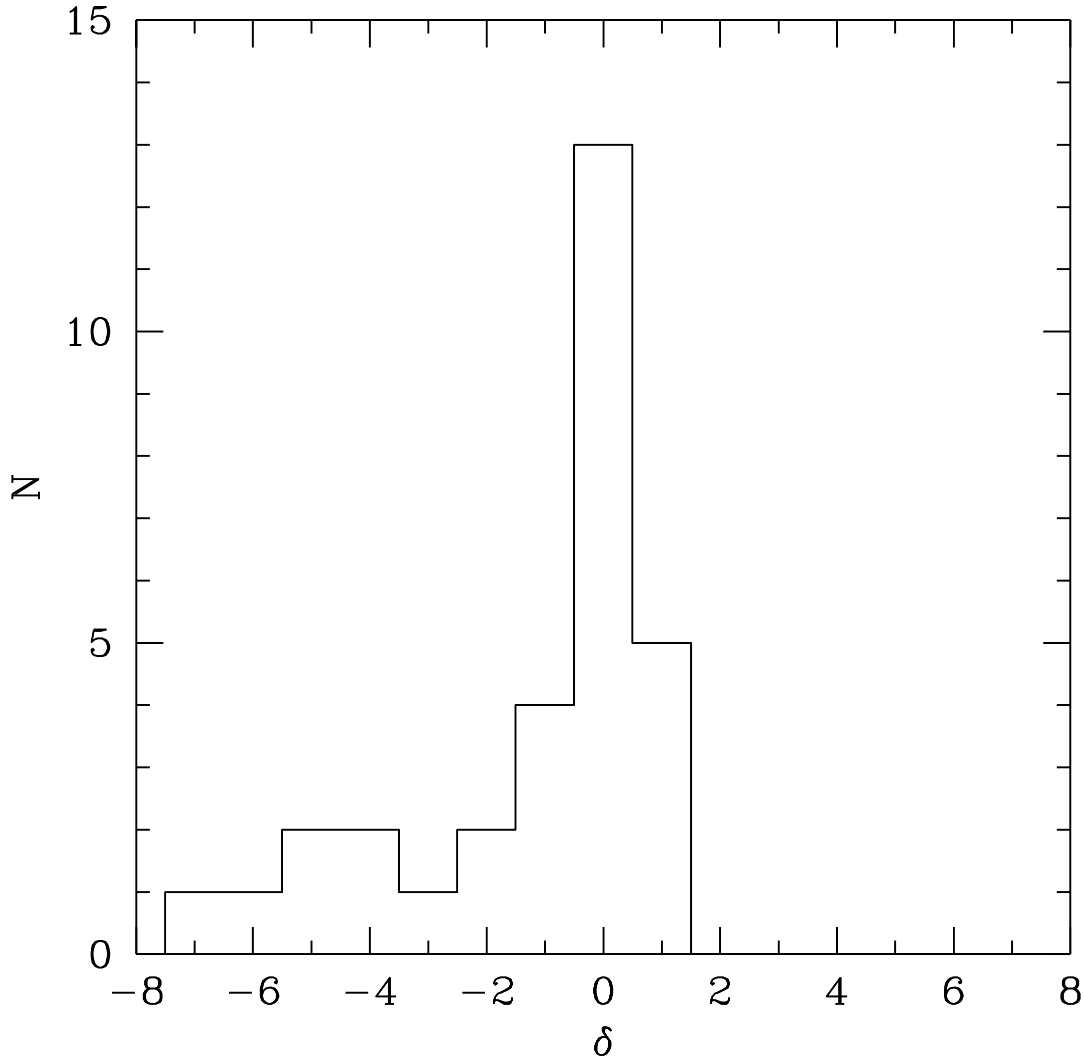

Figure 5.10 Distribution of δ in the blue filter for the clump giant events in the 9 fields used for the primary optical depth result.

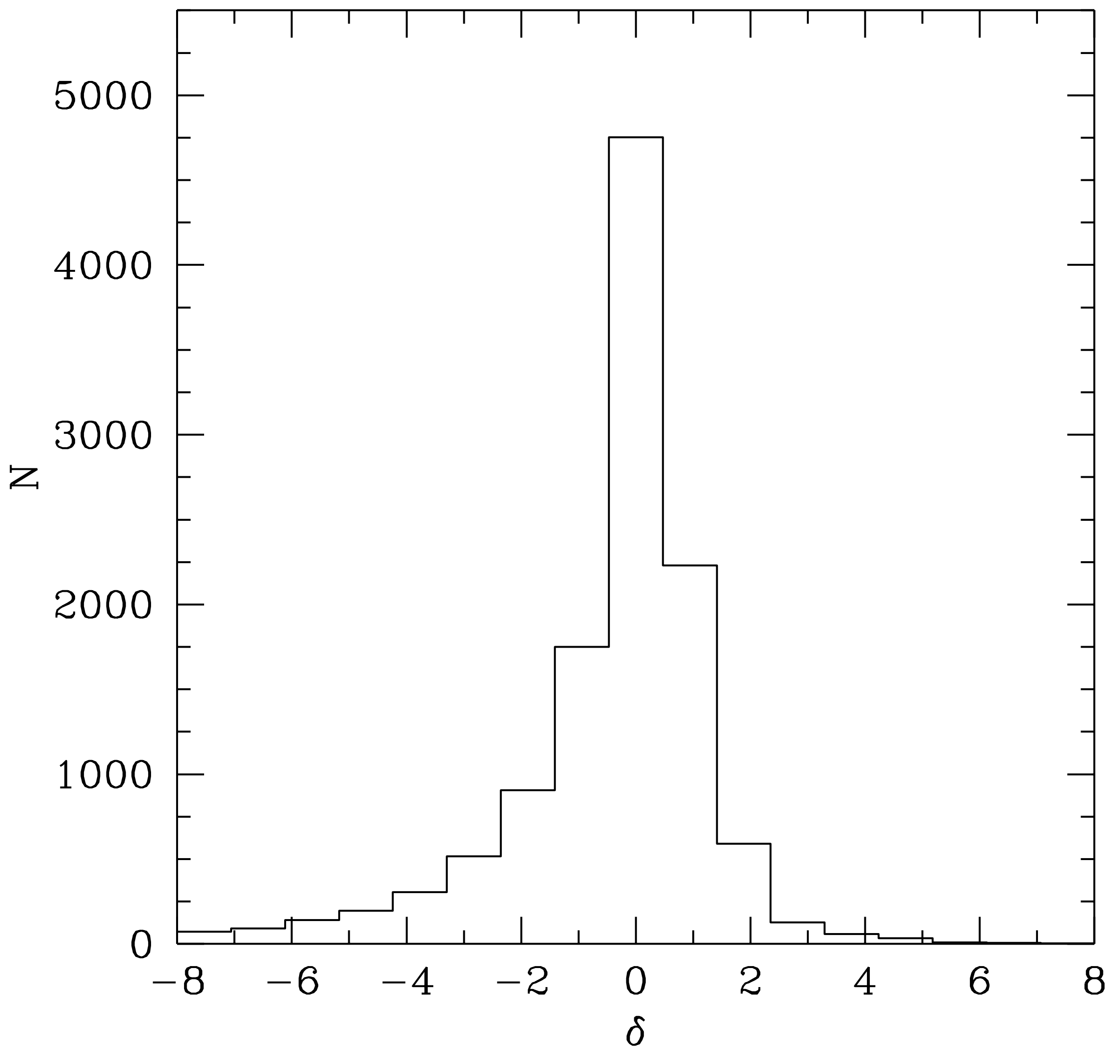

Figure 5.11: Distribution of δ for simulated unblended events.

Table 5.4: Blend Fractions for Clump Events with Binary Lenses

Event	$f_{b,red}$	$f_{b,blue}$
108.18951.593 (97-BLG-28)	1.00	0.90
118.18141.731 (94-BLG-4)	1.06	1.04
401.48408.649 (98-BLG-14)	1.08	1.10
402.47862.1576 (97-BLG-41)	0.86^a	0.84^a
	0.95^b	0.92^b

For the first three events, blend fractions are taken from Alcock et al. (2000c). The solutions for 97-BLG-41 are designated as follows:
^{a} binary with a planet obtained by Bennett et al. (1999),
^{b} rotating binary solution obtained by Albrow et al. (2000).
The blend fraction is reported in MACHO filters, columns $f_{b,red}$ and $f_{b,blue}$. For all cases, the statistical errors in blend fractions are $\lesssim 0.05$.

5.3 The Optical Depth

We propose using an estimator of the optical depth that is slightly different from the one that has been used previously. Previously we have used

$$\tau = \frac{\pi}{4E} \sum_{i=1}^{N_{events}} \frac{\hat{t}_i}{\epsilon(\hat{t}_i)}\,, \tag{5.15}$$

where E is the exposure in star-days, $\hat{t}$ is the Einstein diameter crossing time, and $\epsilon(\hat{t})$ is the efficiency of detecting events with a given $\hat{t}$ averaged over amplification. Any observing program will miss some events and so the efficiency correction is required to correct for this. We use a formula that, with large numbers of events, gives the same result as the estimator above, but is more efficient computationally:

$$\tau = \frac{1}{E} \sum_{i=1}^{N_{events}} \frac{t_i}{\epsilon(t_i)} \,. \tag{5.16}$$

Here t is the time spent with $A \geq 1.34$ and the efficiency, $\epsilon(t_i, A_{max,i})$, is calculated for both the duration and amplification of each event. The benefit of this estimator is in the efficiency calculation; it takes much less computer time if we do not average over amplification. Our new estimator, equation (5.16), is the probability that a given star is lensed ($A_{max} \geq 1.34$ or equivalently $u_{min} \leq 1$) at anytime, whereas the old estimator, equation (5.15), is the fraction of sky within one Einstein radius of a lens ($u_{min} \leq 1$ or equivalently $A_{max} \geq 1.34$). As long as the probability that a source star lie within an Einstein radius of two lenses is much less than unity these two estimators are equivalent.

We include a cut that limits $A_{max} \geq 1.5$ instead of $A_{max} \geq 1.34$ and so we require an additional geometric factor of 1.09. This factor is the ratio of the Einstein ring area to the area covered by our cuts. The area missed is shown in Figure 5.12. We miss events with $1.34 \leq A_{max} < 1.5$, or equivalently, $1.0 \geq u_{min} > 0.826$, thus a small fraction of (1.0-0.826) is missed. When using the previous optical depth estimator this factor was not needed since events with $1.34 \leq A_{max} < 1.5$ were used in the efficiency calculation which reduces the efficiency to compensate for the missed events.

Our sample contains five likely binary events; not only are their parameters harder to determine, but the efficiency pipeline (described below) is designed for single lenses. We must include these binary events, otherwise we would decrease the optical depth, but we must treat them carefully to assure we do not distort the optical depth. We considered multiple methods for determining the duration t for these events and decided the simplest was best; we use the t generated by the single lens fits. We examined the light curves carefully and found that this t was an accurate measure of the time with $A \geq 1.34$ and agrees well with what is found from binary-lens fits (Alcock et al., 2000a). We note that binaries are only 1/12

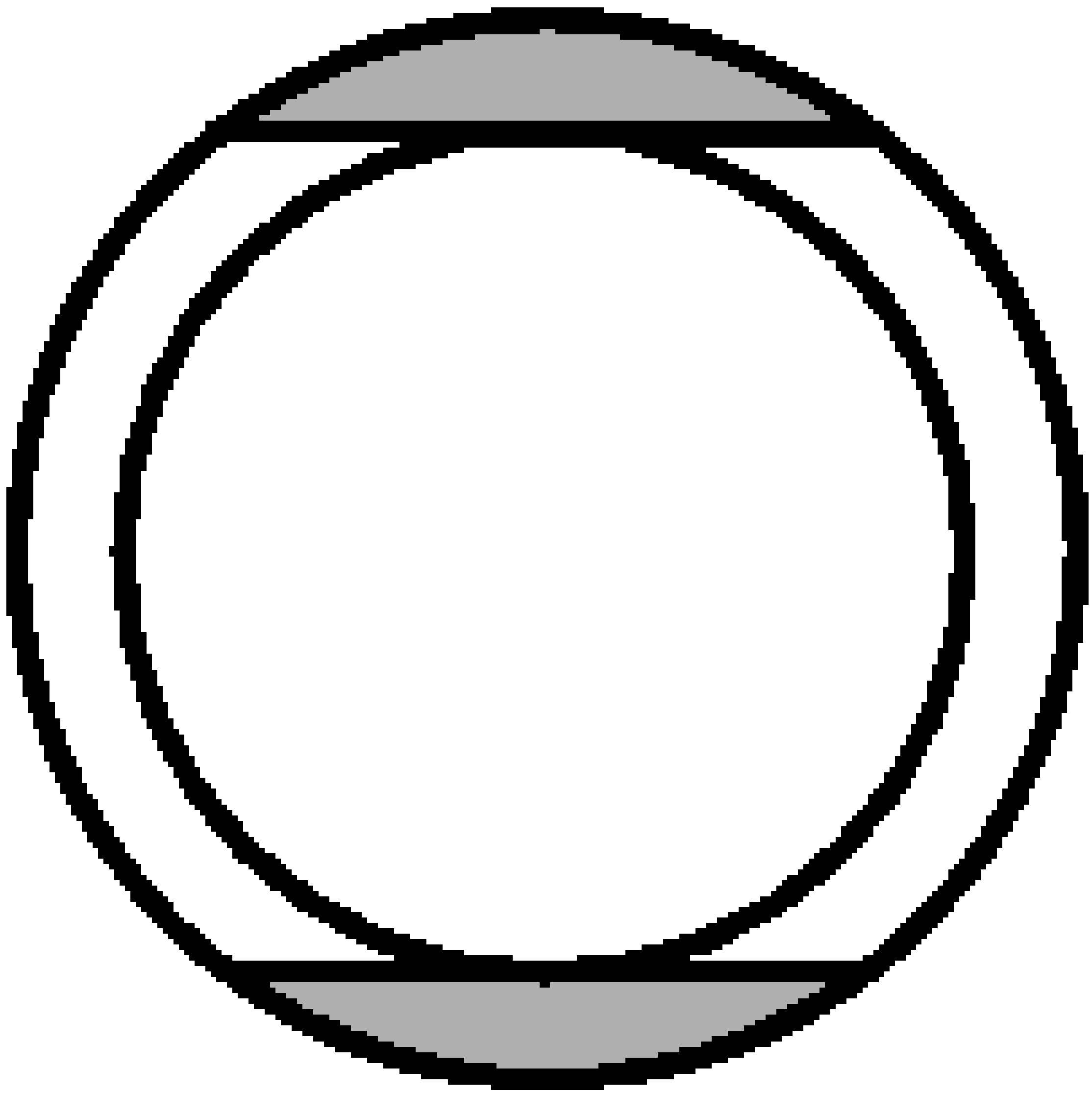

Figure 5.12 Area of Einstein ring and the area covered by our cuts. The two shaded regions are missed by our cuts.

of our sample so even a 50% error in measurement here would only result in a 4% error in optical depth. A more important effect is the likely exclusion of binary events due to our cuts. Our cuts are designed to find single lens events, so binaries, with their large deviations from the single lens light curve, should fail our cuts more easily than single lens events. From the entire sample of events (including non-clump events), which was selected with a much broader criteria, we find 10% of events are binaries. This fraction would imply six events whereas we see five. These numbers are consistent, but if we were to add an event as a correction it would only increase the optical depth by $\sim 1/60 \sim 1.7\%$, a small value compared to the statistical uncertainty of our result.

5.3.1 The Efficiency Calculation

The sampling efficiency is calculated using a Monte Carlo simulation. The primary reason for missing events is sampling and time coverage; we have large gaps in the data when the LMC is being observed and events that fall in those gaps will be missed, in addition shorter events may have too few observations during the event to pass our cuts. To correct for this we find the efficiency of detecting each event. During analysis 1% of objects are pulled out and put into a separate database. We use the clump giants from this database to generate events for the efficiency calculation. Because the sampling is the most important factor we use flat light curves from the field in which the event occurred to create Monte Carlo light curves, this ensures each light curve will have observations at all the same times. We use the same observations, but adjust the flux for each observation according to the single lens light curve formula (1.14) using the A_{max} and $\hat{t}$ from the event and a random t_0. The errorbars are adjusted appropriately as well. The Monte Carlo events are then analyzed using the same pipeline as is used to select real events. The efficiency is computed as the fraction of events recovered. We make several sets of light curves to get better statistics.

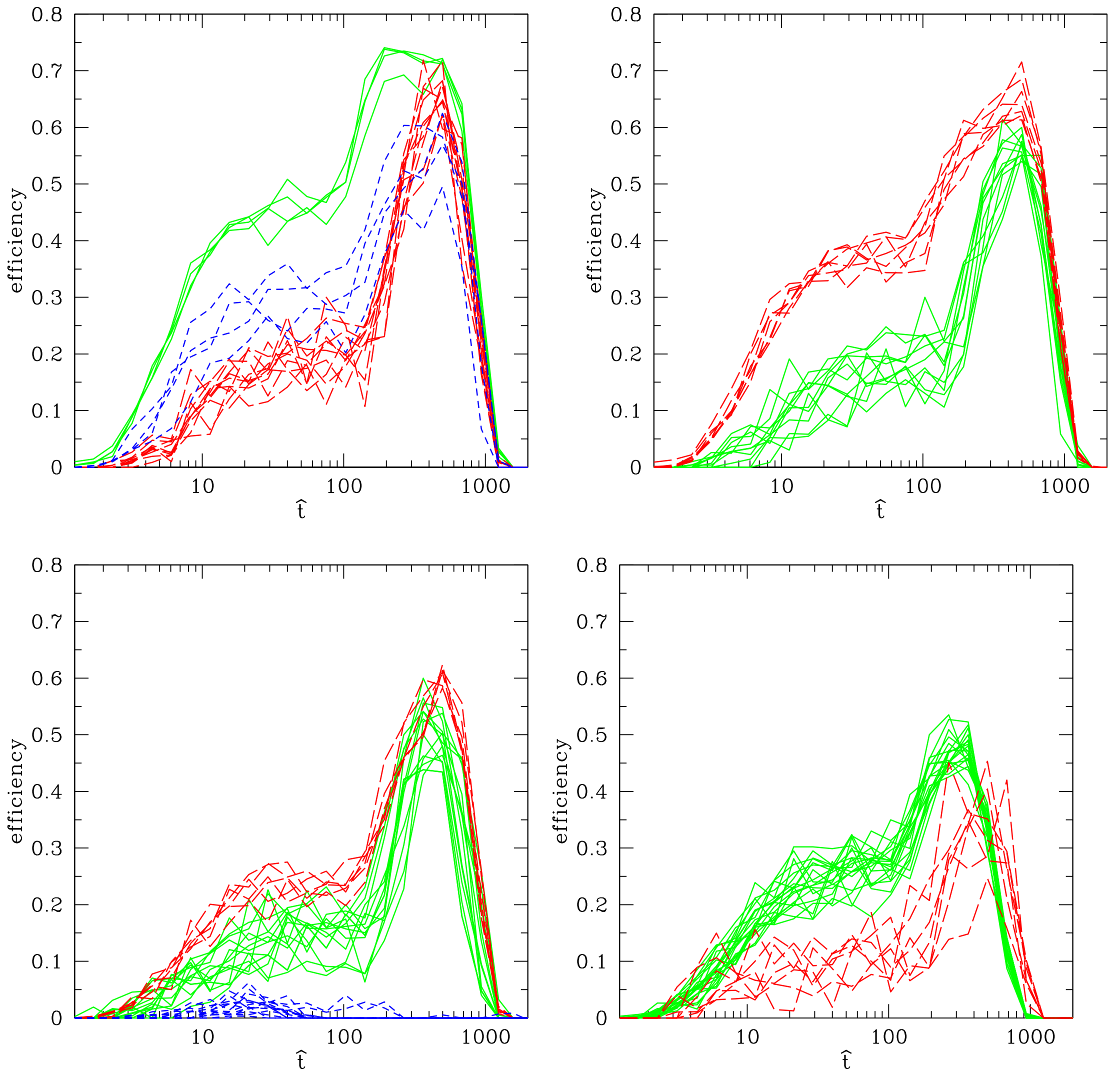

Figure 5.13 Clump detection efficiencies versus $\hat{t}$ for all fields. **(a)** solid green - 108, 113, 118, 119; red long dashed - 116, 124, 125, 136, 142, 143, 146, 148, 149, 155; blue short dashed - 110, 159, 161, 162 **(b)** solid green - 111, 122, 131, 132, 137, 150, 152, 158, 163, 171, 174; red dashed - 101, 104, 105, 109, 114, 120, 128 **(c)** solid green - 127, 133, 138, 144, 147, 151, 153, 154, 156, 157, 160, 166, 168; red long dashed - 102, 103, 115, 121, 167; blue short dashed - 106, 107, 112, 117, 123, 126, 129, 130, 135, 141, 164, 165, 169, 170 **(d)** solid green - 176-180, 301-311, 401-403; red dashed - 134, 139, 140, 145, 172, 173, 175. Note that fields 176-180 and fields 401-403 efficiencies are low because they were not observed for the whole 7 year period. As explained earlier, fields 301-311 are not included in the analysis but are included here for completeness.

Table 5.5: Data On The 94 Bulge Fields

field	l	b	$\frac{n_{stars}}{100}$	$\frac{n_{clumps}}{100}$	n_{events}	$n_{exposures}$	$\epsilon(50days)$	$\epsilon(200days)$
101	3.73	−3.02	6284	629.5	30	804	0.41	0.61
102	3.77	−4.11	6545	444	15	421	0.24	0.46
103	4.31	−4.62	6349	368	5	331	0.21	0.36
104	3.11	−3.01	5813	652	28	1639	0.40	0.59
105	3.23	−3.61	6375	539	21	640	0.39	0.52
106	3.59	−4.78	6648	346	0	12	< 0.003	< 0.003
107	4.00	−5.31	6159	269	0	51	0.007	< 0.003
108	2.30	−2.65	6498	790	32	1031	0.49	0.75
109	2.45	−3.20	6926	661	19	761	0.35	0.60
110	2.81	−4.48	6649	408	11	650	0.32	0.57
111	2.99	−5.14	6036	298	5	305	0.21	0.34
112	3.40	−5.53	5147	246.5	0	43	< 0.003	< 0.003
113	1.63	−2.78	6252	834	31	1127	0.51	0.72
114	1.81	−3.50	6665	617	20	776	0.39	0.59
115	2.04	−4.85	5756	325.5	9	357	0.24	0.35
116	2.38	−5.44	5812	268.5	4	314	0.21	0.38
117	2.83	−6.00	5185	198	0	39	0.006	< 0.003
118	0.83	−3.07	6347	741.5	29	1053	0.44	0.74
119	1.07	−3.83	7454	542.5	27	1815	0.45	0.68
120	1.64	−4.42	5599	394	9	676	0.35	0.54
121	1.20	−4.94	5855	344	10	352	0.22	0.37
122	1.57	−5.45	4890	266	3	186	0.15	0.23
123	1.95	−6.05	5119	210.5	1	40	0.006	< 0.003
124	0.57	−5.28	5716	265.5	3	337	0.22	0.39
125	1.11	−5.93	5839	189	1	287	0.21	0.37
126	1.35	−6.40	4789	182	0	36	< 0.003	< 0.003
127	0.28	−5.91	4975	192	0	178	0.13	0.24
128	2.43	−4.03	6160	516.5	9	711	0.35	0.55
129	4.58	−5.93	5123	234.5	0	31	0.006	< 0.003
130	5.11	−6.49	4864	169.5	2	20	0.02	0.02
131	4.98	−7.33	4256	130	1	106	0.12	0.22
132	5.44	−7.91	4533	102	2	180	0.17	0.33
133	6.05	−8.40	4174	70.5	0	176	0.15	0.17
134	6.34	−9.07	3370	46.5	1	197	0.08	0.14
135	3.89	−6.26	5476	179	0	30	0.004	< 0.003
136	4.42	−6.82	5623	137.5	1	207	0.17	0.25
137	4.31	−7.60	4488	101	4	193	0.15	0.36
138	4.69	−8.20	4380	95.5	0	201	0.16	0.21
139	5.35	−8.65	4112	81	1	191	0.11	0.10
140	5.71	−9.20	3723	64	0	209	0.12	0.24
141	3.26	−6.59	5001	159	0	28	0.03	0.02
142	3.81	−7.08	4985	126.5	2	218	0.15	0.35
143	3.80	−8.00	4767	97	0	210	0.17	0.25
144	4.68	−9.02	3798	50.5	1	210	0.10	0.18
145	5.20	−9.50	3385	49.5	1	210	0.12	0.23
146	3.26	−7.54	3798	106	0	207	0.19	0.33

Continued on Next Page...

Table 5.5

. . . Continued from Previous Page

field	l	b	$\frac{n_{stars}}{100}$	$\frac{n_{clumps}}{100}$	n_{events}	$n_{exposures}$	$\epsilon(50days)$	$\epsilon(200days)$
147	3.96	−8.81	4135	66	0	208	0.19	0.20
148	2.33	−6.71	5824	161.5	2	229	0.18	0.30
149	2.43	−7.43	4042	112.5	2	236	0.19	0.34
150	2.96	−8.01	4474	98.5	1	229	0.18	0.28
151	3.17	−8.89	3432	85	1	194	0.14	0.23
152	1.76	−7.07	4995	124	2	235	0.22	0.31
153	2.11	−7.87	4763	85.5	3	231	0.16	0.35
154	2.16	−8.51	3936	82	3	247	0.19	0.20
155	1.01	−7.44	4481	95.5	1	247	0.17	0.36
156	1.34	−8.12	4660	88.5	1	249	0.13	0.32
157	0.08	−7.76	3822	105.5	0	258	0.20	0.37
158	7.08	−4.44	4703	246.5	4	260	0.20	0.29
159	6.35	−4.40	5890	258.5	6	464	0.27	0.46
160	6.84	−5.04	4940	248	1	208	0.15	0.26
161	5.56	−4.01	5878	366	6	467	0.32	0.45
162	5.64	−4.62	5914	301	5	382	0.22	0.38
163	5.98	−5.22	5311	259	2	251	0.19	0.36
164	6.51	−5.90	4901	167.5	0	20	0.002	< 0.003
165	7.01	−6.38	4349	135	0	14	< 0.003	< 0.003
166	7.10	−7.07	4175	131.5	1	110	0.09	0.14
167	4.88	−4.21	6268	388.5	5	364	0.26	0.40
168	5.01	−4.92	4724	298	3	210	0.17	0.26
169	5.40	−5.63	4896	208	0	24	0.004	< 0.003
170	5.81	−6.20	4886	170	0	17	< 0.003	< 0.003
171	6.42	−6.65	4834	120.5	0	125	0.15	0.19
172	6.82	−7.61	4036	89	2	132	0.13	0.17
173	6.92	−8.41	3532	87	1	146	0.06	0.09
174	5.71	−6.92	4979	143.5	1	144	0.18	0.22
175	6.10	−7.55	4173	111.5	1	97	0.06	0.10
176	2.93	−2.30	7741	814.5	10	423	0.25	0.43
177	6.75	−3.82	5950	319	3	416	0.30	0.43
178	5.24	−3.42	8186	477	7	376	0.27	0.41
179	4.92	−2.83	7159	510	10	349	0.20	0.39
180	5.93	−2.69	6388	478	6	343	0.21	0.38
301	18.77	−2.05	5608	–	6	925	0.31	0.46
302	18.09	−2.24	5175	–	3	365	0.28	0.37
303	17.30	−2.33	4029	–	0	369	0.22	0.40
304	9.07	−2.70	5080	–	6	458	0.30	0.50
305	9.69	−2.36	4628	–	3	411	0.29	0.46
306	8.46	−3.03	5886	–	3	423	0.28	0.40
307	7.84	−3.37	6565	–	4	435	0.27	0.43
308	10.02	−2.98	5038	–	2	360	0.26	0.40
309	9.40	−3.31	5494	–	1	347	0.23	0.39
310	8.79	−3.64	6488	–	10	387	0.26	0.42
311	8.17	−3.97	7514	–	10	396	0.28	0.39
401	2.02	−1.93	6630	964.5	17	429	0.25	0.45

Continued on Next Page. . .

Table 5.5

... Continued from Previous Page

field	l	b	$\frac{n_{stars}}{100}$	$\frac{n_{clumps}}{100}$	n_{events}	$n_{exposures}$	$\epsilon(50days)$	$\epsilon(200days)$
402	1.27	−2.09	7098	1153	29	1256	0.26	0.45
403	0.55	−2.32	6798	1085	24	473	0.26	0.45

Efficiencies (columns 8 and 9) are averaged over A_{max}. The classification of stars as clump giants is expected to be very difficult in 300 series fields, so we refrain from quoting specific numbers for these fields.

We report the efficiencies for each field as a function of event duration ($\epsilon(\hat{t}_i)$) in Figure 5.13 and at 50 and 200 days in Table 5.5. For each event we report the efficiency for its amplification and duration ($\epsilon(t_i, A_{max,i})$) along with the efficiency averaged over amplification ($\left\langle\epsilon(\hat{t}_i)\right\rangle$) in Table 5.7. The efficiencies for each field are shown in Figure 5.13, where fields are grouped with other fields with similar sampling and efficiencies. The scatter can be considered a measure of the error. In general the efficiencies increase until about 20 days and then remain roughly flat until around 100 days when they rise as the events become long enough to span the gaps in observation during LMC observations. The efficiencies for each event are given in Table 5.7 along with the other important parameters for the optical depth.

5.4 The Optical Depth and Gradient

Using the method described above we calculate and report optical depth contributions from each event in Table 5.7 and the optical depth to each field that contains clump giant events in Table 5.6. This table also includes the field center, number of stars, number of clumps and number of events. For this calculation we use an exposure, $E = NT$, set by the total number of clump giants and the duration used for the efficiency calculation, 2530 days. The error on the optical depth in each field is dominated by Poisson statistics because of the small number of events. We report errors for each field using the formula suggested by Han & Gould (1995). The spatial distribution of optical depths is shown in Figure 5.14, while the errors are large it seems there is an optical depth gradient in b, we examine this next.

Table 5.7: Optical Depth Contribution by Event

7 field.tile.seq	t_i	$\hat{t}$	$A_{\max,i}$	$\epsilon(t_i, A_{\max,i})$	$\langle\epsilon(\hat{t})\rangle$	$\tau(t_i)$	$\tau(\hat{t})$
101.21689.315	161	165	4.80	0.68	0.55	1.62	1.47
102.22466.140	147	153	3.88	0.39	0.32	3.67	3.34
104.19992.858	93.4	107	2.23	0.55	0.43	1.12	1.19
104.20119.6312	25.7	38.3	1.62	0.48	0.38	0.36	0.47
104.20251.50	285	287	10.1	0.77	0.63	2.44	2.18
104.20251.1117	38.7	45.6	2.09	0.46	0.39	0.56	0.56
104.20259.572	9.22	14.2	1.58	0.41	0.33	0.15	0.20
104.20382.803	250	254	5.73	0.78	0.62	2.11	1.95
104.20515.498	40.4	53.5	1.76	0.48	0.39	0.56	0.65
104.20640.8423	21.4	30.8	1.65	0.47	0.4	0.30	0.37
104.20645.3129	118	152	1.82	0.66	0.52	1.19	1.38
105.21813.2516	17.5	17.5	13.2	0.40	0.31	0.35	0.32
108.18947.3618	38.4	45.6	2.05	0.56	0.48	0.38	0.38
108.18951.593	45.8	47.3	4.05	0.57	0.47	0.44	0.39
108.18951.1221	39.5	45.8	2.16	0.57	0.48	0.38	0.38
108.18952.941	59.7	66.9	2.39	0.58	0.46	0.56	0.57
108.19074.550	7.07	9.26	1.78	0.41	0.34	0.09	0.11
108.19334.1583	17.9	18.5	4.09	0.53	0.42	0.18	0.17
109.20119.1051	19.4	28.7	1.62	0.44	0.4	0.29	0.34
109.20640.360	20.4	28.7	1.67	0.45	0.4	0.29	0.34
110.22455.842	18.0	19.8	2.54	0.41	0.33	0.46	0.46
113.18552.581	21.2	27.9	1.77	0.53	0.46	0.21	0.23
113.18804.1061	4.44	6.53	1.62	0.29	0.27	0.08	0.09
113.19192.365	30.4	36.9	1.97	0.59	0.49	0.27	0.28
114.19712.813	22.7	23.7	3.57	0.44	0.36	0.36	0.33
114.19846.777	40.0	64.9	1.55	0.46	0.39	0.61	0.84
114.19970.843	14.3	14.7	4.47	0.45	0.32	0.22	0.23
118.18014.320	16.3	25.5	1.58	0.54	0.44	0.18	0.24
118.18141.731	9.74	9.77	12.6	0.45	0.34	0.12	0.12
118.18271.738	46.9	53.7	2.23	0.56	0.46	0.49	0.49
118.18402.495	22.8	23.8	3.60	0.54	0.43	0.24	0.23

Continued on Next Page...

Table 5.7

. . . Continued from Previous Page

field.tile.seq	t_i	$\hat{t}$	$A_{\max,i}$	$\epsilon(t_i, A_{\max,i})$	$\langle\epsilon(\hat{t})\rangle$	$\tau(t_i) \times 10^6$	$\tau(\hat{t}) \times 10^6$
118.18797.1397	125	126	8.35	0.73	0.58	1.00	0.91
118.19182.891	13.4	13.6	6.28	0.49	0.39	0.16	0.15
118.19184.939	64.0	74.4	2.14	0.56	0.48	0.66	0.65
121.22032.133	12.5	19.4	1.58	0.27	0.21	0.59	0.85
158.27444.129	36.8	41.7	2.31	0.22	0.2	2.96	2.59
162.25865.442	39.5	60.9	1.58	0.33	0.24	1.73	2.63
162.25868.405	28.5	30.8	2.77	0.30	0.24	1.38	1.33
176.18826.909	18.4	24.3	1.77	0.26	0.24	0.37	0.39
178.23531.931	11.9	13.7	2.18	0.25	0.19	0.43	0.46
180.22240.202	297	312	3.42	0.58	0.44	4.62	4.62
401.47991.1840	36.2	44.7	1.92	0.29	0.24	0.55	0.60
401.47994.1182	58.2	60.6	3.68	0.31	0.25	0.83	0.78
401.48052.861	66.0	72.0	2.65	0.34	0.25	0.88	0.93
401.48167.1934	113	125	2.54	0.38	0.33	1.34	1.23
401.48229.760	15.7	20.1	1.82	0.24	0.20	0.29	0.33
401.48408.649	70.1	74.6	3.07	0.32	0.25	0.98	0.96
401.48469.789	5.59	5.67	6.01	0.098	0.059	0.25	0.31
402.47678.1666	12.3	13.7	2.48	0.26	0.20	0.17	0.18
402.47737.1590	5.06	5.46	2.8	0.13	0.086	0.15	0.17
402.47742.3318	49.8	50.1	8.64	0.32	0.26	0.59	0.52
402.47796.1893	19.3	19.3	22.7	0.29	0.24	0.25	0.22
402.47798.1259	46.6	47.6	4.95	0.31	0.26	0.56	0.49
402.47799.1736	101	115	2.26	0.38	0.32	0.99	0.98
402.47856.561	10.5	12.3	2.14	0.24	0.20	0.16	0.17
402.47862.1576	53.8	54.3	7.52	0.34	0.26	0.6	0.55
402.48158.1296	15.4	15.9	3.94	0.29	0.21	0.20	0.21
402.48280.502	21.7	25.5	2.08	0.3	0.24	0.27	0.28
403.47491.770	43.5	48.5	2.43	0.31	0.26	0.57	0.53
403.47550.807	11.1	11.6	3.60	0.21	0.16	0.20	0.20
403.47610.576	9.37	9.59	4.76	0.2	0.14	0.19	0.19
403.47845.495	12.6	15.0	2.03	0.25	0.20	0.20	0.22

To measure the gradient we bin the data in strips, $0\overset{\circ}{.}5$ in b and $1\overset{\circ}{.}0$ in l. We calculate the optical depth in each strip in the same way as described above, but only use clump giants and clump giant events within $5\overset{\circ}{.}5$ of the Galactic center.

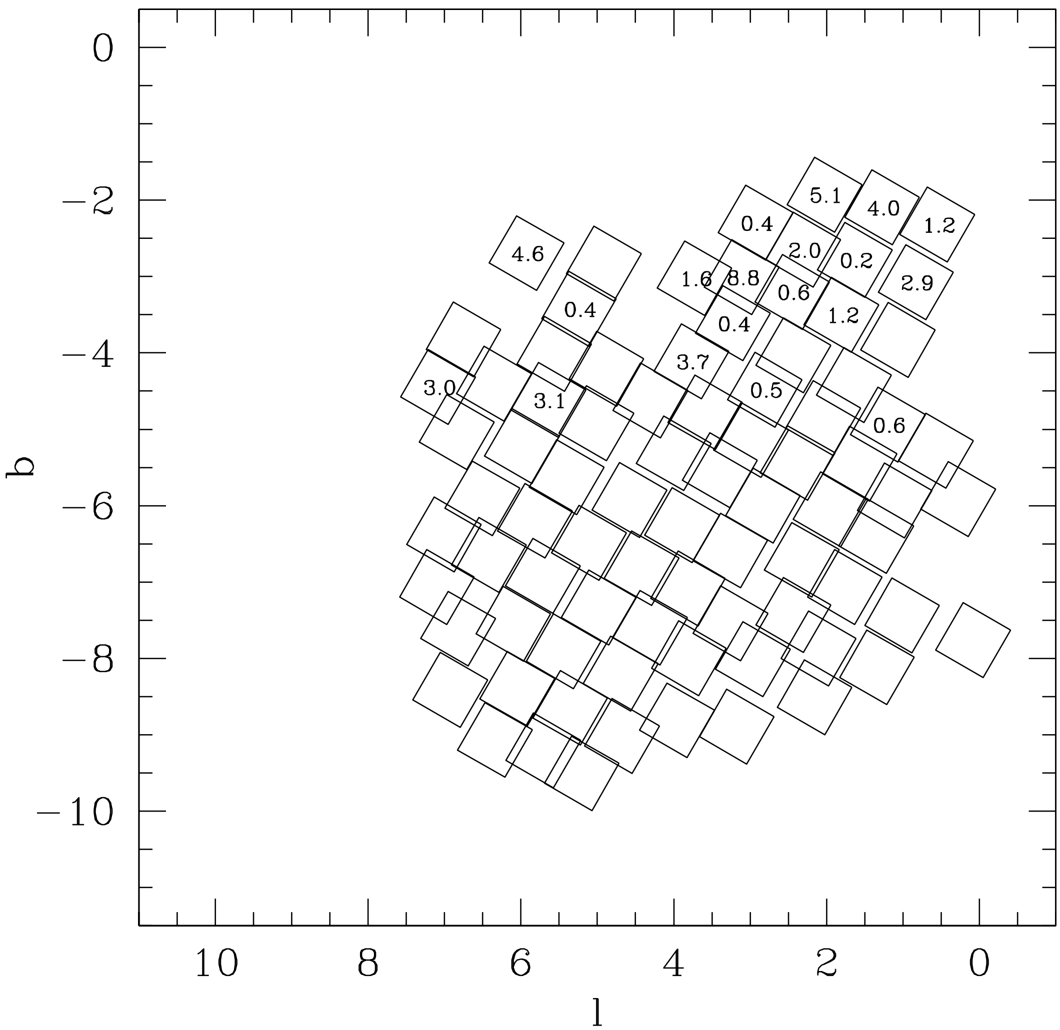

Figure 5.14: Optical depth for each field ($\times 10^6$).

Table 5.6. Optical Depth by Field

Field	(l, b)	$N_{\rm stars}/100$	$N_{\rm clumps}/100$	$N_{\rm events}$	$\tau/10^{-6}$
101	(3.73, −3.02)	6284	629.5	1	1.62 ± 1.62
102	(3.77, −4.11)	6545	444	1	3.67 ± 3.67
104	(3.11, −3.01)	5813	652	9	8.76 ± 3.73
105	(3.23, −3.61)	6375	539	1	0.35 ± 0.35
108*	(2.30, −2.65)	6498	790	6	2.04 ± 0.92
109*	(2.45, −3.20)	6926	661	2	0.58 ± 0.41
110	(2.81, −4.48)	6649	408	1	0.46 ± 0.46
113*	(1.63, −2.78)	6252	834	3	0.55 ± 0.35
114*	(1.81, −3.50)	6665	617	3	1.19 ± 0.74
118*	(0.83, −3.07)	6347	741.5	7	2.85 ± 1.35
119*	(1.07, −3.83)	7454	542.5	0	—
121	(1.20, −4.94)	5855	344	1	0.59 ± 0.59
158	(7.08, −4.44)	4703	246.5	1	2.96 ± 2.96
162	(5.64, −4.62)	5914	301	2	3.11 ± 2.21
176	(2.93, −2.30)	7741	814.5	1	0.37 ± 0.37
178	(5.24, −3.42)	8186	477	1	0.43 ± 0.43
180	(5.93, −2.69)	6388	478	1	4.62 ± 4.62
401*	(2.02, −1.92)	6630	964.5	7	5.13 ± 2.16
402*	(1.27, −2.09)	7098	1153	10	3.95 ± 1.50
403*	(0.55, −2.32)	6798	1085	4	1.16 ± 0.66
CGR[a]	(1.50, −2.68)	60668	7388.5	42	$2.17^{+0.47}_{-0.38}$

Only fields with at least one clump giant event (and field 119) are shown.

*Field is near the Galactic center and included in CGR as defined on page 93.

[a]Average towards the group of 9 fields designated as CGR.

This includes 1,260,000 clump giants. We find a gradient in the b-direction of $(1.06 \pm 0.71) \times 10^{-6}\,\mathrm{deg}^{-1}$ and a gradient in the l-direction of $(0.29 \pm 0.43) \times 10^{-6}\,\mathrm{deg}^{-1}$. The gradient in the b-direction is significant, but the gradient in the l-direction is consistent with 0.

5.4.1 Optical Depth Limits for Fields Without Events

For the fields that do not have any clump giant events we calculate a 1σ upper limit to the optical depth given by

$$\tau_{\mathrm{lim}}^{\mathrm{CL}} = \nu^{\mathrm{CL}} \tau_{1\ \mathrm{event}} \,, \tag{5.17}$$

where $\tau_{1\ \mathrm{event}}$ would be the optical depth if we had one event in that field and ν^{CL} is a factor that depends upon the confidence level (CL). Using the optical depth estimator (5.15) we can rewrite this as

$$\tau_{\mathrm{lim}}^{\mathrm{CL}} = \nu^{\mathrm{CL}} \frac{\pi}{4E} \left\langle \frac{\hat{t}_i}{\epsilon(\hat{t}_i)} \right\rangle \,, \tag{5.18}$$

where the angle brackets indicate an average in that field and E is the exposure for the single field. We are finding limits precisely because we do not have any events in some fields so we do not know the average event duration. Instead we assume that events in each field follow the same distribution. While this may not be an accurate assumption, as discussed in §5.5, it is the best we can do. We find the efficiency corrected optical depth contribution per event in field f:

$$\left\langle \frac{\hat{t}}{\epsilon(\hat{t})} \right\rangle_f = \frac{\sum_{i=1}^{N_{\mathrm{events}}} \frac{\hat{t}_i}{\epsilon(\hat{t}_i)_i}}{\sum_{i=1}^{N_{\mathrm{events}}} \frac{\epsilon(\hat{t}_i)_f}{\epsilon(\hat{t}_i)_i}} \,, \tag{5.19}$$

where the efficiency $\epsilon(\hat{t}_i)_i$ refers to the efficiency of each observed event and $\epsilon(\hat{t}_i)_f$ is the efficiency for an event of the same duration in field f.

We now calculate the factor ν^{CL}. The number of events in a field is a Poisson variable so to find a $n\,\sigma$ upper limit on the optical depth we use the $n\,\sigma$

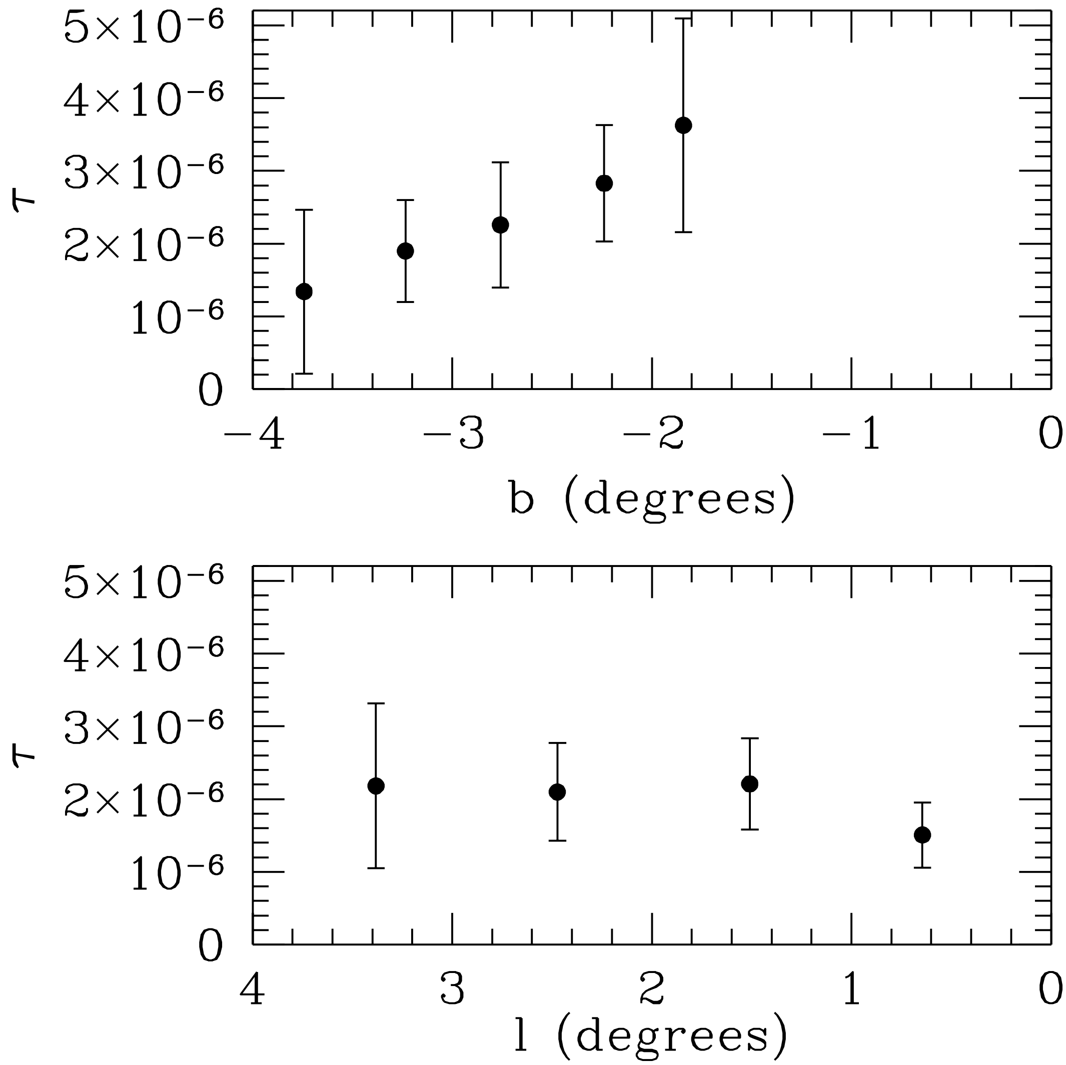

Figure 5.15 Average optical depth in strips binned in l and b. There is a gradient in b, but in l the gradient is consistent with 0.

limit on number of events given that we observed zero given by

$$e^{-\nu^{\mathrm{CL}}} = \frac{1.0 - CL}{2} \, . \tag{5.20}$$

For a $1\,\sigma$ limit we have a 68.17% confidence level and find $\nu^{1\,\sigma} = 1.8379$. Thus the $1\,\sigma$ upper limit for a field with no observed events is

$$\tau^{\mathrm{CL}}_{\mathrm{lim}} = 1.8379 \frac{\pi}{4E} \left\langle \frac{\hat{t}_i}{\epsilon(\hat{t}_i)} \right\rangle \, . \tag{5.21}$$

We calculate these limits and present them in Table 5.8.

Table 5.8: One sigma upper limits on the optical depth for fields with no clump events

field	$\tau^{\lim,1\sigma}$	Field	$\tau^{\lim,1\sigma}$	Field	$\tau^{\lim,1\sigma}$	Field	$\tau^{\lim,1\sigma}$
103	3.26×10^{-6}	128	1.45×10^{-6}	144	4.62×10^{-5}	161	2.52×10^{-6}
106	7.90×10^{-6}	129	9.87×10^{-5}	145	4.10×10^{-5}	163	5.84×10^{-6}
107	4.22×10^{-5}	130	1.13×10^{-4}	146	1.42×10^{-5}	164	3.68×10^{-4}
111	4.56×10^{-6}	131	2.01×10^{-5}	147	3.10×10^{-5}	165	6.81×10^{-4}
112	7.12×10^{-5}	132	2.04×10^{-5}	148	9.71×10^{-6}	166	2.52×10^{-5}
115	3.58×10^{-6}	133	3.25×10^{-5}	149	1.39×10^{-5}	167	2.83×10^{-6}
116	5.02×10^{-6}	134	5.45×10^{-5}	150	1.59×10^{-5}	168	6.30×10^{-6}
117	8.37×10^{-5}	135	9.14×10^{-5}	151	2.67×10^{-5}	169	1.05×10^{-4}
119	1.10×10^{-6}	136	1.23×10^{-5}	152	1.18×10^{-5}	170	4.54×10^{-4}
120	1.91×10^{-6}	137	1.72×10^{-5}	153	1.83×10^{-5}	171	2.08×10^{-5}
122	6.90×10^{-6}	138	1.97×10^{-5}	154	2.14×10^{-5}	172	2.91×10^{-5}
123	7.70×10^{-5}	139	2.80×10^{-5}	155	1.65×10^{-5}	173	4.44×10^{-5}
124	4.94×10^{-6}	140	3.42×10^{-5}	156	1.85×10^{-5}	174	1.36×10^{-5}
125	7.95×10^{-6}	141	9.01×10^{-5}	157	1.39×10^{-5}	175	3.58×10^{-5}
126	1.35×10^{-4}	142	1.28×10^{-5}	159	3.57×10^{-6}	177	3.09×10^{-6}
127	1.02×10^{-5}	143	1.80×10^{-5}	160	8.12×10^{-6}	179	2.61×10^{-6}

5.4.2 Optical Depth Toward the Galactic Center

As seen from Table 5.6 the error on τ for each field is very large due to the low number of events, to reduce this error we calculate the optical depth over a larger region close to the Galactic center. We use 9 fields close to the Galactic center that contain 2/3 of our clump giant events, we call this region the central Galactic region (CGR) to emphasize its proximity to the Galactic center, but note that it does not contain the Galactic center. The CGR comprises fields 108, 109, 113, 114, 118, 119, 401, 402, and 403, with a total area of about 4.5 square degrees. Using the 42 events in the CGR, we find an optical depth of $\tau_{\rm CGR} = 2.17^{+0.47}_{-0.38} \times 10^{-6}$ at $(l, b) = (1\overset{\circ}{.}50, -2\overset{\circ}{.}68)$ [1]. The exposure for this set of fields is $E = 1.869 \times 10^9$ star-days (738850 clump giant stars times 2530 days). We note that the result found using the old optical depth estimator (5.15) and interpolated efficiencies a function of $\hat{t}$ only is nearly identical ($2.16^{+0.46}_{-0.38} \times 10^{-6}$).

The error estimate is found with Monte Carlo simulations as done previously (Alcock et al., 1997b), and is somewhat larger than the simple Poisson error. Since the number of events measured is a Poisson variable we simulate many experiments each finding a number of events given by Poisson statistics. We draw the timescales for each event randomly from the the observed events' timescales. When we have simulated enough experiments to have good statistics we calculate the upper and lower limits to give a 68% confidence interval. This gives larger errors than simple Poisson statistics ($\pm 0.33 \times 10^{-6}$), but is consistent with the formula of Han & Gould (1995), which gives $\pm 0.42 \times 10^{-6}$.

Field 104, which has the largest optical depth, falls just outside of the CGR. To test how sensitive the optical depth is to the detailed shape of the region selected, we create a rectangular region "CGR+3", which is composed of CGR plus the three adjacent fields at the same galactic latitudes (fields: 176, 104, 105). The optical depth in this extended region is $\tau_{\rm CGR+3} = 2.37^{+0.47}_{-0.39} \times 10^{-6}$ at $(l, b) =$

[1] The unweighted average position for 9 CGR fields is $(l, b) = (1\overset{\circ}{.}55, -2\overset{\circ}{.}82)$

$(1^\circ\!.84, -2^\circ\!.73)$, entirely consistent with our principal result. An optical depth using all our events has little meaning due to the large optical depth gradient, but for completeness we note that using all 2.44 million clump giants and all 62 events the optical depth over all 83 analyzed fields is $\tau_{\rm all} = (1.21 \pm 0.21) \times 10^{-6}$ at $(l, b) = (3^\circ\!.18, -4^\circ\!.30)$.

In summary, we see no evidence that our optical depth results are strongly affected by blending. Furthermore, we find that a small amount of blending will not strongly affect the measured optical depth.

5.5 Clustering of Events and Concentration of Long Events in Field 104

The optical depth in field 104 is the largest for any field, we would like to investigate if this is just a statistical fluctuation or a sign of some galactic structure. Of our 62 clump events 9 are in field 104 and the average duration is longer than in other fields. In fact four of the ten events with $\hat{t} > 100$ are in field 104 including two of the three longest. The long duration of the events could indicate that the substructure contained heavier objects such as black holes. Alternatively, it could indicate a concentration of orbits through the Milky Way and a place where the orbital speeds were slower than normal.

We investigate the statistical significance of the apparent concentration. We do not account for the change in the detection efficiency, which generally increases with $\hat{t}$, so we only place a lower limit on significance of the difference between duration distributions in field 104 and the other fields. The efficiency for detecting long events is similar in most fields because this does not depend very strongly on the sampling pattern. The detection of short events is lower in sparsely sampled fields; therefore, the number of short events in some of the fields used for comparison may be relatively too small with respect to a frequently-sampled field

104. This may lower the significance of the $\hat{t}$ distribution difference computed here.

We use the Wilcoxon number-of-element-inversions statistic to test significance. We divide events into two populations: events in field 104 and the remaining events. We divide the events into two groups in two different ways: (1) we take all events in field 104 to the first group (9 events) and all the remaining events (except duplicates from field 109) to the second sample (51 events) and (2) we put the seven events in field 104 (and not duplicated in 109) in one group and the remaining events (53) in the other. Either way the entire sample of 60 unique clump giants is used.

Cases (1) and (2) are each tested separately according to the following procedure. We order all the events from the shortest to the longest. We then count how many times one would have to exchange the events from field 104 with the other events to have all the 104 field events at the beginning of the list. If we have N_1 and N_2 elements in the 104 and non-104 groups respectively, then the Wilcoxon statistic is approximately Gaussian distributed with an average of $N_1 N_2/2$ and a dispersion $\sigma = \sqrt{N_1\, N_2\,(N_1 + N_2 + 1)/12}$.

For case (1), the Wilcoxon statistic is 324 and the expected value is 230 ± 48, a 1.96σ difference; for case (2) the Wilcoxon statistic is 282 and the expected value is 186 ± 43, a 2.22σ difference. Together the two cases indicate that events in fields 104 are inconsistent at about the $2\ \sigma$ level with being drawn from the same distribution as events in the remaining fields. Using the entire set of criteria "c" events, not just clump-giant stars, we find similar results. This result is somewhat less significant than one previously derived by Popowski et al. (2001a); however, similar analysis of an almost independent difference imaging analysis sample (Alcock et al., 2000c) also suggests anomalous character of duration distribution in field 104 (Popowski, 2002). We conclude that the unusual character of field 104 should be further investigated, but we cannot completely exclude the possibility that this effect is due to a statistical fluctuation.

In addition to the unusual number of long events in field 104, there seem to be spatial clusters of events on the sky in fields 104, 108, and 402. If microlensing events are clustered on the sky above random chance it indicates clustering of lenses, perhaps in some bound Galactic substructure or very young star forming regions. In order to test the significance of the apparent clustering of RCG events we use a Monte Carlo test in which we simulate 10000 microlensing experiments, each detecting 60 unique clump giant events similar to what was done in §4.4.1 for the entire criteria "c" sample. For each experiment we find the diameter of the densest cluster of 3 events and the densest cluster of 4 events. We compare the diameters of the densest 3-cluster ($0\overset{\circ}{.}0453$) and densest 4-cluster ($0\overset{\circ}{.}11$) in the actual data to the distributions formed by our Monte Carlo experiments. This gives us the probability of finding a 3-cluster (or 4-cluster) as small as we found in the actual data. If a star is in an overlap region we count it only once.

We select 60 clump giant stars at random from the one percent data base in order to match the spatial distribution of lensing sources in the data. We also weight each event by the 50-day efficiency of its field (Table 5.5), so fields with low sampling efficiency are properly under-represented. Finally we consider various optical depth gradients across our fields, specifically we test two cases: a uniform optical depth across our fields and a steep linear gradient which results in the optical depth changing from a maximum at the Galactic center to 0 at $|b| = 4°$. The latter case is somewhat steeper than, but roughly consistent with, the gradient shown in Figure 5.15. The actual gradient is most likely between these two extremes. Because events are concentrated close to the galactic plane when a gradient is considered, the second case decreases the typical 3- and 4-cluster size.

With no optical depth gradient we find a probability of 1.9% of finding a 3-cluster as dense as in the data, and 4.6% of finding a 4-cluster this dense. For the steep optical depth gradient, we find probabilities of 8.7% and 27% respectively. Unfortunately these results are only marginally significant, certainly not compelling.

5.6 Conclusions

We have presented a new determination of the optical depth to microlensing towards the Galactic bulge using the full MACHO dataset (7 years). We used the subset of clump-giant criteria "c" events (62) to calculate optical depths for each of our fields and a subsample of 42 clump-giant events to calculate an optical depth of $\tau = 2.17^{+0.47}_{-0.38} \times 10^{-6}$ at $(l, b) = (1\overset{\circ}{.}50, -2\overset{\circ}{.}68)$.

We can compare our results with previous MACHO collaboration results by using the events in the fields they examined. In the 24 fields used by Alcock et al. (1997a), we have 37 clump events giving $\tau = 1.36^{+0.35}_{-0.28} \times 10^{-6}$, which is two sigma below the earlier result of $\tau = 3.9^{+1.8}_{-1.2} \times 10^{-6}$. Over the 8 fields in the MACHO difference imaging study (Alcock et al. 2000a), our current, almost independent, sample gives $\tau = 2.20^{+0.67}_{-0.52} \times 10^{-6}$ at $(l, b) = (2\overset{\circ}{.}68, -3\overset{\circ}{.}35)$, which is in good agreement with the earlier result of $\tau = 2.43 \pm 0.38 \times 10^{-6}$, though using the correction factor discussed in §1.2 would make this agreement somewhat worse.

Our new value of $\tau = 2.17^{+0.47}_{-0.38} \times 10^{-6}$ is also very consistent with the recent EROS collaboration (Afonso et al. 2003) measurement. They found $\tau = (0.94 \pm 0.29) \times 10^{-6}$ at $(l, b) = (2\overset{\circ}{.}5, -4\overset{\circ}{.}0)$ from 16 clump giant events and an efficiency calculation similar to ours. The values are different but they are reported at different position. The difference becomes entirely insignificant if we take into account either the numerical value of the gradient reported in §5 or read off the approximate optical depth value at $b = -4.0$ from Figure 5.15. The OGLE-II results (Sumi et al., 2006) are also in agreement with our results. They use a sample of 32 events from an extended red clump giant region of the color-magnitude diagram to find $\tau = 2.37^{+0.53}_{-0.43} \times 10^{-6}$ at $(l, b) = (1\overset{\circ}{.}16, -2\overset{\circ}{.}75)$. In addition, our new optical depth is in very good agreement with the recent theoretical prediction of the Galactic bulge optical depth ($\tau = 1.63 \times 10^{-6}$) by Han & Gould (2003). In fact, this is the first time theory and observation have agreed.

We note that about 41% of the optical depth is in events longer than 100 days (10 out of 62 events), and about 63% of the optical depth is in events longer than 50 days (21 out of 62 events). This may be at odds with some models of the Galactic structure and kinematics (e.g., Han & Gould 1996), but consistent with others (Evans & Belokurov 2002) which include streaming motion along the bar. The distributions of event durations are shown in Figure 5.16 where we plot histograms for uncorrected and efficiency-corrected cases. We note that the mean Einstein diameter crossing time of all our clump giant events is $\langle \hat{t} \rangle = 56 \pm 64$ days and for our fields close to the Galactic center $\langle \hat{t} \rangle_{CGR} = 39 \pm 31$ days. To facilitate proper comparison with theoretical models we have to weight each event by its inverse efficiency (Table 5.7). Then the averages become: $\langle \hat{t} \rangle\,(\mathrm{eff}) = 40 \pm 50$ days for all fields and $\langle \hat{t} \rangle_{CGR}\,(\mathrm{eff}) = 30 \pm 29$ days for fields in the CGR[2]. Evans & Belokurov (2002) find average Einstein crossing times range from around 100 days in models that include bar streaming motion to 30 days in models without bar streaming. Our values are too uncertain to distinguish between these kinematic possibilities and are consistent with both types of models.

[2]Because the distribution is non-Gaussian we also give the median and quartiles, which are (23.7, 12.0, 47.8) for all clump events and (18.7, 9.5, 46.9) for clump events in the CGR.

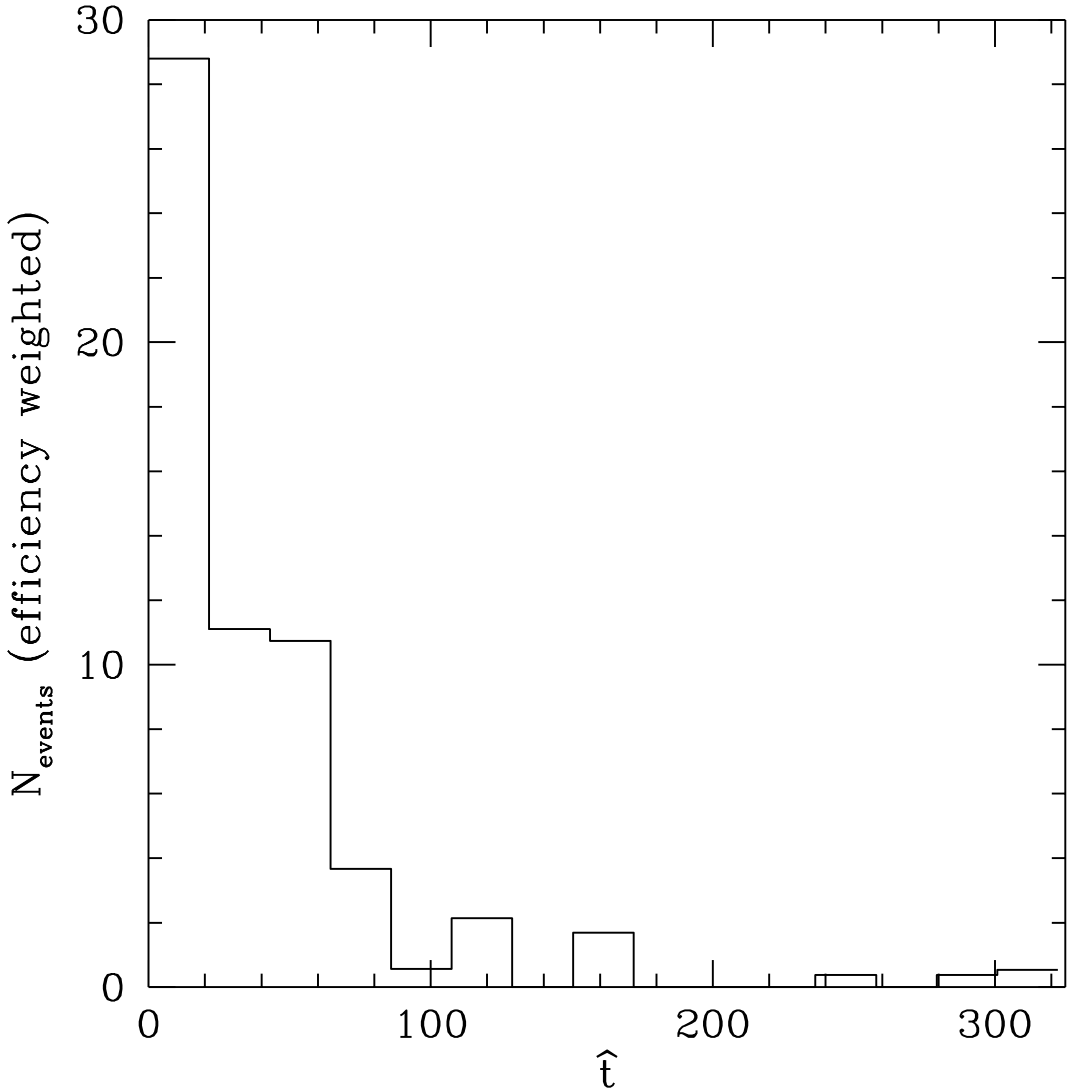

Figure 5.16 We show the distribution of Einstein diameter crossing times with each event weighted by its inverse efficiency

6

The Theory of Fitting Blended Light Curves[1]

6.1 Introduction

Gravitational microlensing has become a useful tool in measuring the amount of matter along the line-of-sight to distant stars. Since gravitational lensing depends only on mass, microlensing is sensitive to all compact forms of matter independent of their luminosity. Thus measurements out of the plane of the Galaxy towards the LMC, SMC, and M31 have given important limits/detections of dark matter in the halo (Aubourg et al. 1993; Lasserre et al. 2000; Alcock et al. 1993; 1997a; 2000b; Paulin-Henriksson et al. 2003; de Jong et al. 2004), and measurements towards the Galactic bulge give important constraints on the mass and distribution of Galactic stars, including those too faint to observe directly. Several measurements toward the bulge have been made and are compared to our result in the previous Chapter and described in §1.2.

The signal of microlensing is a specific transient magnification of a back-

[1]This chapter is largely a reprint, with permission, of work already published as Thomas, C. L. and Griest, K., 2006, "Fitting Photometry of Blended Microlensing Events", ApJ, 640, 299.

ground source star as the lens object passes in front of it, and thus microlensing experiments repeatedly monitor many ordinary stars to find microlensing light curves. The probability of microlensing occurring to a given star is called the optical depth, τ and is of order 10^{-6} or less for many Milky Way lines-of-sight. The smallness of τ means that microlensing experiments concentrate on very crowded star fields where many hundreds of thousands of stars can be simultaneously imaged. This allows many light curves to be created simultaneously but also results in blending of the source stars together. This blending causes two problems in using the detected microlensing events to infer the optical depth. First, since each "source object" may contain the light from many stars, the number of stars being monitored is not just the number of objects being photometered. Second, the magnification profile of a microlensing event is changed when unlensed light is blended with the lensed light of the source star.

In this Chapter we revisit the problem of blending in microlensing light curves. There are several methods of dealing with the blending problem. Among these are 1) obtaining high resolution images from space, which will usually allow separation of the source object into its different components, giving a direct measurement of the fraction of light from the lensed source in the PSF (Alcock et al., 2001), 2) if the unlensed light is not exactly centered on the lensed source, then the centroid of the light will shift during the microlensing event allowing limits on blending to be placed (Alard, Mao, & Guibert, 1995), 3) if the lensed source is a different color than the unlensed light then a color shift will occur as the event proceeds, allowing limits on lensed-light fraction to be made (Alard, Mao, & Guibert, 1995), and 4) for image subtraction light curves, the source can in principle be removed and this can help break the degeneracy in some cases (Gould & An, 2002).

However, we will not discuss the above methods in this paper but will focus on the fitting and interpretation of the photometric data alone; that is, we include the lensed-light fraction as a parameter in the microlensing fit and hope to use the shape of the light curve to recover this information. In principle this allows recovery of the actual event duration, and a measurement of the amount of blending in the sample of events, allowing corrections to be made in estimating the optical depth. A related and popular method is to calculate lensing optical depth using only a subsample of very bright source stars (e.g. clump giants). The idea is that very bright source stars are less likely to be blended, and when they are blended, should be blended only by a small amount. In this case one would like to use the blend fits only to determine whether or not a given event is blended.

Unfortunately, as pointed out previously (e.g. Han 1999; Di Stefano & Esin 1995; Woźniak & Paczyński 1997; Alard 1997, &c.) blended fits tend to be quite degenerate. A light curve with a small lensed-light fraction looks very much like an unblended light curve with a smaller maximum magnification and a smaller event duration. As pointed out previously, this means that this fitting method will be of limited use in many cases. Our study adds strength to the conclusions of previous workers, points out several new problems with blend fits, and makes recommendations on how best to proceed with blend fits for those who choose to do them. We will discuss what happens when the microlensing event contains signal from other physical effects such as weak parallax or binary effects. These effects are not rare, and since the difference between blended and unblended light curves is small, even an almost undetectable real deviation from the standard point-source-point-lens light curve can render blend fit results meaningless.

The plan of the paper is as follows:

- In § 6.2 we define our notation, discuss the similarities and differences between unblended microlensing and blended microlensing, and give an analytic approximation that gives the underlying event duration and peak magnification from the lensed-light fraction and the easily measured apparent event duration and maximum magnification.

- In § 6.3 we discuss the usefulness of blend fits and compare with earlier work.
- In § 6.4 we discuss the optimal times to take follow-up data in order to improve recovery of parameters from the blend fit.
- In § 6.5 we discuss the problem of the baseline magnitude, and
- In § 6.6 we discuss the problem of non-Gaussian data and whether the errors returned by fitting programs are reliable.

6.2 Degeneracies in Blended Light Curves: Analytic Approximations for Event Duration and A_{max}

When an isolated lens object crosses close to the line-of-sight of an isolated background source star, the source is magnified and a microlensing light curve is generated with magnification

$$A(u) = \frac{u^2+2}{u(u^2+4)^{1/2}}, \quad u^2(t) = u_{min}^2 + \left(\frac{t-t_{\rm max}}{t_{\rm E}}\right)^2, \tag{6.1}$$

where u is the projected distance between the lens and source in units of the Einstein ring radius, $t_{\rm E}$ is the time to cross the Einstein radius, and t is time, with maximum magnification, A_{max}, occurring at $t_{\rm max}$.

The most important parameter is the event duration $t_{\rm E}$ since the optical depth depends upon the sum of efficiency weighted event durations:

$$\tau = \frac{\pi}{2E}\sum_{\rm events}\frac{t_{\rm E}}{\epsilon(t_{\rm E})}, \tag{6.2}$$

where the exposure E is the product of the length in days of the observing program and the number of observed stars, and ϵ is the efficiency of detecting an event of duration $t_{\rm E}$.

When other sources of light are contained in the same seeing element as the lensed source star, the microlensing light curve is altered since only a fraction of the light is actually lensed:

$$A'(u) = f_{\rm ll} A(u) - f_{\rm ll} + 1, \tag{6.3}$$

where $f_{\rm ll}$ is the fraction of light that is lensed (a.k.a. the blend fraction, i.e. coming from the source star) as measured at the baseline (before or after the lensing event).[2] Compared with unblended events, blended photometric microlensing light curves suffer from a smaller apparent maximum magnification, $A'_{\rm max}$, and shorter apparent event duration, $t'_{\rm E}$, as well as from potential color shifts if the blended light has a different spectrum. We distinguish the apparent values of all parameters from their real values with a '$'$'.

In fact, a blended light curve looks remarkably like an unblended light curve with different values of $t_{\rm E}$ and A_{max} (e.g. Han 1999; Di Stefano & Esin 1995; Woźniak & Paczyński 1997; Alard 1997). However, as illustrated in Figure 6.1, this similarity is not perfect and there are differences in the shapes of blended and unblended light curves. It is these differences which give rise to the hope that information about blending can be extracted by fitting light curves with blending parameters. If this similarity were perfect, then there would be no use in fitting blended light curves to photometric data. Figure 6.1 shows that the shape differences are typically small, meaning that extracting blending information will be difficult. Woźniak & Paczyński 1997 (WP) studied this in detail and gave regions of the $f_{\rm ll}$, A_{max} plane where blended fits were useful and where they were not. We return to this subject in § 6.3, but the qualitative results of WP can be seen from Figure 6.1, where low magnification events show a maximum difference between the blended light curve and the best fit unblended light curve of only 1% or so,

[2]Several terms have been used in different ways in the literature for blend fraction, most commonly f_b which either means the fraction of light coming from the lens or the fraction of the light coming from non-lens sources. We introduce the new symbol $f_{\rm ll}$ = (sourceflux)/(total flux in PSF) to avoid the extant confusion of nomenclature.

while the higher magnification events show more substantial differences.

Previous workers have also given analytic formulas relating the measured (apparent) maximum magnification $A'_{\rm max}$, and the apparent event duration $t'_{\rm E}$ to $f_{\rm ll}$, A_{max}, and $t_{\rm E}$. For example, Woźniak and Paczyński (WP) studied the degeneracies by performing expansions of the above equations in the limits of small u_{min} and large u_{min} and in these limits give the formulas relating the actual values of $t_{\rm E}$ and A_{max} to $f_{\rm ll}$ and the measured $A'_{\rm max}$ and $t'_{\rm E}$. For small u_{min} (large A_{max}) they found $u'_{\rm min} \approx u_{min}/f_{\rm ll}$, and $t'_{\rm E} \approx f_{\rm ll} t_{\rm E}$, while in the limit of large u_{min} ($A_{max} \approx 1$) they found $u'_{\rm min} \approx u_{min}/f_{\rm ll}^{1/4}$, and $t'_{\rm E} \approx f_{\rm ll}^{1/4} t_{\rm E}$.

Di Stefano & Esin (1995), and Han (1999), and Alard (1997) took a different approach, solving equation (6.3) for A_{max} and giving the actual $t_{\rm E}$ in terms of $t'_{\rm E}$ by requiring that the two different parameterizations give the same amount of time with $A > 1.3416$. They found:

$$A_{max\,({\rm Han})} = (A'_{\rm max} - 1 + f_{\rm ll})/f_{\rm ll}, \quad t_{\rm E(Han)} = t'_{\rm E} \left(\frac{u_1^2 - u_{min}^2}{1 - {u'_{\rm min}}^2} \right)^{1/2}, \tag{6.4}$$

where $u'_{\rm min} = u(A'_{\rm max})$, and $u_1 = u(A(A' = 1.3416))$, can be found from the inverse of equation (6.1):

$$u(A) = (2/\sqrt{1 - 1/A^2} - 2)^{1/2} \tag{6.5}$$

Noting in Figure 6.1 that the differences between the blended and unblended light curves tend to be large in the peak, and that the values of $t'_{\rm E}$ and $A'_{\rm max}$ are found by fitting, we worried that the Han formula, which assumes equality in the peak, might not be accurate. We also wondered about the range of applicability of the WP formulas and so decided to test these formulas. We did this by fitting artificial blended light curves with an unblended source model and finding the best fit values of $t'_{\rm E}$ and $A'_{\rm max}$. We also fit these light curves with blended source models and correctly extracted the input blend parameters.

As shown in Figure 6.2, we found that the WP formulas are not very useful over most of the parameter range, and that the Han equations work well only

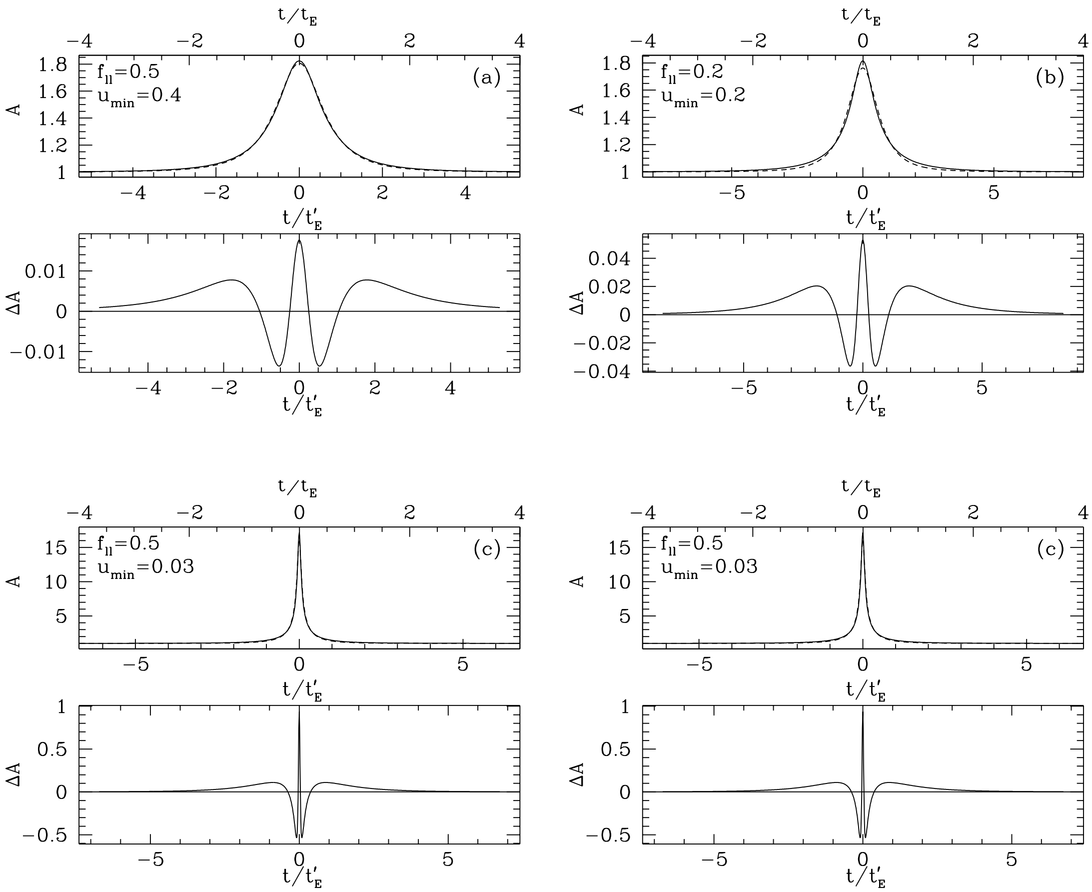

Figure 6.1 Four example blended light curves (solid) compared with the best fit unblended light curve (dashed), as well as the difference, ΔA, between them (blend fit minus unblended fit). The bottom labeled time axis is in units of the *apparent* Einstein Ring crossing time, $t'_{\rm E}$, that is easily available from the data and an unblended fit. However, the extent of the time axis is $\pm 4t_{\rm E}$, (labeled on the top) where $t_{\rm E}$ is the underlying event duration used in optical depth estimates. Thus the extent of all the time axes is roughly 160 days for a typical microlensing event of duration 20 days. Part (a) has values: $f_{\rm ll} = 0.5$, $u_{min} = 0.4$, $u'_{\rm min} = 0.634$, and $t'_{\rm E}/t_{\rm E} = 0.754$. Part (b) has values: $f_{\rm ll} = 0.2$, $u_{min} = 0.2$, $u'_{\rm min} = 0.655$, and $t'_{\rm E}/t_{\rm E} = 0.475$. Part (c) has values: $f_{\rm ll} = 0.5$, $u_{min} = 0.03$, $u'_{\rm min} = 0.062$, and $t'_{\rm E}/t_{\rm E} = 0.594$. Part (d) has values: $f_{\rm ll} = 0.05$, $u_{min} = 0.03$, $u'_{\rm min} = 0.46$, and $t'_{\rm E}/t_{\rm E} = 0.144$.

over a restricted range of parameters. For the WP formulas this is not surprising since they were created only to show that the degeneracies exist in certain limits. For relatively large lensed-light fraction and for relatively low values of A_{max} the Han equations give a good estimation of the best fit $A'_{\rm max}$ and $t'_{\rm E}$, but for small lensed-light fraction or high A_{max} the estimates of these equation can be far off.

As expected, it is just where the blended light-curve shape differs the most from an unblended fit that the Han approximations do not work well. The reason can be seen in Figure 6.1, where for high magnification events and low lensed-light fraction the blended light curve differs strongly in the peak area, but not so much in the rising and falling regions of the light curve. Thus, the best fit unblended light curve will allow the actual peak magnification to overshoot and compensate for these points by undershooting in the middle regions. Since the Han formula forces the light curves to match at the peak and when $A'_{\rm max} = 1.34$, it will overestimate the best fit peak magnitude and underestimate the event duration.

By studying many such examples, one can come up with a formula that does a better job of relating the best fit $A'_{\rm max}$ and $t'_{\rm E}$ to A_{max}, $t_{\rm E}$, and $f_{\rm ll}$ in the parameter ranges where the Han formula does not work well. The points in Figure 6.2 show the best fit values of $A'_{\rm max}$ and $t'_{\rm E}$, found by fitting artificial blended light curves with no scatter and enough points that sampling would not be an issue (2000 points over 4 $t_{\rm E}$), vs $f_{\rm ll}$ (input). The dashed lines show the Han estimates and long dash lines the WP estimates for $t'_{\rm E}/t_{\rm E}$. At small values of A_{max} (< 3) the Han formulas do work very well (better than the new formula) and they should be used. However for $A_{max} > 3$ the Han formulas do not give accurate estimates. To find a better approximation, one can fit a straight line to the data for a given u_{min} and get a formula which fits well except for very low lensed-light fraction. Repeating this procedure for different values of u_{min}, one discovers that the slopes and zero points of the linear fits are also quite linear in u_{min}. Thus a simple fitting linear formula that covers much of the parameter space can be found. However, if one fits a quadratic for the low $f_{\rm ll}$ events one can get an even better formula which works very well for $f_{\rm ll} < 0.3$. Thus we find an approximation:

$$A_{max} \approx \begin{cases} A_{\rm Han}, & \text{if} A_{max} < 3; \\ \frac{A'_{\rm max} - 0.9785 + 0.4150 f_{\rm ll}}{0.8153 f_{\rm ll} + 0.00021}, & \text{if} A_{max} > 3 \text{ and } A'_{\rm max} < 10; \\ \frac{A'_{\rm max} - 0.3618 + 0.2106 f_{\rm ll}}{1.0282 f_{\rm ll} - 0.04433}, & \text{if} A_{max} > 3 \text{ and } A'_{\rm max} > 10, ; \end{cases}$$

$$t'_{\rm E}/t_{\rm E} \approx \begin{cases} t'_{\rm E(Han)}/t_{\rm E}, & \text{if} A_{max} < 3; \\ (-1.0946 u_{min} + 0.9418) f_{\rm ll} & \\ +1.141 u_{min} + 0.0564, & \text{if} A_{max} > 3 \text{ and } f_{\rm ll} > 0.3; \\ \mathbf{FCU}, & \text{if} A_{max} > 3 \text{ and } f_{\rm ll} < 0.3, \end{cases} \tag{6.6}$$

where

$$\mathbf{F} = \left(1, f_{\rm ll}, f_{\rm ll}^2\right), \tag{6.7}$$

$$\mathbf{U} = \begin{pmatrix} 1 \\ u_{min} \\ u_{min}^2 \end{pmatrix}, \tag{6.8}$$

$$\mathbf{C} = \begin{pmatrix} 0.02548 & 1.0626 & -1.6504 \\ 1.1914 & 7.284 & -11.50 \\ -0.8824 & -26.58 & 44.28 \end{pmatrix}, \tag{6.9}$$

and u_{min} is found from A_{max} and equation (6.5).

In using this formula, one typically starts with measured values of $t'_{\rm E}$, $A'_{\rm max}$, and an initial guess of A_{max} and uses different (unknown) values of $f_{\rm ll}$, to find the corresponding underlying A_{max} and $t_{\rm E}$. If the value of A_{max} found using the new fitting formula is smaller than 3, then one should use the Han formula instead. This formula allows one to derive A_{max} and $t_{\rm E}$ for measured values of $A'_{\rm max}$, $t'_{\rm E}$, and $f'_{\rm ll}$. This is useful in trying to estimate optical depth under various assumptions of blending.

The new fitting formula is shown as the solid line in Figure 6.2 and does better than Han or WP for $A_{max} > 3$. Over the range $0.01 < f_{\rm ll} < 1.1$, and $3 < A_{max} < 70$ the new fit formula gives a typical error in $t_{\rm E}$ (compared with actually fitting the microlensing light curve with a blend fit model) of around 3% and a maximum error of 9%. For A_{max} the typical error is 4% and the maximum error is 12%. The Han formula can be off by more than 50% in $t_{\rm E}$ and 24% in A_{max} in this region of parameter space.

In summary, we tested the Han formula, Woźniak and Paczyński (WP) formulas and equation (6.6) over a wide range of parameters and found the new fitting function works better than Han for all values of $f_{\rm ll}$ when $A_{max} > 3$ and $A'_{\rm max} > 1.34$, while the old Han formula works better for low values of A_{max} and $A'_{\rm max}$. The WP large A_{max} formula gives $t_{\rm E}$ within 10% only for large $f_{\rm ll}(> 0.5)$, and large A_{max}, while the other WP formula is not useful except for $A_{max} \ll 1.34$.

Since in microlensing experiments the event durations are found by photometric fitting and since the optical depth is proportional to the sum of the fit $t_{\rm E}$'s, when making corrections for blending it is important to properly relate the lens-light fraction of each event to the underlying event duration.

6.3 Usefulness of Blend Fits

Woźniak and Paczyński (1997) (WP) studied the degeneracy of blend fits and concluded that in many cases blended and unblended light curves cannot be distinguished by photometric fitting. They described areas of parameter space where blend fits would be useful and areas where they would not. While we think that WP did an accurate and very useful calculation, and we agree with their conclusion that blend fits are usually not very useful, we wanted to repeat their analysis for several reasons. First, WP did not include the baseline magnitude in their fits, reasoning that since many measurements are taken before and after the event, the error in baseline magnitude was not significant. In fact, we find that error

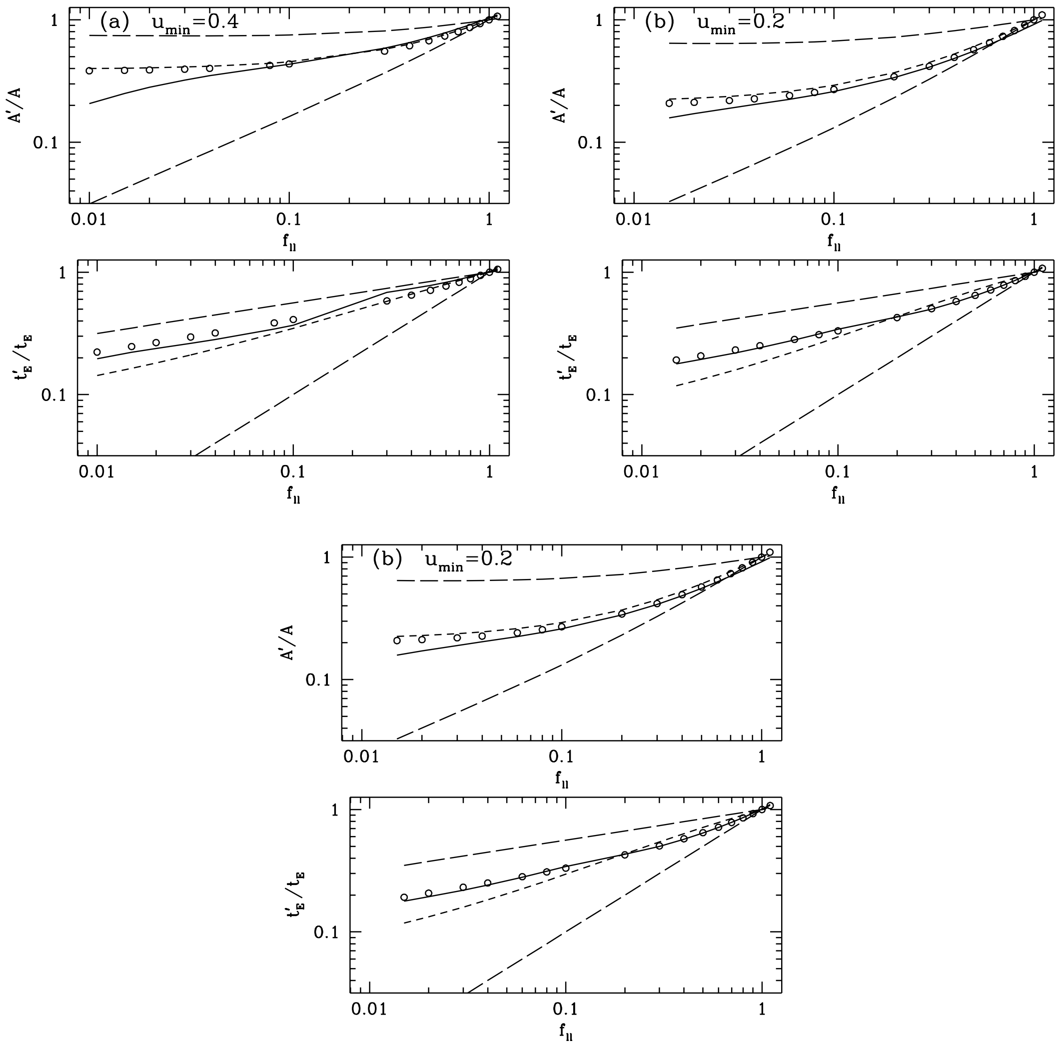

Figure 6.2 Comparison of approximation formulas for relating the underlying microlensing event duration t_{E} and maximum magnification A_{max}, to the blend fraction, f_{ll}, and easily measured apparent event duration and maximum magnification, t'_{E}, and A'_{max}. The circles give the actual blended and unblended results from our light-curve fitting program, while the solid lines show our new approximation formula. The short dashed line shows the Han approximation, while the long dashed lines show the WP approximations in their two limits. Part (a) is for an actual $u_{min} = .4$ ($A_{max} = 2.65$), part (b) shows $u_{min} = .2$ ($A_{max} = 5.07$) , and part (c) shows $u_{min} = .03$ ($A_{max} = 33$).

in the baseline magnitude is one of the most severe problems in blend fits. We find that errors even at the few percent level can drastically alter the parameter values extracted from the fit. Second, WP considered only evenly spaced observations and we wanted to consider whether different follow-up strategies could improve the ability to extract the parameters.

In our studies, we find the error in fit parameters three ways. First we create artificial light curves using the theoretical formula and add Gaussian random noise to each measurement and perform blended and unblended fits on these light curves using Minuit (James, 2003). Second we calculate the error matrix by inverting the Hessian matrix as discussed in Gould (2003). Finally to understand the effect of the non-Gaussianity of the errors in real microlensing experiments we create artificial lensing light curves by adding microlensing signal into actual non-microlensing light curves obtained by the MACHO collaboration, and then fit these.

Since the method of calculating the error matrix is closest to what WP did, we first give these results. Briefly, we calculate the Hessian matrix (the matrix of second derivatives of the light curve residuals with respect to each parameter) then invert it. The square roots of the diagonal elements of the resulting matrix are then the one sigma errorbars of the parameters. This accounts for correlations in the parameters, but not any nonlinearities. WP used a very similar method, but used it to calculate the $\Delta\chi^2$ instead of the error bars. In figure 6.3 we show that our method brackets WP's for the same choice of sampling and errorbars. We show limits calculated this way as both the one sigma lower limit on $f_{\rm ll}$ for a $f_{\rm ll} = 1$ light-curve fit with blending and the value of $f_{\rm ll}$ that gives 1 as the one sigma upper limit.

We note, as WP found, that parameter errors scale linearly with

$$a = \frac{\sigma}{\sqrt{N}} \tag{6.10}$$

for N points taken during the peak (defined as lasting $4t_{\rm E}$)[3]. Thus our results can be scaled for other numbers of observations with different values of σ. Thus, we find that our results agree with those of WP if we assume the baseline magnitude is known and take a uniform sampling.

6.4 Follow-up Observations

Figure 6.1 shows that the difference between blended and unblended light curves is not always uniform across the light curve. So if one wanted to plan follow-up observations to improve the accuracy of the blend fit, one should concentrate on the regions of the light curve where the differences are largest. Thus it may be possible to do better than WP suggested with their equal spaced observation calculations. To test this hypothesis we calculated the error matrix for blended fits adding in follow-up observations at different points on the light curve. As seen in the Figure 6.1 examples, for any choice of parameters there are five places where the difference light curves are maximum, and therefore where follow-up data is more useful than average: at the peak, in the rising/falling portion of the curve, and in the wings. The precise locations change with the choice of parameters but for Figure 6.1a they are found to be localized near the peak at ($|t/t_{\rm E}| < 0.1$), in the falling (or rising region) at ($0.3 < |t/t_{\rm E}| < 0.6$), and near the baseline at ($1.0 < |t/t_{\rm E}| < 1.5$). Observations taken between these regions do little in constraining the parameters. In addition points t greater than $2t_E$ are very helpful because they fix the baseline in our simulated light curve. We discuss the baseline separately in § 6.5.

In Figure 6.4 we compare the relative value of added points as a function of the time they are added. We find that, in this case, with 40 observations, 4 extra focused observations can reduce the error on f_{ll} by 7.7%. To get the same reduction

[3] This is true for large enough values of N, for small values of $N \lesssim 16$ parameter errors increase faster than a.

of error on f_{ll} with evenly distributed observations we would need 7 observations, in other words, each added focused observation is equivalent to increasing the sampling by 1.75 points over 4 $t_{\rm E}$. The numerical value of the extra effectiveness obtained using focused versus evenly spaced observations varies with underlying parameters and the total number of added points. It may seem curious at first that the peak is not the best place to add observations since it is where the difference between blended and non-blended light curves is the greatest. This is explained by the rapid variation of the difference curve there, points near the peak can be accommodated by small shifts in t_0 since the difference curve is varying rapidly there.

Precise follow-up measurements at multiple focused locations can improve the determination of f_{ll} even more as they further constrain the shape of the light curve. In order to see the effect of adding multiple follow-up observations at two distinct times we compare this with adding evenly spaced observations. In Figure 6.5 we plot the increase (or decrease) in effectiveness of extra focused observations as a function of the two times at which they are taken. The contours around the light areas show regions of increased effectiveness, while dark areas show areas where the focused observations are less valuable than evenly spaced observations. In this example the effectiveness is increased by up to a factor two.

It is important to note that with more observations or higher accuracy in each follow-up region the advantage per added observation is reduced and the relative values of the various minimums vary, though they stay in roughly the same place. For practical use it is important to note that the time of the optimum second follow-up observation(s) varies with the time of the first follow-up observations(s). In practice one would need to calculate optimum observing times for an event in progress as a function of all the previous measurements.

One problem with the above approach is that without knowing the underlying parameters, particularly $t_{\rm E}$, it is difficult to predict the best times to take follow-up data. To test whether a practical experiment could be designed to take advantage of focused follow-up data we simulated an experiment. First we generated light curves with 80 points over $8t_{\mathrm{E}}$ with .05 Gaussian errors at the baseline drawing f_{ll} randomly from the interval $(.01, 1)$ and u_{min} randomly from the interval $(0, 1)$ requiring $A'_{max} > 1.34$ in the Han approximation. We also adjusted t_{E} to keep ${t_{\mathrm{E}}}' \sim 10$ days also using the Han approximation. We then generated 9 follow-up observations over 3 days at the peak and fit the first half of the light curve plus the follow-up data. From this first fit we calculated the optimum times for two more bouts of follow-up. We generated these, both with 9 observations over 3 days, and then fit the entire light curve with the added 27 points. We also generated 27 points of follow-up uniformly distributed over the 20 days starting at the peak, added it to the initial light curve and fit the resulting data. To see the relative improvement for the two methods we calculate a parameter $\zeta = (f'_{ll_{focused}} - f_{ll})/(f'_{ll_{unfocused}} - f_{ll})$, which is the ratio of the error in blend fraction given by focused observations to the error in blend fraction given by uniform follow-up sampling. We plot the distribution of ζ in Figure 6.6 finding that our strategy gives an improvement ($\zeta < 1$) for 71% of the events and a worsening in 29% of the events. We find a substantial improvement ($\zeta < .5$) for 45% of the events, and and even larger improvement ($\zeta < 0.1$) 18% of the time. Thus we conclude that for the the same amount of observing time we can make a more accurate measurement of f_{ll} by focussing the follow-up observations.

In summary we find that observations concentrated at a few times can constrain the microlensing parameters as well as many measurements distributed throughout an event. The best places for these measurements are at the peak, in the falling/rising portion, and in the wings, with regions between where added observations do no good. For data of the quality we assumed in most cases it is possible to constrain the event parameters well enough with the first half of the data and some follow-up observations near the peak to predict the last two optimum observing times.

6.5 Baseline Magnitude

The baseline magnitude of a light curve can in principle be very well determined since many measurements can be taken before or after the microlensing event. WP assumed that this was the case and so did not include the baseline magnitude as one of their fit parameters. In real microlensing surveys, however, it may be that the error in average magnitude is not entirely statistical, and may not average down as expected. There may be a systematic limit to the accuracy with which the baseline magnitude can be determined. In fact, detectors and telescope systems drift over time and so measurements made much later may actually reduce the accuracy of the baseline magnitude. To investigate the importance of the baseline magnitude, we simulate systematic error in the baseline by creating artificial light curves without any errors and fit them with a model with a fixed value of baseline magnitude that differs from the actual baseline magnitude by various amounts. Our results are shown in Figure 6.7. We find that the dependence on baseline is very strong for low amplification events and not as strong for higher amplification events, but in any case even a 1-2% error in baseline magnitude determination can strongly bias the recovered blend fraction.

To investigate how well baseline magnitudes converge in real data, we used the MACHO collaboration database of random clump stars (Alcock et al., 2000b). We split the data from each of 150 light curves in MACHO field 119, one of the most frequently observed fields, into two parts, the first half and the second half of the observation period. We find the mean and standard deviation for each half and compare them. We normalize the flux such that the median value is 1. In Figure 6.8 we plot both the difference in flux, $\Delta f = \bar{f}_1 - \bar{f}_2$, and $t = \left(\bar{f}_1 - \bar{f}_2\right) / \left(\sqrt{\sigma^2_{\bar{f}_1} + \sigma^2_{\bar{f}_2}}\right)$ for these light curves. From the width of the distribution of t, mean flux values obtained from the first half are clearly inconsistent with mean flux values obtained from the second half ($\sigma_t > 1$).

Using half the difference in mean flux between the first and second half of the light curve as a rough estimate of the error in the baseline due to the systematic drift and non-Gaussian nature of the magnitude errors we can estimate the error in $f'_{\rm ll}$ due to baseline systematics. We find that the distribution of means has a half width of 1.5%. Referring to Figure 6.7 we see that, for a typical event with $u_{min} = 0.5$, this implies a typical spread in $f_{\rm ll}$ of 0.23 due to baseline alone. Since half of all events have $u_{min} > 0.5$, half of all events will have an even larger error. For more sparsely sampled fields this dispersion due to error in baseline fit would be even larger.

6.6 Errors in Fit Parameters

From MACHO Project data (Table 5.3) it seems likely that blend fits return an amount of blending larger than is reasonable for the set of clump giants. For the set of MACHO clump giant events, which are believed to be minimally blended from their positions on the color magnitude diagram, many are best fit with blending. If many of the events are not blended then a systematic bias in the fits must make them appear to be blended. A systematic bias in recovered lensed-light fraction would lead to a bias in the optical depth as well. For this reason the MACHO collaboration investigated the blending of their clump giant sample and decided to use the parameters from the unblended fits. They also used a subsample of events that were less likely to be blended to check for a bias due to blending and found no such bias.

To test for a systematic bias we generate 1000 light curves with Gaussian errors for each of three different values for the error on each point: $\sigma = 0.01$, $\sigma = 0.05$, and $\sigma = 0.15$. We used the same input parameters for each event, $u_{min} = 0.5$ and $f_{\rm ll} = 1$, and used 40 points over $4t_{\rm E}$. The recovered lensed-light fractions for these events are shown in Figure 6.9. As the error on each datum increases the distribution of f'_{ll} becomes increasingly skewed. We find the same shift occurs as the sample rate decreases as well. In fact, the distribution stays roughly constant with the accuracy parameter (a) discussed in §6.3. We find that while the mean f'_{ll} may not decrease, the most probable value does decrease. This reduction in the mode is at least partially compensated by the large tail of the distribution with $f'_{ll} > 1$, but for the small number of events a microlensing experiment observes it is unlikely that many of the few events with $f'_{ll} \gg 1$ will be observed. Even if one event with $f'_{ll} \gg 1$ is observed it may be ignored as it is an unphysical value of the parameter, thus leading to an underestimate of the average value of f_{ll}. Thus we find that as the errors in measurement increase, blend fitting becomes more and more likely to return biased results. The direction of the bias is more often toward small values of f_{ll}. Thus events that are in reality unblended become more and more likely to return fit values implying that they are heavily blended.

6.7 Conclusions

We find agreement with previous workers that blend fits are problematic, but can be useful especially for high magnification events. When performing blend fits it is helpful to get extra measurements near the peak and at other specific points along the light curve. We find that if care is not taken in the treatment of the light-curve baseline magnitude the fit results can be severely biased and in real data the errors returned on fit parameters should be treated with caution. We find that blend fits return a biased, skewed distribution of the underlying parameters tending to indicate more blending than actually exists. Finally, note that when the microlensing event contains signal from other physical effects such as weak parallax or binary effects blend fits can yield unreliable results. These effects are not rare, and since the difference between blended and unblended light curves is small, even an almost undetectable real deviation from the standard point-source-point-lens light curve can render blend fit results meaningless.

The text of this chapter, in full, is a reprint of material previously published in the Astrophysical Journal as Thomas, C. & Griest, K., "Fitting Photometry of Blended Microlensing Events", ApJ, Vol. 640, Issue 1, 299-307. I was the primary researcher and author and the research was conducted under the supervision of my advisor and coauthor, Kim Griest.

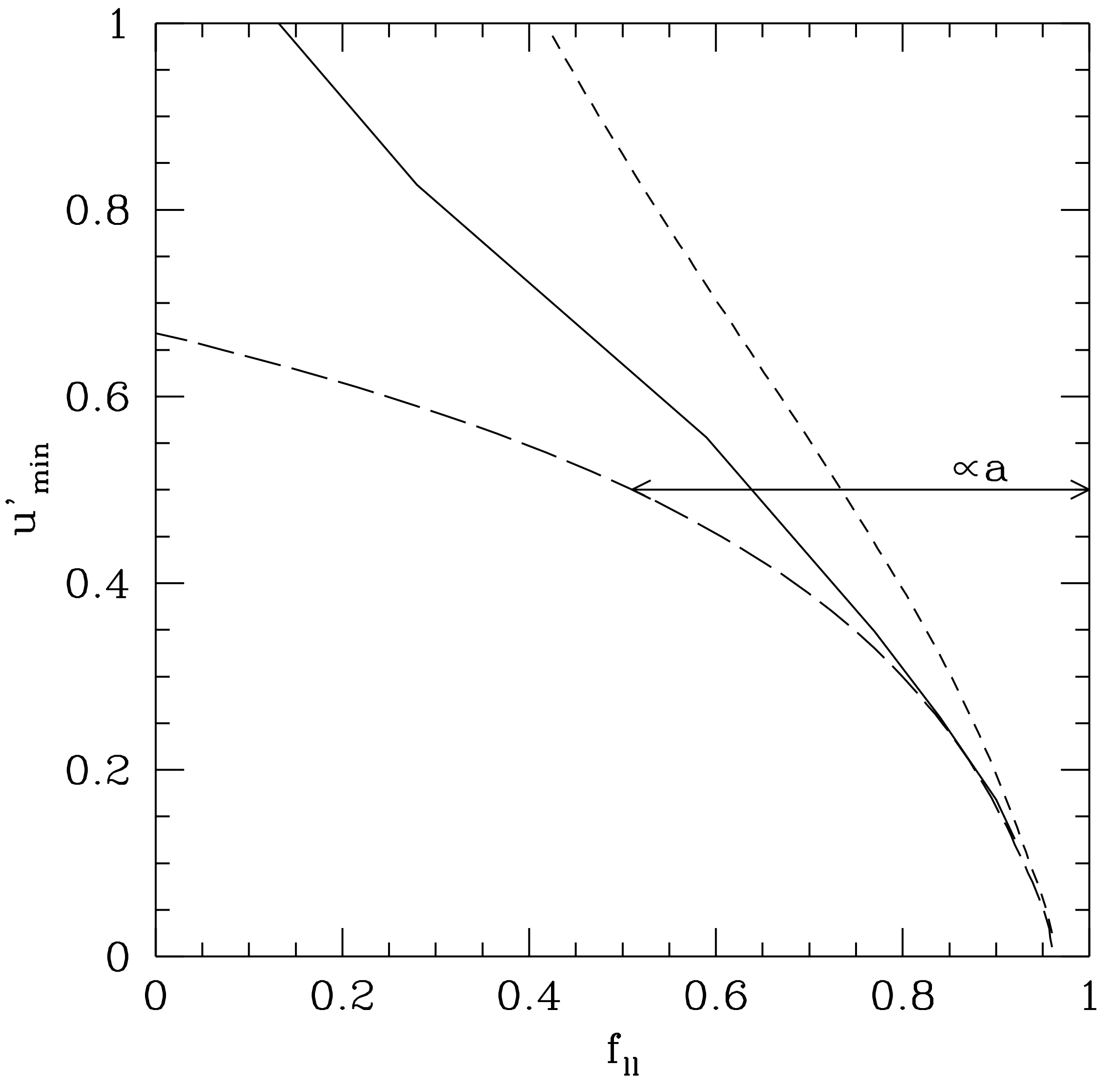

Figure 6.3 Comparison of our results to the previous results of Woźniak and Paczyńskione sigma limits on f_{ll} (real) for the range of apparent u_{min} (from non-blend fits). The solid line is from WP, the long dashed line is the one sigma lower limit on f_{ll} for a unblended light curve, and the short dashed line is the value of f_{ll} for which the one sigma upper limit is 1. In the region below the long dashed line blending is detectable at the one sigma level, above the short dashed line blended events are indistinguishable from unblended events, and in-between the two dashed lines detection is marginal. The region where blending is distinguishable can be scaled with a (eqn. [6.10]).

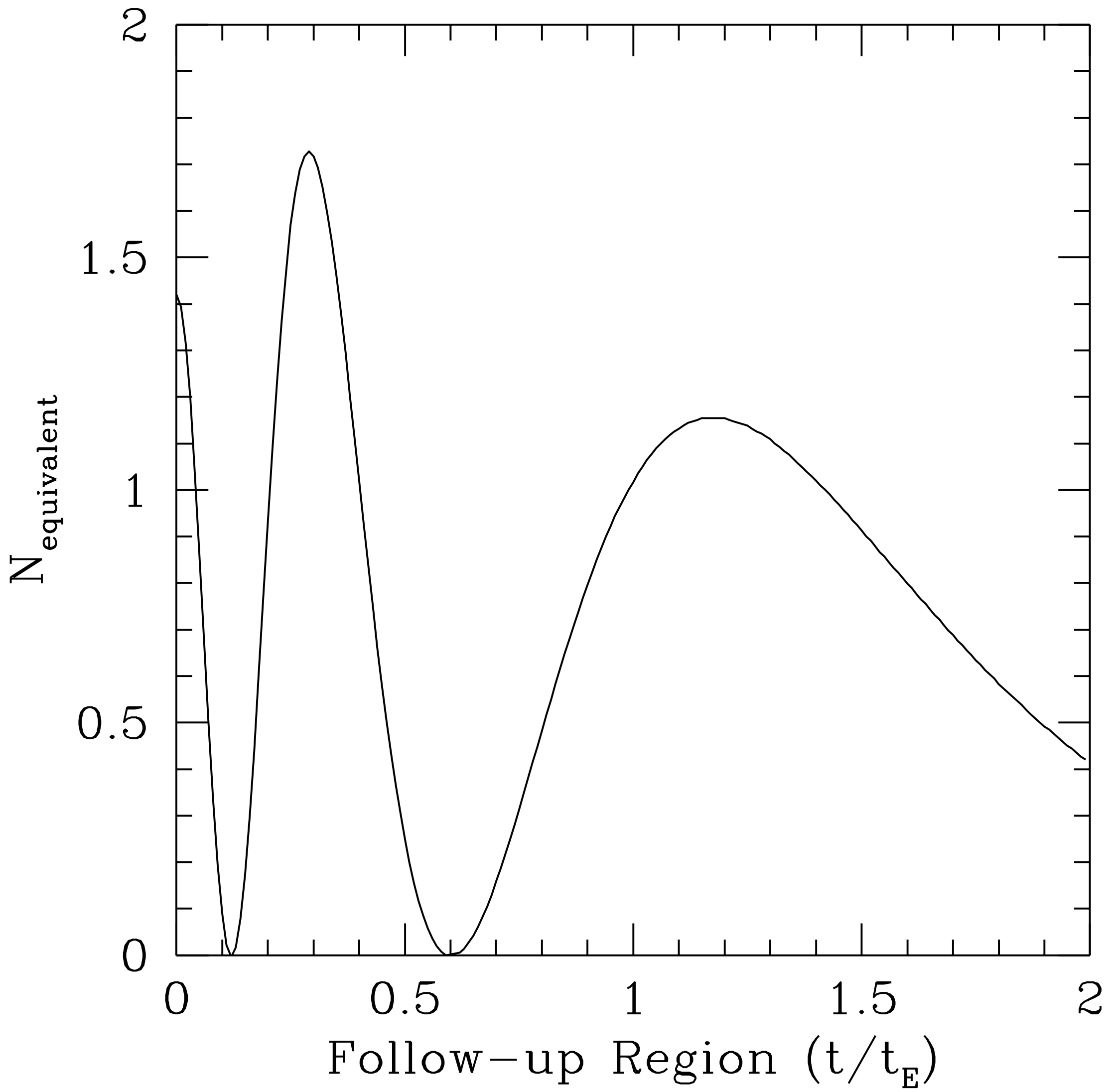

Figure 6.4 The equivalent number of uniform follow-up data points required to improve measurement of f_{ll} as much as a single follow-up observation is plotted as a function of when the single follow-up observation is taken. In this case $u_{min} = 0.25$, $f_{ll} = 0.25$, and 4 follow-up points are added (all at same time t). Times with $N_{\rm equivalent} > 1$ are the most effective, while times with $N_{\rm equivalent} < 1$ are less useful.

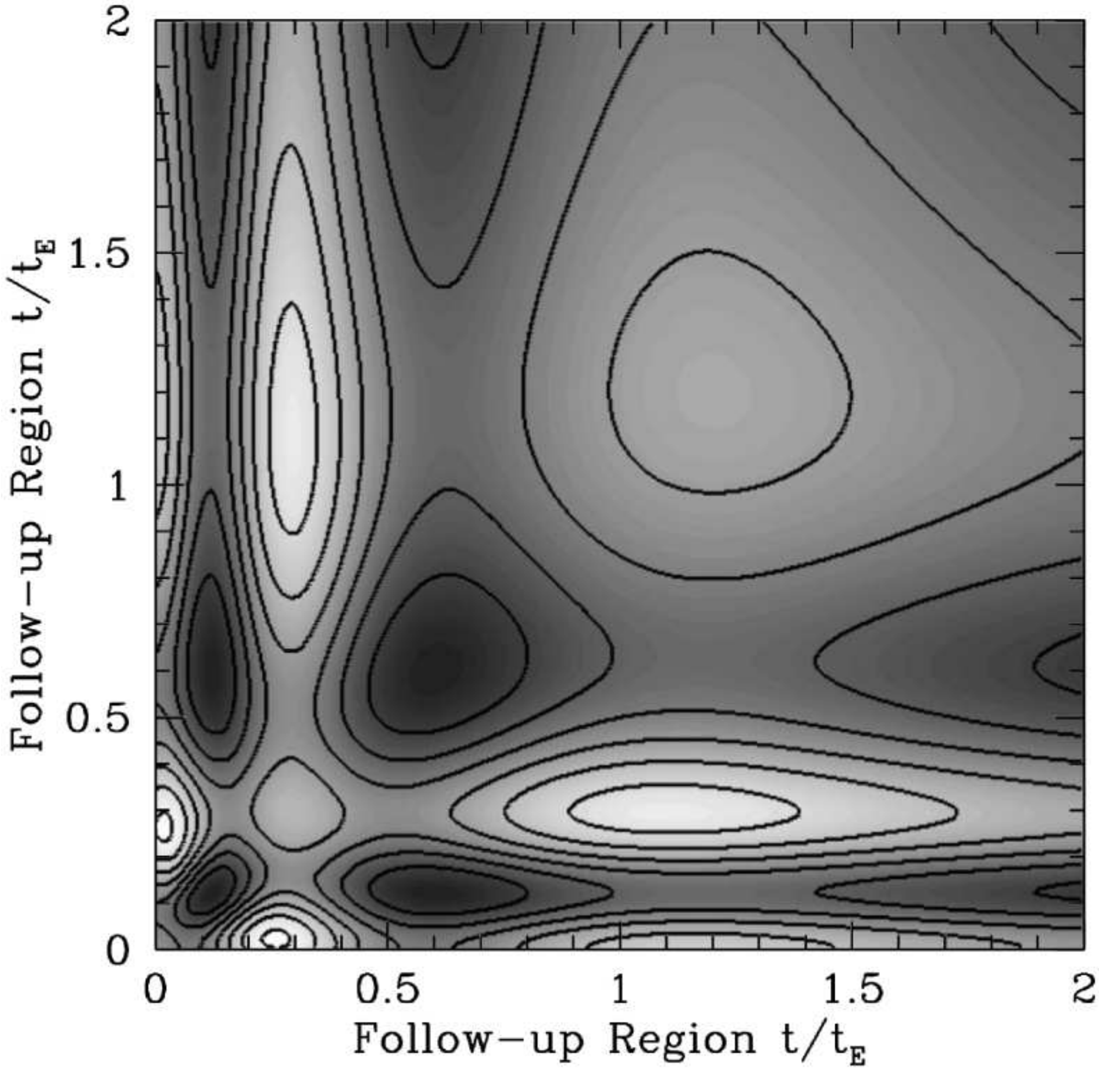

Figure 6.5 Number of additional uniformly distributed observations required for the same improvement as 8 focused observations (2 follow-up regions each with 4 observations). The seven contours are 2 (darkest regions), 4, 6, 8, 10, 12, & 14 (lightest regions). In this case $u_{min} = 0.25$ and $f_{ll} = .25$. Values above (below) 8 indicate an advantage (disadvantage) relative to uniform follow-up.

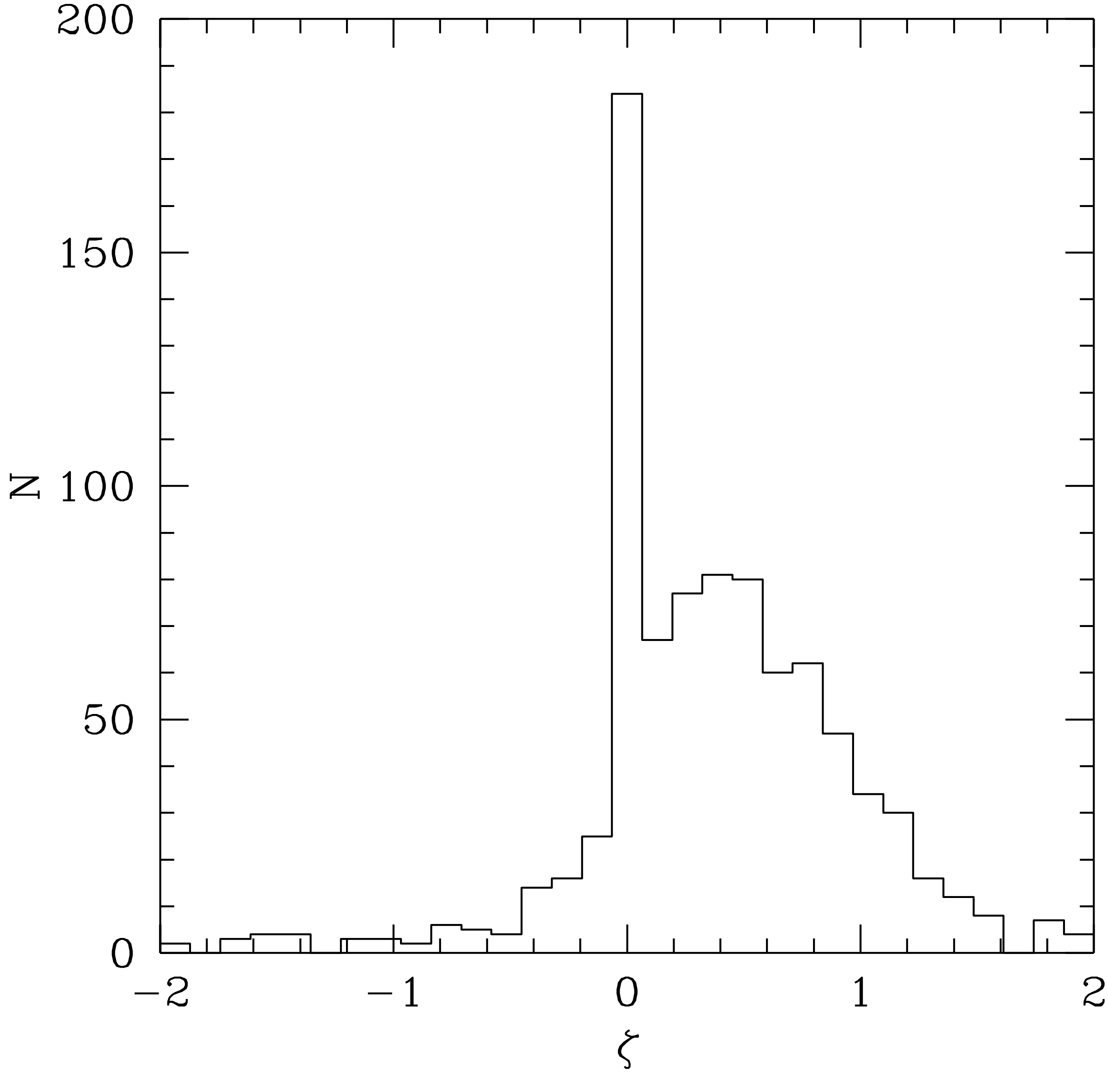

Figure 6.6 The ratio ζ showing the advantage of a focused follow-up strategy for 71% of events ($\zeta < 1$ - unshaded region). 15% of the events in our simulation are outside the range of this plot $|\zeta| > 2$.

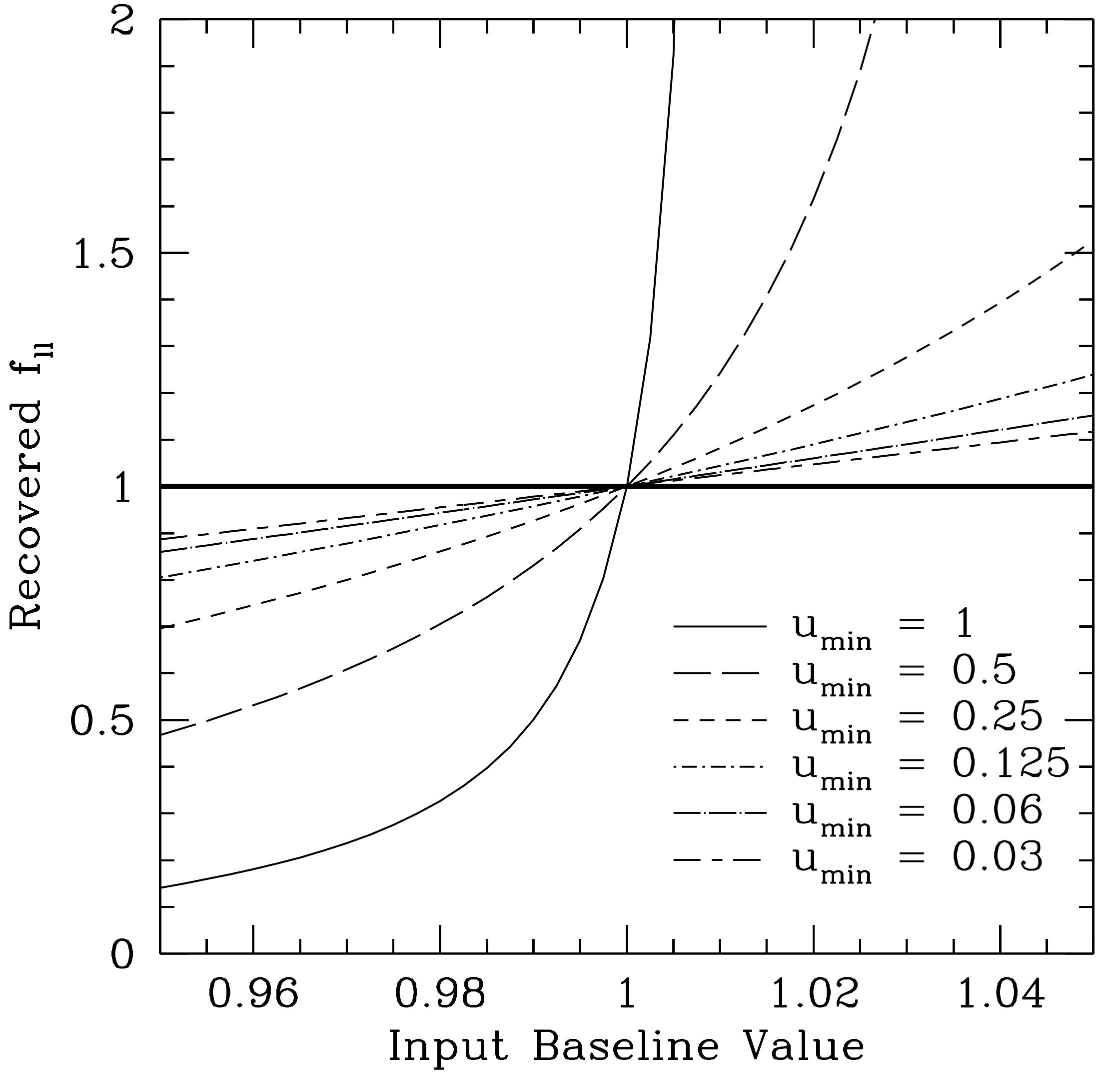

Figure 6.7 The recovered f_{ll} for unblended light curves as a function of an input baseline magnitude (fixed at a given value). Forty points over 4 t_{E} are used.

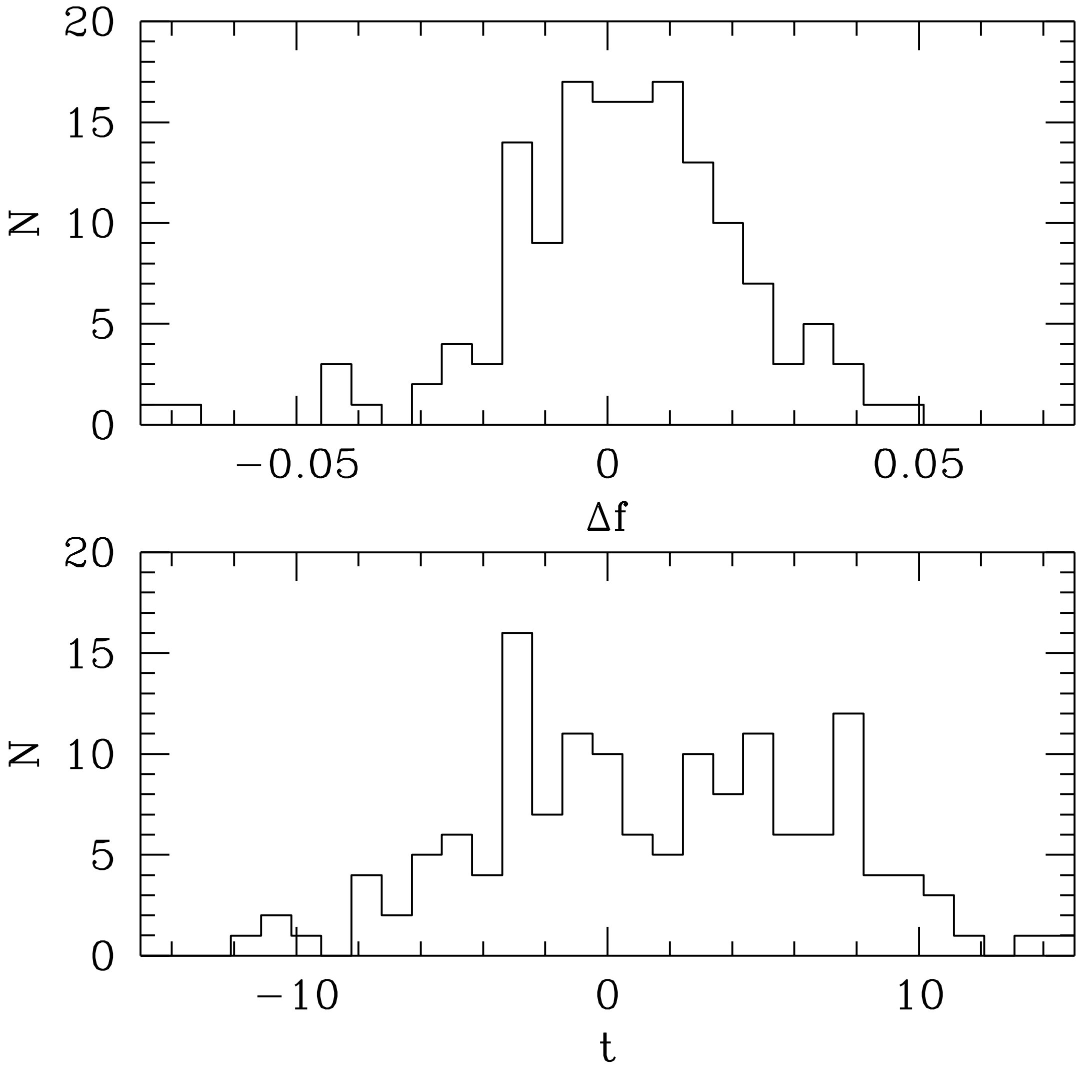

Figure 6.8 Distribution of flux differences (top) and the normalized difference, t, (bottom) for first and last half of data from MACHO light curves.

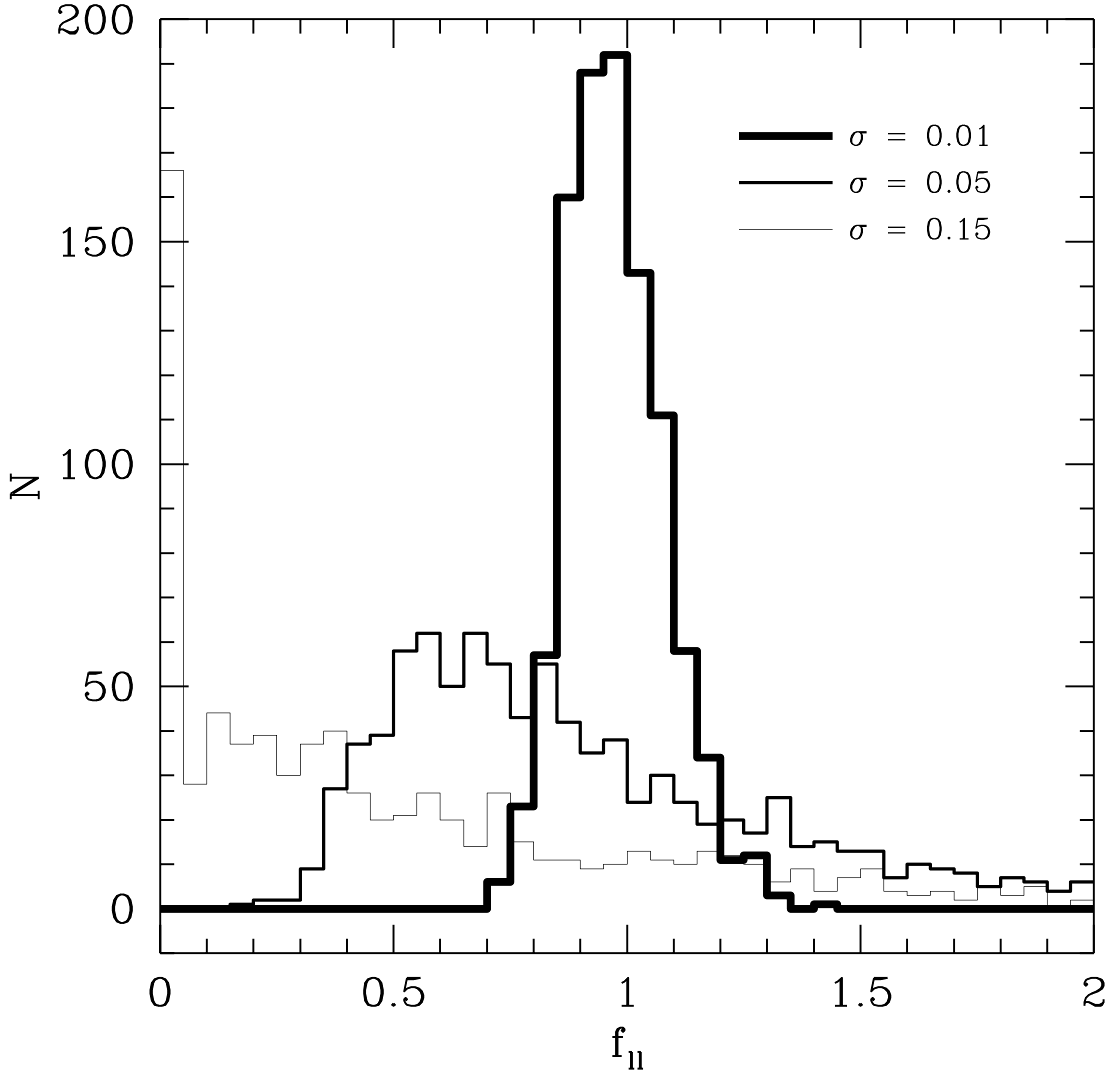

Figure 6.9 Recovered f_{ll} for data with Gaussian errors of $0.01, 0.05$, and 0.15. As the errors on individual data points increase the distribution becomes increasingly skewed with the mode shifting toward 0 for larger errors. Also note that 11% of the $\sigma = 0.05$ events and 24% of the $\sigma = 0.15$ events had recovered $f'_{ll} > 2$ while none of the events with $\sigma = 0.01$ were fit best with $f'_{ll} > 2$.

7

Correcting For Weak Lensing[1]

An important problem of modern astrophysics is to measure the expansion history of the Universe and explain the unexpected results that have already been found. From type Ia supernovae (SNe Ia) observations we know that the universe is not only expanding, but that the expansion rate is accelerating (Perlmutter et al. 1998, 1999, Garnavich et al. 1998, Riess et al. 1998). The acceleration is attributed to "dark energy," an apparent vacuum energy whose energy density is either constant or varies with the expansion of the universe in a way different from any known matter or energy. One way of understanding the nature of this dark energy is to understand its equation of state, the ratio of pressure to energy density and its dependence on time or redshift, $w(z)$. Currently the best candidate for constraining $w(z)$ is the measurement of standard candles (objects with known luminosity). As these measurements are pushed to higher redshifts, weak lensing, the slight shearing and magnification of distant objects due to intervening matter, becomes important.

[1]This chapter describes work in progress, intended to document recent work and suggest avenues for further research.

7.1 Standard Candles

Type Ia supernovae are used as standard candles because their luminosity is well known. SNe Ia have a brightness that is known to about 15% after calibrating for the variation in timescale, or stretch, and so the luminosity distance to them can be calculated fairly accurately. It has been found that at high redshifts SNe are dimmer than expected (Perlmutter et al., 1998) and this unexpected result has been attributed to the accelerating expansion of the universe. While the uncertainty of SNe brightness is not a problem at low redshift, where many can be observed and the mean value found with relatively high precision, at high redshift the observing time required will limit the number observed.

At higher redshifts it may be possible to use super-massive binary black holes in their inspiral phase as gravitational wave standard candles (Holz & Hughes, 2005). Because the gravitational wave physics of the early phase inspiraling black hole binaries is well understood, these standard candles would have much higher intrinsic precision than SNe Ia. The Laser Interferometer Space Antenna (LISA) is a proposed NASA mission currently scheduled to launch in 2015 that would detect gravitational waves from these standard candles and other sources. The luminosity distance could be measured with less than one percent error if an optical counterpart is found to eliminate the degeneracies between position and distance. Since these binary black holes are expected to be the engines at the center of some of the most luminous things in the universe, finding optical counterparts is likely. With optical counterparts a few gravitational wave standard candles would constrain $w(z)$ as well as a few thousand SNe Ia (Holz & Hughes, 2005).

It seems gravitational wave standard candles would make a great substitute or addition to SNe standard candles, and they would, were it not for gravitational lensing. As observations push to higher and higher redshifts weak lensing becomes an important effect. At $z = 1$ magnification due to weak lensing adds a few percent uncertainty and by $z = 2$ it is a 10-15% effect. While lensing affects light and gravitational waves exactly the same, the large number of observable SNe can make up for the added uncertainty, but gravitational wave standard candles are expected to be scarce. If we could correct for the lensing on a case-by-case basis we could overcome the weak lensing for the gravitational waves and make very accurate measurements. This correction has been discussed previously and it has been claimed that it cannot be done accurately enough (Dalal et al., 2003); however, previous work only considered using measurements of the weak lensing shear to find the magnification. We propose to calculate the weak lensing effect from the visible foreground galaxies as well as measuring it by observing the lensing induced shear as described in §7.2. Our proposed method might be impractical for SNe Ia, where there is already a 15% intrinsic uncertainty; however, for gravitational waves their high intrinsic precision makes each event much more valuable. For these events it may be worth putting more resources toward correcting each event for lensing.

7.2 Introduction to Weak Lensing

Weak lensing is a slight shearing and magnification or demagnification due to intervening matter. At high redshifts nearly everything is distorted (sheared or magnified) by all the intervening matter. Unlike microlensing, discussed in §1.1, with weak lensing objects are at cosmological distances and the lenses are galaxies with extended mass distributions.

We make a couple of assumptions commonly made in weak lensing. We project the mass of each galaxy into a lens plane. We model each galaxy with a singular isothermal sphere (SIS) for which the surface mass density is given by

$$\Sigma(r) = \frac{\sigma_v^2}{2Gr}\,. \tag{7.1}$$

While this mass distribution does diverge at $r = 0$ it accurately models the mass distribution of galaxy halos in all but the central core and at very large radius. We truncate the halo at the tidal radius, r_{200}, the radius for which the mean density of enclosed matter is 200 times critical density, mathematically it is given in §7.4. This prevents the total mass from diverging as it would if we considered infinitely large SIS.

The first step to calculating the magnification due to weak lensing is to find the relationship between the apparent and real positions of an object. The lensing angle can be calculated in the same way as was done in §1.1, except in this case the mass varies with radius. For a SIS, or any axially symmetric lens, the deflection angle is

$$\alpha(r) = \frac{4G}{c^2 r} M_{enc}(r)\,, \tag{7.2}$$

where $M_{enc}(r)$ denotes the mass enclosed at a radius of r. For the SIS lens this is

$$M_{enc}(r) = \frac{\pi \sigma_v^2}{G} r\,, \tag{7.3}$$

which, when combined with equation (7.2), gives a constant deflection angle of

$$\alpha(r) = 4\pi \frac{\sigma_v^2}{c^2}\,. \tag{7.4}$$

The lensing equation, analogous to equation (1.4), is then

$$\vec{y} = \vec{x} - 4\pi \frac{\sigma_v^2}{c^2} \frac{D_s}{D_l D_{ls}} \frac{\vec{x}}{|\vec{x}|}\,, \tag{7.5}$$

where we have replaced r with $\vec{y}$ for the real position and $\vec{x}$ for the apparent position of a source relative to the center of the lens to emphasize the direction of the deflection. When we consider multiple lenses, symmetry is broken and we cannot use radial symmetry to simplify the problem.

Our goal is to calculate the magnification, which can be done from the Jacobian matrix,

$$A_{ij} = \frac{\partial y_i}{\partial x_j}\,. \tag{7.6}$$

The magnification is then

$$\mu(\vec{x}) = \frac{1}{\det A(\vec{x})}\,. \tag{7.7}$$

The distortion of the source can be described by the convergence, κ, and the shear components, $\gamma_{1,2}$. The convergence is a measure of the mass in the line of sight, and the shear is determined by the mass distribution outside the the line-of-sight. The Jacobian matrix can be written in terms of κ and $\gamma_{1,2}$ as

$$A = \begin{pmatrix} 1-\kappa-\gamma_1 & -\gamma_2 \\ -\gamma_2 & 1-\kappa-\gamma_1 \end{pmatrix}\,, \tag{7.8}$$

from which it can be seen that

$$\det A = (1-\kappa)^2 - \gamma^2\,, \tag{7.9}$$

where $\gamma^2 = \gamma_1^2 + \gamma_2^2$, and the magnification is then

$$\mu = \frac{1}{(1-\kappa)^2 - \gamma^2}\,. \tag{7.10}$$

To extend this to multiple lenses one uses the image in the first lens plane to find the image in the second lens plane and so on, as shown in Figure 7.1. Mathematically the position in the n^{th} lens plane is given by

$$\vec{y} = \frac{D_s}{D_1}\vec{x}_1 - \sum_{i=1}^{n} D_{is}\alpha(\vec{x}_i)\,. \tag{7.11}$$

To find the real position, $\vec{y}$, equation (7.11) is used incrementing n to find the image position in successive lens planes until the source plane is reached ($n = N_{\mathrm{lenses}} + 1$). The Jacobian matrix can then be calculated as before,

$$A_{ij} = \frac{\partial y_i}{\partial x_{1j}}\,. \tag{7.12}$$

For a detailed explanation and analysis of lensing we refer the reader to Schneider et al. (1992).

Observationally weak lensing can be observed by looking at the slight correlation of orientation in large numbers of galaxies. The shear will cause galaxies to appear to be aligned. The convergence cannot be seen since it is a magnification which is impossible to measure without knowing the true size of the source. The

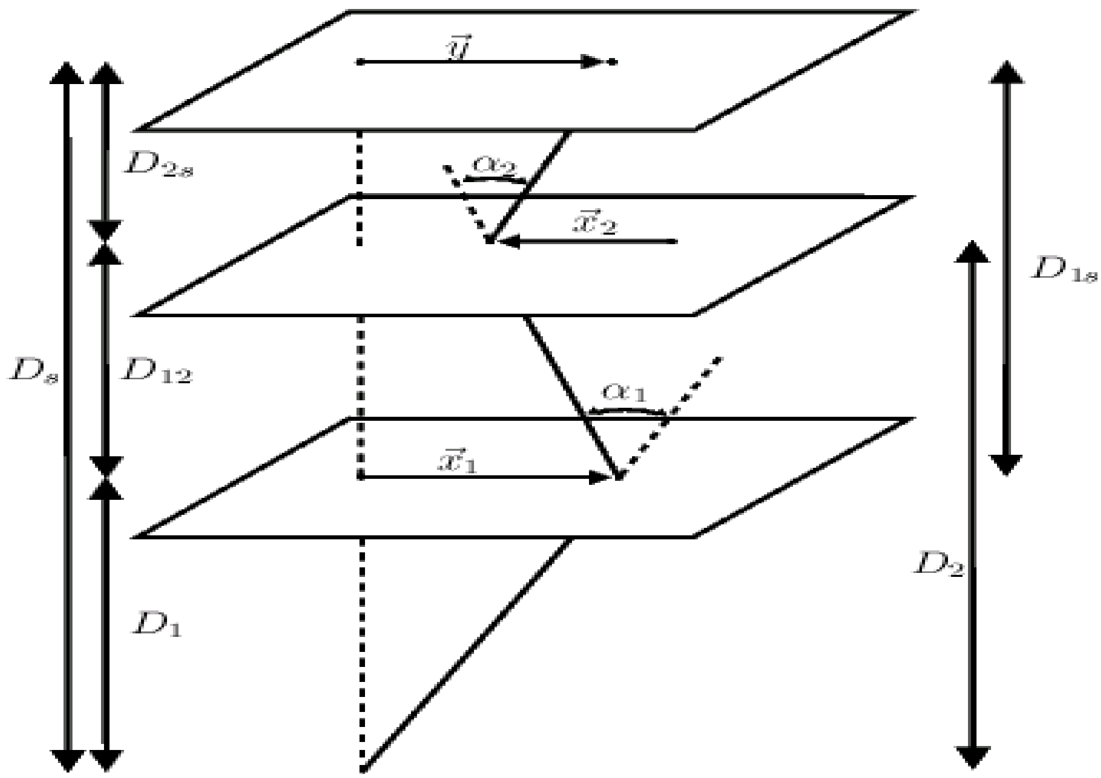

Figure 7.1 We show the geometry of lensing with multiple lens planes for two lenses. For each plane the deflection angle can be calculated as for a single lens, but the real position, r_s, will depend on all the angles and the distances between lenses.

two components of the shear correspond to a horizontal compression or elongation (γ_1) and a diagonal compression or elongation (γ_2) as shown in Figure 7.2. The convergence can be calculated from the shear with a method such as described in Kaiser & Squires (1993).

7.2.1 Normalization of Magnification

Gravitational lensing always magnifies a source relative to empty space, though the magnification is often given as the magnification relative to a homogeneous and isotropic universe with the same matter density as we observe. For a homogeneous and isotropic universe there is only a convergence; the shear will be zero ($\gamma = 0$). This can be seen from symmetry: the shear has a magnitude and direction, but isotropy means there can be no preferential direction for the shear, therefore it must be zero. For lensing in a homogeneous universe one need only calculate the convergence to find μ. The convergence is given by the integral of the density over the line-of-sight,

$$\begin{aligned} \kappa &= \int_0^{D_s} \frac{\rho(D_l) dD_l}{\Sigma_{\mathrm{crit}}(D_l)} \\ &= \int_0^{z} \frac{\rho(z)\frac{dD_l}{dz}}{\Sigma_{\mathrm{crit}}(z)} dz \,, \end{aligned} \tag{7.13}$$

and μ is then given by,

$$\mu = \frac{1}{(1-\kappa)^2} \,. \tag{7.14}$$

While we report magnifications without normalizing, it should be noted that some discussions of lensing report values normalized by this factor while others do not.

7.3 Correcting for Weak Lensing

We now make an estimate of the accuracy of a lensing correction using observed foreground galaxies. We use an analytic approximation for the number

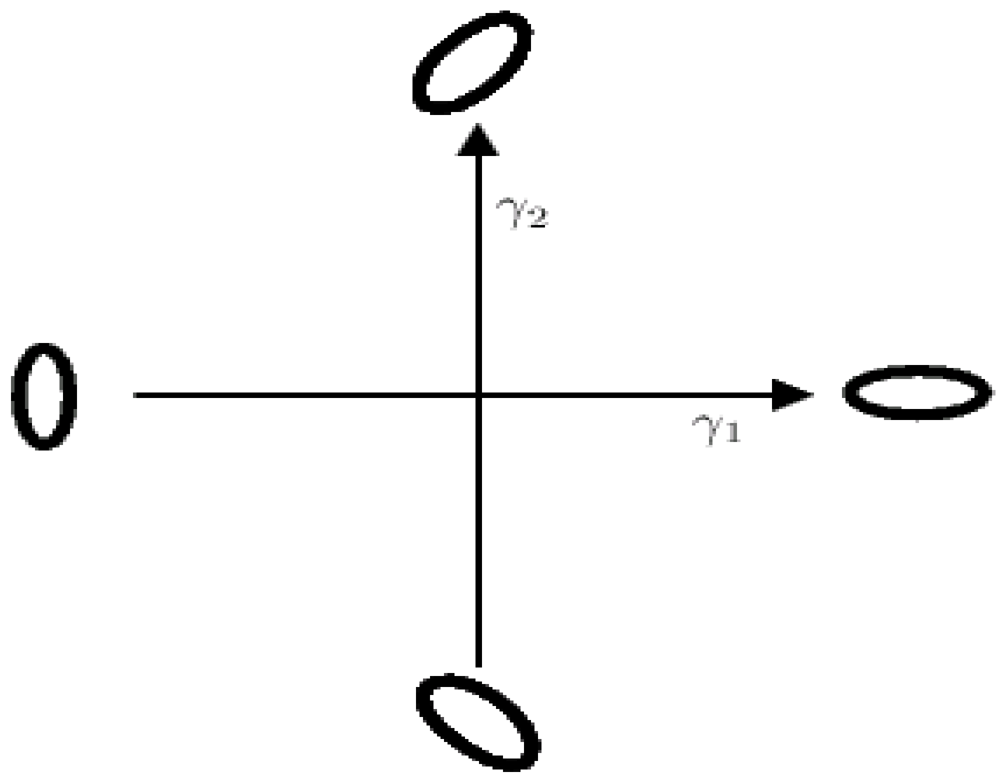

Figure 7.2 The shear is described by γ_1 and γ_2. A compression or elongation in the horizontal direction is described by γ_1 as shown. Similarly, a diagonal compression or elongation is described by γ_2 as shown.

density of galaxies and compare the difference between the lensing due to the galaxies that can be seen and the total lensing.

7.3.1 Halo Distributions

We use an extended form of the Press-Schecter (1974) mass function ($n(M,z)$) to calculate halo density. Press & Schecter calculated the mass function by assuming any spherical region of the universe with a density above a critical density (δ_c) would collapse. To go from mass to radius it is assumed that the universe is homogeneous:

$$R(M) = \left(\frac{3M}{4\pi\bar{\rho}}\right)^{1/3} , \tag{7.15}$$

where $\bar{\rho}$ is the average density of the universe at the present epoch ($z = 0$). The number of halos of mass M is then the number of spheres of radius $R(M)$ with a density greater than a critical density for collapse, δ_c. This can be calculated if a power spectrum is assumed.

Sheth & Tormen (1999) extended the Press-Schecter calculation to include elliptical collapse. We use the Sheth-Torman mass function as used in Mo & White (2002), specifically the number density of galaxies with mass in the range $(M, M + dM)$ is given by their equation (14):

$$n(M,z)dM = A\left(1 + \frac{1}{\nu'^{2q}}\right)\sqrt{\frac{2}{\pi}}\frac{\bar{\rho}}{M}\frac{d\nu'}{dM}\exp\left(-\frac{\nu'^2}{2}\right)dM\,. \tag{7.16}$$

The constants and equations for ν' can be found in Mo & White (2002) equations (6-8, 10, 11).

7.3.2 Observing Faint Galaxies

The deepest exposure to date is the Hubble Ultra Deep Field (UDF) (Beckwith, S. & HUDF Team, 2004) which was observed in filters B,V, i, and z. The limiting magnitudes were 28.7 in B, 29.0 in both V and i, and 28.4 in z.

We will assume a limiting magnitude of 29 in the K filter, from which a better measure of stellar mass can be made. While this may be slightly optimistic for current observing the time frame for any observations is so long (decades) that this a very reasonable assumption, in fact it is probably pessimistic. We use Figure 1 of Nagamine et al. (2005) to find a lower limit on the observable stellar mass limit and, for a limiting magnitude of 29, we find a lower limit on stellar mass of $\sim 10^8 M_\odot/h$ at a redshift of 2.0.

We believe this is a very conservative estimate of what we could practically observe in the time frame we are considering for two reasons. One reason is that by the time we can observe massive black hole binaries inspiraling there will most likely be a space telescope superior to HST. The other is that using months of space telescope time is fairly reasonable considering current plans for a dedicated SNe space telescope (SNAP).

7.4 How Accurately Can We Correct For Lensing?

We will now test how accurately we can correct for lensing and whether the lenses that are too small to observe will add too much dispersion for our proposed method to be useful. We assume the ratio of total halo mass to stellar mass is ~ 10 and we can observe any halo with $M \geq 10^9 M_\odot$.

First we populate 100 fields, each $10''$ square, with galaxies using the mass function described in §7.3.1. We populate the field with halos in the range $10^8 < M/M_\odot < 10^{16}$. This includes halos with masses down to a tenth of the lowest observable mass. The lower limit is necessary to keep computing time reasonable, but the upper limit does very little since the probability of finding one halo with $M > 10^{16} M_\odot$ in our 100 fields is about 1/10000. For each halo we generate a circular velocity and a radius as described by Mo & White (2002):

$$r_{200} = \left(\frac{GM}{100\Omega_m(z)H^2(z)} \right)^{1/3} , \tag{7.17}$$

$$V_c = \left(\frac{GM}{r_{200}} \right)^{1/2} . \tag{7.18}$$

The circular velocity is directly proportional to the velocity dispersion, $\sigma_v = V_c/\sqrt{2}$.

Once we have generated our 100 fields we calculate the lensing for nine positions in each field, separated by $2.5''$ to keep each value almost independent, generating a total of 900 values of the magnification. We use the same fields but remove galaxies to do this for six different mass ranges. We show the distribution of μ for three mass ranges in Figure 7.3 ($10^8 M_\odot < M < 10^9 M_\odot$, $10^9 M_\odot < M < 10^{10} M_\odot$, and $10^{10} M_\odot < M < 10^{11} M_\odot$) and for three ranges in Figure 7.4 ($M > 10^8 M_\odot$, $M > 10^9 M_\odot$, and $M > 10^{10} M_\odot$). While there are nonlinear effects Figure 7.3 should give an idea of the contribution from each group of lenses and Figure 7.4 shows the total magnification for all lenses more massive than a lower limit giving a better idea of the total lensing.

At first glance it seems that the low mass halos contribute the most to the magnification, but the range of their contribution is the narrowest so it may be possible to correct for them. Since the distribution is not Gaussian we characterize the width of the distribution by the width of the middle 50% of μ values. We find that the magnification due to low mass (unobservable) halos varies by 0.011, while the magnification due to mid mass range halos varies by 0.014, and the magnification from high mass halos varies by 0.020. If we look at the width of the μ distribution with all lenses we find a width of 0.065. For all halos with $M > 10^9 M_\odot$ and $M > 10^{10} M_\odot$ we find 0.057 and 0.042 respectively.

The small width of the μ distribution for the low mass, invisible halos implies that we should be able to see the most important lenses. The dispersion due to all lenses we could detect is 0.057, over five times the dispersion due to invisible

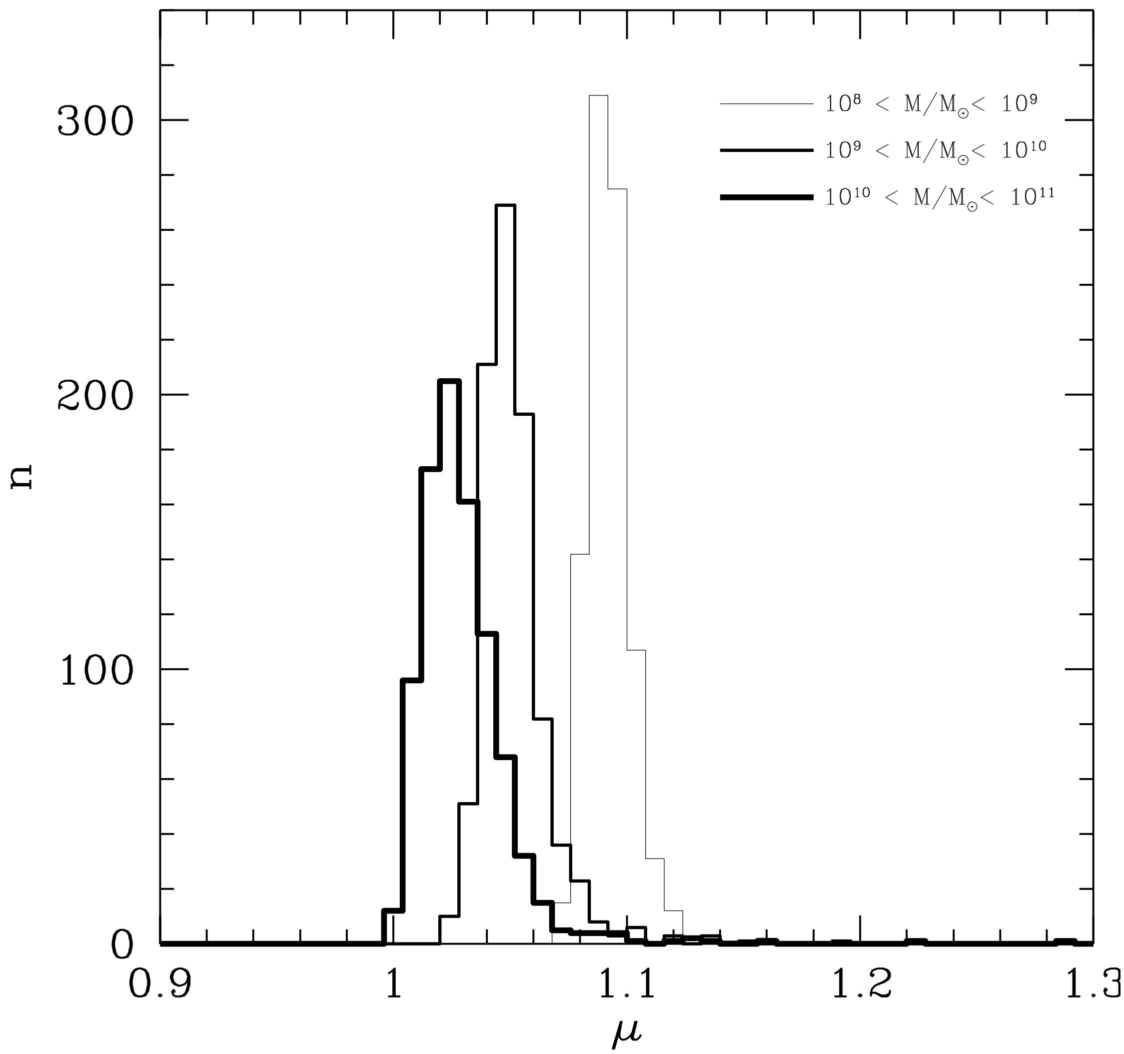

Figure 7.3: Distribution of μ for halos in different mass ranges.

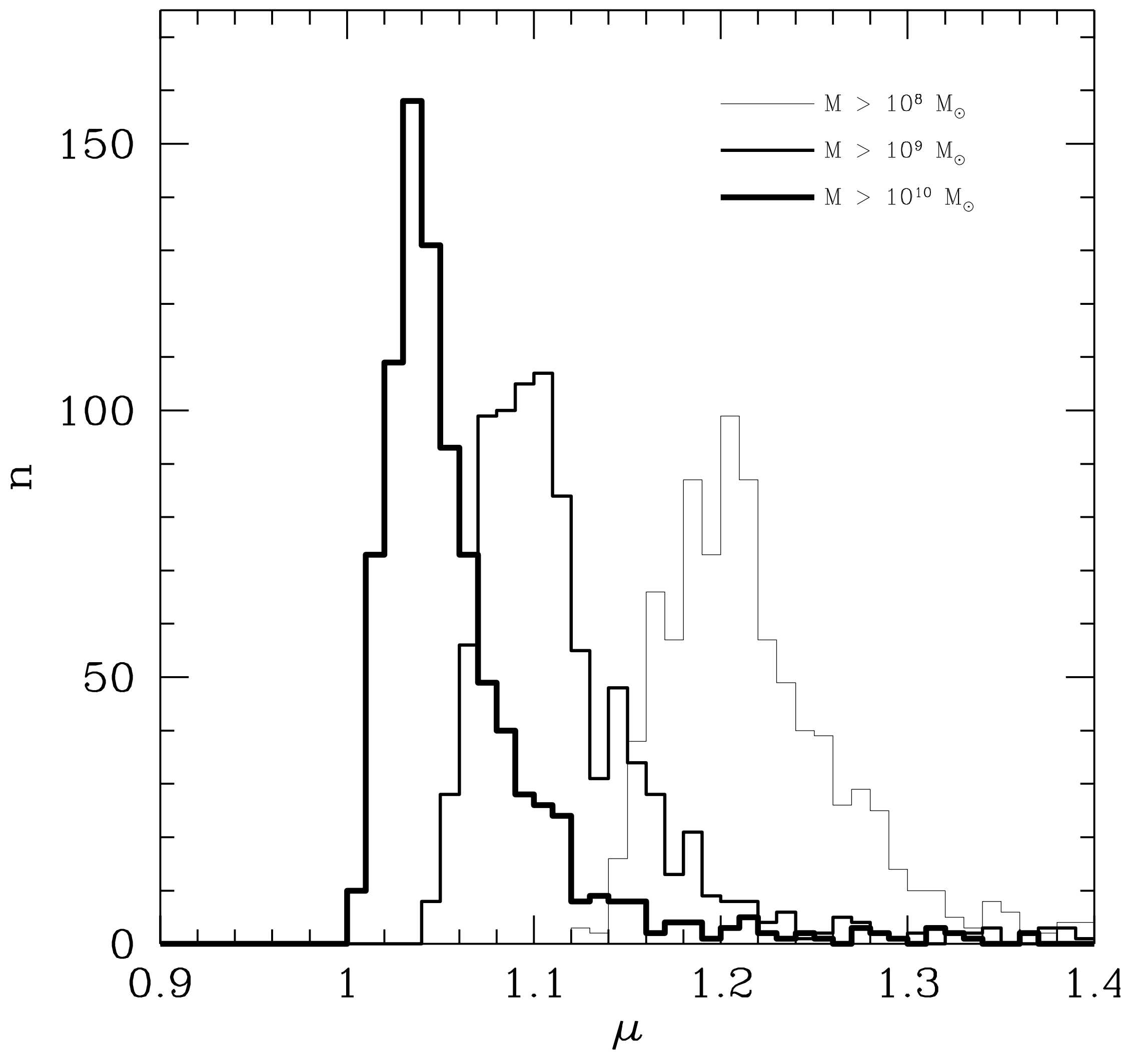

Figure 7.4: Distribution of μ with various lower mass limits.

lenses, 0.011. Another way to look at these results is via the total dispersion for all lenses (0.065) and the dispersion for all lenses except those too small to observe (0.057). This implies that 88% of the uncertainty from lensing is due to lenses we would be able to detect.

7.5 Conclusions and Future Work

We conclude that it may be possible to correct for lensing with a final uncertainty on μ of 1-2%, but there are many factors that need to be considered before any conclusive statement can be made. A number of effects and sources of error we have ignored will increase the uncertainty, but we have at least a decade before gravitational wave standard candles are observed in which to understand them. We need to consider halos with mass below $10^8 M_\odot$ which we expect to contribute significantly to μ but to add little dispersion. Galaxy clustering will also be very important as well as the mass distribution of each galaxy. Incorporating shear measurement may also improve the measured mass of foreground lenses. We discuss some of these factors below.

Galaxy correlations will reduce the number density in some regions and increase it in others. If we were to find a standard candle on a line-of-sight with few intervening halos it would be easier to correct for lensing. On the other hand, some lines-of-sight may contain large clusters making correction much more difficult. In these denser regions galaxies may obscure each other making it more difficult to correct for lensing. Even in less dense regions some lenses may be obscured.

The details of the mass distribution of the dark matter halos will change the magnification. There are several mass models for dark matter halos that are more accurate (and more complicated) than the SIS such as the NFW (Navarro et al., 1997) or Sersic models (both 2- and 3-dimensional) (Sersic, 1968). It is possible that these mass models, with faster falloff at large radii, may increase the precision of lensing correction by decreasing the importance of all but the galaxies closest to the line-of-sight. Other considerations for the halo model are the truncation radius and the accuracy of determining halo mass and other parameters which, in this analysis, we have assumed are known.

Another method of correcting for lensing is to measure the shear and calculate the convergence from it. It may be possible to use measurements of the shear to refine lens parameters and refine the value for the magnification.

We conclude that there is potential for correcting luminosities for weak lensing at the level of $\sim 1 - 2\%$ and work in this direction should be continued. While there are many hurdles to be cleared, the pay-off would be great and there is plenty of time for work to be done.

A

Tables

Table A.1: Event Parameters

field.tile.seq	α (2000)	δ (2000)	V	$V-R$	t_0	$\hat{t}$	A_{max}	$\frac{\chi^2}{n_{dof}}$	Gr.	Sel.	Notes
101.20650.1216[a]	18 04 20.25	−27 24 45.3	18.01	0.67	1971.8	10.3	2.19	1.09	A	cb	bin
101.20658.2639	18 04 22.39	−26 53 15.3	20.73	0.97	1204.7	22.3	7.66	0.84	A	c	
101.20908.1433	18 04 57.68	−27 33 18.4	18.57	0.82	1598.6	14.1	1.41	0.46	C	a	bin
101.20910.2922[b]	18 04 54.54	−27 25 50.0	19.43	0.74	2265.9	243	9.12	1.03	A	c	
101.20913.2158	18 04 56.18	−27 13 40.0	19.56	0.92	2484.9	57.0	4.91	0.88	B	a	
101.20914.3873	18 04 56.32	−27 10 41.3	20.06	0.94	2008.8	33.8	1.85	1.74	B	c	
101.21042.5059[c]	18 05 28.27	−27 16 21.3	20.14	0.84	2805.4	44.0	4.45	0.73	B	c	
101.21045.2528	18 05 12.63	−27 05 47.1	19.29	0.69	2426.3	19.2	4.82	0.80	B	ab	bin
101.21170.2699	18 05 48.16	−27 24 16.4	18.88	0.71	2807.3	11.4	4.22	0.79	B	a	
101.21171.4799	18 05 38.16	−27 23 07.8	20.20	1.00	1599.4	14.5	2.04	1.04	B	c	bin
101.21174.1990	18 05 39.23	−27 08 53.8	18.86	0.72	1356.7	9.67	2.72	1.12	B	e	
101.21174.2534[d]	18 05 38.71	−27 08 30.0	19.17	0.78	1909.2	15.3	1.83	0.75	B	e	
101.21176.5465	18 05 31.60	−27 03 11.5	21.12	0.75	2426.1	16.6	3.37	0.93	B	e	
101.21307.880	18 06 05.20	−26 59 38.3	20.32	0.86	537.8	53.4	8.10	0.86	A	c	
101.21428.2452	18 06 21.15	−27 33 57.8	19.07	0.75	2751.2	36.4	2.09	1.15	B	c	bin
101.21437.2090	18 06 20.53	−26 58 39.6	19.21	0.91	611.5	42.1	2.16	1.07	B	c	
101.21437.2192	18 06 23.82	−26 58 54.3	19.01	0.81	2384.7	30.8	1.91	1.44	A	c	
101.21558.2113	18 06 37.58	−27 35 40.1	19.00	0.74	553.9	12.6	56.1	1.23	A	c	
101.21561.5337	18 06 25.89	−27 22 47.7	20.39	0.76	2669.0	17.2	3.64	1.12	B	c	
101.21564.4657	18 06 28.73	−27 09 35.6	20.52	0.98	1230.2	17.2	7.66	1.02	A	c	
101.21689.2648	18 06 54.84	−27 29 21.8	19.27	0.84	2370.6	53.7	1.46	0.75	C	e	
101.21689.315[†]	18 06 58.30	−27 27 45.8	17.51	1.10	593.5	165	4.80	1.19	A	c	
101.21691.836	18 06 52.73	−27 23 18.9	17.28	0.70	1212.3	30.4	2.01	0.35	A	c	
101.21821.128	18 07 04.26	−27 22 06.3	16.24	1.37	1321.2	68.3	23.5	25.8	A	e	
101.21948.3692	18 07 23.42	−27 35 28.8	20.87	0.90	2408.0	17.2	3.78	0.79	B	e	
101.21949.2465	18 07 32.65	−27 31 35.6	19.92	0.86	579.9	34.4	6.00	1.40	A	c	
101.21950.1897	18 07 24.99	−27 24 40.5	19.27	0.78	1249.1	5.74	1.60	0.92	B	c	
101.21950.861	18 07 20.78	−27 24 09.7	18.48	0.90	1340.7	24.7	2.64	0.41	A	c	
102.22466.140[†]	18 08 47.04	−27 40 47.3	16.81	0.95	1275.6	153	3.88	0.95	A	c	

Continued on Next Page...

Table A.1

... Continued from Previous Page

field.tile.seq	α (2000)	δ (2000)	V	$V-R$	t_0	$\hat{t}$	A_{max}	$\frac{\chi^2}{n_{dof}}$	Gr.	Sel.	Notes
102.22598.2894	18 09 00.08	−27 35 38.9	19.72	0.84	2688.8	15.5	1.51	1.30	C	e	
102.22725.1408	18 09 13.53	−27 45 45.0	19.27	0.94	1916.9	121	1.81	0.57	B	c	
102.22851.2409	18 09 44.70	−28 00 58.6	19.64	0.96	2368.4	40.2	2.32	0.96	B	c	
102.22851.4872[e]	18 09 30.68	−28 00 48.8	20.21	0.74	1307.7	18.0	3.38	0.84	B	e	$R \neq B$
102.23112.1759	18 10 09.43	−27 56 45.7	19.41	0.76	1977.7	27.1	5.04	1.23	A	c	
102.23246.5046	18 10 34.52	−27 40 24.5	20.28	0.63	2715.1	9.21	3.62	1.09	B	e	
102.23370.476	18 10 50.72	−28 04 47.6	18.09	0.86	2010.1	25.4	1.70	1.07	A	c	bin
102.23379.2909	18 10 58.82	−27 31 01.6	19.71	0.80	1693.0	45.5	2.19	0.68	B	c	
102.23501.4570	18 11 03.79	−27 59 58.8	20.16	0.84	2684.2	55.7	1.93	1.44	C	a	bin
102.23503.2521	18 11 10.12	−27 54 34.3	19.64	0.85	454.3	74.3	5.40	0.76	A	c	
102.23503.4283	18 11 01.59	−27 53 59.0	19.82	0.80	2335.4	29.3	2.98	0.64	B	c	
102.23635.1426	18 11 32.49	−27 45 27.0	18.82	0.69	1282.9	62.6	4.16	1.04	A	c	
103.24024.1785	18 12 26.00	−27 48 37.8	19.04	0.70	2318.9	98.0	1.34	0.83	B	e	
103.24030.3425	18 12 14.65	−27 25 39.0	19.57	0.70	2004.5	16.1	3.78	1.12	A	c	
103.24161.2085	18 12 45.87	−27 20 04.4	19.15	0.69	2730.5	50.0	3.43	0.99	A	c	
103.24286.768	18 12 49.71	−27 41 42.6	18.19	0.82	2064.0	77.0	1.36	2.38	B	e	
103.24544.794	18 13 27.58	−27 49 11.6	19.80	0.81	2065.0	58.4	1.70	0.89	B	a	
104.19990.4674	18 03 00.48	−28 04 45.7	18.30	0.78	1175.2	53.9	1.63	1.25	C	e	
104.19992.858[†]	18 02 53.82	−27 57 50.0	18.60	1.08	1169.7	106	2.23	2.15	A	c	
104.20119.6312[f†]	18 03 20.75	−28 08 14.5	18.02	1.09	1975.3	38.7	1.62	1.62	A	c	
104.20121.1692	18 03 15.25	−28 00 14.1	18.62	0.89	1986.1	166	2.54	0.97	A	c	
104.20121.2255	18 03 09.05	−28 01 45.3	19.34	1.01	480.5	34.6	3.62	0.42	A	c	
104.20251.1117[†]	18 03 29.02	−28 00 31.0	18.23	0.98	463.2	45.5	2.09	0.93	A	c	
104.20251.50[†]	18 03 34.05	−28 00 18.9	17.34	0.93	493.9	287	10.1	1.75	A	c	
104.20259.572[†]	18 03 33.39	−27 27 47.3	18.17	1.20	538.5	14.2	1.58	1.56	A	c	
104.20382.803[†]	18 03 53.19	−27 57 35.7	17.80	0.96	1765.8	254	5.72	4.40	A	c	
104.20387.2071	18 03 51.43	−27 37 40.2	19.04	0.72	2093.4	12.8	1.64	1.79	A	e	
104.20388.2766	18 03 53.97	−27 33 30.5	19.83	1.01	1691.5	75.5	7.70	0.6	A	c	bin
104.20514.1500	18 04 06.08	−27 48 26.3	18.95	1.09	1993.0	2.58	15.1	1.03	C	a	

Continued on Next Page...

Table A.1

. . . Continued from Previous Page

field.tile.seq	α (2000)	δ (2000)	V	$V-R$	t_0	$\hat{t}$	A_{max}	$\frac{\chi^2}{n_{dof}}$	Gr.	Sel.	Notes
104.20515.498[†]	18 04 09.66	−27 44 35.1	17.66	1.00	2061.7	53.6	1.76	1.42	A	c	
104.20640.8423[g†]	18 04 33.65	−28 07 31.9	17.16	0.97	2374.9	30.8	1.65	2.23	A	c	
104.20645.3129[†]	18 04 26.17	−27 47 35.1	17.69	1.07	1558.3	152	1.82	0.77	A	c	
104.20775.2644	18 04 50.73	−27 45 57.3	20.02	0.92	1899.9	46.3	5.42	0.92	A	c	
104.20779.9616	18 04 54.08	−27 30 07.0	20.03	0.94	2678.6	37.4	1.74	0.94	B	e	
104.20904.3155	18 05 07.31	−27 51 11.4	19.95	0.97	1310.4	33.5	2.41	0.94	A	c	
104.20906.3973	18 05 02.50	−27 42 17.2	19.93	0.83	1738.6	654	2.05	1.85	B	a	bin
104.20910.7700[b]	18 04 54.54	−27 25 49.8	19.34	0.85	2266.2	211	8.64	0.93	A	c	
104.21032.4118	18 05 15.42	−27 58 25.0	19.87	0.73	1620.1	29.3	2.50	0.92	A	c	
104.21161.1997[h]	18 05 34.45	−28 02 51.8	18.66	0.81	1301.7	37.5	7.66	1.02	A	c	
104.21162.3642[i]	18 05 47.75	−27 56 32.2	19.70	0.87	1694.6	71.6	1.76	1.59	C	c	
104.21164.4093[j]	18 05 41.42	−27 51 03.1	20.07	0.97	1601.8	33.8	1.77	0.71	B	e	
104.21293.1164[k]	18 06 03.99	−27 55 05.0	17.83	0.71	1294.0	37.2	1.61	0.63	B	c	bin
104.21421.131[ae]	18 06 08.65	−28 00 22.4	17.78	0.85	2640.8	7.54	2.61	20	A	c	
104.21423.530[l]	18 06 09.10	−27 53 38.7	19.77	0.78	1634.1	37.3	1.77	1.49	B	c	
105.21161.7671[h]	18 05 34.44	−28 02 51.2	18.79	0.76	1301.7	39.2	8.16	0.94	A	c	
105.21162.7174[i]	18 05 47.79	−27 56 32.6	19.77	0.86	1695.7	61.2	1.72	2.04	B	c	
105.21164.9983[j]	18 05 41.46	−27 51 03.3	20.14	0.85	1601.2	37.2	1.83	0.82	B	c	
105.21287.3893	18 05 49.89	−28 17 19.5	20.25	0.99	2082.9	21.6	2.79	0.97	C	e	
105.21293.6550[k]	18 06 04.01	−27 55 04.9	17.90	0.71	1295.7	28.3	1.71	0.63	B	c	
105.21417.101	18 06 11.95	−28 16 52.8	16.22	1.08	1540.7	108	1.91	16.6	A	ab	bin
105.21422.1228	18 06 20.41	−27 56 13.4	17.94	0.88	2256.9	75.2	2.80	2.93	A	e	
105.21423.5762[l]	18 06 09.11	−27 53 38.6	19.90	0.79	1636.8	40.2	1.84	0.75	B	c	
105.21425.3499	18 06 08.51	−27 46 13.2	19.11	0.91	1361.5	24.8	2.77	0.95	B	e	
105.21681.2244	18 06 53.94	−28 01 16.5	19.36	0.75	2665.4	9.31	1.54	0.85	C	e	$R \neq B$
105.21807.4900	18 07 18.17	−28 17 38.4	20.94	1.11	2013.9	9.27	3.83	0.80	B	e	
105.21813.2516[†]	18 07 07.07	−27 52 34.3	17.41	1.08	1928.5	17.5	13.2	1.14	A	c	
105.22075.1451	18 07 43.89	−27 44 22.0	18.91	0.87	1220.2	17.4	1.61	0.59	B	c	
105.22200.1712	18 07 59.87	−28 05 24.6	19.24	0.86	2272.4	22.9	2.03	1.25	B	e	

Continued on Next Page. . .

Table A.1

...Continued from Previous Page

field.tile.seq	α (2000)	δ (2000)	V	$V-R$	t_0	$\hat{t}$	A_{max}	$\frac{\chi^2}{n_{dof}}$	Gr.	Sel.	Notes
105.22206.366	18 08 00.21	−27 40 52.8	19.53	1.54	1654.3	49.6	2.08	1.52	B	e	
105.22327.3556	18 08 17.90	−28 16 16.6	19.60	0.68	1620.5	22.6	2.30	0.90	A	c	
105.22329.1480	18 08 28.56	−28 11 20.7	19.67	0.62	539.8	126	8.07	5.59	A	c	bin
105.22332.2555	18 08 25.19	−27 58 38.2	19.25	1.15	1210.1	137	1.84	0.75	A	c	
105.22459.1549	18 08 46.10	−28 10 08.6	19.42	1.02	2116.3	20.9	2.35	1.15	B	c	
105.22462.5692	18 08 42.71	−27 59 39.6	19.84	0.89	535.5	140	3.12	0.59	C	e	bin
108.18558.329	17 59 41.85	−28 12 10.3	19.50	0.98	1362.2	83.7	2.11	2.16	A	c	
108.18559.526	17 59 42.21	−28 08 41.5	20.13	1.01	1279.1	23.7	2.94	1.35	B	c	
108.18685.3171	18 00 01.28	−28 27 41.2	19.90	1.16	580.6	42.8	2.88	0.66	A	c	
108.18686.3423	17 59 56.61	−28 23 01.9	19.84	0.95	2667.8	23.4	2.53	0.6	A	c	
108.18689.1979	17 59 49.63	−28 10 56.4	19.05	1.00	976.3	20.5	3.60	2.05	A	c	var
108.18943.3744^m	18 00 21.61	−28 32 01.2	19.23	0.84	2270.7	50.2	3.12	0.68	B	c	
108.18947.3618†	18 00 29.14	−28 19 20.3	17.73	1.10	1287.9	45.6	2.05	0.94	A	c	
108.18951.1221†	18 00 25.87	−28 02 35.2	18.93	1.19	583.6	45.8	2.16	0.92	A	c	
108.18951.593†	18 00 33.78	−28 01 10.5	18.08	1.18	1991.6	47.3	4.05	7.02	A	cb	bin
108.18952.941†	18 00 36.05	−27 58 30.0	18.92	1.17	1324.9	66.9	2.39	1.11	A	c	
108.19073.2291	18 00 39.56	−28 34 43.8	...	...	1975.1	57.6	1.41	0.42	B	b	bin
108.19074.550†	18 00 52.24	−28 29 52.0	17.55	1.03	2050.6	9.26	1.78	0.97	A	c	
108.19082.1466	18 00 39.34	−27 58 34.9	19.25	1.02	1681.4	48.4	1.76	0.40	B	e	
108.19082.3434	18 00 49.97	−27 58 45.1	20.54	1.02	2033.6	43.9	1.75	0.72	B	a	
108.19204.267	18 01 07.72	−28 31 41.4	16.74	1.04	2678.5	39.9	2.28	0.81	A	c	
108.19204.2857	18 01 10.52	−28 31 22.2	19.39	0.89	533.2	44.9	1.63	1.23	C	e	
108.19211.3382	18 01 13.75	−28 01 24.7	19.85	0.83	1359.4	17.8	3.95	0.49	B	e	
108.19212.869	18 01 09.01	−27 57 58.8	18.38	0.85	1636.9	80.3	6.94	0.83	A	c	
108.19333.1878	18 01 21.18	−28 32 39.4	17.33	0.98	1937.0	73.3	1.82	3.28	A	b	bin
108.19333.4264	18 01 30.83	−28 32 17.0	19.81	1.09	2012.1	7.99	1.61	0.70	B	c	
108.19334.1583†	18 01 26.31	−28 31 14.0	17.68	0.96	1231.4	18.5	4.09	0.38	A	c	
108.19337.417	18 01 24.41	−28 17 32.9	18.57	0.99	2769.5	83.3	1.51	0.92	A	c	
108.19341.1936^n	18 01 28.55	−28 02 13.9	19.92	1.02	2356.0	61.4	7.08	0.68	A	c	

Continued on Next Page...

Table A.1

...Continued from Previous Page

field.tile.seq	α (2000)	δ (2000)	V	$V-R$	t_0	$\hat{t}$	A_{max}	$\frac{\chi^2}{n_{dof}}$	Gr.	Sel.	Notes
108.19464.254	18 01 33.95	−28 28 02.2	16.98	1.30	2086.7	58.1	1.70	10	A	c	
108.19464.5201	18 01 38.88	−28 30 03.4	20.45	0.73	1974.5	36.2	3.21	0.54	A	c	
108.19466.2869	18 01 47.14	−28 21 25.8	19.30	0.91	1306.6	21.8	1.40	0.83	C	e	
108.19595.2757	18 02 09.89	−28 26 03.8	19.27	0.86	572.8	22.7	18.0	0.65	A	c	
108.19599.1605	18 01 57.09	−28 08 05.3	19.12	1.17	1347.1	68.8	8.46	1.12	A	c	
108.19602.2404	18 01 59.16	−27 56 32.9	19.61	1.00	2757.1	49.0	1.55	1.30	C	a	
108.19602.415	18 01 59.72	−27 57 21.6	18.82	2.25	1909.5	92.5	4.32	12.3	B	e	var
108.19853.8058[o]	18 02 29.01	−28 33 12.0	19.15	0.88	2289.4	35.4	2.01	0.64	A	c	
108.19985.8020	18 02 46.97	−28 25 39.3	20.17	0.86	1661.4	28.1	1.82	1.36	C	e	
109.19720.3549	18 02 21.89	−28 47 02.4	19.67	1.05	1736.0	9.36	3.40	1.17	B	a	
109.19850.956	18 02 29.06	−28 45 39.0	17.83	0.98	1279.6	60.4	1.42	0.80	A	e	
109.19853.2074[o]	18 02 29.02	−28 33 12.1	19.13	0.95	2288.8	37.3	1.97	0.64	A	c	
109.19853.4889	18 02 44.36	−28 33 08.9	20.13	0.77	2633.6	14.1	2.45	0.70	B	e	
109.19858.3675	18 02 31.34	−28 12 20.6	19.50	0.85	2297.6	17.5	1.59	1.14	C	e	
109.19986.2444[p]	18 03 01.11	−28 21 08.6	19.07	0.77	1258.4	43.8	1.80	0.56	B	c	
109.19987.2565	18 02 55.86	−28 16 55.9	18.94	0.83	1947.6	9.90	2.31	1.63	A	c	
109.20118.5042	18 03 15.48	−28 15 23.7	20.20	0.90	2231.5	47.9	14.7	1.38	C	a	
109.20119.1051[f†]	18 03 20.74	−28 08 14.5	18.11	0.97	1977.6	28.7	1.62	1.01	A	c	
109.20246.4248	18 03 24.69	−28 20 22.4	19.86	0.90	1304.6	58.6	2.08	0.87	A	c	
109.20370.5166[q]	18 03 58.75	−28 47 38.0	20.79	0.96	2787.6	22.0	5.87	0.94	A	c	
109.20379.2012	18 03 59.42	−28 10 35.5	20.57	0.83	1262.0	85.9	2.21	0.69	A	c	
109.20635.2121	18 04 18.66	−28 25 43.1	19.57	0.76	2544.5	707	1.77	2.12	C	c	
109.20635.2193	18 04 34.45	−28 25 33.5	19.53	0.77	1359.1	38.5	1.84	0.63	A	c	
109.20640.360[g†]	18 04 33.66	−28 07 32.5	17.33	1.05	2375.1	28.7	1.67	0.72	A	c	
109.20893.3423	18 05 05.28	−28 34 41.7	19.78	0.75	2742.0	265	6.07	1.73	B	c	$R \neq B$
109.21024.5007	18 05 18.03	−28 28 52.9	20.36	0.78	1321.2	116	5.24	1.16	A	c	
110.22194.461	18 08 07.32	−28 31 23.4	18.05	0.78	484.7	11.7	1.84	1.08	A	c	
110.22454.1042	18 08 48.95	−28 31 07.7	18.45	0.81	2624.5	62.5	1.38	1.67	B	e	
110.22455.842[†]	18 08 51.27	−28 27 11.2	18.28	0.98	1900.1	19.8	2.54	0.84	A	c	

Continued on Next Page...

Table A.1

. . . Continued from Previous Page

field.tile.seq	α (2000)	δ (2000)	V	$V-R$	t_0	$\hat{t}$	A_{max}	$\frac{\chi^2}{n_{dof}}$	Gr.	Sel.	Notes
110.22585.1719	18 08 55.39	−28 24 57.7	19.32	0.75	1209.2	52.2	1.87	1.42	A	c	
110.22707.1502	18 09 22.31	−28 57 57.1	18.90	0.74	593.1	9.19	1.53	0.97	B	c	
110.22840.2227	18 09 38.97	−28 46 32.1	18.84	0.71	1263.0	9.25	2.15	0.90	C	e	
110.22844.4168	18 09 32.46	−28 30 06.3	21.94	0.82	506.5	37.4	4.55	0.50	B	c	
110.22969.4258	18 10 01.14	−28 48 44.4	20.14	0.72	2250.8	22.9	3.52	0.84	B	c	
110.22970.4137	18 10 00.26	−28 45 42.0	19.96	0.53	2429.7	19.0	3.00	0.98	B	c	$R \neq B$
110.22970.449	18 09 55.98	−28 44 10.8	19.39	0.87	470.3	10.2	2.32	0.99	A	c	
110.23098.4042	18 10 04.86	−28 54 18.4	20.12	0.79	543.7	30.0	2.57	0.65	B	c	
110.23356.3958	18 10 50.13	−29 00 59.6	19.94	0.81	1163.8	122	1.77	0.70	B	e	
111.23746.772	18 11 51.54	−29 00 34.5	18.02	0.76	2303.0	21.6	1.92	1.50	A	c	
111.23873.4918	18 11 54.95	−29 14 09.0	20.70	0.81	1666.7	23.7	541	1.12	C	e	
111.23881.726	18 11 57.13	−28 40 21.2	18.15	0.87	2331.8	27.7	1.52	0.69	C	a	
111.24655.3092	18 13 52.83	−29 06 02.6	19.52	0.62	1995.8	14.9	2.94	1.05	A	c	
111.24784.884	18 14 06.30	−29 08 56.1	18.26	0.73	1604.4	21.2	1.38	0.63	C	e	bin
113.18156.1823	17 58 43.18	−29 00 28.9	19.55	0.95	1649.0	15.6	2.86	1.13	B	e	
113.18283.3925	17 59 06.16	−29 12 07.3	19.37	0.83	2481.5	23.6	1.41e+9	0.62	B	a	
113.18290.3513	17 58 59.05	−28 44 46.4	19.27	0.65	798.5	27.3	1.86	1.22	C	e	
113.18292.2374	17 59 00.59	−28 36 57.5	19.17	1.04	1193.5	46.1	9.11	0.49	A	c	
113.18414.1512	17 59 14.99	−29 08 12.9	18.06	0.79	910.3	24.0	3.04	1.65	A	c	
113.18414.4153	17 59 16.09	−29 10 35.0	19.39	0.85	636.4	11.7	3.51	0.79	A	c	
113.18415.5194	17 59 19.59	−29 06 07.1	20.32	1.18	1692.7	25.8	2.59	0.84	C	a	
113.18422.3531	17 59 16.72	−28 39 16.7	19.47	0.83	820.0	26.0	1.72	0.90	C	e	
113.18550.1664	17 59 40.61	−28 47 24.5	18.44	0.95	1650.2	36.9	1.81	0.35	A	c	
113.18550.3650	17 59 29.86	−28 43 54.8	19.32	0.72	887.9	6.84	1.75	0.70	B	e	
113.18550.4183	17 59 39.96	−28 43 46.8	21.02	1.82	797.8	42.1	1.67	1.09	C	e	
113.18552.581†	17 59 35.90	−28 36 24.3	17.60	1.02	603.7	27.9	1.77	1.11	B	c	
113.18674.756	17 59 53.40	−29 09 07.8	17.42	0.94	1879.0	114	5.82e+7	3.23	A	b	bin
113.18676.4164	18 00 01.33	−29 02 04.8	19.40	0.82	554.5	13.9	1.57	1.33	C	e	$R \neq B$
113.18680.3511	18 00 01.98	−28 45 17.8	19.36	0.80	1613.8	23.5	3.20	1.18	A	c	

Continued on Next Page. . .

Table A.1

. . . Continued from Previous Page

field.tile.seq	α (2000)	δ (2000)	V	$V-R$	t_0	$\hat{t}$	A_{max}	$\frac{\chi^2}{n_{dof}}$	Gr.	Sel.	Notes
113.18681.4992	17 59 50.67	−28 42 33.1	20.21	0.96	2330.8	20.4	11.6	0.82	B	c	
113.18804.1061[†]	18 00 03.38	−29 11 04.2	18.30	1.02	1166.6	6.53	1.62	0.96	B	c	
113.18807.1433	18 00 13.15	−28 56 16.8	19.77	0.80	1574.8	26.2	1.89	0.64	B	e	
113.18809.3408	18 00 02.91	−28 51 02.3	19.77	0.90	564.5	16.1	3.71	0.64	A	c	
113.18810.2999[r]	18 00 06.81	−28 44 00.0	19.33	0.78	2334.2	14.8	2.27	0.52	B	c	
113.18810.4076	18 00 14.08	−28 44 54.5	19.92	0.83	1756.9	34.2	3.44	10	B	e	
113.18812.4511	18 00 03.62	−28 39 14.1	21.02	0.95	1277.6	17.3	3.04	0.88	B	c	
113.18932.2003	18 00 37.45	−29 17 22.5	19.55	0.96	1642.8	11.1	1.59	0.74	B	e	
113.18934.4131	18 00 28.84	−29 09 34.9	19.82	0.82	1183.0	6.31	4.61	0.39	A	c	
113.18940.2606	18 00 37.60	−28 45 22.1	19.16	0.75	861.8	9.73	1.58	0.73	B	e	
113.19064.1665	18 00 44.21	−29 10 32.8	18.95	1.04	949.5	28.7	1.63	0.96	A	c	
113.19066.2168	18 00 54.05	−29 01 08.7	18.96	0.96	533.2	10.4	1.80	1.13	B	e	
113.19192.365[†]	18 01 06.92	−29 18 53.8	17.80	1.17	2092.6	36.9	1.97	0.52	B	c	
113.19196.3672	18 01 15.02	−29 01 48.4	19.77	0.89	2049.2	10.2	7.94	0.84	A	c	
113.19325.2001	18 01 18.14	−29 05 49.4	19.07	0.90	2285.2	37.7	9.48	0.24	A	c	
114.19583.5176	18 01 59.13	−29 12 41.4	19.58	0.84	2019.6	39.2	8.94	1.87	A	c	
114.19587.3861	18 02 00.22	−28 57 27.4	19.67	0.90	2306.8	21.8	6.07	1.11	A	c	
114.19589.4067	18 02 06.33	−28 50 45.3	18.66	0.83	1371.9	19.1	1.97	0.96	A	c	
114.19589.4149	18 01 58.45	−28 50 07.5	18.65	0.79	2020.2	20.0	1.72	1.24	A	c	
114.19712.1763	18 02 17.96	−29 18 11.3	19.15	0.92	2660.8	9.78	1.40	0.62	B	e	
114.19712.813[†]	18 02 11.41	−29 19 20.8	18.13	1.09	1643.4	23.7	3.58	0.62	A	c	
114.19846.777[†]	18 02 36.82	−29 01 42.1	18.00	1.02	545.4	65.0	1.55	1.86	A	c	
114.19970.843[†]	18 02 54.45	−29 26 29.5	17.99	0.96	1281.9	14.7	4.47	0.65	A	c	
114.20104.617	18 03 16.02	−29 08 20.3	19.12	0.82	2220.4	81.3	1.01e+6	0.75	C	a	
114.20235.908	18 03 39.60	−29 05 38.6	20.12	0.89	2057.6	47.4	1.89	1.11	A	c	
114.20360.1661	18 03 44.17	−29 26 16.9	18.76	0.90	1895.9	25.1	2.63	0.98	A	c	
114.20370.6070[q]	18 03 58.80	−28 47 38.6	20.47	0.80	2788.0	28.2	6.25	1.59	A	c	
114.20489.3552	18 04 10.63	−29 28 57.8	20.01	0.86	2653.8	6.74	1.85	1.2	B	e	
114.20491.1613	18 04 02.25	−29 21 09.8	18.61	0.69	558.4	19.9	3.83	0.91	A	c	

Continued on Next Page. . .

Table A.1

...Continued from Previous Page

field.tile.seq	α (2000)	δ (2000)	V	$V-R$	t_0	$\hat{t}$	A_{max}	$\frac{\chi^2}{n_{dof}}$	Gr.	Sel.	Notes
114.20494.3907	18 04 04.91	−29 11 37.9	19.98	0.66	1938.8	23.8	3.99	1.02	A	c	
114.20496.5206	18 04 09.01	−29 03 11.3	20.06	0.84	1748.4	107	15.8	0.68	A	c	
114.20621.2010	18 04 29.17	−29 22 22.9	18.83	0.73	2037.6	14.6	2.23	1.11	B	c	
114.20750.2236	18 04 51.50	−29 24 42.3	19.42	0.80	1183.0	5.15	3.01	0.68	B	c	
114.20751.4978	18 04 51.82	−29 22 40.3	20.06	0.87	1602.8	8.07	3.46	0.77	A	c	
115.22181.2973	18 08 01.71	−29 21 01.7	19.77	0.82	2719.8	10.4	1.90	0.77	C	e	$R \neq B$
115.22435.1045	18 08 46.35	−29 44 13.8	18.64	0.78	2722.0	32.6	1.60	1.30	A	c	
115.22442.1010	18 08 38.61	−29 17 23.6	18.52	0.77	2703.3	13.2	2.59	1.30	A	c	
115.22564.2355	18 09 00.22	−29 48 38.2	19.15	0.62	2428.8	9.68	1.64	1.29	C	e	$R \neq B$
115.22565.2060	18 09 02.87	−29 44 12.7	19.19	0.68	463.4	28.0	2.38	20	B	c	$R \neq B$
115.22698.3919	18 09 18.89	−29 32 58.8	19.89	0.44	1975.5	8.90	1.94	1.85	C	e	
115.22701.743	18 09 15.79	−29 19 49.1	18.16	0.77	1617.7	19.0	4.26	0.74	A	c	
115.22959.667	18 10 04.14	−29 31 03.5	17.85	0.76	1573.2	91.9	1.41	0.82	B	e	
116.23740.1193	18 11 40.72	−29 27 19.6	18.94	0.83	1636.0	16.2	7.96	0.31	A	c	
116.23864.503	18 12 07.28	−29 47 54.5	17.88	0.84	1971.2	41.3	2.57	1.42	A	c	
116.24255.4464	18 12 57.37	−29 45 11.0	20.10	0.61	2355.0	18.5	5.15	0.62	A	c	
116.24384.2597	18 13 14.33	−29 50 33.6	19.50	0.63	2401.1	28.3	1.93	0.89	B	c	
118.18009.35	17 58 25.53	−30 08 08.6	17.60	1.57	2808.6	55.5	2.58	3.98	A	e	$R \neq B$ var
118.18012.1863	17 58 14.82	−29 56 13.2	18.73	0.77	1969.3	29.8	1.64	0.66	B	c	
118.18014.320†	17 58 25.30	−29 47 59.5	17.02	0.98	877.6	25.5	1.58	1.05	A	c	
118.18014.4514	17 58 29.84	−29 50 02.0	20.20	1.03	2794.5	42.7	1.68	1.15	C	e	
118.18015.1406	17 58 25.94	−29 44 47.7	18.75	1.03	878.0	9.78	1.41	0.69	B	e	
118.18018.2379	17 58 16.01	−29 32 10.9	19.09	0.84	1245.4	84.6	2.69	0.39	A	c	
118.18141.731†	17 58 36.77	−30 02 19.3	17.93	1.07	884.1	9.77	12.6	0.65	B	cb	bin
118.18270.3615^{s}	17 59 04.77	−30 07 06.0	20.46	1.13	1893.4	9.91	2.52	0.87	B	c	
118.18271.738†	17 58 52.46	−30 02 08.0	18.30	1.20	456.4	53.7	2.23	0.69	A	c	
118.18276.129	17 59 03.29	−29 42 59.8	17.16	0.53	530.7	14.5	4.06	0.88	A	c	
118.18278.3065	17 58 55.62	−29 34 24.7	20.21	0.88	594.5	21.1	1.79	1.28	A	c	
118.18402.495†	17 59 13.85	−29 55 53.4	17.65	1.11	454.1	23.8	3.60	0.96	A	c	

Continued on Next Page...

Table A.1

...Continued from Previous Page

field.tile.seq	α (2000)	δ (2000)	V	$V-R$	t_0	$\hat{t}$	A_{max}	$\frac{\chi^2}{n_{dof}}$	Gr.	Sel.	Notes
118.18407.1167	17 59 16.32	−29 38 04.1	18.61	1.12	891.3	3.19	1.60	0.73	B	e	$R \neq B$
118.18529.538	17 59 35.34	−30 08 47.7	19.58	1.05	1952.0	97.4	17.0	1.44	A	c	
118.18531.1816	17 59 37.69	−30 00 52.7	19.27	0.85	1561.5	57.2	1.34	1.26	B	e	
118.18536.3276	17 59 34.61	−29 39 48.4	19.93	0.83	1060.5	142	2.93	0.66	C	c	
118.18660.3016	17 59 45.20	−30 05 18.6	19.88	0.96	1169.0	8.76	2.56	1.45	C	e	
118.18662.1151^t	17 59 46.51	−29 57 28.3	18.40	0.85	2622.7	15.1	3.18	0.76	A	c	
118.18662.2180	17 59 56.33	−29 56 38.0	19.65	1.00	1944.5	26.4	1.76	0.90	A	c	
118.18662.3919	17 59 57.17	−29 58 58.0	20.53	0.82	980.0	15.8	1.94	0.81	B	e	$R \neq B$
118.18668.3942	18 00 00.81	−29 32 40.0	20.51	1.04	954.5	12.4	2.04	1.52	B	e	
118.18669.3968	17 59 52.03	−29 31 14.4	20.71	1.04	1972.7	15.3	2.17	0.87	B	e	
118.18797.1397†	18 00 06.94	−29 38 06.0	19.37	1.33	2013.1	126	8.35	1.07	A	c	
118.19182.891†	18 01 09.75	−29 56 18.9	17.98	0.93	2367.0	13.6	6.28	1.2	A	c	
118.19184.1814	18 01 02.88	−29 48 40.2	18.70	0.73	2441.7	11.7	7.46	0.82	A	c	
118.19184.3770	18 00 58.13	−29 49 50.6	20.05	0.88	1601.1	12.2	3.75	0.89	A	c	
118.19184.939†	18 01 10.23	−29 48 55.4	18.08	0.99	2692.8	74.4	2.14	1.13	A	c	
118.19311.1429	18 01 20.85	−30 00 08.6	20.49	1.06	599.7	6.81	2.11	1.05	B	e	
119.19441.2773	18 01 38.41	−30 02 02.6	19.58	0.71	1896.1	21.7	2.34	1.23	C	e	$R \neq B$
119.19442.370	18 01 51.03	−29 56 50.3	18.26	0.95	2776.0	49.7	1.31	10	A	a	
119.19444.2055	18 01 45.53	−29 49 46.9	19.24	0.79	1543.8	51.4	20.3	2.49	A	ab	bin
119.19568.3510	18 01 54.13	−30 12 17.4	19.75	0.79	2625.6	9.77	2.01	1.26	B	c	
119.19576.2024	18 02 04.77	−29 43 15.9	18.80	0.72	1371.0	40.0	2.27	1.29	A	c	$R \neq B$
119.19576.6481	18 01 56.62	−29 39 54.7	20.29	0.72	2697.0	6.92	4.32	0.87	B	e	$R \neq B$
119.19701.1513	18 02 11.79	−30 00 58.4	19.00	0.96	2700.6	26.2	1.53	2.15	B	c	
119.19704.5147	18 02 11.09	−29 51 21.1	20.15	0.80	1294.1	15.2	2.52	0.47	B	e	
119.19832.5483	18 02 44.85	−29 58 18.3	20.41	0.69	2366.0	36.1	2.14	0.64	B	c	
119.19834.46	18 02 37.08	−29 47 58.9	15.21	0.90	612.0	107	1.12	1.08	C	e	$R \neq B$
119.19835.4282	18 02 35.10	−29 47 18.7	19.72	0.71	1563.8	7.78	2.47	1.54	C	e	
119.19837.1072	18 02 37.51	−29 39 35.9	18.94	1.08	1185.8	2.47	5.43	1.38	A	c	
119.19959.4320	18 03 03.12	−30 09 56.5	19.93	0.71	488.9	56.5	2.36	1.17	C	e	bin

Continued on Next Page...

Table A.1

...Continued from Previous Page

field.tile.seq	α (2000)	δ (2000)	V	$V-R$	t_0	$\hat{t}$	A_{max}	$\frac{\chi^2}{n_{dof}}$	Gr.	Sel.	Notes
119.20088.2601	18 03 10.74	−30 15 33.5	20.24	0.79	538.8	7.14	3.09	1.10	B	e	
119.20091.1789	18 03 06.65	−30 02 37.5	19.44	0.67	2104.2	11.8	3.32	0.76	A	c	
119.20092.3109	18 03 10.93	−29 58 12.9	19.70	0.83	2690.4	17.7	2.23	0.74	A	c	
119.20219.2348	18 03 30.09	−30 09 55.9	19.39	0.88	2066.5	94.3	2.19	0.53	A	e	
119.20226.2119	18 03 35.79	−29 42 01.3	19.19	0.83	553.6	106	2.63	3.81	C	b	bin
119.20352.2589	18 03 58.67	−29 58 48.7	17.52	0.64	1987.4	24.9	1.76	1.57	A	c	bin $R \neq B$
119.20354.3615	18 03 42.72	−29 49 20.1	19.67	0.75	1213.6	24.6	1.43	1.2	B	e	
119.20356.407	18 03 54.14	−29 42 30.8	17.16	0.95	592.2	13.3	2.42	3.35	A	e	
119.20480.2914	18 04 16.37	−30 07 23.3	19.76	0.87	1938.1	52.3	1.89	1.08	A	c	
119.20610.5200	18 04 24.83	−30 05 58.9	20.41	0.71	531.9	50.1	2.59	0.79	A	e	
119.20611.6102	18 04 20.29	−30 02 22.1	20.66	0.68	2639.6	22.3	2.11	0.92	B	c	
119.20737.740	18 04 50.62	−30 16 34.2	18.56	1.01	2309.1	21.0	1.34	1.74	B	e	
119.20738.3418	18 04 37.24	−30 12 11.5	20.05	0.94	1229.9	26.8	28.3	0.45	A	c	
119.20741.4276[u]	18 04 48.52	−30 01 15.7	19.78	0.84	564.3	15.4	1.90	0.74	C	e	
120.21010.1474	18 05 30.73	−29 26 15.1	17.86	0.77	1264.1	21.2	1.67	1.53	A	c	
120.21140.3398	18 05 33.87	−29 24 52.9	20.20	0.93	1648.2	14.9	1.70	0.99	C	a	
120.21263.1213	18 06 04.77	−29 52 38.1	18.89	0.89	1262.5	148	2.64	3.01	A	cb	bin
120.21392.1243	18 06 07.94	−29 59 26.1	18.95	0.97	2037.0	243	1.38	0.45	B	a	
120.21522.2448	18 06 35.36	−29 57 43.8	19.67	0.84	1173.7	10.6	5.65	1.11	B	e	
120.21523.2457	18 06 29.67	−29 53 06.3	19.63	0.82	1632.6	13.4	1.69	1.04	C	e	
120.21912.3560	18 07 37.03	−29 56 08.2	20.25	0.68	2474.3	71.0	5.83e+12	1.09	B	a	
120.21917.4650	18 07 26.44	−29 39 34.2	20.94	0.67	538.2	29.7	4.47	0.65	B	c	
120.22043.4380	18 07 50.84	−29 54 21.8	19.93	0.85	1980.5	57.9	2.41	0.92	B	c	bin
121.21903.1151[v]	18 07 23.53	−30 32 55.4	19.30	0.81	470.9	31.5	5.06	0.91	A	c	
121.21909.1805	18 07 25.28	−30 09 39.0	19.41	0.74	1954.6	21.1	1.70	0.69	A	c	
121.21910.1940	18 07 33.59	−30 06 36.8	19.60	0.87	2031.1	7.35	1.86	1.50	A	e	
121.22032.133[†]	18 07 46.89	−30 39 41.5	16.39	0.87	1287.3	19.5	1.58	2.51	A	c	
121.22033.917	18 07 56.49	−30 34 03.3	18.84	0.81	534.4	30.7	3.30	0.84	A	c	
121.22292.2289[w]	18 08 23.17	−30 36 18.6	19.59	0.72	456.5	39.0	2.71	1.35	A	c	

Continued on Next Page...

Table A.1

. . . Continued from Previous Page

field.tile.seq	α (2000)	δ (2000)	V	$V-R$	t_0	$\hat{t}$	A_{max}	$\frac{\chi^2}{n_{dof}}$	Gr.	Sel.	Notes
121.22423.1032	18 08 49.98	−30 31 55.9	18.89	0.86	2718.8	432	3.52	2.60	A	c	
121.22425.177	18 08 51.10	−30 24 34.7	16.59	0.87	2766.7	7.45	3.07	0.89	A	a	
122.22816.2315	18 09 28.78	−30 22 40.7	19.93	0.94	1329.7	49.3	1.62	1.37	C	e	
122.23205.1241	18 10 40.17	−30 26 53.7	19.24	0.70	1308.2	9.06	2.24	0.70	A	c	
122.23855.1875	18 12 12.44	−30 26 19.2	19.32	0.58	561.5	10.1	1.65	0.67	B	e	
123.24378.2299	18 13 10.53	−30 11 43.1	20.00	0.72	481.2	17.1	1.64	0.71	B	c	
124.21377.353	18 06 23.60	−30 59 03.1	19.54	0.92	1677.4	34.9	1.79	1.04	A	c	
124.21503.1711	18 06 39.24	−31 15 19.4	19.64	0.89	2376.5	18.1	1.60	1.62	B	c	
124.22024.4124	18 07 51.91	−31 09 19.8	20.33	0.75	544.8	35.5	2.00e+3	0.89	A	e	
124.22155.295	18 08 11.48	−31 03 48.0	18.98	0.76	1299.9	42.2	1.43	1.06	A	e	
124.22157.151	18 08 14.74	−30 57 48.3	17.20	0.94	418.2	140	1.47e+4	1.43	A	e	
128.21145.1300	18 05 40.59	−29 05 59.7	18.89	0.87	1635.7	37.3	2.46	0.6	B	e	
128.21147.5157	18 05 36.49	−28 58 20.4	20.84	0.83	2653.2	14.4	4.12	0.80	B	e	
128.21407.2080[af]	18 06 24.29	−28 55 46.7	19.18	0.78	2111.9	44.7	2.99	0.39	C	e	
128.21541.1133	18 06 42.40	−28 41 15.9	18.81	0.97	1749.7	53.8	5.81	10	A	c	
128.21666.982	18 06 57.62	−29 00 55.2	18.35	0.85	597.6	16.0	7.15	1.15	A	c	
128.21800.522	18 07 11.15	−28 46 58.9	18.26	0.97	1315.2	2.73	4.70	0.43	A	e	
128.21932.1362[ag]	18 07 20.58	−28 36 50.7	18.96	0.84	1285.4	72.8	1.71	1.48	B	c	
128.22057.2384	18 07 38.97	−28 57 11.8	19.17	0.60	1714.3	73.1	1.69	1.30	A	c	
130.28701.2042	18 23 11.74	−28 00 38.0	20.70	0.53	484.3	15.8	5.51	1.25	A	c	
130.28964.2444	18 23 50.50	−27 51 39.9	20.26	0.56	483.0	40.9	3.89	0.70	A	c	
131.29214.519[x]	18 24 27.07	−28 31 37.3	18.21	0.57	1633.6	56.2	1.80	1.40	A	c	
132.30916.803	18 28 36.19	−27 42 47.7	19.14	0.60	958.5	22.1	1.70	0.86	A	c	
132.31306.841	18 29 33.12	−27 41 35.1	19.16	0.63	2739.8	147	2.60	1.33	A	c	
134.33390.299	18 34 25.64	−27 26 44.5	18.25	0.56	889.2	8.79	4.80	10	A	c	
136.27650.2370[y]	18 21 01.78	−28 46 46.0	19.90	0.71	2044.7	115	4.91	1.24	A	c	
137.29210.2447	18 24 37.98	−28 43 43.8	20.16	0.66	874.2	61.9	1.52	1.11	B	c	
137.29214.59[x]	18 24 27.05	−28 31 36.8	18.33	0.55	1634.6	52.5	1.81	1.16	A	c	$R \neq B$
137.29731.2320	18 25 46.34	−28 42 55.7	20.19	0.67	892.8	31.0	2.02	1.22	C	e	

Continued on Next Page. . .

Table A.1

...Continued from Previous Page

field.tile.seq	α (2000)	δ (2000)	V	$V-R$	t_0	$\hat{t}$	A_{max}	$\frac{\chi^2}{n_{dof}}$	Gr.	Sel.	Notes
137.29986.2769	18 26 29.74	−29 03 39.9	20.56	0.58	1620.0	64.8	7.36	1.02	A	c	
139.32203.2073	18 31 35.56	−28 34 04.8	20.27	0.57	2711.4	32.1	2.54	0.77	A	c	
142.27650.6057[y]	18 21 01.83	−28 46 45.0	19.87	0.68	2044.4	109	4.86	0.99	A	c	
142.27776.3952	18 21 03.28	−29 01 06.0	20.91	0.73	2351.6	66.7	4.43	0.6	B	c	
144.32453.1528	18 32 14.17	−29 12 07.0	20.43	0.73	940.7	7.83	3.25	1.56	C	e	
148.26586.2310	18 18 24.33	−30 23 37.1	19.72	0.59	2312.1	32.6	3.56	1.31	A	e	$R \neq B$
148.26590.3689	18 18 33.14	−30 04 48.5	21.24	1.18	1488.9	421	114	20	C	e	
149.27233.2244	18 19 50.87	−30 34 50.4	20.71	0.62	497.6	39.0	2.59	0.64	B	e	
149.27237.3033	18 19 51.90	−30 16 00.0	20.87	0.72	850.4	24.3	2.78	0.91	B	e	
150.28409.2370	18 22 45.01	−30 08 46.0	20.48	0.38	2500.6	446	1.91	1.21	C	e	
151.31133.1607	18 28 59.51	−30 31 54.5	19.88	0.46	883.8	11.9	1.61	1.63	B	e	
152.26320.2643	18 17 52.02	−30 45 06.1	20.17	0.46	921.7	54.7	2.11	1.04	B	e	
152.26964.3183	18 19 16.03	−31 10 47.0	20.41	0.64	2697.3	22.1	1.75	0.85	B	c	
153.27488.3450	18 20 36.33	−30 54 01.5	20.55	0.38	1265.4	50.8	5.89	1.42	B	e	$R \neq B$
153.28787.720[z]	18 23 34.30	−30 57 56.0	18.03	0.63	915.0	167	2.50	0.68	A	c	
154.28787.2812[z]	18 23 34.31	−30 57 55.9	18.52	0.59	915.1	169	2.53	0.90	A	c	
154.29041.2113	18 24 06.12	−31 20 33.8	20.31	0.53	1587.3	46.9	2.01	1.08	A	c	
154.29175.2554	18 24 36.47	−31 05 27.1	20.85	0.61	1591.1	55.1	4.15	0.74	B	c	
155.26043.1938	18 17 22.14	−31 54 54.0	19.67	0.44	1979.4	8.52	1.58	0.81	C	e	
156.27606.899	18 20 54.08	−31 41 12.6	19.12	0.50	1615.3	15.5	1.89	0.65	A	c	
158.26536.1361	18 18 02.24	−25 01 37.4	19.30	0.82	1286.6	28.1	2.07	1.05	B	e	
158.26665.3141	18 18 27.21	−25 05 56.5	19.96	0.66	2007.6	11.5	1.58	0.78	C	e	$R \neq B$
158.26802.1155	18 18 43.16	−24 37 43.7	19.83	0.84	2018.0	47.7	1.97	0.97	B	c	
158.27052.2802	18 19 24.84	−25 18 10.2	19.78	0.67	2085.5	142	4.94e+5	0.91	A	e	
158.27444.129[†]	18 20 10.24	−25 08 26.0	16.97	0.77	2376.4	41.7	2.31	1.80	A	c	
159.25486.1627	18 15 42.82	−25 41 03.2	19.49	0.86	2010.2	68.3	1.83	0.84	C	c	
159.25615.941	18 15 54.71	−25 43 59.5	18.73	0.77	2681.1	58.8	2.62	0.44	A	c	$R \neq B$
159.25748.2254	18 16 16.98	−25 32 25.7	19.69	0.80	2364.9	39.1	2.35	0.85	B	c	
159.25872.1610	18 16 33.13	−25 57 52.6	19.23	0.55	1284.1	15.8	1.95	0.88	B	c	

Continued on Next Page...

Table A.1

... Continued from Previous Page

field.tile.seq	α (2000)	δ (2000)	V	$V-R$	t_0	$\hat{t}$	A_{max}	$\frac{\chi^2}{n_{dof}}$	Gr.	Sel.	Notes
159.26132.3182	18 17 14.80	−25 55 58.0	20.90	0.79	1277.0	26.6	5.32	1.7	B	e	
159.26525.1401	18 18 07.98	−25 46 46.9	21.29	0.71	507.4	72.7	9.90	1.12	A	c	
160.27701.3570	18 20 49.55	−25 20 14.0	20.05	0.66	1650.5	27.4	1.75	1.15	B	e	
161.24182.1566	18 12 44.08	−25 57 17.6	19.97	1.07	1952.8	110	3.92	1.26	A	c	
161.24568.876	18 13 29.30	−26 13 58.1	18.51	0.69	1219.1	21.1	2.27	1.08	A	c	
161.24695.1323	18 14 00.99	−26 27 21.6	18.62	0.74	1668.8	57.9	1.69	0.68	A	c	
161.24696.1161	18 13 51.87	−26 20 42.1	18.83	0.84	559.2	36.2	2.28	0.67	C	e	
161.24827.4269	18 14 13.00	−26 16 49.6	20.58	0.83	1553.0	23.3	2.35	0.79	B	c	
161.24956.2466	18 14 31.72	−26 20 17.3	19.77	0.92	2307.4	98.7	1.71	0.75	A	c	
162.25212.3830	18 14 59.66	−26 36 48.1	20.18	0.77	587.4	43.8	2.12	0.70	B	c	
162.25865.442[†]	18 16 30.60	−26 26 58.3	17.54	0.90	1225.3	60.9	1.58	1.32	A	c	
162.25868.405[†]	18 16 45.98	−26 11 43.1	17.33	0.83	1222.8	30.8	2.77	1.39	A	c	
162.25869.432[aa]	18 16 44.34	−26 09 25.7	17.52	0.71	522.0	26.6	2.26	2.08	A	c	bin
163.27297.2111	18 19 52.42	−26 18 05.4	20.25	0.68	505.1	23.9	2.50	1.81	C	e	$R \neq B$
163.27684.1669	18 20 48.38	−26 31 06.2	19.63	0.77	1600.1	12.9	1.65	0.82	B	c	
166.30682.3768	18 27 46.30	−25 57 08.8	21.19	0.82	497.6	35.2	3.16	0.77	B	e	
167.23910.3170	18 11 55.15	−26 46 32.7	20.03	0.86	1607.9	65.5	1.79	1.38	B	c	
167.24169.3673	18 12 45.02	−26 50 53.4	20.16	0.74	564.9	45.5	2.20	0.74	C	e	
167.24173.2623	18 12 44.90	−26 34 50.3	19.62	0.73	1722.1	93.8	1.10e+3	0.97	B	e	
167.24564.5066	18 13 32.15	−26 31 10.3	20.36	0.87	484.1	32.8	3.03	0.81	A	c	
167.24815.4558	18 14 09.36	−27 04 57.7	20.20	0.73	1954.8	8.05	2.89	0.87	B	e	$R \neq B$
167.24815.4984	18 14 06.96	−27 05 38.0	20.59	0.90	1296.9	38.9	2.46	0.63	B	e	
168.25079.1100	18 14 56.37	−26 51 09.9	17.89	1.65	550.8	47.8	1.52	1.35	B	e	
168.25853.1778	18 16 30.98	−27 14 18.7	18.83	0.63	501.5	43.8	1.59	0.69	B	c	
168.25985.4014	18 17 01.65	−27 05 45.0	20.63	0.67	1476.1	360	18.1	1.76	B	e	
172.31579.2624	18 30 07.75	−26 48 20.5	20.37	0.69	2736.5	128	2.31	1.33	B	c	
172.32358.313	18 31 53.24	−26 51 42.6	18.15	0.58	2700.9	42.0	1.63	0.92	A	c	
174.29360.352	18 24 42.09	−27 25 41.6	17.59	0.66	2735.7	75.5	17.7	1.32	A	c	
175.31446.1290	18 29 34.21	−27 03 14.2	20.96	0.82	845.1	23.4	2.17	0.76	C	c	

Continued on Next Page...

Table A.1

...Continued from Previous Page

field.tile.seq	α (2000)	δ (2000)	V	$V-R$	t_0	$\hat{t}$	A_{max}	$\frac{\chi^2}{n_{dof}}$	Gr.	Sel.	Notes
176.18693.267	17 59 46.63	−27 53 51.4	17.72	1.43	2344.5	6.36	1.29e+8	2.18	A	e	
176.18826.909[†]	18 00 15.45	−27 42 47.8	18.78	1.21	2364.7	24.3	1.77	1.17	A	c	
176.18827.1911	18 00 11.98	−27 36 10.6	19.59	0.96	2346.3	20.3	2.27	1.06	A	c	
176.18954.6538	18 00 20.85	−27 48 31.2	21.39	0.93	2657.1	94.7	3.74	1.06	B	c	
176.19214.2902	18 01 01.99	−27 51 26.5	20.83	1.04	1264.6	48.1	2.91	0.71	B	c	
176.19214.5296	18 01 11.11	−27 49 22.2	20.43	0.97	1907.7	14.7	2.44	0.98	A	e	
176.19219.978	18 01 04.41	−27 30 41.4	18.77	1.30	1228.9	56.7	4.71	4.40	A	b	bin
176.19343.5828	18 01 27.84	−27 52 21.0	20.13	0.72	2665.1	18.0	1.81	0.73	C	a	
176.19602.1226	18 01 59.22	−27 56 34.4	20.20	0.90	2754.2	62.4	2.23	1.27	B	c	
176.19735.2709	18 02 20.27	−27 45 53.4	19.59	0.91	2025.5	12.0	1.72	1.12	B	c	
176.19997.3338	18 02 48.51	−27 38 51.8	20.70	1.05	2790.0	75.6	1.11e+4	1.23	B	a	
177.25109.1274	18 14 54.37	−24 49 34.9	21.07	1.05	1261.0	55.5	4.89	0.58	B	c	
177.25111.120	18 14 52.70	−24 41 07.9	17.21	1.20	1566.9	25.9	7.64	2.20	A	c	
177.25756.2480	18 16 24.87	−25 03 26.5	20.41	1.01	2025.2	18.5	1.65	0.94	B	e	
178.23136.5133	18 10 10.18	−26 21 03.6	20.32	0.74	1915.9	157	5.92	0.40	A	e	
178.23273.6023	18 10 38.12	−25 53 15.3	20.59	0.95	2362.9	11.8	57.0	0.87	C	a	
178.23398.4814	18 10 59.48	−26 13 16.5	20.51	0.94	2420.4	37.1	2.90	0.74	A	c	
178.23531.931[†]	18 11 17.41	−25 59 51.4	18.72	1.11	1590.3	13.7	2.18	1.08	A	c	
178.23660.2137	18 11 23.70	−26 04 57.0	20.58	1.02	1191.4	101	3.63	0.82	B	c	
179.21577.1740	18 06 31.70	−26 16 01.6	19.79	0.99	2327.8	23.3	9.32	7.51	A	b	bin
179.21578.2080	18 06 32.82	−26 15 13.6	20.80	1.41	2382.4	63.0	8.16	1.24	A	c	
179.21584.3189	18 06 28.52	−25 49 02.1	21.08	1.26	2690.3	34.9	1.52	0.75	B	a	
179.21844.84	18 07 08.43	−25 49 20.7	16.98	1.36	1970.2	80.6	1.68	1.86	A	c	
179.21971.6468	18 07 28.27	−25 59 59.7	21.53	1.24	2369.2	34.8	2.37	0.80	B	e	
179.21971.936	18 07 22.06	−25 59 44.7	19.00	1.19	2618.6	20.9	2.95	0.91	A	a	
179.22226.151	18 07 59.13	−26 22 46.8	17.49	1.30	2581.0	70.9	1.11e+16	1.02	B	a	
179.22486.3353	18 08 34.24	−26 21 13.6	20.08	0.91	1615.0	20.6	3.37	0.94	A	c	
179.22616.2234	18 09 08.05	−26 20 34.3	19.77	1.06	2321.9	13.9	27.7	1.44	C	e	
179.22619.3190	18 08 58.42	−26 08 07.6	21.06	1.33	1623.5	174	4.27	0.79	B	c	bin

Continued on Next Page...

Table A.1

...Continued from Previous Page

field.tile.seq	α (2000)	δ (2000)	V	$V-R$	t_0	$\hat{t}$	A_{max}	$\frac{\chi^2}{n_{dof}}$	Gr.	Sel.	Notes
180.22240.202†	18 07 57.82	−25 24 48.1	18.98	1.44	1286.9	311	3.42	1.15	A	c	
180.22242.2664	18 08 09.34	−25 15 56.7	20.15	1.01	2426.9	9.88	1.70	0.86	B	e	
180.22633.2883	18 08 58.65	−25 14 22.3	20.56	1.06	2760.5	25.7	3.71	0.82	A	c	
180.22759.707	18 09 17.80	−25 29 03.7	19.21	1.15	2832.0	71.8	2.14	1.98	A	a	
180.22767.1452	18 09 15.50	−24 58 14.9	20.33	1.30	1957.9	22.2	7.92	1.40	A	c	
180.23412.3949	18 10 53.70	−25 17 28.0	21.18	1.14	2358.8	19.2	2.11	0.89	B	c	
301.45441.747	18 31 36.15	−13 31 37.4	21.56	1.37	2682.9	45.4	5.23	1.07	C	c	
301.45445.840	18 31 38.13	−13 16 01.1	19.32	1.00	1895.4	197	1.81	0.92	B	a	bin
301.46110.1056	18 32 43.60	−13 44 19.0	19.81	1.15	1951.2	98.5	2.10	0.87	A	c	
301.46285.1166	18 33 09.38	−13 16 54.1	21.20	1.20	2661.8	279	3.69	0.76	C	c	
301.46613.3271	18 33 38.09	−13 50 23.9	20.99	1.06	2079.3	112	2.68	0.99	B	c	
301.46616.2156	18 33 36.01	−13 35 09.1	20.18	0.94	1962.7	41.3	2.55	0.98	A	c	
302.44927.2559	18 30 41.95	−14 14 08.1	19.52	0.97	1993.3	86.2	1.41	1.29	B	e	
302.44928.3523	18 30 49.42	−14 10 52.9	21.41	1.07	2770.3	86.7	25.4	1.12	A	c	bin
302.45258.1038	18 31 20.04	−14 34 07.9	19.05	0.81	1605.1	146	1.99	0.94	A	c	
304.35391.650	18 15 08.27	−22 45 05.1	20.04	0.90	1252.8	10.9	1.58	0.78	C	e	
304.35564.26	18 15 11.46	−22 22 59.1	17.64	1.78	1705.4	25.4	2.11	1.97	A	c	
304.35730.425	18 15 35.67	−22 32 11.2	19.43	1.41	2686.1	81.9	2.42	0.87	A	c	
304.35899.3004	18 15 54.97	−22 27 33.5	21.17	1.12	2632.6	38.5	3.42	0.67	B	e	
304.36403.2137	18 16 38.95	−22 28 52.8	21.12	1.05	1244.5	57.6	2.25	0.99	B	c	
304.36904.698	18 17 24.55	−22 41 57.2	19.94	1.04	1750.6	208	2.11	0.94	B	c	
305.35237.685	18 14 43.51	−21 48 10.6	19.65	1.11	2655.4	260	1.47	1.66	C	e	
305.35738.35	18 15 36.08	−22 01 54.7	17.43	1.80	1285.9	36.2	4.52	2.95	A	c	
305.36746.2411	18 17 16.16	−22 01 18.3	20.75	1.17	2375.6	40.7	69.0	0.86	A	c	
306.35894.1371	18 15 53.15	−22 47 22.9	20.64	1.17	1192.5	184	2.51	0.76	A	e	
306.36223.3023	18 16 32.59	−23 17 26.8	20.29	0.86	1921.5	11.4	2.27	1.35	B	c	
307.35374.3058	18 15 02.51	−23 52 41.5	20.95	1.14	2740.4	50.7	2.67	0.85	B	c	
307.35709.1490	18 15 37.63	−23 55 11.1	19.68	0.93	1557.6	15.3	2.33	0.96	B	e	
307.36378.482	18 16 35.35	−24 09 12.5	19.61	1.22	1267.3	32.8	1.58	0.82	B	c	

Continued on Next Page...

Table A.1

...Continued from Previous Page

field.tile.seq	α (2000)	δ (2000)	V	$V-R$	t_0	$\hat{t}$	A_{max}	$\frac{\chi^2}{n_{dof}}$	Gr.	Sel.	Notes
307.36884.258[ab]	18 17 28.63	−23 59 45.9	17.69	1.10	1315.4	30.8	2.32	0.85	A	c	
308.38259.1981	18 19 43.15	−21 57 45.4	20.15	0.76	2388.3	8.30	1.54	2.37	C	e	
308.38595.1020	18 20 30.03	−21 57 04.3	19.81	1.01	2769.4	58.0	14.2	1.2	A	c	
309.38081.3420	18 19 30.55	−22 37 56.0	21.12	1.01	1712.1	68.4	5.48	0.69	B	c	
310.37067.3803	18 17 50.51	−23 02 22.8	21.12	0.96	1605.6	10.8	2.20	1.34	C	e	
310.37233.3924	18 18 06.37	−23 10 06.5	20.77	0.92	1230.4	11.8	4.69	0.74	B	e	
310.37235.3685	18 18 04.38	−23 02 11.1	21.15	1.09	2056.8	70.0	2.98	0.87	A	c	
310.37398.2274	18 18 19.82	−23 19 08.9	21.00	0.85	1283.1	118	2.20	0.68	B	c	
310.37400.1067	18 18 19.85	−23 14 45.3	19.43	0.98	2663.3	83.7	4.74	0.69	A	c	
310.37407.336	18 18 28.16	−22 45 50.9	18.75	1.02	2802.6	182	1.52	1.86	C	c	bin
310.38237.1062	18 19 52.32	−23 25 35.7	18.94	0.81	1311.7	11.9	1.57	0.81	C	e	$R \neq B$
310.38242.570	18 19 40.58	−23 04 44.2	20.00	0.94	1304.2	11.3	1.55	2.71	C	e	$R \neq B$
310.38407.3684	18 19 56.45	−23 18 41.4	20.64	0.80	2726.0	639	1.71	1.30	D	c	
310.38573.911	18 20 24.90	−23 25 17.5	19.34	0.87	1222.5	127	1.95	0.85	A	c	
311.36884.287[ab]	18 17 28.62	−23 59 47.0	17.55	0.93	1315.4	30.9	2.42	0.65	A	c	
311.36890.444	18 17 39.60	−23 36 07.4	18.67	1.09	2813.1	200	4.38	1.49	A	c	
311.37050.344	18 17 45.38	−24 09 04.0	17.93	0.80	1295.2	27.4	1.40	1.09	A	e	
311.37223.967	18 18 10.73	−23 47 16.5	20.99	1.09	1600.6	21.8	3.76	0.56	A	c	
311.37727.1742	18 18 59.74	−23 49 26.7	20.10	0.95	1577.7	99.5	3.05	1.25	B	c	bin
311.37893.6302	18 19 20.38	−23 55 36.9	21.47	0.77	2705.9	71.5	11.5	0.76	A	c	
311.38229.2494	18 19 43.81	−23 58 55.4	19.52	0.66	2689.3	5.79	1.67	1.82	C	e	
311.38394.386	18 20 04.48	−24 08 11.1	19.65	0.76	1268.3	31.1	3.14	1.49	A	c	bin
311.38567.3476	18 20 19.31	−23 49 41.5	20.32	0.79	2028.1	7.20	1.80	1.19	C	e	
401.47870.1026	17 56 22.00	−28 14 32.3	18.75	1.23	2433.3	51.7	1.49	1.33	B	e	
401.47990.2762	17 56 51.83	−28 14 47.7	20.28	1.32	1714.1	118	2.18	0.78	B	c	
401.47991.1840[†]	17 57 07.51	−28 13 44.2	19.48	1.39	1953.0	44.7	1.92	0.61	A	c	
401.47994.1182[†]	17 57 07.82	−28 00 27.9	19.68	1.55	2362.7	60.6	3.68	1.05	A	c	
401.48047.3195	17 57 14.57	−28 29 23.9	20.05	1.09	2272.9	46.9	2.19	0.41	B	c	
401.48049.670	17 57 13.63	−28 19 12.3	18.34	1.14	1587.0	25.1	1.34	1.74	C	e	

Continued on Next Page...

Table A.1

. . . Continued from Previous Page

field.tile.seq	α (2000)	δ (2000)	V	$V-R$	t_0	$\hat{t}$	A_{max}	$\frac{\chi^2}{n_{dof}}$	Gr.	Sel.	Notes
401.48052.861†	17 57 23.81	−28 10 24.6	18.77	1.32	2291.5	72.0	2.65	0.69	B	c	
401.48114.174	17 57 42.91	−28 01 02.6	18.72	1.96	2624.0	51.9	6.79	0.66	A	c	
401.48167.1934†	17 57 57.40	−28 27 09.6	18.44	1.23	2179.0	125	2.53	0.89	C	c	
401.48167.2536	17 58 00.72	−28 27 24.3	19.59	1.32	2682.2	14.1	1.40	1.07	B	e	
401.48229.760†	17 58 13.42	−28 20 32.2	18.07	1.15	2694.5	20.1	1.82	1.18	A	c	bin $R \neq B$
401.48230.2825	17 58 13.75	−28 17 16.2	20.07	1.00	1698.3	9.43	6.43	0.46	A	c	
401.48406.2341	17 59 01.59	−28 31 28.1	20.09	1.09	2340.3	7.64	2.83	1.15	B	e	
401.48408.649†	17 59 08.99	−28 24 54.7	17.72	1.22	2325.4	74.6	3.07	1.30	B	cb	bin
401.48410.1407	17 58 58.85	−28 16 30.2	18.83	1.20	2022.4	6.70	1.81	1.54	B	e	
401.48467.4621	17 59 16.98	−28 29 42.0	20.12	0.93	2339.8	45.2	2.57	1.11	A	c	
401.48469.789†	17 59 22.27	−28 20 21.9	18.22	1.18	1554.8	5.67	5.96	0.42	B	c	
402.47619.1009	17 55 13.59	−28 58 33.6	20.23	1.09	1605.1	31.2	3.25	2.4	B	c	bin
402.47623.80	17 55 15.07	−28 43 23.6	18.62	2.42	2139.5	341	1.59	5.36	D	c	var
402.47678.1353	17 55 21.18	−29 04 12.6	18.89	1.24	2470.2	21.9	1.65	0.95	B	e	
402.47678.1666†	17 55 22.60	−29 04 12.9	19.21	1.33	2393.1	13.6	2.48	0.88	A	c	
402.47681.2971	17 55 28.72	−28 50 43.5	19.96	1.22	1731.8	29.6	3.32	0.85	B	e	
402.47682.912	17 55 34.50	−28 48 26.8	18.79	0.88	1550.4	243	2.77	1.27	A	c	
402.47736.2869	17 55 45.00	−29 13 59.1	19.58	1.07	2647.2	58.0	2.45	0.54	B	e	
402.47737.1590†	17 55 41.50	−29 09 00.6	18.49	1.05	1552.3	5.47	2.79	1.03	B	c	
402.47742.3318†	17 55 42.88	−28 49 17.6	20.21	1.63	1377.1	50.1	8.64	1.21	A	c	
402.47745.3587	17 55 52.82	−28 36 43.7	21.10	1.27	2763.1	28.3	2.52	0.93	C	c	
402.47796.1893†	17 56 10.91	−29 10 44.2	19.51	1.34	1678.7	19.3	22.5	1.47	B	c	
402.47797.1914	17 56 09.36	−29 08 30.2	19.70	1.43	2725.3	18.8	1.49	0.92	B	e	$R \neq B$
402.47798.1259†	17 56 11.12	−29 06 13.9	19.75	1.40	1583.7	47.6	4.94	1.38	A	c	
402.47798.2435	17 56 04.72	−29 05 20.8	20.07	1.13	1908.2	68.3	2.15	0.29	C	e	
402.47799.1736†	17 56 07.24	−28 58 32.6	19.59	1.29	2410.0	115	2.26	0.47	A	c	
402.47804.4101	17 56 02.99	−28 38 47.9	20.43	1.26	2657.6	12.6	2.25	1.59	C	c	$R \neq B$
402.47805.1858	17 55 56.31	−28 37 09.0	19.18	1.09	1924.7	7.40	1.71	1.04	C	e	
402.47856.561†	17 56 25.05	−29 12 56.5	18.82	1.39	1566.6	12.3	2.14	1.63	B	c	

Continued on Next Page. . .

Table A.1

. . . Continued from Previous Page

field.tile.seq	α (2000)	δ (2000)	V	$V-R$	t_0	$\hat{t}$	A_{max}	$\frac{\chi^2}{n_{dof}}$	Gr.	Sel.	Notes
402.47862.1576†	17 56 20.69	−28 47 42.0	19.48	1.31	2028.5	54.3	7.52	6.13	A	cb	bin
402.47862.3234	17 56 19.14	−28 47 20.3	20.50	1.21	1649.0	50.0	2.88	0.90	B	c	
402.47863.110	17 56 18.16	−28 46 05.0	16.64	1.18	2312.4	13.6	1.57	0.92	B	ab	bin
402.47978.4996	17 57 07.44	−29 05 28.7	20.86	0.97	2039.1	5.59	3.33	0.83	B	e	
402.48103.1719	17 57 32.81	−28 42 45.4	19.66	1.11	2395.9	425	4.37	1.25	A	c	
402.48156.2413	17 57 46.25	−29 12 04.6	20.17	1.02	1604.3	42.8	2.41	0.95	B	c	
402.48156.4509	17 57 51.08	−29 13 55.4	19.84	1.04	1327.0	28.9	2.21	0.83	A	c	
402.48158.1296†	17 57 47.57	−29 03 54.3	18.69	1.12	2325.7	15.9	3.94	0.98	A	c	
402.48219.2582	17 58 15.37	−29 01 38.2	19.39	1.05	2257.9	12.9	3.94e+12	1.12	A	c	
402.48219.5086	17 58 05.42	−29 02 27.4	20.54	1.23	1538.9	17.9	2.17	0.85	B	c	
402.48279.1043	17 58 22.79	−28 59 54.5	19.63	1.05	1990.5	33.0	3.25	0.62	A	c	
402.48280.502^{ac†}	17 58 25.07	−28 57 46.3	18.16	1.18	1342.5	25.5	2.08	1.14	A	c	
403.47427.353	17 54 22.62	−29 49 57.4	19.01	0.94	2688.5	18.3	2.00	0.91	B	c	
403.47491.770†	17 54 38.66	−29 33 12.8	17.95	1.29	2633.9	48.5	2.43	0.99	A	c	
403.47546.2003	17 54 43.89	−29 51 19.5	18.76	1.10	2436.3	65.8	1.48	0.68	B	e	
403.47548.1799	17 54 46.89	−29 44 17.1	18.87	1.09	2757.3	7.05	2.46	1.14	B	e	
403.47550.807†	17 55 00.07	−29 35 03.8	17.95	1.21	2774.3	11.6	3.60	0.87	A	c	
403.47554.630	17 54 49.36	−29 20 24.8	18.14	1.30	2291.7	31.1	1.45	1.36	B	e	
403.47605.5112	17 55 11.84	−29 55 25.2	20.39	0.93	1606.4	3.96	2.93	0.51	B	c	
403.47610.576†	17 55 17.07	−29 37 40.7	17.52	1.11	2657.9	9.59	4.75	2.56	A	c	$R \neq B$
403.47669.1859	17 55 36.42	−29 42 13.9	18.55	1.22	2078.3	26.5	1.47	1.40	B	e	
403.47670.5074	17 55 25.15	−29 34 50.2	20.25	0.86	1887.7	51.2	6.07	1.15	B	e	
403.47671.57	17 55 28.68	−29 33 41.7	16.07	1.33	2058.8	37.0	5.68	1.26	A	c	
403.47728.5938	17 55 55.62	−29 45 17.7	20.78	1.08	2338.4	13.1	3.90	1.09	B	c	
403.47785.3267	17 56 10.68	−29 56 57.2	19.95	1.06	1330.4	12.2	2.37	0.69	B	e	
403.47788.5281	17 56 06.47	−29 46 16.5	20.96	0.95	1667.8	36.4	16.8	0.70	B	e	
403.47790.3199	17 56 12.84	−29 37 35.1	21.19	1.05	2019.5	28.8	9.08	0.56	A	c	
403.47793.1349	17 56 10.97	−29 26 15.8	19.95	1.07	2082.2	18.0	1.79	0.66	B	e	
403.47793.2961^{ad}	17 55 57.99	−29 26 12.2	18.85	1.44	1688.6	24.1	2.50	1.2	B	b	bin

Continued on Next Page. . .

Table A.1

. . . Continued from Previous Page

field.tile.seq	α (2000)	δ (2000)	V	$V-R$	t_0	$\hat{t}$	A_{max}	$\frac{\chi^2}{n_{dof}}$	Gr.	Sel.	Notes
403.47845.495†	17 56 22.79	−29 55 16.4	18.22	1.24	1945.8	15.0	2.03	0.88	A	c	
403.47846.2778	17 56 14.29	−29 50 58.2	20.21	1.13	2429.0	11.6	2.07	1.09	C	a	
403.47848.35	17 56 30.71	−29 46 29.6	16.06	1.58	2335.2	18.2	1.91	5.10	A	e	var
403.47849.756	17 56 25.18	−29 40 31.2	15.85	1.32	2732.7	293	4.30	6.37	A	e	
403.47907.3004	17 56 48.81	−29 49 31.3	20.20	1.02	1716.5	15.9	5.42	0.84	B	c	
403.47912.376	17 56 36.14	−29 29 19.2	18.54	1.80	2545.8	179	1.68	1.39	C	e	

The dagger symbol (†) denotes clump giants. Letter superscripts denote the same event found in multiple objects, the other event in the pair may be present in Table A.2. The grades (column 10) are on an A-F scale, and the selection methods (column 11) are "c" for our clump-like selection criteria, "e" for events found by eye, "a" for events found via the alert system, and "b" for events from the binary paper.

Table A.2: Contaminate Event Parameters

field.tile.seq	α (2000)	δ (2000)	V	$V-R$	t_0	$\hat{t}$	A_{max}	$\frac{\chi^2}{n_{dof}}$	Gr.	Sel.	Notes
101.20650.3427[a]	18 04 20.25	−27 24 47.3	19.61	0.77	1971.2	12.7	2.75	0.6	B	e	
101.21042.1247[c]	18 05 28.07	−27 16 21.3	17.92	0.59	2806.9	19.3	1.64	0.55	B	e	
101.21174.3112[d]	18 05 38.77	−27 08 28.4	19.59	0.89	1908.5	9.89	1.83	0.78	C	e	$R \neq B$
102.22851.5108[e]	18 09 30.47	−28 00 49.2	20.48	0.80	1307.6	15.9	2.25	0.84	C	e	
104.19991.1951	18 03 01.33	−28 01 45.1	19.34	0.83	1739.0	54.4	2.96	1.80	C	c	cv
104.21421.273[ae]	18 06 08.61	−28 00 24.7	18.61	0.70	2641.0	6.57	8.30	1.15	B	e	
105.21291.7441	18 05 53.59	−28 03 29.8	18.59	0.79	1603.1	8.11	2.53	3.46	C	e	cv
108.18943.3528[m]	18 00 21.74	−28 32 01.1	19.34	0.84	2271.8	20.0	4.68e+10	0.54	C	e	
108.19341.2253[n]	18 01 28.51	−28 02 15.4	19.90	0.89	2356.0	26.1	3.95	0.69	B	e	
109.19986.3305[p]	18 03 01.12	−28 21 09.5	19.33	0.70	1258.6	19.9	2.19	0.72	B	e	
109.20370.5051[q]	18 03 58.70	−28 47 40.3	20.16	0.81	2787.7	10.2	7.29	0.82	B	e	
113.18676.5195	18 00 01.25	−29 02 06.4	19.86	0.73	2255.4	12.5	2.03	2.25	C	e	cv
113.18810.4409[r]	18 00 06.69	−28 44 00.3	20.04	0.82	2333.2	25.0	2.32	0.82	B	e	
114.19842.2283	18 02 40.21	−29 19 20.1	19.67	1.11	1721.6	12.1	1.74	1.7	C	a	cv
115.22695.3361	18 09 13.79	−29 47 36.4	19.77	0.66	2657.3	21.7	2.15	2.19	C	e	cv $R \neq B$
118.18270.4540[s]	17 59 04.60	−30 07 06.7	20.53	1.02	1894.2	6.11	2.04	0.96	B	e	
118.18662.2288[t]	17 59 46.56	−29 57 30.1	19.65	0.99	2623.5	14.0	2.61	0.53	C	e	
119.19707.2379	18 02 25.95	−29 39 40.4	19.84	0.80	2770.3	20.5	1.53	1.52	D	c	cv
119.20742.2884[u]	18 04 48.74	−29 58 35.5	19.29	0.83	564.9	9.90	1.69	0.78	C	e	
121.21903.3479[v]	18 07 23.50	−30 32 56.6	20.27	0.84	467.7	37.4	3.06	0.38	B	e	
121.22292.3358[w]	18 08 23.00	−30 36 18.1	19.88	0.68	457.6	38.0	2.11	0.94	A	c	
125.23850.4190	18 11 58.88	−30 43 54.0	20.71	0.74	2724.1	18.9	2.64	0.77	C	a	cv
128.21407.1674[af]	18 06 24.32	−28 55 47.9	18.91	0.92	2106.5	27.9	2.45	0.67	B	e	$R \neq B$
128.21926.3361	18 07 33.92	−29 00 36.5	19.52	0.67	552.2	15.2	2.00	1.24	C	e	cv $R \neq B$
128.21932.2196[ag]	18 07 20.51	−28 36 51.9	19.66	1.07	1283.8	69.1	1.45	0.79	C	e	
145.34015.1280	18 35 55.58	−29 04 44.2	24.41	0.37	854.9	168	33.2	1.37	C	c	cv
153.28398.2677	18 22 35.67	−30 54 35.3	22.95	−0.06	858.7	134	10.1	0.67	D	c	cv $R \neq B$
162.25869.1615[aa]	18 16 44.38	−26 09 27.2	20.10	0.74	523.6	72.8	4.52	0.40	A	c	
173.33002.479	18 33 17.45	−27 16 09.2	19.54	0.50	953.4	37.2	1.91	4.91	B	e	cv $R \neq B$

Continued on Next Page...

Table A.2

... Continued from Previous Page

field.tile.seq	α (2000)	δ (2000)	V	$V-R$	t_0	$\hat{t}$	A_{max}	$\frac{\chi^2}{n_{dof}}$	Gr.	Sel.	Notes
178.23266.2918	18 10 35.18	−26 23 40.4	19.91	0.94	1323.5	6.99	7.00e+5	1.14	C	e	cv
178.24048.3166	18 12 20.91	−26 14 03.0	20.54	0.73	2035.5	11.4	3.01	2.05	B	e	cv $R \neq B$
306.36059.752	18 16 05.96	−23 02 38.9	25.20	−0.39	1265.1	536	130	5.90	D	c	cv $R \neq B$
311.37730.4143	18 18 50.30	−23 36 14.9	21.89	0.76	1271.6	26.8	5.64	1.92	C	e	cv $R \neq B$
402.48280.894^{ac}	17 58 25.01	−28 57 44.8	19.36	0.99	1343.3	22.6	3.28	0.62	A	e	
403.47614.3183	17 55 05.97	−29 20 32.2	20.09	1.14	1323.1	14.4	1.78	2.06	C	e	cv
403.47793.3138^{ad}	17 55 58.04	−29 26 11.6	19.24	1.27	1689.5	19.4	3.01	0.68	B	e	

Letter superscripts denote the same event found in multiple objects, events in this table are due to blending of flux from a real event and should be ignored for any analysis. The grades (column 10) are on an A-F scale, and the selection methods (column 11) are "c" for our clump-like selection criteria, "e" for events found by eye, "a" for events found via the alert system, and "b" for events from the binary paper.

B

Light Curves

B.1 Sample Light Curves

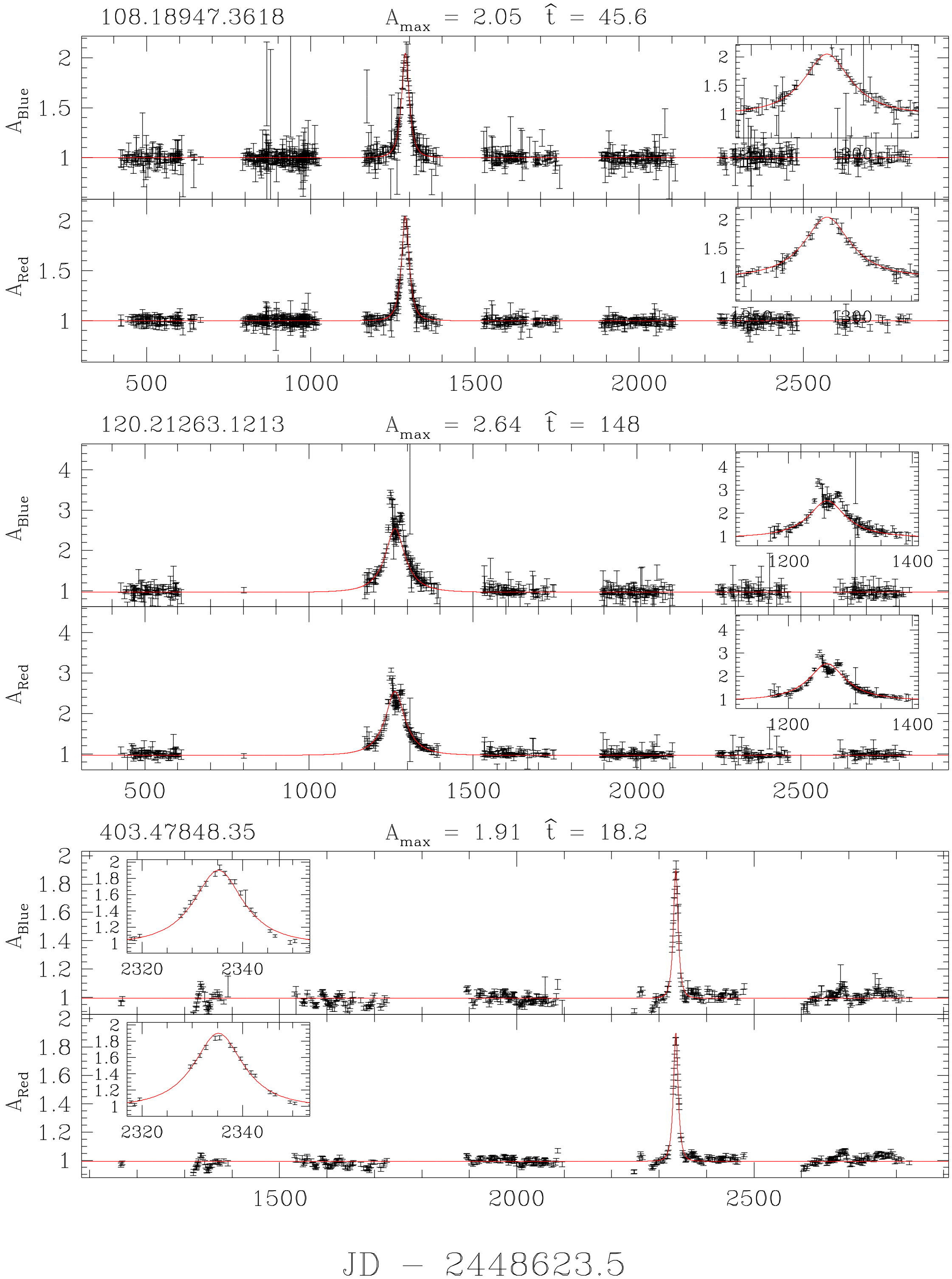

Figure B.1 We show a few iteresting light curves (from top to bottom): a standard point-lens point-source event, a binary lens event, and a lensed periodic variable.

B.2 Representative Sample of Contaminate Events

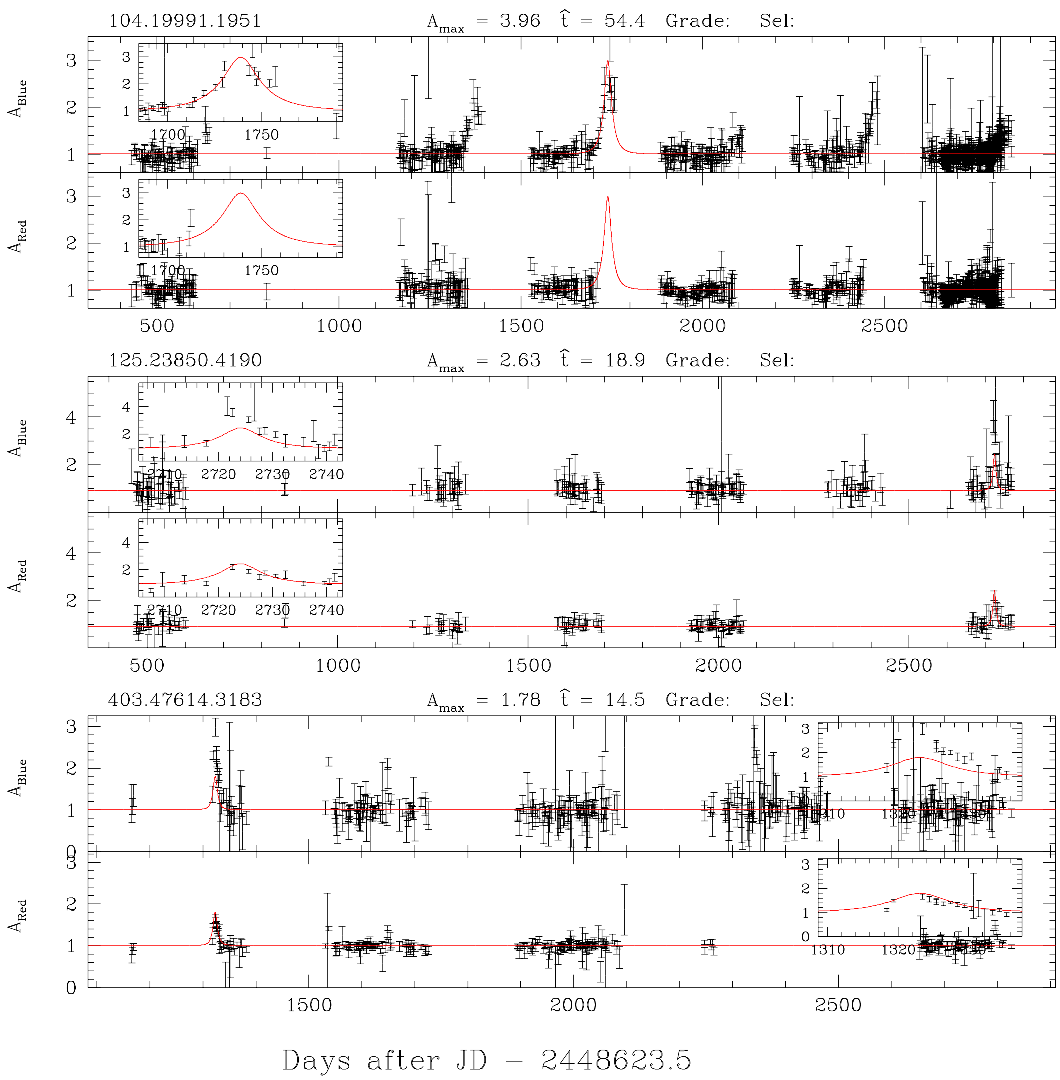

Figure B.2: Sample of Contaminate Events

B.3 Light Curves of Clump-Giant Events

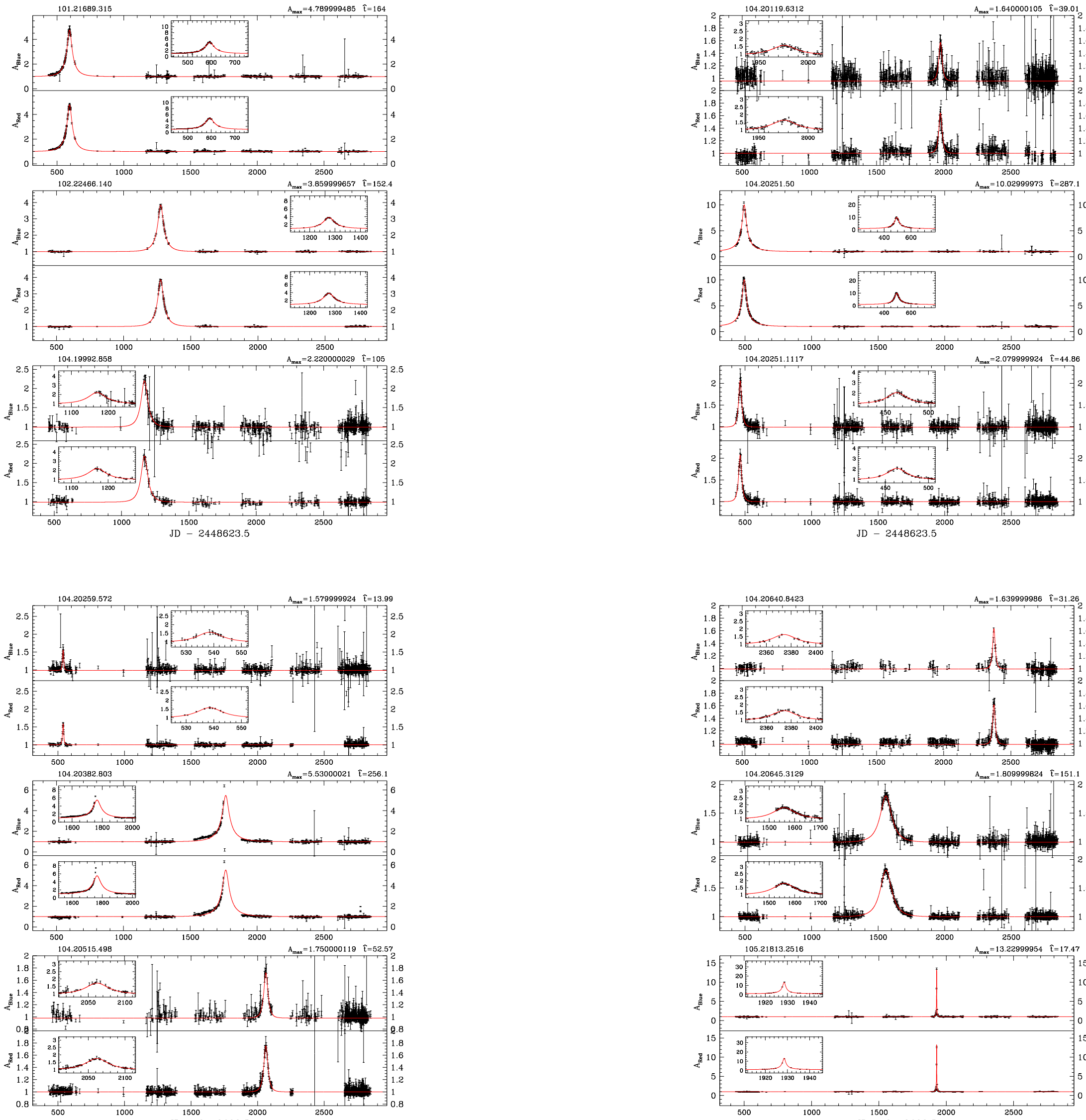

Figure B.3: Clump-giant light curves

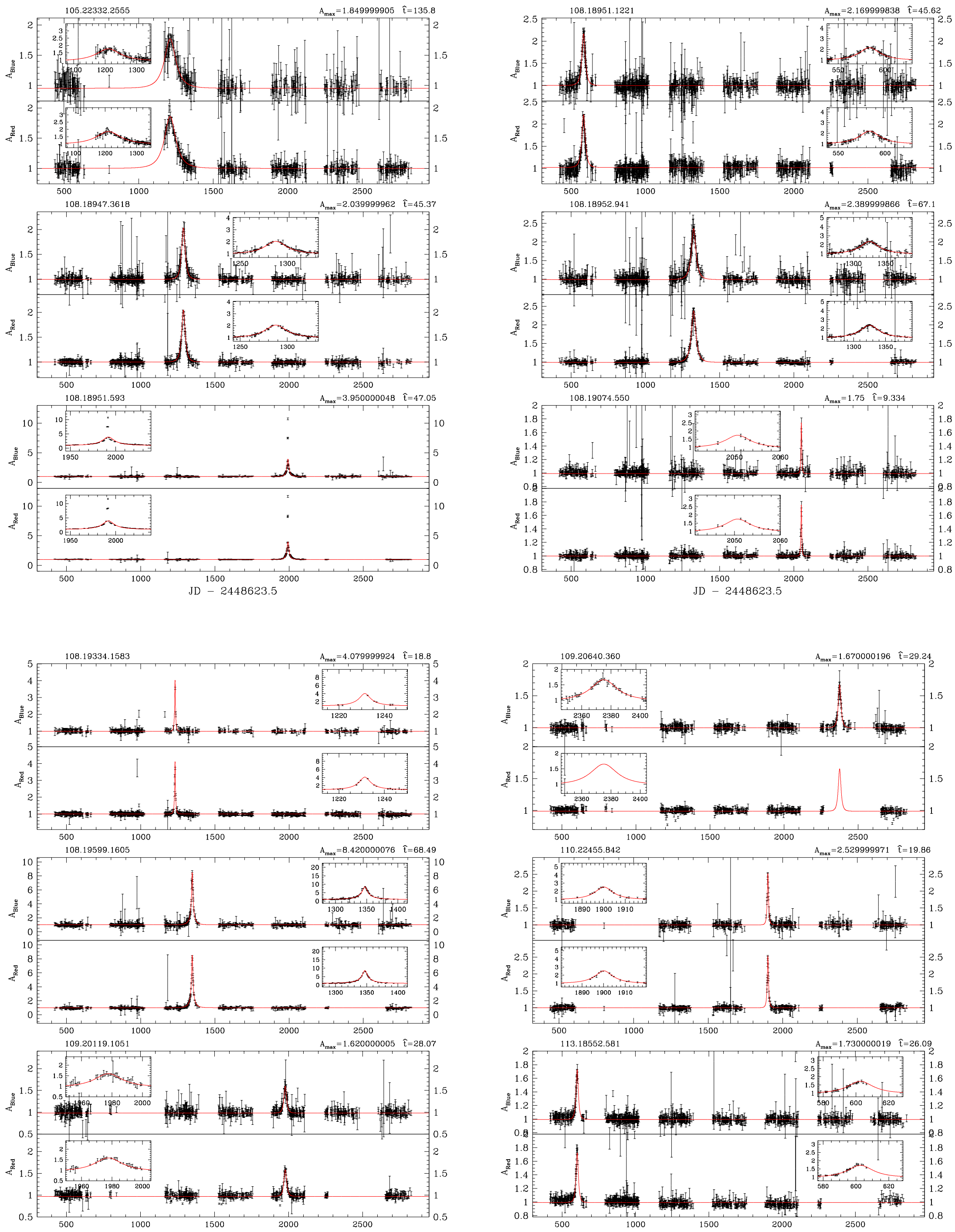

Figure B.3: *continued*

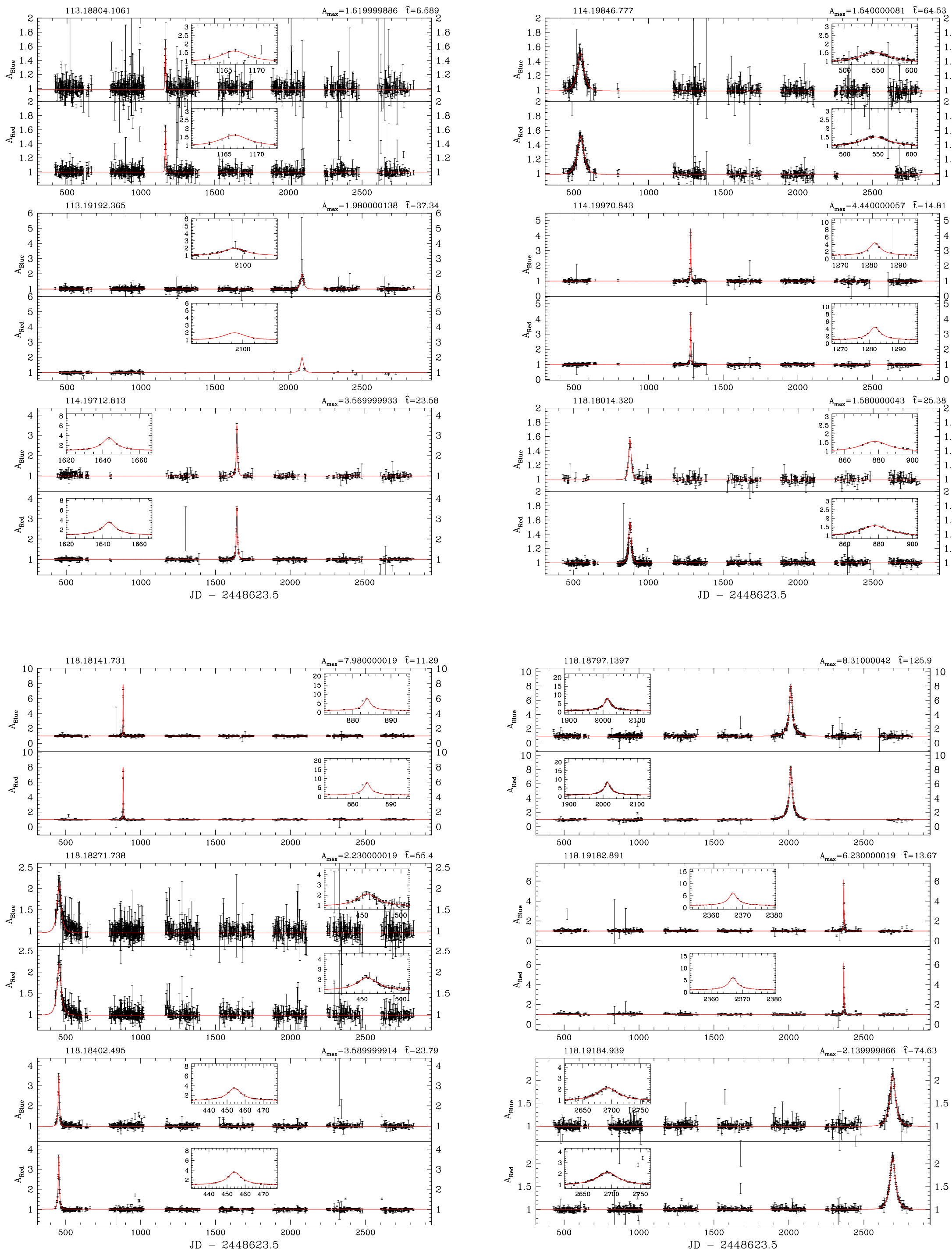

Figure B.3: *continued*

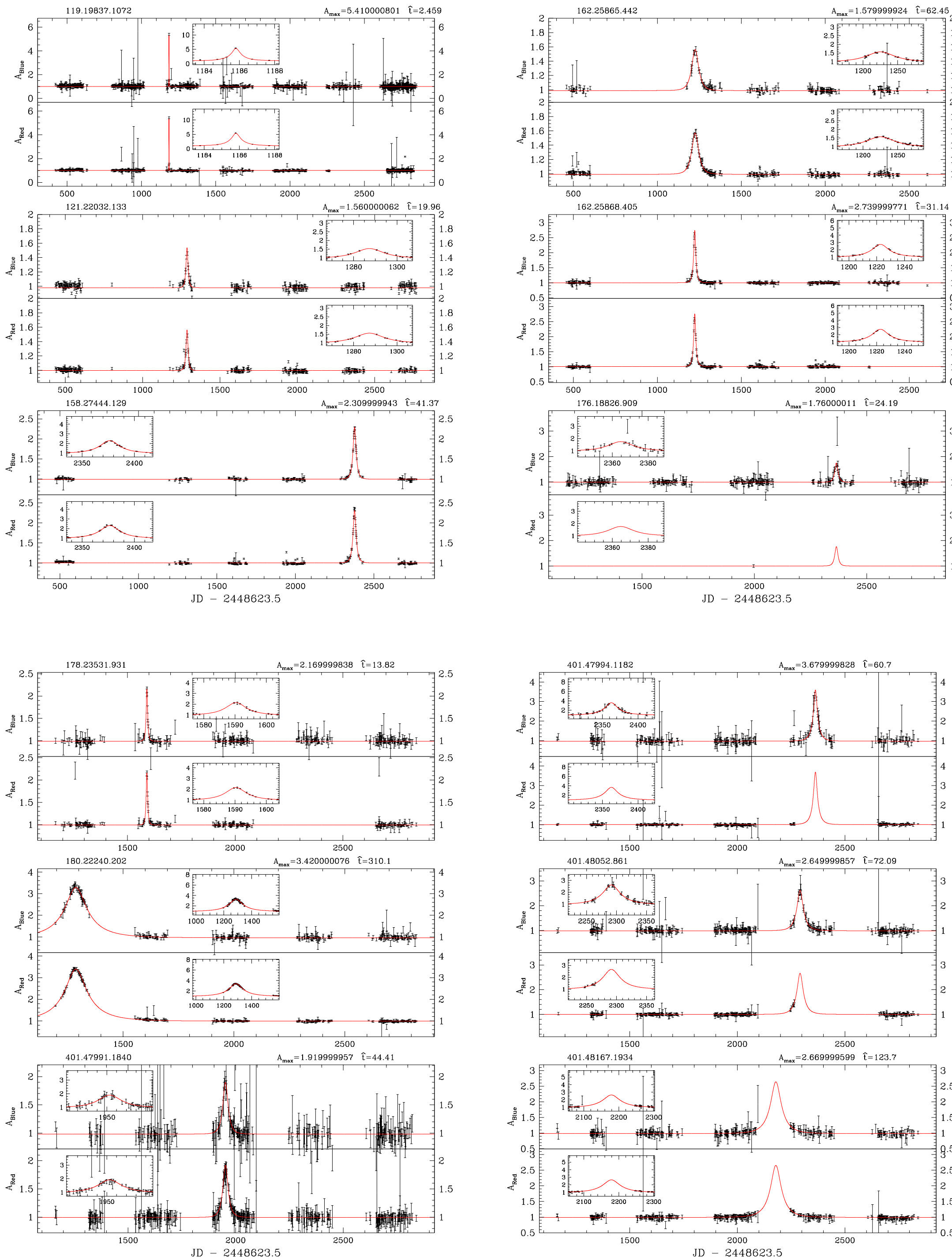

Figure B.3: *continued*

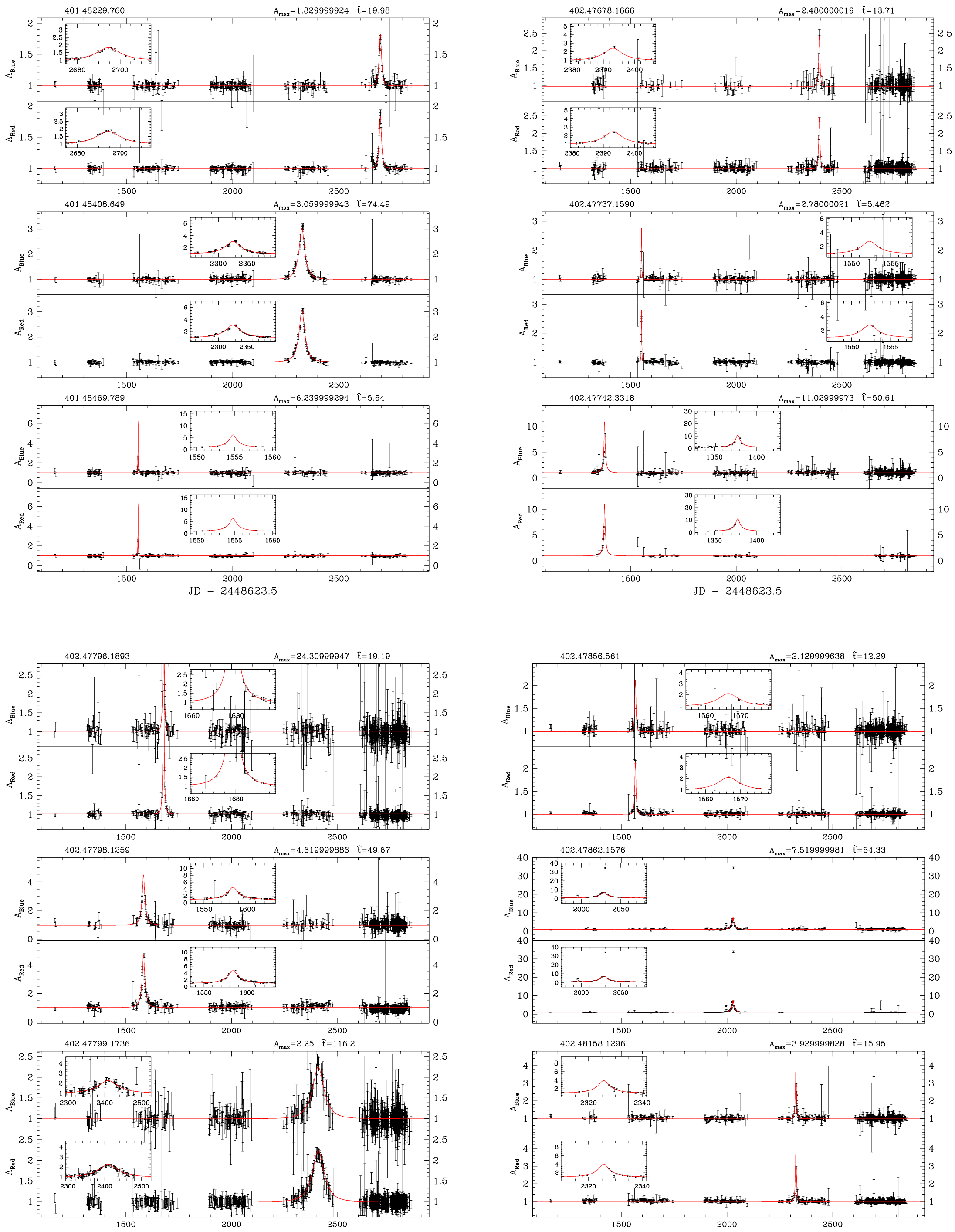

Figure B.3: *continued*

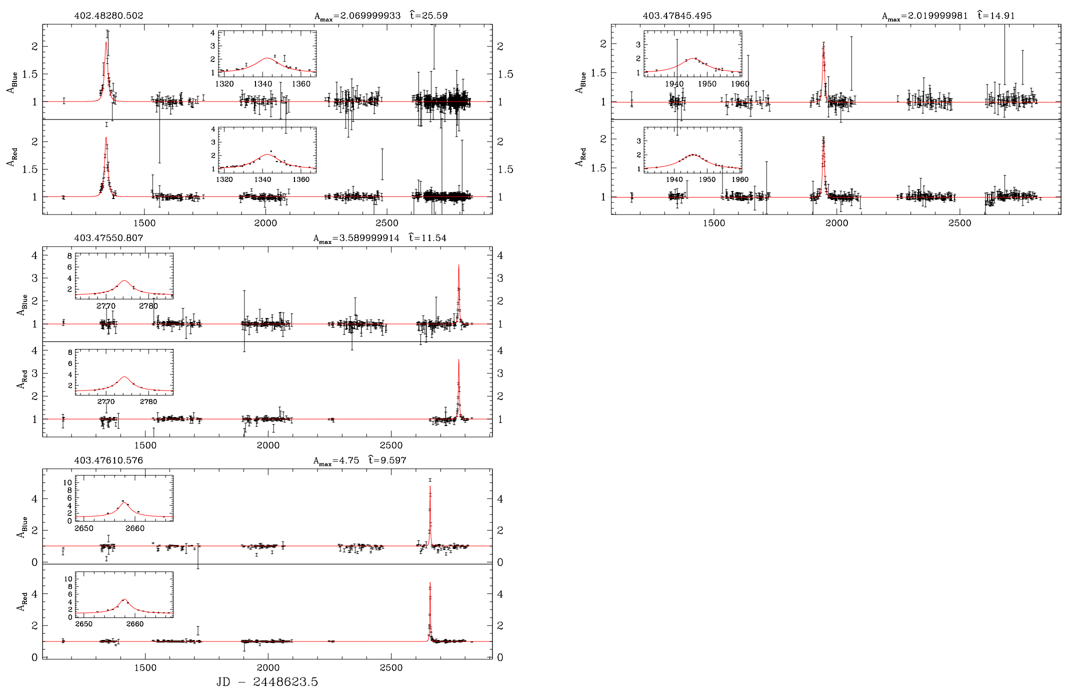

Figure B.3: *concluded*

Bibliography

Afonso, C., Albert, J. N., Alard, C., Andersen, J., Ansari, R., Aubourg, É., Bareyre, P., Bauer, F., Beaulieu, J. P., Blanc, G., Bouquet, A., Char, S., Charlot, X., Couchot, F., Coutures, C., Derue, F., Ferlet, R., Fouqué, P., Glicenstein, J. F., Goldman, B., Gould, A., Graff, D., Gros, M., Haissinski, J., Hamadache, C., Hamilton, J. C., Hardin, D., de Kat, J., Kim, A., Lasserre, T., LeGuillou, L., Lesquoy, É., Loup, C., Magneville, C., Mansoux, B., Marquette, J. B., Maurice, É., Maury, A., Milsztajn, A., Moniez, M., Palanque-Delabrouille, N., Perdereau, O., Prévot, L., Regnault, N., Rich, J., Spiro, M., Tisserand, P., Vidal-Madjar, A., Vigroux, L., & Zylberajch, S. 2003, A&A, 404, 145

Alard, C. 1997, A&A, 321, 424

Alard, C., Mao, S., & Guibert, J. 1995, A&A, 300, L17+

Albrow, M. D., Beaulieu, J.-P., Caldwell, J. A. R., Dominik, M., Gaudi, B. S., Gould, A., Greenhill, J., Hill, K., Kane, S., Martin, R., Menzies, J., Naber, R. M., Pollard, K. R., Sackett, P. D., Sahu, K. C., Vermaak, P., Watson, R., Williams, A., Bond, H. E., & van Bemmel, I. M. 2000, ApJ, 534, 894

Alcock, C., Akerloff, C. W., Allsman, R. A., Axelrod, T. S., Bennett, D. P., Chan, S., Cook, C. H., Freeman, K. C., Griest, K., Marshall, S. L., Park, H. S., Perlmutter, S., Peterson, B. A., Pratt, M. R., Quinn, P. J., Rodgers, A. W., Stubbs, C. W., & Sutherland, W. 1993, Nature, 365, 621

Alcock, C., Allsman, R. A., Alves, D., Axelrod, T. S., Becker, A. C., Bennett, D. P., Cook, K. H., Freeman, K. C., Griest, K., Guern, J., Lehner, M. J., Marshall, S. L., Peterson, B. A., Pratt, M. R., Quinn, P. J., Reiss, D., Rodgers, A. W., Stubbs, C. W., Sutherland, W., Welch, D. L., & The MACHO Collaboration. 1996, ApJ, 463, L67

Alcock, C., Allsman, R. A., Alves, D., Axelrod, T. S., Becker, A. C., Bennett, D. P., Cook, K. H., Freeman, K. C., Griest, K., Guern, J., Lehner, M. J., Marshall, S. L., Peterson, B. A., Pratt, M. R., Quinn, P. J., Rodgers, A. W., Stubbs, C. W., Sutherland, W., Welch, D. L., & The MACHO Collaboration. 1997a, ApJ, 486, 697

Alcock, C., Allsman, R. A., Alves, D., Axelrod, T. S., Bennett, D. P., Cook, K. H., Freeman, K. C., Griest, K., Guern, J., Lehner, M. J., Marshall, S. L., Park, H.-S., Perlmutter, S., Peterson, B. A., Pratt, M. R., Quinn, P. J., Rodgers, A. W., Stubbs, C. W., & Sutherland, W. 1997b, ApJ, 479, 119

Alcock, C., Allsman, R. A., Alves, D. R., Axelrod, T. S., Becker, A. C., Bennett, D. P., Cook, K. H., Freeman, K. C., Griest, K., Gould, A., Guern, J. A., Lehner, M. J., Marshall, S. L., Minniti, D., Peterson, B. A., Popowski, P., Pratt, M. R., Quinn, P. J., Rodgers, A. W., Stubbs, C. W., Sutherland, W., Vandehei, T., Welch, D. L., & The MACHO Collaboration. 1998, ApJ, 494, 396

Alcock, C., Allsman, R. A., Alves, D. R., Axelrod, T. S., Becker, A. C., Bennett, D. P., Cook, K. H., Drake, A. J., Freeman, K. C., Geha, M., Griest, K., Lehner, M. J., Marshall, S. L., Minniti, D., Peterson, B. A., Popowski, P., Pratt, M. R., Nelson, C. A., Quinn, P. J., Stubbs, C. W., Sutherland, W., Tomaney, A. B., Vandehei, T., Welch, D. L., & The MACHO Collaboration. 1999, PASP, 111, 1539

Alcock, C., Allsman, R. A., Alves, D., Axelrod, T. S., Baines, D., Becker, A. C., Bennett, D. P., Bourke, A., Brakel, A., Cook, K. H., Crook, B., Crouch, A., Dan, J., Drake, A. J., Fragile, P. C., Freeman, K. C., Gal-Yam, A., Geha, M., Gray, J., Griest, K., Gurtierrez, A., Heller, A., Howard, J., Johnson, B. R., Kaspi, S., Keane, M., Kovo, O., Leach, C., Leach, T., Leibowitz, E. M., Lehner, M. J., Lipkin, Y., Maoz, D., Marshall, S. L., McDowell, D., McKeown, S., Mendelson, H., Messenger, B., Minniti, D., Nelson, C., Peterson, B. A., Popowski, P., Pozza, E., Purcell, P., Pratt, M. R., Quinn, J., Quinn, P. J., Rhie, S. H., Rodgers, A. W., Salmon, A., Shemmer, O., Stetson, P., Stubbs, C. W., Sutherland, W., Thomson, S., Tomaney, A., Vandehei, T., Walker, A., Ward, K., & Wyper, G. 2000a, ApJ, 541, 270

Alcock, C., Allsman, R. A., Alves, D. R., Axelrod, T. S., Becker, A. C., Bennett, D. P., Cook, K. H., Dalal, N., Drake, A. J., Freeman, K. C., Geha, M., Griest, K., Lehner, M. J., Marshall, S. L., Minniti, D., Nelson, C. A., Peterson, B. A., Popowski, P., Pratt, M. R., Quinn, P. J., Stubbs, C. W., Sutherland, W., Tomaney, A. B., Vandehei, T., & Welch, D. 2000b, ApJ, 542, 281

Alcock, C., Allsman, R. A., Alves, D. R., Axelrod, T. S., Becker, A. C., Bennett, D. P., Cook, K. H., Drake, A. J., Freeman, K. C., Geha, M., Griest, K., Lehner, M. J., Marshall, S. L., Minniti, D., Nelson, C. A., Peterson, B. A., Popowski, P., Pratt, M. R., Quinn, P. J., Stubbs, C. W., Sutherland, W., Tomaney, A. B., Vandehei, T., & Welch, D. L. 2000c, ApJ, 541, 734

Alcock, C., Allsman, R. A., Alves, D. R., Axelrod, T. S., Becker, A. C., Bennett, D. P., Cook, K. H., Drake, A. J., Freeman, K. C., Geha, M., Griest, K., Keller, S. C., Lehner, M. J., Marshall, S. L., Minniti, D., Nelson, C. A., Peterson,

B. A., Popowski, P., Pratt, M. R., Quinn, P. J., Stubbs, C. W., Sutherland, W., Tomaney, A. B., Vandehei, T., & Welch, D. 2001, Nature, 414, 617

Aubourg, E., Bareyre, P., Brehin, S., Gros, M., Lachieze-Rey, M., Laurent, B., Lesquoy, E., Magneville, C., Milsztajn, A., Moscoso, L., Queinnec, F., Rich, J., Spiro, M., Vigroux, L., Zylberajch, S., Ansari, R., Cavalier, F., Moniez, M., Beaulieu, J. P., Ferlet, R., Grison, P., Vidal-Madjar, A., Guibert, J., Moreau, O., Tajahmady, F., Maurice, E., Prevot, L., & Gry, C. 1993, Nature, 365, 623

Beckwith, S. & HUDF Team. 2004, http://www.stsci.edu/hst/udf

Bennett, D. P., Rhie, S. H., Becker, A. C., Butler, N., Dann, J., Kaspi, S., Leibowitz, E. M., Lipkin, Y., Maoz, D., Mendelson, H., Peterson, B. A., Quinn, J., Shemmer, O., Thomson, S., & Turner, S. E. 1999, Nature, 402, 57

Binney, J., Bissantz, N., & Gerhard, O. 2000, ApJ, 537, L99

Bissantz, N., Englmaier, P., Binney, J., & Gerhard, O. 1997, MNRAS, 289, 651

Cavallo, R. M., Cook, K. H., Minniti, D., & Vandehei, T. 2003, in Discoveries and Research Prospects from 6- to 10-Meter-Class Telescopes II. Edited by Guhathakurta, Puragra. Proceedings of the SPIE, Volume 4834, pp. 66-73 (2003)., ed. P. Guhathakurta, 66–73

Chwolson, O. 1924, Astronomische Nachrichten, 221, 329

Cook, K. H. 2005, submitted ApJ

Dalal, N., Holz, D. E., Chen, X., & Frieman, J. A. 2003, ApJ, 585, L11

de Jong, J. T. A., Kuijken, K., Crotts, A. P. S., Sackett, P. D., Sutherland, W. J., Uglesich, R. R., Baltz, E. A., Cseresnjes, P., Gyuk, G., Widrow, L. M., & The MEGA collaboration. 2004, A&A, 417, 461

Di Stefano, R., & Esin, A. A. 1995, ApJ, 448, L1

Eddington, A. S. 1920, Space, time and gravitation. an outline of the general relativity theory (Cambridge Science Classics, Cambridge: University Press, 1920)

Einstein, A. 1911, Annalen der Physik, 35, 898

—. 1915, Sitzungsberichte der Königlich Preußischen Akademie der Wissenschaften (Berlin), Seite 831-839., 831

Evans, N. W., & Belokurov, V. 2002, ApJ, 567, L119

Garnavich, P. M., Jha, S., Challis, P., Clocchiatti, A., Diercks, A., Filippenko, A. V., Gilliland, R. L., Hogan, C. J., Kirshner, R. P., Leibundgut, B., Phillips, M. M., Reiss, D., Riess, A. G., Schmidt, B. P., Schommer, R. A., Smith, R. C., Spyromilio, J., Stubbs, C., Suntzeff, N. B., Tonry, J., & Carroll, S. M. 1998, ApJ, 509, 74

Gould, A., Popowski, P., & Terndrup, D. M. 1998, ApJ, 492, 778

Gould, A., & An, J. H. 2002, ApJ, 565, 1381

Gould, A. 2003, astro-ph/0310577

Griest, K. 1991, ApJ, 366, 412

Griest, K., Alcock, C., Axelrod, T. S., Bennett, D. P., Cook, K. H., Freeman, K. C., Park, H.-S., Perlmutter, S., Peterson, B. A., Quinn, P. J., Rodgers, A. W., Stubbs, C. W., & The MACHO Collaboration. 1991, ApJ, 372, L79

Gyuk, G. 1999, ApJ, 510, 205

Han, C., & Gould, A. 1995, ApJ, 449, 521

Han, C. 1999, MNRAS, 309, 373

—. 2003, ApJ, 592, 172

Holtzman, J. A., Watson, A. M., Baum, W. A., Grillmair, C. J., Groth, E. J., Light, R. M., Lynds, R., & O'Neil, E. J. 1998, AJ, 115, 1946

Holz, D. E., & Hughes, S. A. 2005, ApJ, 629, 15

Ibata, R. A., Gilmore, G., & Irwin, M. J. 1995, MNRAS, 277, 781

James, F. 2003, MINUIT: Function Minimization and Error Analysis Reference Manual, Version 94.1 (Geneva: CERN), http://wwwasdoc.web.cern.ch/wwwasdoc/minuit/minmain.html

Kaiser, N., & Squires, G. 1993, ApJ, 404, 441

Kiraga, M., & Paczyński, B. 1994, ApJ, 430, L101

Lasserre, T., Afonso, C., Albert, J. N., Andersen, J., Ansari, R., Aubourg, É., Bareyre, P., Bauer, F., Beaulieu, J. P., Blanc, G., Bouquet, A., Char, S., Charlot, X., Couchot, F., Coutures, C., Derue, F., Ferlet, R., Glicenstein, J. F., Goldman, B., Gould, A., Graff, D., Gros, M., Haissinski, J., Hamilton, J. C., Hardin, D., de Kat, J., Kim, A., Lesquoy, É., Loup, C., Magneville, C., Mansoux, B., Marquette, J. B., Maurice, É., Milsztajn, A., Moniez, M., Palanque-Delabrouille, N., Perdereau, O., Prévot, L., Regnault, N., Rich, J., Spiro, M., Vidal-Madjar, A., Vigroux, L., Zylberajch, S., & The EROS collaboration. 2000, A&A, 355, L39

Marshall, S. 1994, in IAU Symp. 161: Astronomy from Wide-Field Imaging, 67–+

Metcalf, R. B. 1995, AJ, 110, 869

Mo, H. J., & White, S. D. M. 2002, MNRAS, 336, 112

Nagamine, K., Cen, R., Hernquist, L., Ostriker, J. P., & Springel, V. 2005, ApJ, 627, 608

Nair, V., & Miralda-Escudé, J. 1999, ApJ, 515, 206

Navarro, J. F., Frenk, C. S., & White, S. D. M. 1997, ApJ, 490, 493

Nemiroff, R. J. 1991, A&A, 247, 73

Newton, I. 1704, Opticks

Paczyński, B. 1986, ApJ, 304, 1

—. 1991, ApJ, 371, L63

Paulin-Henriksson, S., Baillon, P., Bouquet, A., Carr, B. J., Crézé, M., Evans, N. W., Giraud-Héraud, Y., Gould, A., Hewett, P., Kaplan, J., Kerins, E., Le Du, Y., Melchior, A.-L., Smartt, S. J., Valls-Gabaud, D., & The POINT-AGAPE Collaboration. 2003, A&A, 405, 15

Perlmutter, S., Aldering, G., della Valle, M., Deustua, S., Ellis, R. S., Fabbro, S., Fruchter, A., Goldhaber, G., Groom, D. E., Hook, I. M., Kim, A. G., Kim, M. Y., Knop, R. A., Lidman, C., McMahon, R. G., Nugent, P., Pain, R., Panagia, N., Pennypacker, C. R., Ruiz-Lapuente, P., Schaefer, B., & Walton, N. 1998, Nature, 391, 51

Perlmutter, S., Aldering, G., Goldhaber, G., Knop, R. A., Nugent, P., Castro, P. G., Deustua, S., Fabbro, S., Goobar, A., Groom, D. E., Hook, I. M., Kim, A. G., Kim, M. Y., Lee, J. C., Nunes, N. J., Pain, R., Pennypacker, C. R., Quimby, R., Lidman, C., Ellis, R. S., Irwin, M., McMahon, R. G., Ruiz-Lapuente, P., Walton, N., Schaefer, B., Boyle, B. J., Filippenko, A. V., Matheson, T., Fruchter, A. S., Panagia, N., Newberg, H. J. M., Couch, W. J., & The Supernova Cosmology Project. 1999, ApJ, 517, 565

Popowski, P., Vandehei, T., Griest, K., Alcock, C., Allsman, R. A., Alves, D. R., Axelord, T. S., Becker, A. C., Bennett, D. P., Cook, K. H., Drake, A. J., Freeman, K. C., Geha, M., Lehner, M. J., Marshall, S. L., Minniti, D., Nelson, C. A., Peterson, B. A., Quinn, P. J., Stubbs, C. W., Sutherland, W., & Welch, D. T. 2001a, in ASP Conf. Ser. 239: Microlensing 2000: A New Era of Microlensing Astrophysics, ed. J. W. Menzies & P. D. Sackett, 244

Popowski, P., Vandehei, T., Griest, K., Alcock, C., Allsman, R. A., Alves, D. R., Axelord, T. S., Becker, A. C., Bennett, D. P., Cook, K. H., Drake, A. J., Freeman, K. C., Geha, M., Lehner, M. J., Marshall, S. L., Minniti, D., Nelson, C. A., Peterson, B. A., Quinn, P. J., Stubbs, C. W., Sutherland, W., & Welch, D. T. 2001b, in ASP Conf. Ser. 245: Astrophysical Ages and Times Scales, ed. T. von Hippel, C. Simpson, & N. Manset, 358

Popowski, P. 2002, preprint, astro-ph/0205044

Popowski, P., Cook, K. H., & Becker, A. C. 2003, AJ, 126, 2910

Popowski, P. 2004, talk presented at the Hawaiian Gravitational Microlensing Workshop

Popowski, P., Griest, K., Thomas, C. L., Cook, K. H., Bennett, D. P., Becker, A. C., Alves, D. R., Minniti, D., Drake, A. J., Alcock, C., Allsman, R. A., Axelrod, T. S., Freeman, K. C., Geha, M., Lehner, M. J., Marshall, S. L., Nelson, C. A., Peterson, B. A., Quinn, P. J., Stubbs, C. W., Sutherland, W., Vandehei, T., & Welch, D. 2005, ApJ, 631, 879

Press, W. H., & Schechter, P. 1974, ApJ, 187, 425

Riess, A. G., Filippenko, A. V., Challis, P., Clocchiatti, A., Diercks, A., Garnavich, P. M., Gilliland, R. L., Hogan, C. J., Jha, S., Kirshner, R. P., Leibundgut, B., Phillips, M. M., Reiss, D., Schmidt, B. P., Schommer, R. A., Smith, R. C., Spyromilio, J., Stubbs, C., Suntzeff, N. B., & Tonry, J. 1998, AJ, 116, 1009

Schechter, P. L., Mateo, M., & Saha, A. 1993, PASP, 105, 1342

Schneider, P., Ehlers, J., & Falco, E. E. 1992, Gravitational Lenses (Gravitational Lenses, XIV, 560 pp. 112 figs.. Springer-Verlag Berlin Heidelberg New York. Also Astronomy and Astrophysics Library)

Sersic, J. L. 1968, Atlas de galaxias australes (Cordoba, Argentina: Observatorio Astronomico, 1968)

Sevenster, M. N., & Kalnajs, A. J. 2001, AJ, 122, 885

Sheth, R. K., & Tormen, G. 1999, MNRAS, 308, 119

Soldner, J. 1804, Berliner Astron. Jahrb., 161

Stanek, K. Z. 1996, ApJ, 460, L37+

Sterken, C., & Jaschek, C. 1996, Light Curves of Variable Stars, A Pictorial Atlas (Light Curves of Variable Stars, A Pictorial Atlas, ISBN 0521390168, Cambridge University Press, 1996.)

Stubbs, C. W., Marshall, S., Cook, K. H., Hills, R. F., Noonan, J., Akerlof, C. W., Alcock, C. R., Axelrod, T. S., Bennett, D., Dagley, K., Freeman, K. C., Griest, K., Park, H.-S., Perlmutter, S., Peterson, B. A., Quinn, P. J., Rodgers, A. W., Sosin, C., & Sutherland, W. J. 1993, in Proc. SPIE Vol. 1900, p. 192-204, Charge-Coupled Devices and Solid State Optical Sensors III, Morley M. Blouke; Ed., 192–204

Sumi, T., Abe, F., Bond, I. A., Dodd, R. J., Hearnshaw, J. B., Honda, M., Honma, M., Kan-ya, Y., Kilmartin, P. M., Masuda, K., Matsubara, Y., Muraki, Y., Nakamura, T., Nishi, R., Noda, S., Ohnishi, K., Petterson, O. K. L., Rattenbury, N. J., Reid, M., Saito, T., Saito, Y., Sato, H., Sekiguchi, M., Skuljan, J., Sullivan, D. J., Takeuti, M., Tristram, P. J., Wilkinson, S., Yanagisawa, T., & Yock, P. C. M. 2003, ApJ, 591, 204

Sumi, T., Woźniak, P. R., Udalski, A., Szymański, M., Kubiak, M., Pietrzyński, G., Soszyński, I., Żebruń, K., Szewczyk, O., Wyrzykowski, Ł., & Paczyński, B. 2006, ApJ, 636, 240

Thomas, C. L., Griest, K., Popowski, P., Cook, K. H., Drake, A. J., Minniti, D., Myer, D. G., Alcock, C., Allsman, R. A., Alves, D. R., Axelrod, T. S., Becker, A. C., Bennett, D. P., Freeman, K. C., Geha, M., Lehner, M. J., Marshall, S. L., Nelson, C. A., Peterson, B. A., Quinn, P. J., Stubbs, C. W., Sutherland, W., Vandehei, T., & Welch, D. L. 2005, ApJ, 631, 906

Tikhov, G. A. 1938, Izvestiya Glavnoj Astronomicheskoj Observatorii v Pulkove, 16

Udalski, A., Szymanski, M., Kaluzny, J., Kubiak, M., Krzeminski, W., Mateo, M., Preston, G. W., & Paczynski, B. 1993, Acta Astronomica, 43, 289

Udalski, A., Szymanski, M., Stanek, K. Z., Kaluzny, J., Kubiak, M., Mateo, M., Krzeminski, W., Paczynski, B., & Venkat, R. 1994a, Acta Astronomica, 44, 165

Udalski, D., Szymanski, M., Kaluzny, J., Kubiak, M., Mateo, M., & Krzeminski, W. 1994b, ApJ, 426, L69+

Vandehei, T. 2000, Ph.D. Thesis

Woźniak, P., & Paczyński, B. 1997, ApJ, 487, 55

Zhao, H., Spergel, D. N., & Rich, R. M. 1995, ApJ, 440, L13

Zhao, H., & Mao, S. 1996, MNRAS, 283, 1197